

Exploring Charge Transport Properties in Group II-VI Semiconductors and their Graphene Composites for Advanced Dye Wastewater Treatment

A Thesis submitted to

Jadavpur University



by

Dhananjay Das

in partial fulfillment of the requirements for the degree of

Doctor of Philosophy (Ph.D.)

(Science)

Department of Physics

Jadavpur University

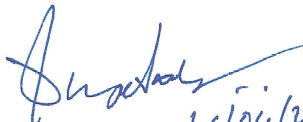
Kolkata, India

April 2024



CERTIFICATE FROM THE SUPERVISOR(S)

This is to certify that the thesis entitled “**Exploring Charge Transport Properties in Group II-VI Semiconductors and their Graphene Composites for Advanced Dye Wastewater Treatment**” submitted by Sri **Dhananjoy Das** who got his name registered on **26.02.2018** (Index No.: 96/18/Phys./25) for the award of Ph. D. (Science) degree of Jadavpur University, is absolutely based upon his own work under the supervision of **Prof. Puspendu Sahu** and **Prof. Partha Pratim Ray** and that neither this thesis nor any part of it has been submitted for either any degree/diploma or any other academic award anywhere before.


16/04/2024
(Prof. Puspendu Sahu)



Dr. Puspendu Sahu
Professor
Department of Physics
Jadavpur University
Kolkata - 700 032


(Prof. Partha Pratim Ray)



16/4/24
Dr. Partha Pratim Ray
Professor
Department of Physics
Jadavpur University

This thesis is dedicated to my parents.

For their endless love, support and encouragement.

ACKNOWLEDGMENT

Embarking on the journey of a Ph.D. is a monumental endeavour, and as I stand at the culmination of this challenging yet rewarding expedition, I am deeply humbled and profoundly grateful for the courageous support and guidance that have shaped this academic odyssey.

First and foremost, I express my deepest gratitude to my supervisors, Prof. Puspendu Sahu and Prof. Partha Pratim Ray. Their mentorship and expertise have been the guiding forces throughout my Ph.D. journey. Their invaluable insights, constructive feedback, and unwavering encouragement have been instrumental in shaping the trajectory of my research. I am deeply appreciative of the time and effort they dedicated to providing constructive criticism, which significantly enhanced the quality and rigour of this research work. Their mentorship has not only enriched my academic journey but has also contributed significantly to my personal and professional growth. I am profoundly grateful for the opportunity to learn from their wisdom and expertise.

I would like to extend my heartfelt appreciation to Prof. Sanjay Kumar; his wisdom and insights have greatly enriched my learning experience at the university. I have always cherished the conversations with him, where Prof. Sanjay Kumar generously shared his knowledge and provided invaluable advice. Throughout my Ph.D. tenure, I also had the privilege to collaborate with esteemed professionals, including Prof. Dirtha Sanyal (VECC, Kolkata), Prof. Chittaranjan Sinha (Jadavpur University, Kolkata), Dr. Saikat Kumar Seth (Jadavpur University, Kolkata), Prof. Shouvik Chattopadhyay (Jadavpur University, Kolkata), Prof. Mohammad Hedayetullah Mir (Aliah University, Kolkata) and Prof. Subrata Mukhopadhyay (Jadavpur University, Kolkata). Working alongside these experts was not only a great experience but also a pathway to acquiring invaluable knowledge and wisdom.

I acknowledge the support and assistance from the Department of Physics, including former and present Heads, office staff, and the research and Ph.D. sections. Their administrative support has been invaluable. I extend my appreciation to Prof. Sukhen Das and Dr. Saikat Kumar Seth for their valuable suggestions and generous provision of lab facilities. Special recognition is due to Mr. Manojit Dey (DEO, Research Section) and Mr. Azizur Rahaman (Ph. D. Cell) for their indispensable assistance in administrative matters. Moreover, it is essential to mention the financial support provided by UGC through the NET-JRF program, which has been crucial in facilitating my research endeavours. I am grateful for the opportunities and resources made available through their support.

Sincere thanks are extended to all my lab mates, a supportive community that has been instrumental in my academic journey. Special recognition goes to Dr. Arka Dey, Dr. Sayantan Sil and Dr. Joydeep Datta, who, transcending their roles as lab mates, assumed the roles of elder brothers, providing invaluable guidance and support throughout my research life. I am equally thankful for the wisdom and suggestions generously shared by other seniors, including Dr. Animesh Layek, Dr. Joydeep Dhar, Dr. Mrinmay Das, Dr. Rajkumar Jana and Dr. Nur Amin Hoque. I am grateful to Dr. Shankha Sanyal, with whom I've cherished engaging conversations and who has been very supportive in various matters.

With great pleasure, I extend my thanks to my fellow lab mates who have contributed immensely to this thesis. The bond of friendship cultivated in the laboratory and the fruitful scientific interactions have collectively enhanced my Ph.D. experience. Unparalleled and special mention goes to my labmate Mr. Mainak Das, whose steady support has been a source of courage

during the most difficult stages of Ph.D. journey. Fruitful discussions on a myriad of topics and the creation of precious moments throughout my research life were made possible with his companionship. My gratitude further extends to other lab mates - Mr. Animesh Biswas, Ms. Pubali Das, Ms. Baishakhi Pal, Dr. Jitendra Saha, Mr. Ramjan Sk and Mr. Supravat Ghosh, for the camaraderie and the shared joyful moments that have defined this collective experience.

Amidst the bustling life of a Ph.D. student, my time at Jadavpur University has proven to be anything but monotonous. Instead, it has unfolded as a captivating experience, painted with a myriad of colours, all thanks to my remarkable friends who have infused my life with vibrancy and joy. I count myself fortunate to be surrounded by individuals like Mr. Tousif Riaz, Mr. Saikat Shyamal, Ms. Soma Rani Das, Ms. Somashree Biswas, Mr. Dhananjoy Mondal, Mr. Tanmoy Chakraborty and Mr. Gopal Rana; whose camaraderie has made my journey both colourful and enjoyable. Special recognition is reserved for Ms. Moisilee Dutta, whose enchanting Sarod playing injected a refreshing melody into the otherwise toneless rhythm of Ph.D. life.

I would like to extend my sincere appreciation to Mr. Dipak Barman, my friend from college days, with whom I shared unforgettable moments and forged a lasting friendship. I would like to thank Mr. Pawan Kumar Kuldeep, my former hostel roommate from Jaipur, Rajasthan; with whom I shared timeless memories in IIT Guwahati. Despite the passage of over a decade, our friendship remains steadfast, and we continue to exchange personal experiences and support each other. I would like to express my deepest gratitude to Dr. Dipankar Bain, my former senior roommate at Jadavpur, for his invaluable support and companionship during the challenging times of the COVID-19 pandemic. Throughout our shared experiences, he proved to be not only a dependable roommate but also a source of inspiration and learning.

My deepest gratitude is extended to my family and friends for their unwavering encouragement, understanding, and patience throughout this transformative journey. Your steadfast belief in my abilities and the constant wellspring of emotional support have served as an unyielding source of strength.

To my partner, Ms. Plabani Ray, your love, encouragement, and profound understanding have been my anchor during the most challenging phases of this Ph.D. Your unwavering support has not only eased the difficulties but has also added a profound and meaningful dimension to this academic pursuit.

Lastly, heartfelt appreciation is directed to my parents, whose sacrifices, encouragement, and unwavering belief in my potential have been the driving forces propelling my pursuit of knowledge. Their enduring support and sacrifices continue to be a wellspring of inspiration. Special respect and gratefulness are owed to my uncle, Shri. Bankim Chandra Das, for his role as a guide, philosopher and a constant source of inspiration. Additionally, words fall short of expressing my gratitude to my dearest sister, whose contribution towards achieving this Ph.D. goal is immeasurable.

This Ph.D. journey has been a transformative experience, and I am grateful to each individual and entity that has played a role, big or small, in this academic endeavour.



(Dhananjoy Das)

Table of Contents

List of Abbreviations	i
Preface	iii

Chapter 1: Introduction to Graphene, Group II-VI Semiconductors and their Graphene Composites

1.1. Introduction	3
1.2. Discovery and Historical Overview of Graphene	4
1.3. Synthesis of Graphene	5
1.3.1. Mechanical Exfoliation or Cleavage Method	6
1.3.2. Epitaxial Growth	7
1.3.3. Chemical Vapour Deposition (CVD)	8
1.3.4. Chemical Derivation	8
1.3.5. Alternative Methods	10
1.4. Properties of Graphene	11
1.5. Group II–VI Semiconductors	12
1.5.1. Zinc Telluride (ZnTe)	13
1.5.2. Zinc selenide (ZnSe)	14
1.6. Graphene-based Inorganic Composites	14
1.6.1. Zinc Telluride (ZnTe) and Graphene Oxide	16
1.7. Synthesis of Graphene-based Composites	16
1.7.1. Hydrothermal Method	17
1.8. Application of Graphene and its Composites	19
1.8.1. High-speed Electronics	19
1.8.2. Solar Cells	20
1.8.3. Data Storage	20
1.8.4. LCD Smart Windows and OLED Displays	20
1.8.5. Supercapacitors	21
1.8.6. Schottky Barrier Diodes	21
1.8.7. Photocatalysis and Wastewater Treatment	22
References	23

Chapter 2: Schottky Barrier Diodes: Theoretical Overview, Fabrication Techniques with an Introductory Insights into their Electrical Study, Impedance Spectroscopy and Positron Annihilation Spectroscopy

2.1. Introduction of Schottky Barrier Diodes (SBD)	31
2.1.1. Energy-Band Relation	31
2.1.2. Modifications of Schottky Theory	37
2.2. Classification of Metal-Semiconductor Interfaces	38
2.3. Contacts with Surface States and an Insulating Interfacial Layer	39
2.4. Fabrication Process of Schottky Diodes	40
2.4.1. Aluminium in Device Fabrication	42
2.4.2. Glass Substrate Coated with Indium Tin Oxide (ITO)	42
2.4.3. Metal Deposition	42
2.5. Electrical Studies of Schottky Barrier Diodes	43
2.5.1. Evaluation of Ideality Factor, Barrier Height and Series Resistance	43

2.5.2. Estimation of Mobility and Transit Time	45
2.5.3. Capacitance-Voltage Measurement	46
2.5.4. Photoelectric Measurement	46
2.5.5. Application of Schottky Diodes	47
2.6. Impedance Spectroscopy	47
2.6.1. Associated Functions in Impedance Spectroscopy	48
2.6.2. Equivalent Circuit Model	49
2.7. Positron Annihilation Spectroscopy	51
2.7.1. Positron Annihilation Process	51
2.7.2. Doppler Broadening Spectroscopy	58
References	61

Chapter 3: Exploring Reduced Graphene Oxide-Zinc Telluride Nanocomposites for Enhanced Charge Transfer in Optoelectronic Devices: A Study of the Metal-Semiconductor Interfaces via Equivalent Circuit Model

3.1. Introduction	65
3.2. Materials and Methods	66
3.2.1. Materials	66
3.2.2. Synthesis of ZnTe	66
3.2.3. Synthesis of GO	66
3.2.4. Synthesis of RGO-ZnTe	67
3.2.5. Fabrication of Schottky Devices	67
3.3. Material Characterization Techniques	68
3.4. Results and Discussion	69
3.4.1. Structural Properties	69
3.4.2. Morphological Studies	69
3.4.3. Impedance Spectroscopy Analysis	71
3.4.4. Current-Voltage (I-V) Measurement	74
3.5. Conclusions	78
References	79

Chapter 4: Effect of Higher Carrier Mobility of Reduced Graphene Oxide-Zinc Telluride Nanocomposite Towards Efficient Charge Transfer Facility and The Photodecomposition of Rhodamine B

4.1. Introduction	83
4.2. Materials and Methods	84
4.3. Material Characterization Techniques	84
4.4. Results and Discussion	85
4.4.1. Structural Properties	85
4.4.2. Optical Properties	90
4.4.3. Thermal Stability Study	91
4.4.4. BET Surface Area Studies	92
4.4.5. Electrical Properties	93
4.4.6. Photocatalytic Activity	97
4.5. Conclusion	103
References	104

Chapter 5: Investigating Carrier Mobility in Hollow and Mesoporous ZnSe/ZnTe Heterostructures: Microscopic Observations of Swift Charge Transfer and Visible-Light-Driven Dye Decomposition

5.1. Introduction	109
5.2. Experimental Section	110
5.2.1. Materials	110
5.2.2. Synthesis of ZnSe/ZnTe Heterostructures	110
5.2.3. Fabrication of Schottky Devices	111
5.3. Materials Characterization Techniques	111
5.4. Results and Discussion	112
5.4.1. Structural Properties	112
5.4.2. Optical Properties	118
5.4.3. Cyclic Voltammetry and Alignment of Energy Levels	119
5.4.4. Surface Area (BET) Analysis	120
5.4.5. Electrical Study	121
5.4.6. Photocatalytic Activity	124
5.5. Conclusion	130
References	132

Chapter 6: From Electron Density to Defect Insights: A Comprehensive Study of ZnSe/ZnTe Heterostructures via Positron Annihilation Spectroscopy

6.1. Introduction	137
6.2. Experimental	138
6.3. Materials Characterization Techniques	138
6.4. Results and Discussion	139
6.4.1. Structural Properties	139
6.4.2. Positron Annihilation Lifetime Spectroscopy (PALS)	139
6.4.3. Coincidence Doppler Broadening (CDB) Spectroscopy	141
6.5. Conclusion	142
References	143

Chapter 7: Summary and Future Outlook

7.1. Summary	147
7.2. Future Outlook	149

List of Publications	155
List of Presentation/Participation in Conferences/Workshops	158

List of Abbreviations

3-D	Three Dimensional
AC	Alternating Current
B. E.	Binding Energy
BET	Brunauer–Emmett–Teller
CB	Conduction Band
CNT	Carbon Nanotube
CV	Cyclic Voltammetry
CVD	Chemical Vapour Deposition
DC	Direct Current
DI	Deionized
DMF	Dimethyl formamide
EDX	Energy Dispersive X-ray Spectroscopy
EIS	Electrochemical Impedance Spectroscopy
e-h⁺	Electron-hole
FEG-TEM	Field Emission Gun Transmission Electron Microscopy
PVD	Physical Vapour Deposition
GO	Graphene oxide
HRTEM	High Resolution Transmission Electron Microscopy
HT	Hydrothermal
IPA	Isopropyl alcohol
I-V	Current-voltage
IR	Infrared
IS	Impedance Spectroscopy
ITO	Indium tin oxide
JCPDS	Joint Committee on Powder Diffraction Standards
kV	Kilovolt
LED	Light Emitting Diode
LUMO	Lowest Unoccupied Molecular Orbital
MS	Metal-Semiconductor
NCs	Nanocomposites
NPs	Nanoparticles
OHT	One-pot hydrothermal
PL	Photoluminescence
R.T.	Room temperature
RGO	Reduced graphene oxide
Rh B	Rhodamine B
R-ZT	Reduced graphene oxide-zinc telluride
SAED	Selected Area Electron Diffraction
SDs	Schottky Diodes
SHE	Standard Hydrogen Electrode
SMU	Source Measuring Unit
SCLC	Space Charge Limited Current
S.I.	Supplementary Information

TE	Thermionic Emission
TEM	Transmission Electron Microscopy
TGA	Thermogravimetric Analysis
UV	Ultraviolet
VB	Valence Band
wt%	Weight Percent
XPS	X-ray Photoelectron Spectroscopy
XRD	X-ray Diffraction

Preface

In the 21st century, the release of dye-containing wastewater into water bodies, primarily by textile industries, has emerged as a significant environmental concern, resulting in diverse ecological issues. Advanced oxidation processes (AOPs), particularly photo-induced catalytic decomposition, have gained prominence as an economical and environmentally friendly approach to wastewater treatment. While metal oxides and chalcogenides, like titanium dioxide (TiO_2), zinc oxide (ZnO), zinc sulphide (ZnS), zinc telluride (ZnTe) and zinc selenide (ZnSe) have been employed for photocatalytic dye degradation, their limitations, such as low surface-to-volume ratio and short lifetimes of photo-generated electron-hole pairs, have led to the exploration of remedial techniques. Two effective approaches identified include synthesizing graphene-based composites of ZnTe and constructing a heterojunction microstructure of two different compound semiconductors, i.e. ZnSe/ZnTe . All of our research works based on reduced graphene oxide (RGO), zinc telluride (ZnTe) and zinc selenide (ZnSe), are compiled and organized in this thesis into 7 chapters, each contributing to a deeper understanding of these effective approaches.

Chapter 1 provides an overview of the properties and synthesis methods of graphene since its 2004 discovery. The unique characteristics of graphene, its versatile role in synthesizing inorganic nanocomposites, and its applications in wastewater management are discussed. A comprehensive review of II-VI semiconductors, focusing on ZnSe , ZnTe , and their graphene composites, is presented.

Chapter 2 introduces the theory of Schottky barrier formation, the fabrication techniques of Schottky diodes, and their electrical study. The theoretical background of impedance spectroscopy and positron annihilation spectroscopy is briefly outlined.

Chapter 3 is dedicated to the synthesis of reduced graphene oxide (RGO), zinc telluride (ZnTe), and their composite (RGO-ZnTe); this chapter explores the fabrication of Schottky barrier diodes using pristine ZnTe and RGO-ZnTe . A thorough analysis of charge transfer properties and examination of metal-semiconductor interfaces via bias-dependent impedance spectroscopy provide valuable insights into the development of optoelectronic device applications.

Chapter 4 investigates the influence of enhanced carrier mobility of reduced graphene oxides on the photo-degradation of azo dyes. Current-voltage characteristics of ZnTe and RGO-ZnTe Schottky devices, along with an analysis of charge transport parameters, contribute to a nuanced understanding. The chapter extends to the simulated solar light-induced photocatalytic performance of both materials in the degradation of azo dye (RhB). A comprehensive analysis is presented to elucidate the role of carriers' mobility in extending the photo-induced charge separation, thereby promoting efficient charge transfer and enhancing the photo-degradation process.

Chapter 5 introduces the incorporation of ZnSe into ZnTe to enhance overall charge separation, aiming for maximum efficiency in the catalytic degradation of the dyes. Unlike the use of graphene oxides in previous chapters, this chapter explores the charge transfer kinetics in the ZnSe/ZnTe heterojunction structure. Furthermore, the chapter delves into a detailed discussion on the dependency of morphology and surface area of hybrid ZnSe/ZnTe catalysts on degradation efficiency. The study utilizes the spatial-charge-limited conduction (SCLC) theory to extract the mobility of each catalyst, offering a nuanced exploration of how charge carrier mobility influences photocatalytic degradation efficiency. This unique interpretation goes beyond conventional macroscopic parameters, emphasizing microscopic parameters like mobility and transit time, crucial for comprehending the photocatalytic process.

Chapter 6 presents a concise analysis of Positron Annihilation Spectroscopy (PAS) and contributes to a comprehensive understanding of the ZnSe/ZnTe heterostructures, synthesized and applied in photocatalysis in Chapter 5. Using PAS, the elucidation of the electron density and defect insights was made to correlate the outcomes we observed in the preceding chapter.

Chapter 7 encapsulates the entire research, offering a succinct conclusion to the undertaken research. This chapter also marks a pivotal moment as we look ahead to future directions. Our focus shifts towards leveraging impedance spectroscopy (IS) and capacitance-voltage (C-V) measurements to gain deeper insights into the electrical and charge transport characteristics of the ZnSe/ZnTe-based Schottky devices.

All the references cited in this thesis are given in the following format:

Journals: Authors, |Journal Name. |**Volume**, | Pages |(Year) |.

Example: D. C. Marcano, D. V. Kosynkin, J. M. Berlin, A. Sinitskii, Z. Sun, A. Slesarev, L. B. Alemany, W. Lu, and J. M. Tour, ACS Nano **4**, 4806 (2010).

Books: Authors, |Title |Edition ed. |(Year) |.

Example: S. M. Sze, Phys. Semicond. Devices Second Ed. (1981).

16th April, 2024

Kolkata, India.

Dhananjoy Das

(Dhananjoy Das)

Introduction to Graphene, Group II-VI Semiconductors and their Graphene Composites

Chapter 1

1.1. Introduction

Every few years, a unique material with extraordinary properties emerges, capturing the imagination of the global scientific community. In 2004, graphene, a sensational material, was discovered, setting off waves of excitement in the research community [1–3]. Graphene's journey began with its separation in 2004, using the 'Scotch Tape' method, developed by Geim and Novoselov [4]. Since then, the study highlighting its distinctive physical, mechanical, and electrical properties, attributed to the π -conjugation extending to long range, has led to an exponential acceleration in the exploration on this material [5–7]. The number of publications on graphene and its applications became so overwhelming that it exceeded 40 publications per day in 2013 [1]. Graphene, a 2-D honeycomb-like structure with sp^2 -hybridized carbon (C) atoms, serves as the fundamental building block for all graphitic carbon forms [8]. While naturally supposed to consist of a single layer sheet, there are also significant concerns in two-layer or few-layer graphene. Graphene sheets can either be layered to form 3-D graphitic structures, rolled or wrapped to obtain 1-dimensional nanotubes and zero-dimensional fullerenes, respectively (Fig. 1.1). Over the last decade, graphene research has promised numerous potential applications, ranging from longer-lasting batteries [9] and Schottky diodes [10] to solar cells [11], preventive measures of corrosion [12], circuit boards [13], display panels [14] and various advancements in medicinal technologies [15].

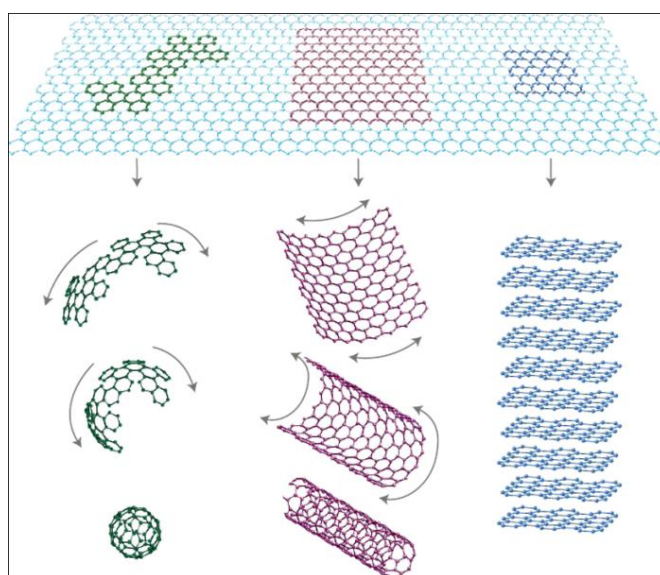


Fig. 1.1: Graphene: the parent of all graphitic forms: fullerene (bottom left); carbon nanotubes (CNT) (bottom centre); and graphite (bottom right). (Adapted from Ref. [7])

The natural compatibility of graphene with thin film processing facilitates its integration within the framework of current semiconducting device technologies. Additionally, it is easily scalable, exhibits minimal contact resistance when interfacing with commonly used metals and can form rectifying junctions with several semiconductor materials. Given these intriguing properties, the synthesis of graphene-inorganic semiconductor nanocomposite materials has garnered significant attention [16]. Inorganic semiconductors play a crucial role in optoelectronic and electrochemical device applications, as well as in the exploration of micro- and nanoscale phenomena. Their significance lies in investigating the dependence of device functional properties on the size and dimensionality of particles. Inorganic semiconductors possess a low work function, high mechanical stability, and a high aspect ratio, making their inherent nanostructure exceptionally suitable for a broad range of applications in electronic systems [17]. The primary motivation for incorporating graphene with inorganic semiconductors has been to realize extensive integration of nano-electronic devices [18]. The introduction of graphene to inorganic semiconductors can prompt charge transport in composite systems, a highly advantageous aspect for electronic devices. This thesis will delve into the synthesis of graphene and its inorganic semiconducting nanocomposites, providing detailed characterizations. The main emphasis will be on implementing the synthesized graphene-based nanocomposites for the photocatalysis of azo dyes and Schottky diode applications.

1.2. Discovery and Historical Overview of Graphene

Understanding the course of graphene research begins with recognizing graphene as the minimal layer limit of graphite. Reports on progressively fewer layers of graphite had been documented for years until a pivotal moment in 2004 when Geim and his colleagues at Manchester University propelled graphene to prominence. In that breakthrough year, they successfully isolated single-layer samples from graphite using the widely accepted 'Scotch Tape method' (Fig. 1.2) [19,20].

Graphite, a naturally occurring mineral known for nearly 500 years, gained significance during the Middle Ages due to weak dispersion forces between its sheets and its layered structure, making it ideal for manufacturing marking instruments. Its unique properties, including high in-plane electrical conductivity ($\sim 10^4 \text{ } \Omega^{-1}\text{cm}^{-1}$) and thermal conductivity ($\sim 3000 \text{ W/mK}$), have led to its diverse applications, such as electrodes and

industrial blast furnaces [21,22]. The global demand for graphite exceeds 1 million tons annually.

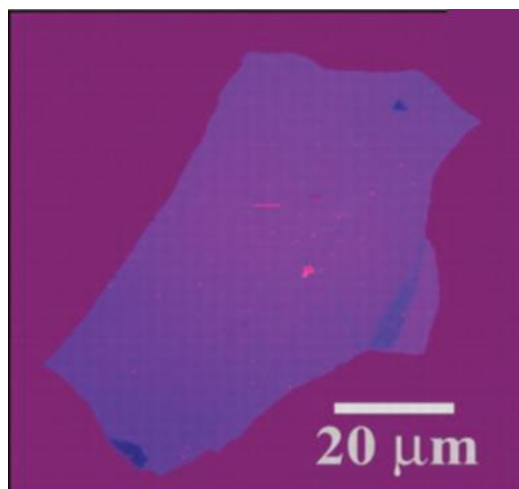


Fig. 1.2: The single (mono)-layer graphene, first discovered by Geim and his colleagues at Manchester University. The image displays a few-layer graphene flakes, with enhanced optical contrast achieved through an interference effect at a meticulously selected oxide thickness. (Adapted from Ref. [4])

1.3. Synthesis of Graphene

Various methodologies have been employed for the synthesis of graphene. The quest for producing ultra-thin carbon films has been a longstanding endeavour employing diverse techniques. Noteworthy historical milestones include the synthesis of graphite oxide in the late 1850s by Brodie [23] and in 1898 by Staudenmaier [24]. The renowned Hummers method, an independent synthesis of graphite oxide by W.S. Hummers in 1958 [25], has gained widespread application. In 1962, reports surfaced on the synthesis of chemically reduced graphene oxides [26]. A significant advancement came in 1975 when A.J. Van Bommel et al. successfully produced monolayer graphene utilizing silicon carbide [27]. However, these early reports fell short in elucidating the distinctive properties of graphene [1].

Mechanical exfoliation of layered compounds aimed to yield thin samples has also been explored. In 1999, Ruoff's group employed an atomic force microscope (AFM) tip for manipulating tiny pillars into highly ordered pyrolytic graphite (HOPG) through plasma etching [28]. Despite their efforts, the thinnest slab produced exceeded 200 nm, equivalent to nearly 600 layers. Subsequently, Kim et al. enhanced this approach by transferring pillars to a tipless cantilever and imprinting the slabs onto SiO₂. This improvement led to the achievement of slabs as thin as 10 nm, approximately equivalent

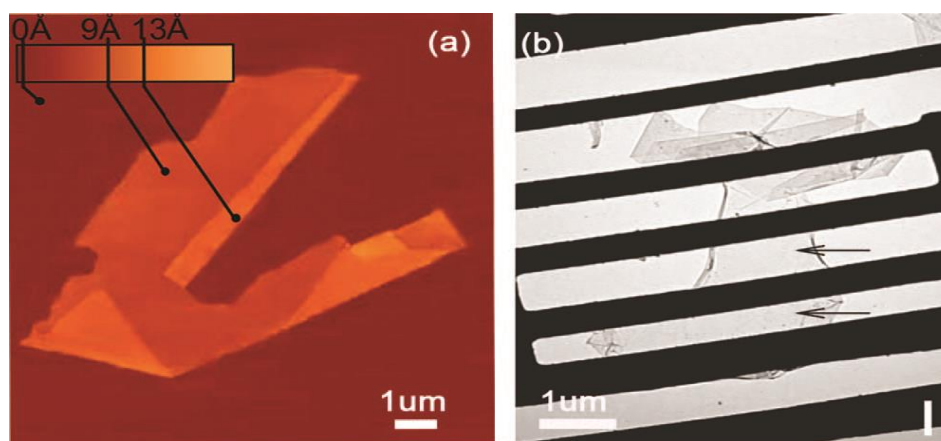


Fig. 1.3: The inception of single-layer graphene through mechanical exfoliation. (a) Atomic force microscopy displaying the substrate graphene step-height (<1 nm) and a folded step-height (0.4 nm) (Adapted from Ref. [20]) (b) Transmission electron microscopy (TEM), capturing a free-standing graphene film with etched underlying substrate (Adapted from Ref. [29]).

to ~ 30 layers [30]. In 2001, Enoki's group in Tokyo utilized high temperatures (~ 1600 °C) to transform nano-diamonds into nanometer-sized graphene on HOPG [31]. Although this technique was instrumental in generating thin samples, a significantly more straightforward approach was introduced by Geim, Novoselov, and collaborators in 2004, heralding a new era in graphene research. The technique dubbed the 'Scotch-Tape method,' pioneered by them, marked the first successful isolation of single-layer graphene (Fig. 1.3). Geim and Novoselov received due recognition, being honoured with the Nobel Prize in Physics (2010) for their pioneering contributions to the realm of two-dimensional atomic physics [29].

1.3.1. Mechanical Exfoliation or Cleavage Method

The method involves utilizing commercially available Highly Oriented Pyrolytic Graphite (HOPG) sheets as the initial material. It includes the repetitive cleaving of layers from a graphite flake using common cellulose tape, which is applied onto a silicon substrate for material deposition. However, the layers adhered to the tape tend to be thicker than a single layer. Nevertheless, upon lifting the tape from the substrate, van der Waals's forces to the substrate make it easier for a single sheet to delaminate. The skilful execution of this technique can yield high-quality crystallites exceeding $100 \mu\text{m}^2$ in size, as illustrated in Fig. 1.4.

Although mechanical exfoliation may result in a complex mixture of thick slabs, making the identification of single layers challenging, the successful isolation of a single-

layer graphene sheet through mechanical cleavage is an essentially serendipitous occurrence. Despite its labour-intensive nature and the production of a limited amount of graphene, this method offers the advantage of not requiring a specialized environment or apparatus. The graphene obtained through mechanical exfoliation retains superior electrical and mechanical properties due to the excellent grade of the initial single-crystal graphite source [32]. Nevertheless, this technique is not ideal for large-scale graphene synthesis, which is imperative for its diverse range of applications.

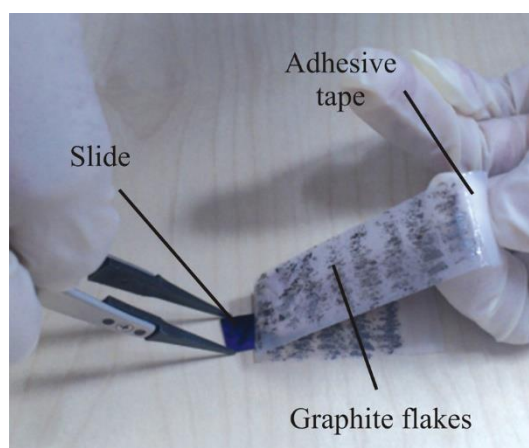


Fig. 1.4: 'Scotch tape' method. (Adapted from Ref. [33])

For large-scale synthesis, alternative methods such as ion implantation [34], chemical-vapour deposition (CVD) [35,36], liquid-phase exfoliation [37,38], and epitaxial growth on a silicon carbide substrate [39] have been proposed. Lee et al. reported that graphene produced by CVD methods exhibited 90% of the theoretical strength of pristine graphene [40]. However, these methods are less utilized compared to the alternative method of exfoliating graphite oxide and then reducing it. Presently, one of the most frequently employed methods for large-scale graphene synthesis is the so-called 'Hummers' method and its various modifications [25]. In this thesis, the modified Hummers method has been employed for the synthesis of graphene, or more precisely, reduced graphene oxide (RGO), presented separately in a subsequent section.

1.3.2. Epitaxial Growth

Graphene synthesis through epitaxial growth involves the reduction of silicon carbide (SiC) at elevated temperatures. Historical reports indicated that subjecting either the C-

face or the Si-face of 6H-SiC $\{(0001) \text{ and } (0001\bar{1})\}$ surfaces to temperatures ranging from 1000 °C to 1500 °C in ultra-high vacuum (UHV) led to Si sublimation, resulting in a carbon-rich surface [27]. The resulting graphene-like structures on the two polarized surfaces can be adequately differentiated. Alternatively, utilizing an evacuated radio frequency (RF) induction furnace instead of UHV for epitaxial growth on the C-face of 4H-SiC has been demonstrated to enhance the quality of graphene-based films [18]. This method can produce 4-13 layers of graphene within 5 to 8 minutes inside a furnace under very low pressure ($\sim 3 \times 10^{-5}$ Torr). Controlling both the growth temperature and time allows for tuning the thickness of the graphene film. The reported carrier mobility is notably high, reaching up to $27,000 \text{ cm}^2 \text{ V}^{-1} \text{ s}^{-1}$, and $\sim 1000 \text{ cm}^2 \text{ V}^{-1} \text{ s}^{-1}$ for the overlapped C-face graphene and the Si-face graphite films, respectively [40].

The epitaxial method's advantage lies in producing graphene films directly on the SiC substrate without the need for a transfer process, making it beneficial for semiconductor device fabrication. Despite differences in physical properties due to interfacial effects, the method maintains graphene's properties to a considerable extent.

1.3.3. Chemical Vapour Deposition (CVD)

Chemical Vapour Deposition (CVD) was first used to successfully synthesise few-layer graphene sheets, and this was accomplished in 2006 [41]. Camphor, a natural hydrocarbon source, was utilized in the pyrolysis process on Ni substrates to produce graphene films, which, however, tended to fold, with a minimum layer count of 20. Recent developments have affirmed the reproducibility of graphene growth using CVD. Several studies highlight CVD as the most promising technique for the large scale fabrication of graphene. Notably, during CVD growth, graphene doping becomes feasible by introducing specific gases, such as NH_3 [42]. Furthermore, the incorporation of plasma in CVD processes enables a reduction in the growth temperature. Under these conditions, the plasma sheath influences the electric field direction, leading to the vertical growth of graphene onto the substrate. This innovative technique for large-scale freestanding few-layer graphene synthesis is recognized as plasma-enhanced CVD (PECVD).

1.3.4. Chemical Derivation

In 1958, Hummers and Offeman introduced a method for the preparation of graphite oxide involving the treatment of graphite with an anhydrous mixture of H_2SO_4 , NaNO_3 ,

and KMnO_4 at temperatures below $45\text{ }^\circ\text{C}$ for 2 hours. This process leads to the intercalation of graphitic sheets, which, upon thermal expansion, can be decomposed to yield few-layer or even single-layer graphene. Subsequent ultrasonic treatment further facilitates the splitting of graphite oxide into individual layers. The introduced phenol, carbonyl, and epoxy groups during oxidative intercalation enhance the colloidal stability of the resulting graphite oxide suspension [32]. However, the electronic properties of graphene obtained through this chemical method differ from those obtained through mechanical exfoliation. While mechanically exfoliated graphene layers exhibit semimetallic properties, the electronic structure of graphene oxide (GO) from the chemical method appears to be semiconductive due to structural defects. Consequently, chemical reduction of GO, typically using hydrazine (N_2H_4) [43] or sodium borohydrate (NaBH_4) [44,45], is necessary to reinstate the pertinent properties of graphene. The reduced material is termed reduced graphene oxide (RGO), and its brown-coloured dispersion in water turns black. Despite becoming less hydrophilic after reduction, complete elimination of oxygen atoms, and thus complete chemical reduction, is not feasible. Therefore, the resulting product remains a transitional state between graphene and GO. X-ray photoelectron spectroscopy (XPS) reveals that chemically reducing GO through hydrazine or thermal annealing (up to $1100\text{ }^\circ\text{C}$) does not fully regenerate the exact structures of graphene [Fig. 1.5 (a-d)]. Reduction by NaBH_4 , on the other hand, leads to the presence of residual hydroxyl functional groups [Fig. 1.5 (e-j)]. When the original graphene structure is crucial, chemical derivation is not considered a viable synthesis technique, and physical exfoliation should be pursued. However, RGO synthesis, despite its inherent simplicity and reasonable properties, results in an intermediate state between graphene and GO. The conductivity and transparency of RGO thin films make it a promising component for future applications as a transparent conductor [46,47]. Chemical exfoliation, while simple and lacking complicated synthesis conditions, is not without defects. Nevertheless, it yields good final product yields, and RGO could be stored in a water-based solution or as a powder after drying, facilitating the handling of graphene sheets or amorphous graphene flakes as a matrix for inorganic semiconductors. In the present thesis work, chemical derivation has been chosen for the synthesis of reduced graphene oxide.

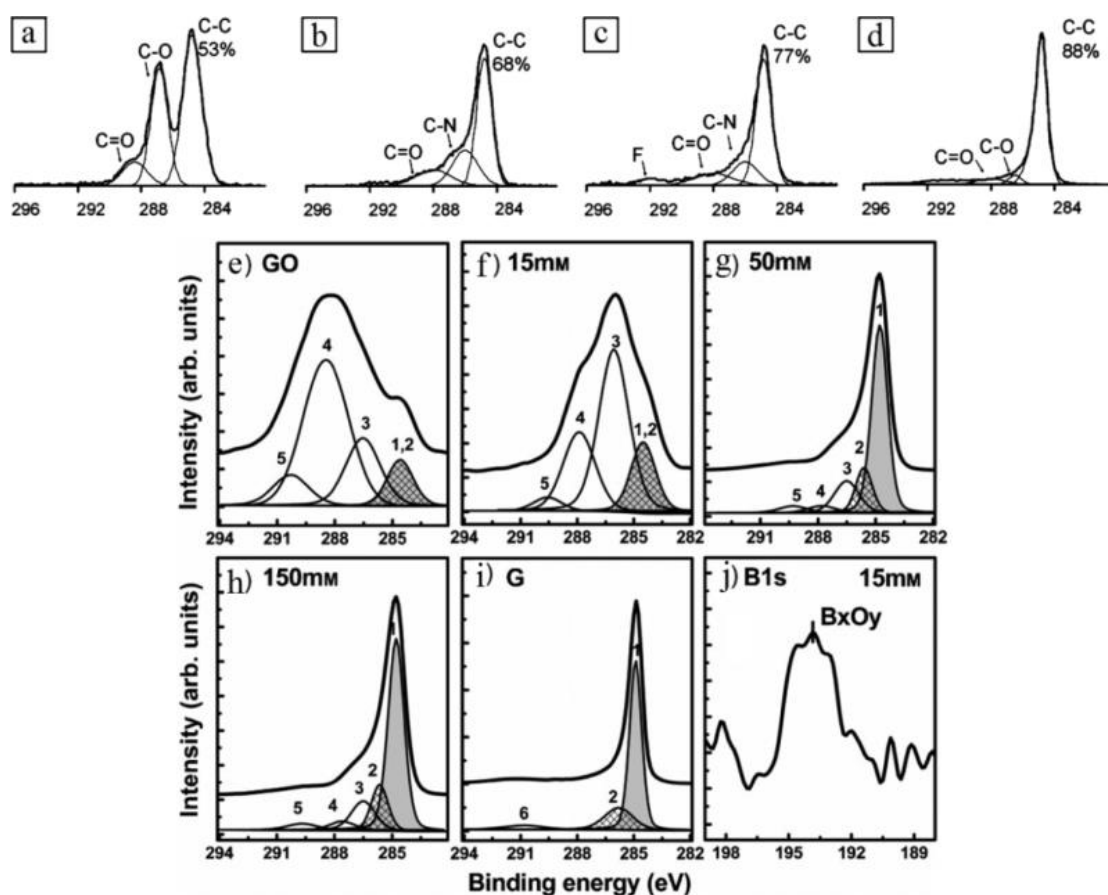


Fig. 1.5: X-ray photoelectron spectroscopy (XPS) reveals the impact of various reduction treatments on graphene oxide (GO). Images a–d show deconvoluted results indicating the presence of C–C, C–N, C–O and C=O species; approximately at B.E. of 284.8, 285.7, 286.2 and 287.8 eV respectively, with the percentage of deoxidized carbon (C–C, ~284.5 eV). (a) Non-reduced. (b) Hydrazine-vapour-treated. (c) Hydrazine vapour and annealed at 400 °C. (d) Thermal annealing in a vacuum (1100 °C). The C–N signal observed in images b and c indicates the formation of hydrazone groups resulting from hydrazine treatment. The presence of an F signal at around 292 eV in image (c), is attributed to contamination from the vacuum system. (e) C 1s peak of graphene oxide. (f–i) Reduced graphene oxide (RGO) was synthesized using sodium borohydride (NaBH₄) concentrations of (f) 15 mM (g) 50 mM and (h) 150 mM and (i) graphite. The curves were fitted considering C=C (peak-1), C–C (peak-2), C–O/C–O–C (hydroxyl and epoxy groups, peak-3), C=O (carbonyl groups, peak-4), O–C=O (carboxyl groups, peak-5) and π – π^* (peak-6) species. (j) B 1s peak in the XPS spectra of RGO originated from 15 mM NaBH₄. (Images a–d and e–j reprinted from Ref. [48] and [44] respectively).

1.3.5. Alternative Methods

An alternative method of achieving physical exfoliation for the production of graphene sheets involves treating graphite dispersions in a suitable liquid solution through ultrasonication. Hernandez et al. were the first to document the exfoliation of graphene sheets by dispersing graphite into N-methyl pyrrolidone (NMP) [49]. Additionally, natural graphite crystals can be dispersed in dimethylformamide (DMF) and

subsequently exfoliated by sonication, resulting in a suspension of thin graphitic platelets comprising single-layer graphene flakes [50]. Despite the abundance of graphene flakes in such a suspension, centrifugation is employed to eliminate large, thick flakes, leaving a well-dispersed mixture of graphene and a few-layer graphite in the remaining suspension.

The resulting graphene from this method exhibits similarities to products derived through chemical methods. However, omitting the oxidation step in the liquid-phase exfoliation ensures that the product does not incur defect-induced limitations or degradation of electrical properties. To obtain dry graphene through this process, graphene suspensions must be deposited onto a solid substrate with the assistance of thermal treatment. Alternatively, liquid-phase exfoliation can be performed in water, necessitating the incorporation of effective surfactants like sodium dodecylbenzene sulfonate (SDBS). These surfactants can be adsorbed onto individual single-layer graphene sheets, preventing aggregation and stabilizing the dispersion. However, drawbacks include the cost of the solvent and the tendency of individual sheets to overlap.

Another method for producing functionalized graphene sheets involves the thermal expansion of graphite oxide [16]. This method shares similarities with the Hummers method, beginning with the treatment of natural graphite flakes in an oxidizing solution of H_2SO_4 , HNO_3 , and KClO_3 . After the reaction is complete, the resulting material is mixed with excess water, washed with HCl , and subsequently rinsed multiple times with water until the pH of the filtrate reaches neutral. For successful production of single-layer graphene via this method, the graphite must be completely oxidized and heated to an exceedingly high temperature. The heating process causes graphite oxide to decompose into individual sheets by releasing CO_2 .

1.4. Properties of Graphene

Since the inception of the graphene revolution, extensive research has been conducted to explore the unique physical properties of this material. Early findings revealed an exceptionally high carrier mobility for graphene within the range of $2000\text{--}5000\text{ cm}^2/\text{Vs}$ [20]. Subsequent advancements have demonstrated that under optimal conditions, suspended graphene solutions can exhibit charge carrier mobility of up to $230,000\text{ cm}^2/\text{Vs}$ [32,51,52]. This remarkable electron-transport capability positions graphene

prominently for applications such as field-effect transistors (FETs). By 2010, there were reports of graphene FETs operating at a frequency of 100 GHz, and more recent studies suggest operability at frequencies as high as terahertz (THz) [53].

Graphene's exceptional optical transparency, reaching up to 97.7% [19], further enhances its potential applications, particularly as transparent electrodes in solar cells [54] and in advanced technologies like holographic data storage [55]. Beyond these attributes, graphene boasts a high Young's modulus exceeding ~ 1 TPa, ensuring superior mechanical properties [56]. Additionally, it exhibits an excellent thermal conductivity approaching $5000 \text{ W m}^{-1} \text{ K}^{-1}$ [57] and an extraordinarily large specific surface area of $2630 \text{ m}^2 \text{ g}^{-1}$ [58]. Although a comprehensive examination of these properties is beyond the scope of this discussion, interested readers can refer to the provided references for detailed analyses.

1.5. Group II-VI Semiconductors

Group II-VI compound semiconductors, particularly binary chalcogenides, represent a vital class of materials in the realm of semiconductor physics and technology. These compounds are composed of elements from Group II (such as zinc, cadmium, and mercury) and Group VI (including sulfur, selenium, and tellurium) of the periodic table. Notable examples of binary chalcogenides include zinc sulfide (ZnS), zinc selenide (ZnSe), zinc telluride (ZnTe), cadmium sulfide (CdS), cadmium selenide (CdSe), and cadmium telluride (CdTe). These compounds exhibit remarkable optical, electrical, and structural properties, making them indispensable for various applications ranging from optoelectronic devices to photovoltaics.

One of the distinguishing features of II-VI compound semiconductors is their tunable bandgap, which can be tailored by adjusting the stoichiometry or composition of the material. This property enables the design and fabrication of semiconductor devices with specific optical and electronic characteristics. For instance, cadmium-based compounds like CdS and CdSe are well-known for their wide bandgaps, making them suitable for blue and green light-emitting diodes (LEDs), while zinc-based compounds like ZnSe and ZnTe with narrower bandgaps are preferred for infrared applications. Moreover, the excellent optical transparency of these materials in the visible and near-infrared regions further enhances their utility in various optical and photonic devices. In addition to their optical properties, II-VI compound semiconductors exhibit favourable

electrical characteristics, including fast response time, high carrier mobility and low trap densities. These attributes make them ideal candidates for electronic devices such as field effect transistors (FETs), solar cells, and photodetectors. Furthermore, the ability to form heterostructures and alloys with other semiconductors expands the range of applications and enables the development of advanced device architectures with enhanced performance.

The fabrication of II-VI compound semiconductors often involves methods such as molecular beam epitaxy (MBE), chemical-vapour deposition (CVD), and solution-based methods like hydrothermal synthesis. These methods allow for precise control over the growth parameters, resulting in materials with tailored properties and high crystalline quality. Additionally, advances in nanotechnology have led to the synthesis of II-VI semiconductor nanostructures, including quantum dots, nanowires, and thin films, offering new opportunities for device miniaturization and integration. Overall, II-VI compound semiconductors, particularly binary chalcogenides, play a crucial role in modern semiconductor technology due to their versatile properties and wide-ranging applications. Ongoing research in this field aims to further explore their potential for next-generation electronic and optoelectronic devices, as well as their integration into emerging technologies such as quantum computing and sensing platforms.

1.5.1. Zinc Telluride (ZnTe)

Zinc telluride (ZnTe) stands out as a highly promising semiconductor within the II-VI group (Zn, Cd, Hg, S, Se, and Te), drawing considerable attention for its outstanding light absorbance and superior thermal and optoelectronic properties. With a narrow bandgap ranging approximately from 2.23 eV to 2.30 eV and a Bohr exciton radius of ~ 6.2 nm, ZnTe facilitates enhanced visible light absorption and the formation of p-n heterostructures with other semiconductor materials [59,60]. The increasing significance of II-VI semiconductors in applications related to the photovoltaic conversion of solar energy can be attributed to their notable absorption coefficients and cost-effectiveness. Operating as a p-type semiconductor, ZnTe serves as a key driver for interfacial electron transfer, showcasing promising applications in various domains, including photocatalysis, solid-state devices, photodetectors, green light-emitting diodes, and solar cells. The narrow bandgap not only ensures efficient visible light absorption but also facilitates effective electron-hole separation, positioning ZnTe as a prospective

photocatalyst extensively investigated for its potential to enhance photocatalytic activity [61].

1.5.2. Zinc Selenide (ZnSe)

Zinc selenide (ZnSe), another semiconductor material within the group II-VI category, has garnered increased attention in recent years owing to its remarkable chemical stability, rendering it highly applicable across diverse industrial sectors. With a suitable direct band gap (2.67-2.7 eV), a significant exciton B.E. (22 meV), high transparency spanning range (0.5–22 μm), and a diminutive exciton Bohr diameter (9 nm), ZnSe possesses superior properties. Its potential applications encompass light-emitting diodes, especially the blue ones, infrared (IR) optical devices, photodetectors and solar cells, positioning it as a promising candidate for industrial production and a potential substitute for toxic materials [62]. Demonstrating nonlinear optical properties, ZnSe is suitable for applications in optoelectronic and visible light communication technologies, as well as photocatalytic processes. Notably, ZnSe films have exhibited a substantial increase in photocurrent under UV irradiation in recent investigations. Beyond its primary applications, ZnSe holds promise in various roles, including windows, lenses, output couplers, beam expanders, and optically controlled switching, leveraging its low absorptivity at infrared wavelengths, visible transmission, and remarkable photosensitivity. Diverse nanostructures of ZnSe, ranging from nanoparticles to intricate hierarchical structures, have been successfully fabricated using various methods. The unique properties and versatile applications of ZnSe in semiconductor research underscore its significance and potential contributions to advancements in optoelectronics, nanotechnology, and industrial processes [63].

1.6. Graphene-based Inorganic Composites

As previously discussed, graphene and its inorganic nanocomposites hold significant promise for electronic devices. However, despite graphene's remarkable properties, challenges arose concerning its electrical and optical characteristics in the context of high-speed electronic applications, primarily due to the missing of any bandgap. Graphene, inherently exhibiting a zero bandgap semiconductor with charge conjugation symmetry between electrons and holes, as well as carriers possessing a chirality-like

internal degree of freedom akin to ultra-relativistic elementary particles, encountered limitations in this regard [64].

To address these challenges, researchers recognized that combining graphene nano-sheets with certain inorganic semiconductors could alleviate or eliminate the zero-gap shortcomings. Strategies such as size constrictions and strain-induced curvature were employed to induce an electronic band gap in graphene. Subsequently, it was determined that attaching nanoscale inorganic semiconductors could achieve this purpose effectively [65,66]. While numerous inorganic semiconductors have demonstrated compatibility with graphene to form composites, the synthesis procedure of graphene plays a crucial role, leading to significant variations in the compatibility of graphene with different inorganic semiconducting materials. Consequently, the optical and electrical properties of the resulting composites undergo substantial changes.

Graphene exerts a profound influence on the charge transport properties of these composite materials. In typical inorganic semiconductors, light irradiation activates charge carriers. The ensuing electronic interactions between graphene and the semiconductor facilitate smooth charge separation and their transport. Graphene, acting as the electron conductor, hinders the rapid recombination of electrons and holes in the composite. Leveraging these advantages, hybrid graphene-inorganic semiconductor materials have emerged as highly appealing options for applications in optoelectronics, electrochemistry, and photochemistry, thereby potentially revolutionizing the electronics and composite industries.

The band gap energy of semiconductor materials, such as quantum dots, is intricately linked to particle size; as the particle size decreases, the band gap increases due to quantum confinement effects [67,68]. This phenomenon is evident in many group II–VI semiconductors like ZnO, ZnS, CdS, ZnSe and ZnTe, where changes in quantum dot size lead to a shift in the absorption threshold [69]. The distinctive optical and electronic properties stemming from quantum confinement make group II–VI semiconductors, such as ZnSe and ZnTe, promising candidates for a range of applications. However, their potential is hindered by the zero-bandgap nature of graphene [16]. Consequently, hybrid structures combining group II–VI semiconductors with graphene have been explored to harness synergistic advantages, demonstrating improved performance compared to individual materials.

This thesis primarily focuses on the synthesis, characterizations, optimizations and practical applications of the reduced graphene oxide-zinc telluride (RGO-ZnTe), with the addition of the zinc selenide-zinc telluride (ZnSe-ZnTe) heterojunction microstructures. Their application in thin film Schottky barrier diodes is explored, emphasizing the impact of graphene on the photoresponse and charge transport properties of the inorganic semiconductors.

1.6.1. Zinc Telluride (ZnTe) and Graphene Oxide

Zinc Telluride (ZnTe), a narrow band gap semiconductor (2.26–2.4 eV) is synergized with graphene oxide (GO) to form composite materials with enhanced charge mobility and optical responsiveness. The integration of ZnTe and GO leverages the semiconducting nature of ZnTe and the versatile properties of GO, resulting in hybrid structures that exhibit superior electrical conductivity, physical and thermal stability, and optical properties. With the rapid generation of the $e-h^+$ pairs upon photo-excitation and favourable energy band positions, ZnTe nanoparticles decorated with graphene present enhanced performances in dye degradations. Ongoing research endeavours seek to further understand the synergistic behaviour of ZnTe and GO in the realm of advanced materials for contemporary physics applications.

1.7. Synthesis of Graphene-based Composites

The synthesis of nanomaterials stands as a pivotal aspect of contemporary nanoscience and technology, leading to a surge in publications addressing nanoparticle synthesis. Various synthetic strategies have been employed to produce nanoparticles of diverse inorganic materials, with a focus on selectively preparing particles of different dimensionalities and shapes. Several methods, such as micro-emulsions, thermal decomposition, hydrothermal and solvothermal synthesis, sol-gel technique, phase-transfer method, microwave synthesis, and utilization of the liquid-liquid interface, have been utilized for the synthesis of inorganic nanoparticles [2]. In this thesis, the hydrothermal and solvothermal methods are adopted for the synthesis of inorganic nanoparticles and graphene nanocomposites, with a specific focus on the hydrothermal method.

Hydrothermal-solvothermal synthesis, conducted under high-pressure conditions, is a widely employed technique for inorganic nanoparticle synthesis.

Hydrothermal synthesis occurs in hot water, whereas solvothermal processes take place in a non-aqueous precursor solution within an autoclave. This method capitalizes on the altered solubility and reactivity of reactants in high-temperature, high-pressure solvent environments. The heightened reactivity enables the synthesis of inorganic nanomaterials at significantly lower temperatures than those required in solid-state reactions. Variables such as pressure, temperature, time, reactant's concentration, reaction-cell fill volume, and pH can be adjusted to control nucleation, growth and particle size distribution. Hydrothermal or solvothermal synthesis has been applied to various inorganic materials, including metals, oxides, chalcogenides, pnictides, and more.

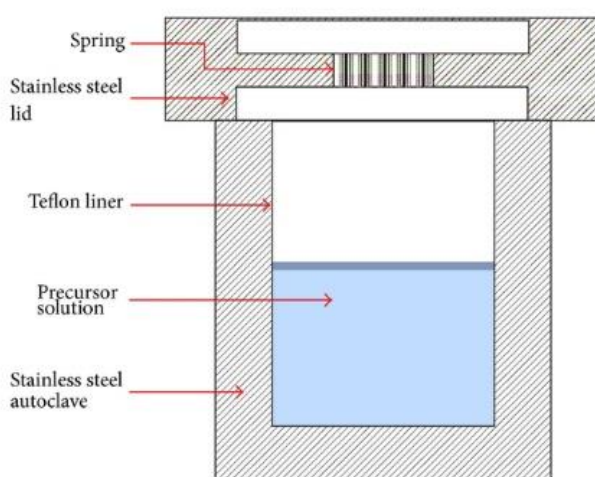


Fig. 1.6: Schematic diagram of the autoclave used in solvothermal/hydrothermal synthesis (Adapted from Ref. [70]).

In this work, the hydrothermal method is employed for producing inorganic nanoparticles and consequently, their graphene composites. Introducing graphene oxide (GO) to hydrothermal reactions aimed at synthesizing inorganic semiconductors leads to the concurrent formation of semiconductor nanomaterials and the reduction of GO.

1.7.1. Hydrothermal Method

The hydrothermal method, employed as a bulk growth technique, operates within a closed system to synthesize desired compounds under elevated temperatures (above 100°C) and pressures (above 1 atm). This method entails both physical and chemical processes occurring within a water solution where the desired materials are typically insoluble. The properties of resulting II-VI binary, ternary, or quaternary compounds are

influenced by factors such as the medium's pH, duration of the process, growth temperature, and pressure within the closed system. The hydrothermal process is conducted within an autoclave, a reaction vessel specifically designed to withstand the harsh conditions of high temperature and pressure. Autoclave materials, often lined with Teflon to prevent corrosion, are carefully selected to ensure durability. Fig. 1.6 depicts a Teflon-lined steel autoclave for the hydrothermal techniques.

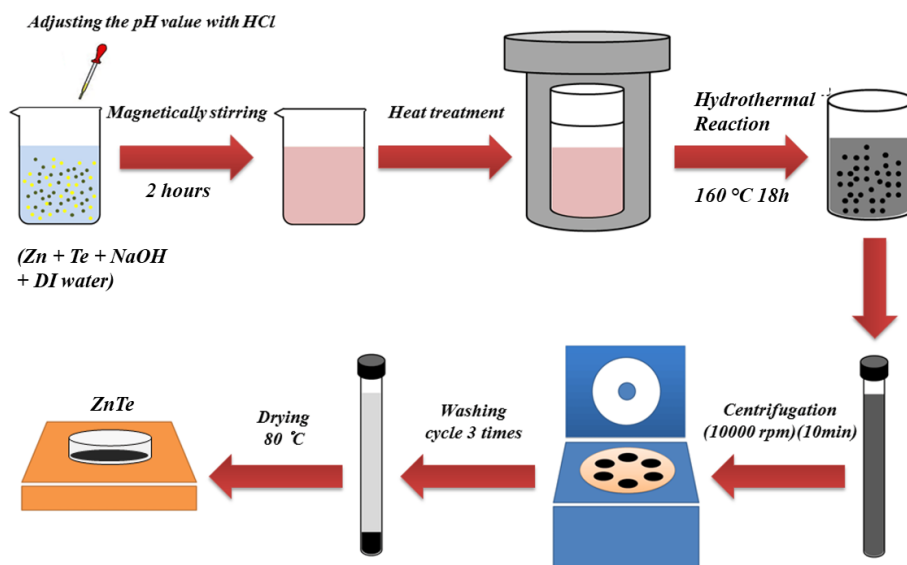


Fig. 1.7: A typical flowchart of the hydrothermal method for ZnTe preparation (Adapted from Ref. [73]).

Nanoparticles of various compounds can be synthesized directly through hydrolysis reactions within the autoclave at elevated temperatures. Alternatively, hydrothermal treatment can be applied to products obtained from solution reactions at ambient conditions. This method offers several advantages, including precise control over oxidation and simplified synthesis of oxidized compounds, particularly transition-metal compounds, due to the use of a closed system [71]. Additionally, resultant products exhibit lower dislocation density owing to reduced thermal strain. The hydrothermal process enables the synthesis of a wide range of materials, including piezoelectric, magnetic, optic, and ceramic materials, on a large scale with high purity. Furthermore, this environmentally friendly method does not require seeds, catalysts, or expensive surfactants, making it a cost-effective and widely accepted technique in the scientific community for synthesizing binary II-VI compounds [72]. Fig. 1.7 depicts a typical flow diagram of the synthesis of ZnTe NPs by the hydrothermal method.

1.8. Application of Graphene and its Composites

The proliferation of academic publications related to graphene has witnessed a significant surge since 2004, highlighting pivotal milestones and the escalating trend in graphene research publications [1]. Diverse types of graphene, synthesized through various methods, offer distinct advantages for a broad spectrum of applications, contingent upon their inherent properties. Fig. 1.8 delineates diverse applications of graphene and graphene-based composites, showcasing a spectrum of potential technologies. The subsequent section will succinctly expound on the practical applications of graphene and its nanocomposites.

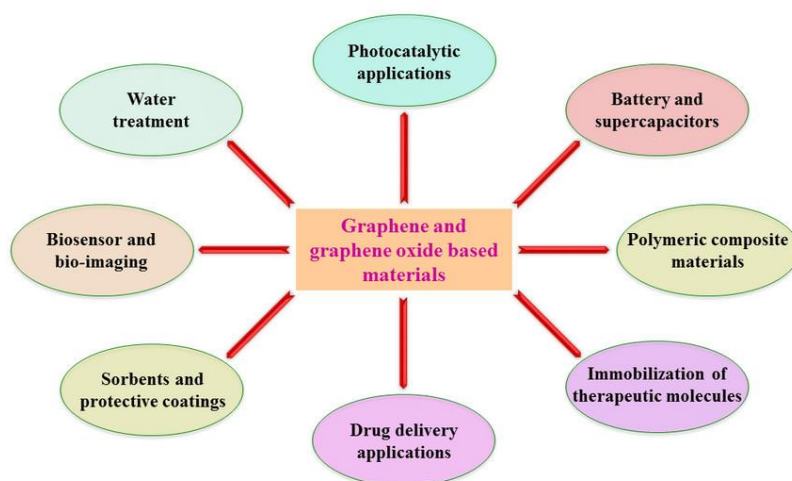


Fig. 1.8: Schematic representation of diverse applications of graphene and graphene oxide-based composite materials (Adapted from Ref. [74]).

1.8.1. High-speed Electronics

Graphene's exceptionally high conductivity renders it an ideal candidate for high-speed electronics. Despite this merit, the widespread commercial implementation of graphene in electronic devices faces limitations because of its zero band-gap. The necessity of a band-gap for 'on and off' states in electronic devices becomes evident. Recent studies have unveiled that the absence of a band-gap in bilayer graphene stems from the twisting of the graphene sheet [75]. Nevertheless, researchers have successfully developed ultra-thin graphene transistors [76]. Notably, a self-aligning $\text{Co}_2\text{Si-Al}_2\text{O}_3$ nanowire has been employed as a gate in graphene transistors, preventing device degradation and demonstrating high operational frequencies of 100–300 GHz [77]. This progress

underscores the rapid advancement of graphene research, hinting at the potential emergence of high-speed graphene transistors in consumer electronics in the near future.

1.8.2. Solar Cells

Graphene finds application in solar cells, a domain crucial for the future. The prevalent use of platinum-based electrodes in current solar cell technologies encounters dual challenges: the limited supply of platinum for creating a planet's worth of solar cells and the associated high costs. Graphene, serving as an excellent conductor, presents substantial potential as an electrode, promising cost and weight reduction. This potential is demonstrated by Wang et al. [11], who fabricated a dye-sensitized solar cell with a graphene electrode at a fraction of the cost compared to a platinum-based counterpart. The efficiency of this graphene-based cell reached 7.8%, merely 0.2% less than its platinum-based counterpart. While large-scale commercial applications remain a prospect, any contribution to green energy is highly anticipated. Graphene nanocomposites, such as Graphene-CdS and Graphene-TiO₂, exhibit promise for enhancing solar cell performance [83,84]. Constant research endeavours in graphene solar cells indicate a promising future [85,86].

1.8.3. Data Storage

The imperative task of augmenting the capacity and diminishing the size of data storage devices has received comparatively less attention in the realm of graphene research. Nonetheless, noteworthy breakthroughs have been achieved, including reports on ITO electrodes modified with polymers and GO for non-volatile memory device applications [78]. Devices based on graphene oxide have subsequently exhibited data capacities of 0.2 Tbits/cm³, approximately ten times the storage capacity of 16 GB USB flash drives [56]. Given the escalating demand for large data storage capacity, focusing graphene research on enhancing storage capacity could potentially lead to the replacement of existing solid-state technologies. The prospect of storing a terabyte on a USB flash drive-sized device, while keeping costs minimal, may soon become a reality.

1.8.4. LCD Smart Windows and OLED Displays

The technology underlying Liquid Crystal Display (LCD) Smart Windows involves a layer of liquid crystals positioned between two flexible electrodes, which typically consist of a flexible polymer and graphene. Additionally, graphene serves as a flexible organic light-

emitting diode (OLED) counter electrode. Current OLED technologies utilize ITO counter electrodes, which, being scarce and fragile, pose challenges [79]. In contrast, graphene, with its abundant supply and flexibility, holds a distinct advantage. OLED devices, potentially marking the commercial debut of graphene applications, have garnered interest from multinational companies such as Samsung. This technology opens avenues for flexible touch screens in mobile and tablet devices. The ongoing robust research suggests a future where curved screens become a standard feature in mobile phones, even extending to flexible three-dimensional displays, a concept inconceivable a decade ago.

1.8.5. Supercapacitors

Supercapacitors, distinguished by their ability to deliver significantly higher currents compared to regular capacitors, favour materials with high internal surface areas. Graphene, with an internal surface area of $2630 \text{ m}^2\text{g}^{-1}$, emerges as a logical choice. In 2010, Liu et al. reported record-breaking capacitive storage by a graphene supercapacitor [80]. Despite extensive efforts in developing graphene-based supercapacitors [81,82], these technologies are not yet readily available. Nevertheless, they hold promise as green energy solutions for electronic cars, trains, and potentially aeroplanes.

1.8.6. Schottky Barrier Diodes

Schottky diodes serve as integral electronic components in modern technology, forming the foundation of various applications, including solar cells, photodetectors, clamped transistors, metal-semiconductor field-effect transistors (MESFETs), high electron-mobility transistors (HEMTs), microwave mixers, RF attenuators, rectifiers, varactors, Zener diodes and several integrated circuits [87]. Enhancing the performance of Schottky junctions holds the potential to elevate the performance of these devices. Schottky barriers, established in metal-semiconductor junctions, traditionally utilize metals such as aluminium, silver, gold, or platinum. Leveraging the semi-metallic properties of graphene, it can replace current metals in Schottky diode fabrication. Indeed, reports underscore extremely promising performance for Schottky diodes with graphene electrodes [10,88,89]. In addition to serving as a metal electrode in the Schottky barrier, graphene-inorganic nanocomposites, such as graphene oxide- Fe_3O_4 and reduced

graphene oxide-ZnTe, have demonstrated promising results in Schottky diodes [90–92]. Despite these advancements, there remains room for improvement and further exploration of the application of graphene-inorganic semiconductor nanocomposites in Schottky diodes, presenting opportunities for diverse future technologies. As expounded earlier, this thesis centres on the synthesis of graphene-inorganic semiconductors and their application in a Schottky barrier diode, setting the stage for the subsequent discussion on the theory and configuration of a Schottky barrier diode.

1.8.7. Photocatalysis and Wastewater Treatment

Graphene and its composites have emerged as promising materials for various applications, including photocatalysis and wastewater treatment. Their distinctive properties, including large surface area and exceptional electrical conductivity, render them attractive candidates for addressing environmental challenges. In photocatalysis, graphene-based materials serve as efficient catalysts for promoting chemical reactions under light irradiation. By combining graphene with semiconductor photocatalysts like TiO_2 , ZnO , CdS , the photocatalytic activity can be significantly enhanced due to improved light absorption and charge carrier separation. Furthermore, graphene composites offer enhanced stability and recyclability, making them suitable for practical applications in wastewater treatment. The incorporation of graphene into membranes or adsorbents facilitates the removal of pollutants from water by adsorption or photocatalytic degradation. Moreover, graphene-based materials exhibit excellent antibacterial properties, further enhancing their effectiveness in wastewater disinfection. Overall, the application of graphene and its composites in photocatalysis and wastewater treatment holds great promise for addressing environmental pollution and promoting sustainable water management practices. Ongoing research in this field aims to optimize the synthesis methods, explore novel composite materials, and scale up the production for practical implementation in real-world applications.

References

1. E. P. Randviir, D. A. C. Brownson, and C. E. Banks, *Mater. Today* **17**, 426 (2014).
2. C. N. R. Rao, H. S. S. R. Matte, R. Voggu, and A. Govindaraj, *Dalt. Trans.* **41**, 5089 (2012).
3. Y. I. Zhang, L. Zhang, and C. Zhou, *Acc. Chem. Res.* **46**, 2329 (2013).
4. K. S. Novoselov, A. K. Geim, S. V Morozov, D. Jiang, Y. Zhang, S. V Dubonos, I. V Grigorieva, and A. A. Firsov, *Science* (80-.). **306**, 666 (2004).
5. K. S. Novoselov, A. K. Geim, S. V. Morozov, D. Jiang, M. I. Katsnelson, I. V Grigorieva, Sv. Dubonos, and and A. A. Firsov, *Nature* **438**, 197 (2005).
6. Y. Zhang, Y.-W. Tan, H. L. Stormer, and P. Kim, *Nature* **438**, 201 (2005).
7. A. K. Geim and K. S. Novoselov, *Nat. Mater.* **6**, 183 (2007).
8. M. J. Allen, V. C. Tung, and R. B. Kaner, *Chem. Rev.* **110**, 132 (2010).
9. X. Zhao, C. M. Hayner, M. C. Kung, and H. H. Kung, *Adv. Energy Mater.* **1**, 1079 (2011).
10. C. C. Chen, M. Aykol, C. C. Chang, A. F. J. Levi, and S. B. Cronin, *Nano Lett.* **11**, 1863 (2011).
11. H. Wang, K. Sun, F. Tao, D. J. Stacchiola, and Y. H. Hu, *Angew. Chemie Int. Ed.* **52**, 9210 (2013).
12. D. Prasai, J. C. Tuberquia, R. R. Harl, G. K. Jennings, B. R. Rogers, and K. I. Bolotin, *ACS Nano* **6**, 4540 (2012).
13. W. J. Hyun, O. O. Park, and B. D. Chin, *Adv. Mater.* **25**, 4729 (2013).
14. Z. Radivojevic, P. Beecher, C. Bower, S. Haque, P. Andrew, T. Hasan, F. Bonaccorso, A. C. Ferrari, and B. Henson, in *Proc. 2012 Virtual Real. Int. Conf.* (2012), pp. 1–3.
15. A. Bonanni and M. Pumera, *ACS Nano* **5**, 2356 (2011).
16. N. Gao and X. Fang, *Chem. Rev.* **115**, 8294 (2015).
17. X. Fang, Y. Bando, U. K. Gautam, C. Ye, and D. Golberg, *J. Mater. Chem.* **18**, 509 (2008).
18. J. Hass, R. Feng, T. Li, X. Li, Z. Zong, W. A. De Heer, P. N. First, E. H. Conrad, C. A. Jeffrey, and C. Berger, *Appl. Phys. Lett.* **89**, (2006).
19. D. A. C. Brownson, D. K. Kampouris, and C. E. Banks, *Chem. Soc. Rev.* **41**, 6944 (2012).
20. K. S. Novoselov, D. Jiang, F. Schedin, T. J. Booth, V. V Khotkevich, S. V Morozov, and A. K. Geim, *Proc. Natl. Acad. Sci.* **102**, 10451 (2005).
21. T. Enoki, M. Suzuki, and M. Endo, *Graphite Intercalation Compounds and Applications*

(Oxford University Press, 2003).

22. P. Delhaes, *Graphite and Precursors* (CRC Press, 2000).
23. B. C. Brodie, Philos. Trans. R. Soc. London 249 (1859).
24. L. Staudenmaier, Berichte Der Dtsch. Chem. Gesellschaft **31**, 1481 (1898).
25. W. S. J. Hummers and R. E. Offeman, J. Am. Chem. Soc. **80**, 1339 (1958).
26. H. P. Boehm, A. Clauss, G. O. Fischer, and U. Hofmann, Zeitschrift Für Anorg. Und Allg. Chemie **316**, 119 (1962).
27. A. J. Van Bommel, J. E. Crombeen, and A. Van Tooren, Surf. Sci. **48**, 463 (1975).
28. X. Lu, M. Yu, H. Huang, and R. S. Ruoff, Nanotechnology **10**, 269 (1999).
29. J. C. Meyer, A. K. Geim, M. I. Katsnelson, K. S. Novoselov, T. J. Booth, and S. Roth, Nature **446**, 60 (2007).
30. Y. Zhang, J. P. Small, W. V Pontius, and P. Kim, Appl. Phys. Lett. **86**, (2005).
31. A. M. Affoune, B. L. V Prasad, H. Sato, T. Enoki, Y. Kaburagi, and Y. Hishiyama, Chem. Phys. Lett. **348**, 17 (2001).
32. C. Soldano, A. Mahmood, and E. Dujardin, Carbon N. Y. **48**, 2127 (2010).
33. R. Van Noorden, Nature **483**, S32 (2012).
34. S. Garaj, W. Hubbard, and J. A. Golovchenko, Appl. Phys. Lett. **97**, (2010).
35. S. Bae, H. Kim, Y. Lee, X. Xu, J.-S. Park, Y. Zheng, J. Balakrishnan, T. Lei, H. Ri Kim, and Y. Il Song, Nat. Nanotechnol. **5**, 574 (2010).
36. D. A. C. Brownson and C. E. Banks, Phys. Chem. Chem. Phys. **14**, 8264 (2012).
37. M. Lotya, P. J. King, U. Khan, S. De, and J. N. Coleman, ACS Nano **4**, 3155 (2010).
38. M. Lotya, Y. Hernandez, P. J. King, R. J. Smith, V. Nicolosi, L. S. Karlsson, F. M. Blighe, S. De, Z. Wang, and I. T. McGovern, J. Am. Chem. Soc. **131**, 3611 (2009).
39. V. Y. Aristov, G. Urbanik, K. Kummer, D. V Vyalikh, O. V Molodtsova, A. B. Preobrajenski, A. A. Zakharov, C. Hess, T. Hänke, and B. Büchner, Nano Lett. **10**, 992 (2010).
40. G. H. Lee, R. C. Cooper, S. J. An, S. Lee, A. Van Der Zande, N. Petrone, A. G. Hammerberg, C. Lee, B. Crawford, and W. Oliver, Science. **340**, 1073 (2013).
41. P. R. Somani, S. P. Somani, and M. Umeno, Chem. Phys. Lett. **430**, 56 (2006).
42. D. Wei, Y. Liu, Y. Wang, H. Zhang, L. Huang, and G. Yu, Nano Lett. **9**, 1752 (2009).

43. C. Gómez-Navarro, R. T. Weitz, A. M. Bittner, M. Scolari, A. Mews, M. Burghard, and K. Kern, *Nano Lett.* **7**, 3499 (2007).
44. H. Shin, K. K. Kim, A. Benayad, S. Yoon, H. K. Park, I. Jung, M. H. Jin, H. Jeong, J. M. Kim, and J. Choi, *Adv. Funct. Mater.* **19**, 1987 (2009).
45. A. B. Bourlinos, D. Gournis, D. Petridis, T. Szabó, A. Szeri, and I. Dékány, *Langmuir* **19**, 6050 (2003).
46. D. Li, M. B. Müller, S. Gilje, R. B. Kaner, and G. G. Wallace, *Nat. Nanotechnol.* **3**, 101 (2008).
47. G. Eda, G. Fanchini, and M. Chhowalla, *Nat. Nanotechnol.* **3**, 270 (2008).
48. H. A. Becerril, J. Mao, Z. Liu, R. M. Stoltenberg, Z. Bao, and Y. Chen, *ACS Nano* **2**, 463 (2008).
49. Y. Hernandez, V. Nicolosi, M. Lotya, F. M. Blighe, Z. Sun, S. De, I. T. McGovern, B. Holland, M. Byrne, and Y. K. Gun'Ko, *Nat. Nanotechnol.* **3**, 563 (2008).
50. P. Blake, P. D. Brimicombe, R. R. Nair, T. J. Booth, D. Jiang, F. Schedin, L. A. Ponomarenko, S. V Morozov, H. F. Gleeson, and E. W. Hill, *Nano Lett.* **8**, 1704 (2008).
51. K. I. Bolotin, K. J. Sikes, Z. Jiang, M. Klima, G. Fudenberg, J. Hone, P. Kim, and H. L. Stormer, *Solid State Commun.* **146**, 351 (2008).
52. K. I. Bolotin, K. J. Sikes, J. Hone, H. L. Stormer, and P. Kim, *Phys. Rev. Lett.* **101**, 96802 (2008).
53. Y. M. Lin, C. Dimitrakopoulos, K. A. Jenkins, D. B. Farmer, H. Y. Chiu, A. Grill, and P. Avouris, *Science.* **327**, 662 (2010).
54. K. S. Kim, Y. Zhao, H. Jang, S. Y. Lee, J. M. Kim, K. S. Kim, J.-H. Ahn, P. Kim, J.-Y. Choi, and B. H. Hong, *Nature* **457**, 706 (2009).
55. X. Li, Q. Zhang, X. Chen, and M. Gu, *Sci. Rep.* **3**, 2819 (2013).
56. C. Lee, X. Wei, J. W. Kysar, and J. Hone, *Science.* **321**, 385 (2008).
57. A. A. Balandin, S. Ghosh, W. Bao, I. Calizo, D. Teweldebrhan, F. Miao, and C. N. Lau, *Nano Lett.* **8**, 902 (2008).
58. Y. Zhu, S. Murali, W. Cai, X. Li, J. W. Suk, J. R. Potts, and R. S. Ruoff, *Adv. Mater.* **22**, 3906 (2010).
59. Y. Wang and T. He, *Curr. Opin. Green Sustain. Chem.* **16**, 7 (2019).
60. W. Mahmood and N. A. Shah, *Phys. B Condens. Matter* **602**, 412557 (2021).
61. D. Suthar, Himanshu, S. L. Patel, S. Chander, M. D. Kannan, and M. S. Dhaka, *Solid State Sci.* **107**, 106346 (2020).

62. L. Zhang, H. Yang, J. Yu, F. Shao, L. Li, F. Zhang, and H. Zhao, *J. Phys. Chem. C* **113**, 5434 (2009).
63. H. Yin, K. Bao, W. Zhang, M. Bai, and J. Wan, *J. Indian Chem. Soc.* **99**, 100284 (2022).
64. M. I. Katsnelson and K. S. Novoselov, *Solid State Commun.* **143**, 3 (2007).
65. M. Y. Han, J. C. Brant, and P. Kim, *Phys. Rev. Lett.* **104**, 56801 (2010).
66. D. I. Son, B. W. Kwon, D. H. Park, W. S. Seo, Y. Yi, B. Angadi, C. L. Lee, and W. K. Choi, *Nat. Nanotechnol.* **7**, 465 (2012).
67. L. E. Brus, *J. Chem. Phys.* **80**, 4403 (1984).
68. L. Brus, *J. Phys. Chem.* **90**, 2555 (1986).
69. A. Henglein, *Chem. Rev.* **89**, 1861 (1989).
70. N. Asim, S. Ahmadi, M. A. Alghoul, F. Y. Hammadi, K. Saeedfar, and K. Sopian, *Int. J. Photoenergy* **2014**, 518156 (2014).
71. J. Zang, G. Zhao, and G. Han, *Front. Chem. China* **2**, 98 (2007).
72. Y. X. Gan, A. H. Jayatissa, Z. Yu, X. Chen, and M. Li, *J. Nanomater.* **2020**, 8917013 (2020).
73. C. Y. Chung, Y. C. Chen, F. R. Juang, K. S. Kao, and E. I. Lee, *Materials (Basel)*. **16**, (2023).
74. S. Dutta, I. Banerjee, and K. Jaiswal, **8**, 106 (2020).
75. K. S. Kim, A. L. Walter, L. Moreschini, T. Seyller, K. Horn, E. Rotenberg, and A. Bostwick, *Nat. Mater.* **12**, 887 (2013).
76. C. Mattevi, F. Colléaux, H. Kim, Y. H. Lin, K. T. Park, M. Chhowalla, and T. D. Anthopoulos, *Nanotechnology* **23**, 344017 (2012).
77. L. Liao, Y. C. Lin, M. Bao, R. Cheng, J. Bai, Y. Liu, Y. Qu, K. L. Wang, Y. Huang, and X. Duan, *Nature* **467**, 305 (2010).
78. X. Zhuang, Y. Chen, G. Liu, P. Li, C. Zhu, E. Kang, K. Noeh, B. Zhang, J. Zhu, and Y. Li, *Adv. Mater.* **22**, 1731 (2010).
79. J. Wu, M. Agrawal, H. A. Becerril, Z. Bao, Z. Liu, Y. Chen, and P. Peumans, *ACS Nano* **4**, 43 (2010).
80. C. Liu, Z. Yu, D. Neff, A. Zhamu, and B. Z. Jang, *Nano Lett.* **10**, 4863 (2010).
81. W. Chen, R. B. Rakhi, and H. N. Alshareef, *Nanoscale* **5**, 4134 (2013).
82. F. Zhang, J. Tang, N. Shinya, and L. C. Qin, *Chem. Phys. Lett.* **584**, 124 (2013).

83. F. W. Low and C. W. Lai, *Renew. Sustain. Energy Rev.* **82**, 103 (2018).
84. Q. Wu, H. Zhao, F. Huang, J. Hou, H. Cao, Z. Liu, S. Peng, and G. Cao, *J. Phys. Chem. C* **121**, 18430 (2017).
85. X. Miao, S. Tongay, M. K. Petterson, K. Berke, A. G. Rinzler, B. R. Appleton, and A. F. Hebard, *Nano Lett.* **12**, 2745 (2012).
86. Z. Yang, M. Liu, C. Zhang, W. W. Tjiu, T. Liu, and H. Peng, *Angew. Chemie Int. Ed.* **52**, 3996 (2013).
87. A. Di Bartolomeo, *Phys. Rep.* **606**, 1 (2016).
88. D. Sinha and J. U. Lee, *Nano Lett.* **14**, 4660 (2014).
89. R. Liu, X. C. You, X. W. Fu, F. Lin, J. Meng, D. P. Yu, and Z. M. Liao, *Sci. Rep.* **5**, 10125 (2015).
90. Ö. Metin, Ş. Aydoğan, and K. Meral, *J. Alloys Compd.* **585**, 681 (2014).
91. N. Minh Triet, L. Thai Duy, B. U. Hwang, A. Hanif, S. Siddiqui, K. H. Park, C. Y. Cho, and N. E. Lee, *ACS Appl. Mater. Interfaces* **9**, 30722 (2017).
92. J. L. Song and X. Wang, *Phys. E Low-Dimensional Syst. Nanostructures* **81**, 14 (2016).

Schottky Barrier Diodes: Theoretical Overview, Fabrication Techniques with an Introductory Insights into their Electrical Study, Impedance Spectroscopy and Positron Annihilation Spectroscopy

Chapter 2

2.1. Introduction of Schottky Barrier Diodes (SBD)

In the year 1874, Braun revealed first time the systematic analysis of conduction between metal and semiconductor (lead sulfide) [1]. By 1904, point-contact rectifiers in various configurations had begun to find practical applications. Based on the band theory of solids, Wilson developed the transport theory for semiconductors in 1931 [2], which was later applied to metal-semiconductor contacts. But, in 1931 Walter Hans Schottky noticed the formation of a potential barrier between the metal-semiconductor contacts [3]. In 1938, Schottky and Mott proposed a model to quantify the shape of the barrier and the barrier height [4,5]. These metal-semiconductor diodes were not effectively imitated or precisely dependable and were replaced by the p-n junction during the 1950s. However, semiconductor and vacuum technology is currently used to create reproducible and reliable metal-semiconductor contacts.

2.1.1. Energy-Band Relation

The interfacial contact between a metal and a semiconductor can lead to two distinct devices: the Ohmic junction or the Schottky (rectifying) junction. This outcome depends on the type of semiconductor (n-type or p-type) and the relative positions of the Fermi level in both the metal and semiconductor. For an n-type semiconductor, the contact is said to be rectifying only if its work function (ϕ_s) is less than the metal work function (ϕ_m), i.e., if $\phi_s < \phi_m$. Conversely, if $\phi_s > \phi_m$, the metal-n-type semiconductor contact is Ohmic. The situation is reversed for p-type semiconductors. A metal-p-type semiconductor contact will be rectifying if $\phi_s > \phi_m$ and non-rectifying if $\phi_s < \phi_m$. The subsequent section will delve into the formation of Schottky junctions.

When a metal establishes contact with a semiconductor, a potential barrier is created at the metal-semiconductor (MS) interface. This kind of barrier forms when the charges separate at the interface, leading to the formation of a high-resistance region in the semiconductor, depleted of mobile carriers. Schottky and Mott presented the initial model to elucidate the barrier height. The process of barrier formation is depicted in the energy band diagrams in Fig. 2.1. In Fig. 2.1(a), the band diagram illustrates a metal and an n-type semiconductor with work functions ϕ_m and ϕ_s , respectively, where $\phi_s < \phi_m$ and the vacuum level serves as the reference point. The work function of the semiconductor undergoes variation due to the fluctuation in the Fermi level caused by doping.

Nevertheless, the electron affinity χ_s of a semiconductor remains unaffected by doping. Both the work functions and the electron affinity are measured and denoted in units of electron volts (eV).

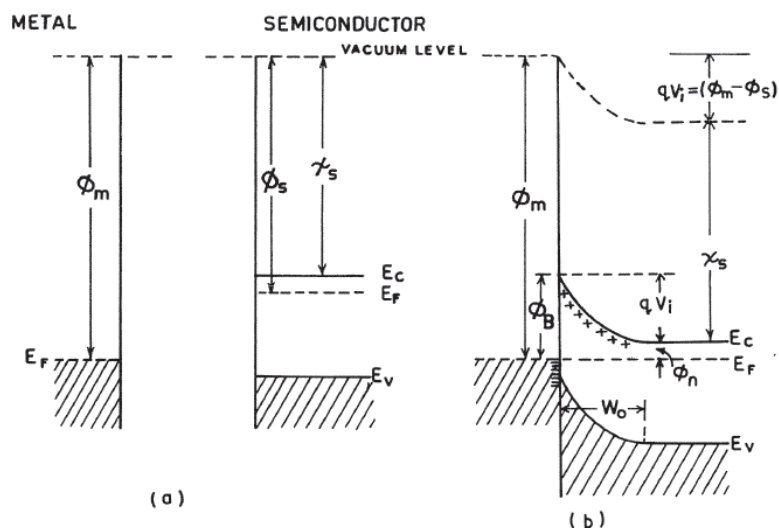


Fig. 2.1: Energy band diagrams depicting the contact of a metal with an n-type semiconductor, where $\phi_m > \phi_s$. Neutral materials when (a) they are separate from one another and (b) in the thermal equilibrium after the contact formation. (Adapted from Ref. [6])

The energy band diagram, shown in Fig. 2.1(b), represents the equilibrium state after the metal-semiconductor (MS) contact has been established. Upon intimate contact, electrons from the CB of the semiconductor, possessing higher energy than the metal electrons, migrate into the metal until the Fermi levels on both sides align. Consequently, the free electron concentration near the boundary decreases, leading to an increased separation between the CB edge (E_c) and the Fermi level (E_F), causing E_c to bend upwards [Fig. 2.1(b)]. This electron transfer results in a positive charge of ionized donors left in the semiconductor region, depleting it of mobile electrons. Simultaneously, a narrow layer of negative charge forms on the metal region, creating an electric field aligning from the semiconductor region to the metal. As the band gap of the semiconductor remains unchanged upon metal contact, the valence band (VB) edge (E_v) moves up parallel to E_c . The vacuum level in the semiconductor undergoes similar variations as E_c , gradually approaching the metal's vacuum level to maintain continuity. The degree of band bending equals the gap between the two vacuum levels, equivalent to the distance between the

two work functions $\phi_m = (\phi_m - \phi_s)$, where V_i is the contact potential difference or built-in potential of the junction. An electron transitioning from the semiconductor to the metal must cross a potential barrier of qV_i . However, when viewed from the metal region to the semiconductor, the barrier value changes and is given by:

$$\phi_B = \phi_m - \chi_s \quad (2.1)$$

Considering,

$$\phi_s = \chi_s + \phi_n \quad (2.2)$$

the barrier becomes,

$$\phi_B = qV_i + \phi_n \quad (2.3)$$

where $\phi_n = (E_C - E_F)$ and q represents the electronic charge. Here, Eq. 2.1 was formulated by Schottky and independently by Mott, referred to as the Schottky limit. The rectifying nature of the MS contact will be explored in the following section.

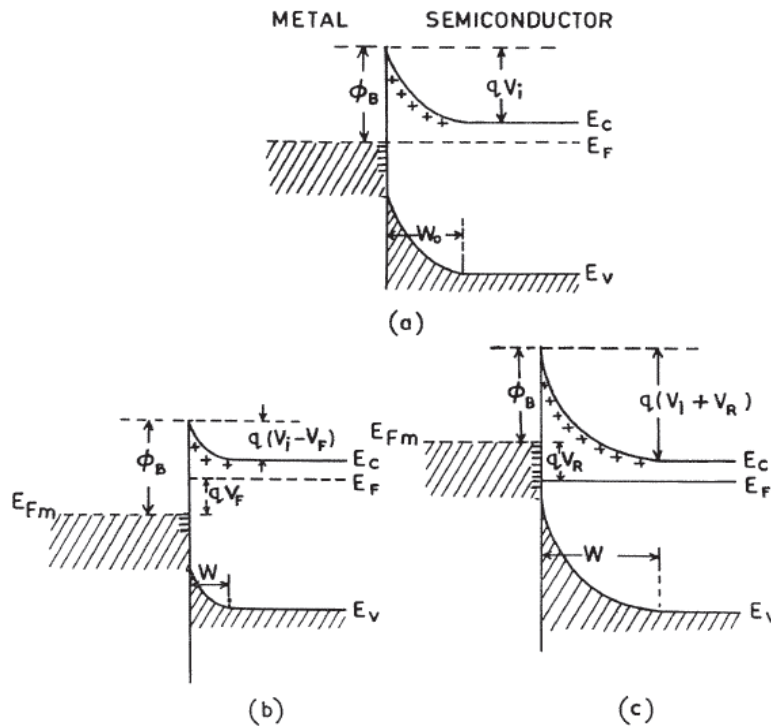


Fig. 2.2: Energy band diagrams of the rectifying contact with a metal and a n-type semiconductor. (a) the thermal equilibrium, (b) the forward bias and (c) the reverse bias condition.

The energy band diagram of the MS contact at thermal equilibrium is depicted in Fig. 2.2. In this state, the rate at which electrons traverse the barrier from the semiconductor to the metal is counterbalanced by the rate at which they travel across the barrier from the metal to the semiconductor, resulting in no net current flow. The semiconductor becomes negatively biased relative to the metal by a voltage $V=V_F$, causing the width of the depletion region to decrease. Consequently, the voltage across this region reduces from V_i to (V_i-V_F) , as displayed in Fig. 2.2(b). Electrons in the semiconductor region encounter a reduced barrier, leading to an increased electron flow from the semiconductor towards the metal compared to the thermal equilibrium value. However, ϕ_B remains unaffected by the bias voltage. Consequently, the electron flux from the metal to the semiconductor does not change from equilibrium. Therefore, when a negative bias is applied to the semiconductor, there is a net movement of electrons from the semiconductor to the metal, resulting in a current in the direction from the metal to the semiconductor. This polarity causes the junction to be forward-biased and the current rises exponentially with the applied voltage V_F . Fig. 2.2(c) illustrates the energy band diagram for a reverse-biased contact. Further, when a positive bias is applied to the semiconductor relative to the metal ($V=-V_R$), the potential drop over the depletion region increases to (V_i+V_R) . As a result, the electron flow from the semiconductor to the metal decreases below the equilibrium value, while the flow from the metal region remains unaltered. This causes a current flow in the opposite direction (i.e., from the semiconductor to the metal) which is typically smaller than the forward current and thus, the metal-semiconductor (MS) contact behaves as a rectifying junction.

The preceding description pertains exclusively to n-type semiconductors, where $\phi_s < \phi_m$. The energy band diagrams for an n-type semiconductor with $\phi_m < \phi_s$ are illustrated in Fig. 2.3. In Fig. 2.3(a), the energy bands illustrate the state of the materials when they are separated. Following the contact, electrons migrate from the metal into the CB of the semiconductor, resulting in a positive charge on the metal and electrons accumulate in the semiconductor region at the interface. Upon reaching equilibrium, the Fermi level in the semiconductor rises by $(\phi_s - \phi_m)$ as depicted in Fig. 2.3(b). The charge in the accumulated region of the semiconductor is localized within the thickness approximately equivalent to the Debye length, effectively forming a surface charge.

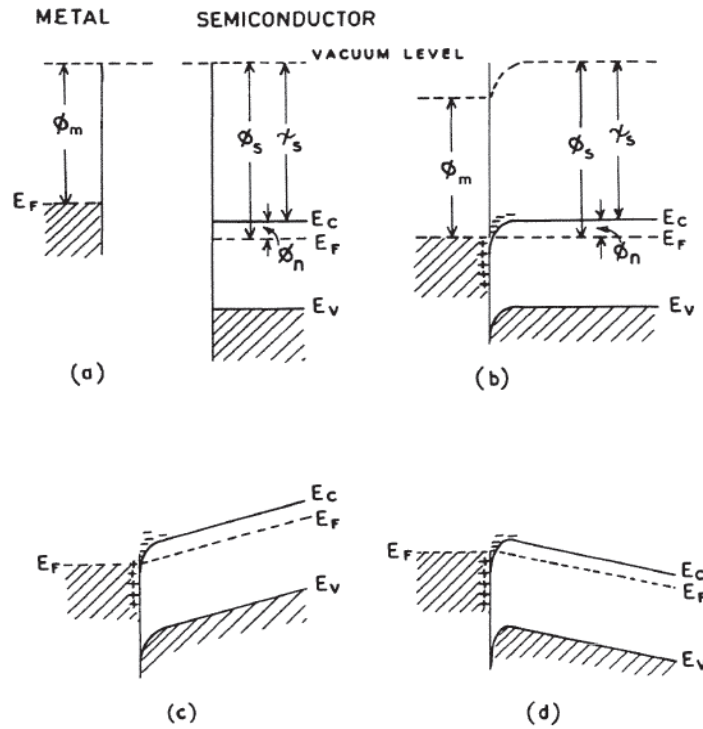


Fig. 2.3: Energy band diagrams for metal contact on an n-type semiconductor where $\phi_m < \phi_s$: (a) Neutral materials when they are separate from one another; (b) Contact at thermal equilibrium; (c) Negative bias and (d) Positive bias on the semiconductor.

Due to the high concentration of electrons in the metal, the positive charge on the metal region also constitutes a surface charge within a small distance ($\sim 0.5 \text{ \AA}$) at the MS interface. Thus there is neither a depletion region nor a potential barrier to prevent electrons from migrating from the semiconductor towards the metal or vice versa.

The electron concentration in the vicinity of the interface increases, and the bulk semiconductor region attains the highest resistance in the system. Almost all of the externally applied voltage is distributed across the bulk region, as depicted in Fig. 2.3(c) and Fig. 2.3(d) for the two current flowing directions. It is evident that the current is governed by the bulk-region resistance and remains unaffected by the direction of the applied bias. This type of non-rectifying contact is commonly known as an Ohmic contact.

For n-type semiconductors, an MS contact is known to be rectifying if $\phi_m > \phi_s$ and is non-rectifying if $\phi_m < \phi_s$. Conversely, for a metal-p-type semiconductor contact, the opposite phenomena occur. When $\phi_m < \phi_s$, the energy band diagrams for separate materials are depicted in Fig. 2.4(a). After the contact, electrons flow from the metal into

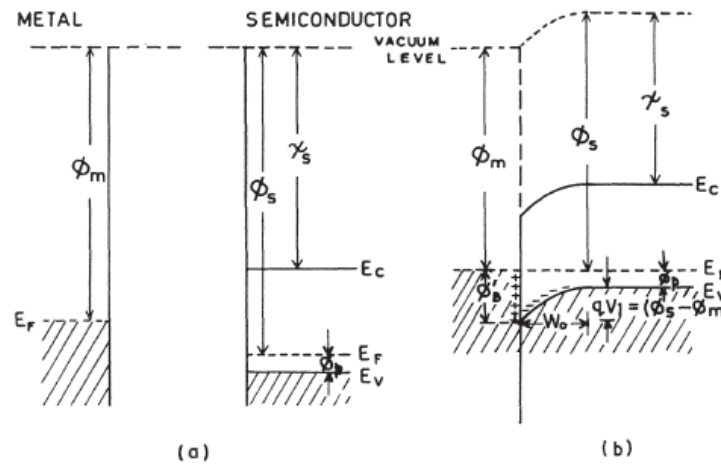


Fig. 2.4: Electron energy band diagrams of metal contact on p-type semiconductor with $\phi_m < \phi_s$ (a) Neutral and separated materials and (b) at thermal equilibrium after the contact has been formed.

the semiconductor until the Fermi levels on both sides align. These electrons, being minority carriers in the p-type semiconductor, subsequently recombine with holes, forming a space-charge layer of ionized acceptors, as illustrated in Fig. 2.4(b). The hole concentration in the space-charge region is significantly smaller in comparison with the acceptor concentration, resulting in the space-charge region on the semiconductor region consisting of a depleted region whose thickness (W_0) depends on the concentration of ionized acceptor atoms.

For p-type semiconductors, barriers for holes in the band diagram must be considered. The barrier height for holes is determined by the following relation:

$$\phi_{B'} = \chi_s + E_g - \phi_m \quad (2.4)$$

where E_g is the band gap of the semiconductor. From equations (2.1) and (2.2), it follows that,

$$\phi_B + \phi_{B'} = E_g \quad (2.5)$$

Similar to the discussion for n-type semiconductors, it can be shown that a contact formed by a metal and a p-type semiconductor is non-rectifying if $\phi_m > \phi_s$. However, it is observed that Schottky barriers with p-type semiconductors typically exhibit smaller barrier heights and are infrequently utilized in practical devices.

2.1.2. Modifications of Schottky Theory

Metal-semiconductor contacts in practical scenarios often deviate from the guidelines outlined above. Specifically, Eq. (2.1) indicates that the barrier height (ϕ_B) varies linearly with the metal work function (ϕ_m). This strong dependence on ϕ_m is prominent in predominantly ionic semiconductors. However, in many covalent semiconductors, the barrier height exhibits less sensitivity to ϕ_m , and in some cases, it is nearly independent of ϕ_m .

Bardeen was the first to elucidate that the barrier height in covalently bonded semiconductors is insensitive to the metal work function. He highlighted the significance of localized surface states in determining the barrier height. At the semiconductor's surface, the periodicity of the crystal lattice comes to an end. In a covalent crystal, surface atoms only have neighbours on the semiconductor region, and on the vacuum region, there are no neighbours available for covalent bonds. Consequently, each surface atom has a broken covalent bond with one electron present and the other missing, known as a dangling bond. These dangling bonds create localized energy states at the semiconductor's surface, with energy levels situated within the forbidden gap.

These surface states generally form a continuous distribution in the band gap, characterized by a neutral level (ϕ_0). The position of the ϕ_0 is such that, in the absence of band bending in the semiconductor, the states are filled by electrons up to ϕ_0 , rendering the surface electrically neutral. When states below ϕ_0 are occupied or empty, they behave like donors or positive, and when they are unoccupied, they function like acceptors. The density of surface states on covalent semiconductor surfaces can substantially decrease the presence of adsorbed layers of foreign atoms, which can complete the broken covalent bonds.

The presence of surface states has a notable impact on the charge distribution in the depletion region, influencing the barrier height. In Fig. 2.5(a), the energy band diagram of an n-type semiconductor with flat-band conditions is depicted. This state is characterized by non-equilibrium conditions, transitioning to equilibrium when electrons from the semiconductor near the surface occupy states above ϕ_0 , aligning the Fermi level at the surface with that in the bulk. This leads to a negatively charged surface and the creation of a depletion region comprising ionized donors on the semiconductor side near the surface. Due to this dipole, a potential barrier is established in the direction

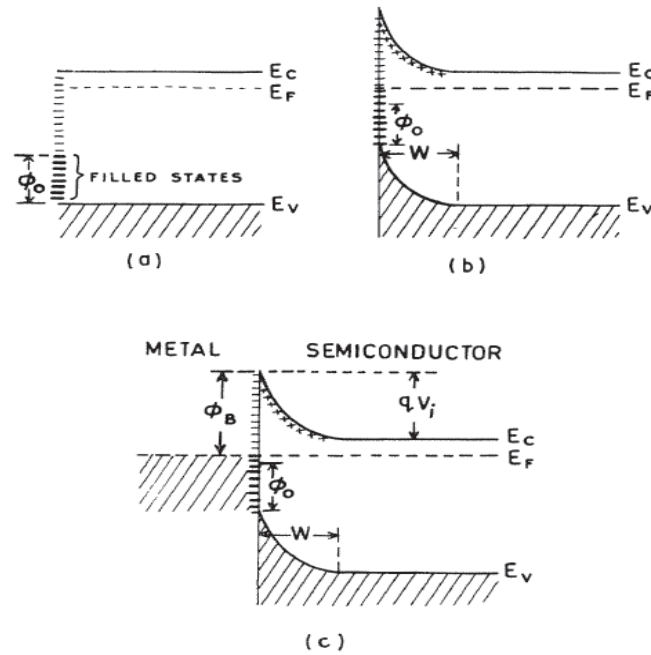


Fig. 2.5: Energy band diagrams of n-type semiconductors incorporating surface states. The diagrams depict (a) a flat-band at the surface, (b) a surface in thermal equilibrium with the bulk, and (c) a semiconductor in contact with a metal.

from the surface to the semiconductor, even when there is no metal contact, as displayed in Fig. 2.5(b).

Upon introducing a metal into contact with the semiconductor and reaching equilibrium, the Fermi level in the semiconductor changes, exchanging charge with the metal. If the density of surface states at the semiconductor surface is substantial, the charge exchange predominantly occurs between the metal and the surface states, with minimal impact on the space charge in the semiconductor. Consequently, the barrier height in Fig. 2.5(c) becomes independent of the metal work function and is determined by the expression:

$$\phi_B = (E_g - \phi_0) \quad (2.6)$$

In this scenario, the barrier height is termed "pinned" by surface states, and Eq. (2.5) is denoted as the Bardeen limit.

2.2. Classification of Metal-Semiconductor Interfaces

The interfaces between metals and non-metals can be systematically classified into

four primary types based on the resulting atomic configuration at the interface. These categories are as follows:

Type I: This category involves non-metal acting as an insulator or semiconductor, where the metal is physisorbed onto its surface. This type of interface exhibits ideal Schottky barrier contact, where the barrier height directly varies with the metal work function.

Type II: In this type, the non-metal is a highly polarizable semiconductor, such as silicon, with a dielectric constant (ϵ_r) greater than 7. The metal forms a weak chemical bond with the semiconductor surface, without reacting to create a bulk compound. They resemble a "Bardeen barrier," assuming that surface states are spread over the space in the semiconductor, allowing for a potential drop across this region. The barrier height in decent contacts of this type is expected to exhibit a weak dependence on ϕ_m .

Type III: In Type III interfaces, the highly polarizable semiconductor undergoes a chemical reaction with the metal, leading to the formation of one or more chemical compounds. They represent a scenario of strong chemical bonding between the metal and the semiconductor. The barrier height is expected to be influenced by factors related to chemical or metallurgical reactions occurring at the interface.

Type IV: This type involves the formation of a thin film of native oxide during the surface preparation of a highly polarizable semiconductor. This film acts as an interfacial layer, hindering intimate contact between the metal and the semiconductor. This type of interface is frequently encountered in practical metal-semiconductor devices; this case involves a brief discussion in the subsequent section.

2.3. Contacts with Surface States and an Insulating Interfacial Layer

In the majority of metal-semiconductor contacts, the semiconductor surface, before metal deposition, undergoes chemical cleaning, resulting in the presence of a thin insulating oxide layer on its surface. The thickness of this interfacial layer is contingent upon the surface preparation method and, for optimal Schottky contacts, should be maintained below approximately 20 Å. The energy band diagram illustrating a contact with an interfacial oxide layer is depicted in Fig. 2.6.

As previously elucidated, the Fermi level remains uniform throughout the system,

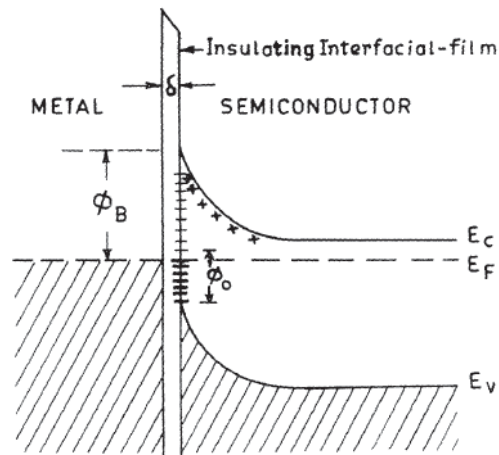


Fig. 2.6: Energy band diagram of a metal-semiconductor contact with surface states and interfacial layer.

and the vacuum level exhibits continuity along the interface. The potential linearly drops across the interfacial oxide layer (Fig. 2.6), assuming it to be an ideal insulator with no charge. Furthermore, it is presumed that the lower edge of the CB in the insulator lies beneath the vacuum level. In instances where the interfacial layer is sufficiently narrow (i.e. $<20 \text{ \AA}$), the potential drop along it is insignificantly small in comparison to that in the semiconductor depletion region. This thin region is electron-transparent, allowing electrons to tunnel through it bi-directionally. Consequently, the ϕ_B and V_i remain largely unchanged by the presence of this thin interfacial layer.

Contacts featuring a thin insulating layer between the metal and semiconductor prove more amenable to theoretical understanding and analysis than their decent and strong counterparts. This is attributed to the insulating layer acting as a separator, enabling the treatment of the metal and semiconductor as distinct systems. Consequently, one can consider interface states as a characteristic of the specific semiconductor-insulator combination, disregarding any alterations in the surface dipole contributions to the work functions of the metal and semiconductor. Such simplifications are not applicable when dealing with clean contacts.

2.4. Fabrication Process of Schottky Diodes

Material Selection: In the fabrication of Schottky diodes, metal choice is crucial and is determined by the semiconductor type. Aluminium (Al) or platinum (Pt) is commonly preferred for n-type semiconductors to establish a rectifying contact. Despite silver's (Ag) excellent electrical conductivity, its susceptibility to oxidation limits its use in metal-

semiconductor junctions. In thin film applications, indium tin oxide (ITO) on a glass substrate is utilized for its resilience at elevated temperatures. Silicon wafers with specific orientation, thickness, and resistivity are selected for silicon-based Schottky diodes.

Cleaning: To ensure an uncontaminated surface, ITO/wafers undergo meticulous cleaning with trichloroethylene, acetone, and methanol solvents. The final cleaning step involves using a 30-40% HF etching solution [7].

Rinsing: Wafers are rinsed in deionized (DI) water repeatedly before subsequent deposition procedures.

Deposition of Semiconducting Materials: The materials to be used as the semiconducting layer are deposited onto the ITO glass substrate with the help of Spin coating units with a rotation of a certain rpm. Any other PVD methods, such as evaporation by electron beam can also be used to deposit the films of the semiconducting materials.

Ohmic Contact Formation: Ohmic contacts on the back side of silicon wafers are established for efficient electrical connections to semiconductor regions. High-purity aluminium or the chosen metal is deposited using vacuum coating units, maintaining a constant low pressure for uniformity up to a few tens of nanometers. Annealing optimizes temperature, duration, and pressure, facilitating inter-diffusion and forming well-defined Ohmic contacts.

Schottky Contacts: Before metal deposition, silicon wafers are cleaned and etched in a 40% HF solution to remove the native oxide layer. A thin layer of the chosen metal is then applied to the semiconductor surface using deposition techniques such as sputtering or evaporation, with thickness controlled for desired electrical characteristics. A few optional steps are:

Photolithography: Photolithography defines the Schottky contact area by applying photoresist, exposing it to UV light through a mask, and developing the pattern through chemical processing.

Etching: Precision etchants selectively remove metal in exposed regions, defining the final geometry of the Schottky diode.

Passivation: Optionally, a passivation layer is deposited over the Schottky diode to enhance long-term stability and shield it from environmental factors.

2.4.1. Aluminium in Device Fabrication

Aluminium, the Earth's most abundant metal, stands out for its exceptional malleability, ductility, and lightweight characteristics. Compared to numerous other metals, it exhibits a relatively soft nature. Beyond its mechanical attributes, aluminium demonstrates commendable electrical and thermal conductivity while maintaining reasonable resistance to corrosion. Remarkably environmentally friendly, it can be recycled without compromising any of its intrinsic properties. In contrast, platinum, a more expensive and heavier metal, has a higher work function of 5.65 eV, in stark contrast to aluminium's lower work function of 4.2 eV.

2.4.2. Glass Substrate Coated with Indium Tin Oxide (ITO)

Indium Tin Oxide (ITO) is a compound consisting of indium (In), tin (Sn), and oxygen (O), with a composition of 74% In, 18% Sn, and 8% O. Widely recognized for its combination of electrical conductivity, optical transparency, ease of deposition as a thin layer, and moisture resistance, ITO stands out as one of the most commonly employed transparent conducting oxides. Typically, thin films of indium tin oxide are deposited onto glass surfaces using physical vapour deposition techniques. These films exhibit an optical transmittance exceeding 80% for thin layers, accompanied by a low electrical resistivity of only $10^{-4} \Omega\text{-cm}$ [8].

2.4.3. Metal Deposition

The fabrication of metal-semiconductor junctions follows a vertical sandwich configuration, specifically Al/synthesized material/ITO, chosen for its simplicity in junction fabrication. Initial to this process is the meticulous cleaning of the ITO, necessitating a thorough cleaning procedure. The ITO-coated glass substrates undergo a sequential cleaning process involving ultra-sonication with a mild basic water solution (containing a small amount of purified sodium hydroxide in distilled water), followed by rinsing with acetone, ethanol, and distilled water. Subsequently, the synthesized material is dispersed/dissolved in a suitable medium under ultra-sonication and is spin-coated on the pre-cleaned ITO substrate at a specified rpm for multiple cycles. The resulting films are then dried in a vacuum chamber for several hours.

The next step involves the deposition of aluminium metal on the thin film of the material through thermal evaporation. This process employs an electron gun within the vacuum coating unit, maintaining a low pressure, generally at 10^{-6} mbar. To define the metal-semiconductor interface precisely, a shadow mask is employed during metal deposition, ensuring an effective junctional area of $7.065 \times 10^{-6} \text{ m}^2$. The schematic structure of the fabricated Schottky diode is provided in the following Fig. 2.7.

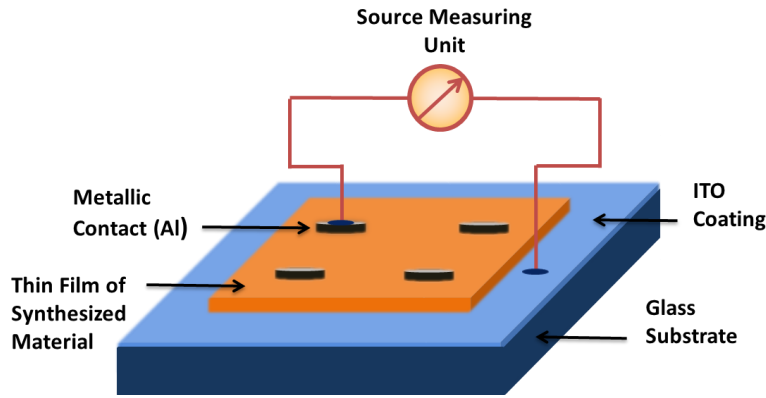


Fig. 2.7: Schematic diagram of fabricated MS junction Schottky diode.

2.5. Electrical Studies of Schottky Barrier Diodes

There are different ways to measure the important Schottky diode parameters (e.g. ideality factor, barrier height and series resistance) and charge transport parameters (e.g. mobility and transit time). They are described shortly in the following section.

2.5.1. Evaluation of Ideality Factor, Barrier Height and Series

Resistance

In Schottky barrier diodes constructed on high mobility semiconductors like Si and GaAs, the current is attributed to the thermionic emission of electrons across the barrier and its dependence on the applied bias V is expressed by the relationship:

$$I = I_0 \left[\exp\left(\frac{qV}{\eta kT}\right) - 1 \right] \quad (2.7)$$

$$\text{where, } I_0 = A_{eff} A^* T^2 \exp\left(\frac{-\phi_B}{kT}\right) \quad (2.8)$$

Here, η represents the diode ideality factor, and A^* denotes the modified Richardson constant for the semiconductor. For forward bias values of V exceeding $3kT/q$, the $\ln(I)$ vs. V plot yields a linear relationship. By extrapolating this line to $V = 0$, I_0 can be determined. Utilizing I_0 , A^* , the diode cross-sectional area A_{eff} , and the temperature T , the zero bias barrier height (ϕ_B) is computed, accounting for the image force barrier lowering distance ($\Delta\phi_B$).

In situations where A^* is unknown, the barrier height can still be deduced. Forward I-V characteristics of the diode are acquired at various temperatures, and I_0 is determined for each temperature. A $\ln(I_0/T^2)$ versus $1/T$ plot results in a straight line, with the slope offering the barrier height ϕ_B , and the intercept on the I_0/T^2 axis providing the value of A^* .

$$\ln\left(\frac{I_0}{T^2}\right) = \ln(A_{\text{eff}} A^*) - \frac{\phi_B}{kT} \quad (2.9)$$

The method yields the barrier height at 0 K, marginally higher than the room-temperature barrier height. Real devices often exhibit deviations from ideal behaviour, with the emergence of a significant series resistance R_s at higher currents, encompassing the series resistance of the semiconductor, metal, and contacts. Thus,

$$V_{\text{eff}} = V - IR_s \quad (2.10)$$

Now, equation (2.7) can be rearranged as,

$$I = I_0 \left[\exp\left\{\frac{q(V - IR_s)}{\eta kT}\right\} - 1 \right] \quad (2.11)$$

In forward bias, for $V > kT/q$ and $V \gg IR_s$, it can be derived from the diode equation that:

$$\frac{dV}{d(\ln I)} = \left(\frac{\eta kT}{q}\right) + IR_s \quad (2.12)$$

The value of η and R_s can be estimated from the intercept and the slope of the straight line of the $dV/d(\ln I)$ vs. I plot.

2.5.2. Estimation of Mobility and Transit Time

The I-V characteristics can further be analysed by interpreting the charge carrier's mobility (μ_{eff}) and lifetime (τ) using the space-charge limited current (SCLC) theory to elucidate the charge transport mechanism for various photo-induced applications [9]. Plotting $\log(I)$ against $\log(V)$ for positive voltages reveals distinct linear regions indicative of different conduction mechanisms. In metal-semiconductor junctions, interfacial trap states significantly influence charge carrier conduction, thereby altering I-V characteristic curves. At low bias, Ohmic behaviour ($I \propto V$) with a slope near unity is observed, indicating predominant conduction by intrinsic charge carriers [10]. Subsequently, as the slope increases (typically reaching 2), injected carriers from the contacts begin to dominate over intrinsic carriers for intermediate potential values, establishing a spatially distributed charge field. Mobility primarily governs quadratic current ($I \propto V^2$) in this region [9,11]. Eventually, at higher applied voltages, the device surpasses the trap-filled limit, resulting in conduction primarily through 'trap-free space-charge limited current' characterized by power-law behaviour ($I \propto V^n$, where $n > 2$), corresponding to region III [11].

The mobility of electrons is estimated from the slope of the I vs. V^2 plot, according to the Mott-Gurney equation [11]:

$$I = \frac{9\mu_{\text{eff}}\epsilon_0\epsilon_r A_{\text{eff}}}{8} \left(\frac{V^2}{d^3} \right) \quad (2.13)$$

where, A_{eff} , ϵ_0 , ϵ_r and d stand for the effective diode area, the free space permittivity, the dielectric constant of materials and the thickness of the diode, respectively.

Here, the dielectric constant (ϵ_r) of the synthesized materials could be estimated from the capacitance (C) vs. frequency (f) plot, obtained from the measurement by an impedance analyser.

$$\epsilon_r = \frac{C_0 d}{\epsilon_0 A_{\text{eff}}} \quad (2.14)$$

where, C_0 is the saturated capacitance[12].

Also, the lifetime or transient time (τ) of the charge carriers could be deduced by employing the following equation [13]:

$$\tau = \frac{9\epsilon_0\epsilon_r A_{eff}}{8d} \left(\frac{V}{I}\right) \quad (2.15)$$

2.5.3. Capacitance-Voltage Measurement

In the capacitance-voltage measurement approach, the diode capacitance is evaluated concerning the applied reverse bias. When subjecting a reverse-biased diode to a small AC voltage of a few millivolts, the depletion region capacitance C is defined by the equation:

$$C = A_{eff} \left[\frac{\epsilon_s q N_d}{2 \left(V_i + V_R - \frac{kT}{q} \right)} \right]^{\frac{1}{2}} \quad (2.16)$$

where A_{eff} represents the cross-sectional area of the diode, ϵ_s the permittivity of the semiconducting material used, V_R is the applied reverse voltage, and all other symbols maintain their conventional meanings. This formulation assumes the absence of a significant interfacial oxide layer in the diode and uniform donor concentration N_d in the n-type semiconductor. Notably, a plot of $1/C^2$ versus V_R yields a linear relationship with a slope of $(2/A_{eff}^2 \epsilon_s q N_d)$ and an intercept on the voltage axis $V_0 = (V_i - kT/q)$. The slope enables the determination of the dopant concentration N_d , and as $qV_i = (\phi_B - \phi_n)$, the barrier height ϕ_B is derived as:

$$\phi_B = qV_0 + \phi_n + kT \quad (2.17)$$

Here, the kT factor accounts for the contribution of the majority carriers to the space charge, and Eq. (2.17) excludes the image force barrier lowering.

2.5.4. Photoelectric Measurement

The photo-electric measurement stands out as the direct and most accurate approach for estimating the barrier height (ϕ_B). In this method, a monochromatic light is directed onto a metal in contact with a semiconductor. If the photon energy ($h\nu$) exceeds the barrier height (ϕ_B) but is less than the band gap of the semiconductor, the incident photons cause electron excitation from the metal over the barrier. The resulting photocurrent (I_{ph}) for $(h\nu - \phi_B) \gg 3kT$ is described by the Fowler theory as:

$$I_{ph} = B(h\nu - \phi_B)^2 \quad (2.18)$$

where B represents the proportionality constant. When I_{ph} is plotted against $h\nu$, a straight line is generated and the intercept of the $h\nu$ axis provides the value of ϕ_B .

2.5.5. Application of Schottky Diodes

Schottky diodes exhibit a superior current drive capability compared to typical p-n junctions and, contingent on the Schottky barrier height (SBH), manifest a larger saturation current. Consequently, in circuit applications necessitating high current and low voltage, Schottky diodes emerge as the favoured rectifying devices. Moreover, Schottky diodes avoid issues associated with minority carriers, as they do not face the limitations tied to minority carrier recombination time that are inherent in a p-n junction. This characteristic makes Schottky diodes notably faster, which makes them suitable for use in digital logic circuits as rapid switches. High-speed Schottky photodiodes find applications in optical measurements and communications technologies. Schottky junctions also serve as cost-effective photovoltaic cells. Additionally, metal-semiconductor contacts play a pivotal role as gate electrodes in field-effect transistors, the drain and source contacts in MOSFETs, the electrodes for high-power IMPATT oscillators, and the third terminal in a transferred-electron device.

2.6. Impedance Spectroscopy (IS)

In the late nineteenth century, Oliver Heaviside introduced the non-destructive technique of Impedance Spectroscopy, which later evolved based on complex mathematical transforms. He contributed terminologies such as Impedance, Admittance, and Conductance. A. E. Kennelly and C. P. Steinmetz further developed this approach [14], representing it through vector diagrams and complex illustrations. Impedance spectroscopy is a potent method for characterizing the electrical properties of materials and interfaces between materials and electrodes. It is applicable for analysing the dynamics of bound and mobile charges in the bulk and interfacial regions of various materials, including ionic, semiconducting, mixed electronic-ionic, and insulators (dielectrics). A significant benefit of impedance spectroscopy for studying the electrical and electrochemical properties of materials and systems is the direct correspondence often seen between the behaviour of a real system and that of an equivalent model circuit

made up of distinct electrical components. Researchers often analyze or fit impedance data to an equivalent circuit that represents the physical processes occurring in the material and at the interfaces.

2.6.1. Associated Functions in Impedance Spectroscopy

Impedance, a more comprehensive concept than resistance, incorporates phase variations, making it a fundamental idea in electrical engineering. Impedance spectroscopy is characterized by the measurement and analysis of the four impedance-related functions: Z , Y , M , and ϵ . The visualization of these functions in the complex plane, as we will investigate, is very advantageous for interpreting the small signal AC response of the electrode material system being studied. The utilization of Z and Y in analysing the response of electrical circuits composed of lumped (ideal) components (R , L , and C) dates back to the early stages of electrical engineering. A significant achievement in the analysis of real systems, particularly those distributed in space, was made by Cole and Cole [1941] through the plotting of ϵ' and ϵ'' for dielectric systems in the complex plane, now known as a Cole-Cole plot. Moreover, Z and/or Y have found extensive application in the theoretical treatment of semiconductor and ionic systems. Complex plane plots are sometimes referred to as Nyquist plots.

Impedance, defined as a complex quantity, is real when $\theta=0$, representing purely resistive conductance, when $Z(\omega) = Z'(\omega)$. In this situation, the impedance remains constant regardless of frequency. However, when Z' is recognized as a frequency-dependent characteristic, the Kronig-Kramers (Hilbert integral transform) and Macdonald, Brachman [1956] approach to integrate the real and imaginary components to ensure that Z'' cannot be zero across all frequencies but should vary with frequency.

Impedance is expressed as $Z^*(\omega) = Z'(\omega) - jZ''(\omega)$; where $Z'(\omega) = |Z|\cos\theta$ and $Z''(\omega) = |Z|\sin\theta$ are real and imaginary parts of the total impedance. In impedance spectroscopy, various measured or derived quantities associated with impedance play pivotal roles. The admittance is represented as, $Y = Z^{-1} = Y' + jY''$. In the complex plane, we can express $v=Zi$ or $i=Yv$, where v , i , and Z are treated as complex. It is additionally standard in impedance spectroscopy to denote Z and Y as far as resistive and capacitance parts as $Z = R_s(\omega) - jX_s(\omega)$ and $Y = G_p(\omega) + jB_p(\omega)$, where the reactance,

$X_s = \{\omega C_s(\omega)\}^{-1}$ and the susceptance, $B_p = \{\omega C_p(\omega)\}$. Here the subscripts s and p mean "Series" and "Parallel". The other two quantities are normally characterized as the modulus function $M = j\omega C_0 Z = M' + jM''$ and the complex dielectric constant or dielectric permittivity $\varepsilon = M^{-1} = Y / (j\omega C_0) = \varepsilon' - j\varepsilon''$. In the above equations, $C_0 = \varepsilon_0 A / l$ C_0 is the capacitance of the empty measuring cell, where A, l and ε_0 denotes the electrode area, separation length and the dielectric permittivity of free space respectively. The relations among the four impedance functions are presented in Table 2.1.

Table. 2.1: Relation between the four Impedance functions [14].

	Z	Y	M	ε
Z	Z	Y^{-1}	$M/j\omega C_0$	$1/j\omega C_0 \varepsilon$
Y	Z^{-1}	Y	$j\omega C_0/M$	$j\omega C_0 \varepsilon$
M	$j\omega C_0 Z$	$j\omega C_0/Y$	M	ε^{-1}
ε	$1/j\omega C_0 Z$	$Y/j\omega C_0$	M^{-1}	ε

2.6.2. Equivalent Circuit Model

Impedance data, often represented in graphical plots showing impedance, dielectric properties, or modulus, is typically analyzed by fitting it to an equivalent electrical circuit model. Various basic electrical circuits, comprising combinations of ideal resistors and capacitors, are used to create representative impedance data plots. In practical settings, the impedance of an unknown system is first measured, generating impedance data plots. These plots are then compared with those of established equivalent circuits, leading to an initial selection of a circuit that best matches the experimentally obtained impedance data and offers a plausible explanation of the observed phenomenon. The choice of equivalent circuits should be guided by an intuitive understanding of the electrochemical system, relying on the chemical and physical properties of the system rather than randomly selected circuit elements [15]. Most circuit components in the model are

fundamental electrical elements, such as resistors, capacitors, and inductors. It is essential to recognize that impedance analysis is an intricate endeavour, encompassing physical, chemical, electrical, and mechanical components translated into electrical terms. Impedance data is often fitted with an equivalent circuit that includes circuit elements corresponding to the physical processes occurring within the investigated device. While ideal circuit components like resistors and capacitors can often be applied, real systems may exhibit deviations from ideal behaviour. Generally, a combination of distributed circuit components, such as the constant phase element (CPE) and the Warburg diffusion impedance, is required to adequately describe the impedance response of real systems, acknowledging their non-ideal nature (Table 2.2) [14][16].

Table. 2.2: The circuit components utilized in the Equivalent circuit (EC) model [14].

Components	Units	Equivalent Element	Impedance
Resistor	Ohm	R	R
Capacitor	F or Ohm ⁻¹ S	C	$\frac{1}{j\omega C}$
Inductor	H or Ohm S	L	$j\omega L$
Infinite Diffusion	Ohm	Z_W	$\frac{R_w}{\sqrt{(j\omega)}}$
Finite Diffusion	Ohm	Z_0	$\frac{R_0 \tanh\left(\sqrt{\frac{j\omega L_0^2}{D}}\right)}{\sqrt{\frac{j\omega L_0^2}{D}}}$
Constant Phase Element	Ohm ⁻¹ S ^α	Q	$\frac{1}{Q(j\omega)^\alpha}$

2.7. Positron Annihilation Spectroscopy (PAS)

Positron Annihilation Spectroscopy (PAS) has proven highly effective in the examination of electron characteristics and the identification of defect structures in various materials, including crystalline solids common in semiconductor applications. In semiconductor materials, lattice defects play a crucial role, akin to "flavours in your food," influencing material properties significantly, whether positively or negatively. These defects impact electrical conductivity by generating, trapping, and scattering charge carriers. Due to thermodynamic equilibrium requirements, a certain concentration of defects is inevitable at finite temperatures, and various factors in practical scenarios contribute to an increased concentration of defects in real crystals.

The application of positron annihilation spectroscopy in studying semiconductor defects dates back to the mid-80s, with earlier reports on radiation damage in silicon and germanium appearing in the 70s. The positron, the antiparticle of the electron theorized by Paul Dirac in 1928 and discovered experimentally in 1932, garnered significant interest and was extensively studied during the 1940s and 1950s. By the late 1960s, it was recognized that positrons exhibited sensitivity to lattice defects in metals. Presently, PAS is widely employed in approximately 200 research labs worldwide, with around 40 operational slow positron beams in about 30 research facilities.

PAS finds applications in investigating a wide range of phenomena, including electron characteristics, defect structures, magnetic properties of solids, plastic deformation at varying temperatures, phase transformations in alloys, semiconductors, polymers, porous materials, and more. Its utility extends beyond solid-state physics and materials science to chemistry, biology, and medical science, where it is utilized, for instance, in tumour detection. PAS stands out as a non-destructive technique, enabling the subsequent analysis of a sample using various methods. Commercially available experimental equipment for PAS is relatively affordable, making it increasingly popular in research laboratories for fundamental studies, diagnostics of system elements operating in challenging conditions, and the characterization of high-tech materials.

2.7.1. Positron Annihilation Process

The annihilation of a positron-electron pair yields photons with a total energy of $2m_0c^2$, slightly less than the electron binding energy, denoted as $\approx 2m_0c^2$ (≈ 511 keV),

representing the electron rest mass energy. In Positron Annihilation Spectroscopy (PAS), these annihilation photons are instrumental in investigating the properties of the electron engaged in the annihilation process. Upon penetration into solids, an energetic positron undergoes thermalization within a few picoseconds, experiencing ionizing collisions, phonon interactions [17], and subsequent diffusion motion before annihilating, converting its entire mass into energy, following Einstein's equation $E=m_0c^2$. The annihilation of a positron and an electron results in the release of energy in the form of photons, with a total energy of 1.022 MeV, corresponding to the combined rest mass energies of the positron and electron. The number of emitted photons depends on the specific annihilation dynamics between the positron and electron. Positron beam energies typically span from 10 eV to 100 keV, with mean stopping depths varying from 1 nm to a few μm , underscoring the potential of positron beams for PAS studies in near-surface regions of condensed matter. Positrons exhibit a brief lifespan within a material for two primary reasons:

- i. They can undergo direct annihilation with electrons, where they collide head-on within the medium, resulting in an annihilation process that yields two photons with an energy of 0.511 MeV. or,
- ii. In certain materials, they may form a bound state with an electron, analogous to a hydrogen atom with a B.E. of approximately 6.8 eV, known as positronium (Ps), which also undergoes annihilation.

The interaction between electrons and positrons enables the annihilation of electron-positron ($e^- - e^+$) pairs, where the total energy of the annihilating pair can be converted into photons (quanta of the electromagnetic fields). The reactions involved are:

$$e^+ + e^- = \gamma(\text{quanta}) \quad (2.19)$$

$$E_{2\gamma} = 2m_0c^2 + E_{e^+} + E_{e^-} \quad (2.20)$$

$$m_0c^2 = 511 \text{ KeV} \quad (2.21)$$

In the given equations, $E_{2\gamma}$, E_{e^+} , and E_{e^-} represent the energies of the resulting photon pair, electron, and positron, respectively. Here, m_0 represents the rest mass of both the electron and the positron, while c denotes the speed of light. The annihilation process

follows specific fundamental conservation laws, such as the conservation of total energy, total angular momentum, total linear momentum, and parity. The lifetime of a positron is inversely related to the electron density it encounters. Therefore, studying the radiation resulting from the annihilation of a positron with an electron is vital for understanding the fundamental properties of the positron and for exploring the characteristics of the surrounding environment at the annihilation site. Annihilation can happen between free positrons and electrons or between particles in a bound state like positronium (Ps). In condensed matter, the positron-electron pairs typically have a lifespan ranging from a few tenths to a few nanoseconds before undergoing annihilation.

➤ *Annihilation of Free Positron*

After thermalization, a positron can annihilate with an electron in the medium either through a singlet collision (where spins are antiparallel, denoted as $s=0$) or through a triplet collision (where spins are parallel, denoted as $s=1$). According to the rules governing annihilation, a singlet collision results in the emission of two photons (2γ -ray) travelling precisely opposite to each other in the centre-of-mass system, each with an energy of about 0.511 MeV ($= m_0c^2$) [18]. Alternatively, a triplet collision can lead to annihilation into three γ -rays. In this case, the rest energy ($= 2m_0c^2$) of the electron-positron pair is distributed among the three photons, which are emitted in one plane but in different directions relative to each other. In this type of decay, the annihilation cross-section for emitting 3γ -rays is reduced by approximately the fine structure constant α ($\alpha=1/137$) of the cross-section [19]. Even though very uncommon from a hypothetical perspective, non-photon and one-photon annihilation are also conceivable however just if a third body is sufficiently close to absorb the recoil momentum such as an electron or nuclei.

➤ *Formation of Positronium*

In an electronic medium, a positron can capture an electron, forming a neutral atom known as Positronium (Ps) when the positron's energy is reduced to less than 10 eV in a medium [20]. The existence of Ps and its chemical reactions with particles were first identified from annihilation photons in 1951 [18]. Positronium exists in two states: para-positronium (p-Ps), which annihilates into 2γ -rays with a lifetime of about 0.125 ns in a vacuum due to the anti-parallel spin combination, and ortho-positronium (o-Ps), which

results from the parallel spin combination. o-Ps has a much longer lifetime (~ 142 ns in a vacuum) because of its self-annihilation, and it decays through 3 photons (γ -ray), all having energies under 0.511 MeV.

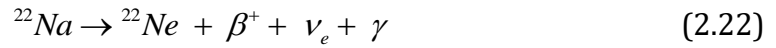
In atomic environments, the positronium (Ps) can interact with electrons from the medium, particularly those with anti-parallel spins to the positron, leading to a process known as 'pick-off' annihilation. This process involves two-photon annihilation of ortho-positronium (o-Ps), significantly reducing its lifetime from 142 ns (for free o-Ps) to a few nanoseconds. Notably, the pick-off annihilation lifetime of o-Ps is about ten times longer in molecular systems compared to crystalline or metallic media. The experimental determination of o-Ps lifetime is critical in positron and positronium research as it provides insights into electron density, a fundamental aspect governing chemical bonding in atoms and influenced by atomic structure. In materials with large open volumes like polymers, the lifetime of Ps can range from 1-2 nanoseconds or more. The ratio of para-positronium (p-Ps) to o-Ps states typically stands at around 1:3 in the absence of external electric and magnetic fields.

➡ *Positron Sources*

The primary techniques for producing low-energy positrons include pair generation in a high-energy accelerator [21] or the radioactive decay of a nucleus [22]. The high-energy accelerator method involves using high-energy electrons that, upon deceleration in matter, emit photons via the Bremsstrahlung process. If the photon energy exceeds twice the electron rest mass energy, positrons (and electrons) can be created through the pair conversion of these photons. This method has been effectively used in different laboratories, providing the benefit of generating a pulsed positron beam suitable for depth-resolved measurements of positron lifetime.

In the case of lab-scale facilities, the beta (β^+) decay of radioactive isotopes is commonly used. The vast majority of positron studies on solids have been conducted using positron sources such as ^{22}Na , ^{58}Co , ^{64}Cu , and ^{86}Sr , chosen for their low production costs, ease of production in the laboratory, and favourable half-lives. The short-lived ^{64}Cu isotope (half-life ≈ 12.8 h) is utilized when it can be generated promptly, e.g., near a nuclear reactor, through irradiation of isotopically enriched ^{63}Cu with thermal neutrons. Isotopes like ^{58}Co and ^{22}Na have relatively long half-lives of 71 days and 2.6 years, respectively. Another critical factor in choosing a radioisotope is the positron branching

ratio, defined as the number of positron emissions divided by the total number of decay emissions. For ^{22}Na and ^{58}Co , these ratios are 0.89 and 0.15, respectively. Considering both half-life and branching ratio, ^{22}Na is typically the preferred choice as a positron source. ^{22}Na emits a prompt 1.274 MeV γ -ray simultaneously with positron emission, facilitating the recording of positron lifetime using a coincidence γ -spectrometer. Moreover, it is conveniently accessible in a dilute solution of $^{22}\text{NaCl}$, which is straightforward to manage and chemically stable. The stopping profile of β^+ particles in solids decreases exponentially with increasing penetration depth (z), represented as $P(z) \sim \exp(-z/z_0)$, where typical mean penetration depths z_0 are approximately 15-100 μm [23]. The radioactive source ^{22}Na decays according to the following reaction:



The ^{22}Na isotope exhibits a remarkably high positron yield of 90.4%. Its decay involves positron emission and electron capture, leading to the first excited state of the neon nucleus (^{22}Ne) and the emission of an energetic positron and an electron neutrino. The excited state promptly de-excites to the ground state by emitting a 1.274 MeV γ -ray with a half-life ($\tau_{1/2}$) of 3 ps. In 10% of cases, ^{22}Na undergoes decay through electron capture. A small fraction (0.05%) of decay leads directly to the ground state of Ne, accompanied by the emission of an additional energetic positron (Fig. 2.8). Consequently, positron emission almost coincides with the emission of the 1.274 MeV γ -ray, while the subsequent positron annihilation is observed through two 0.511 MeV γ -rays.

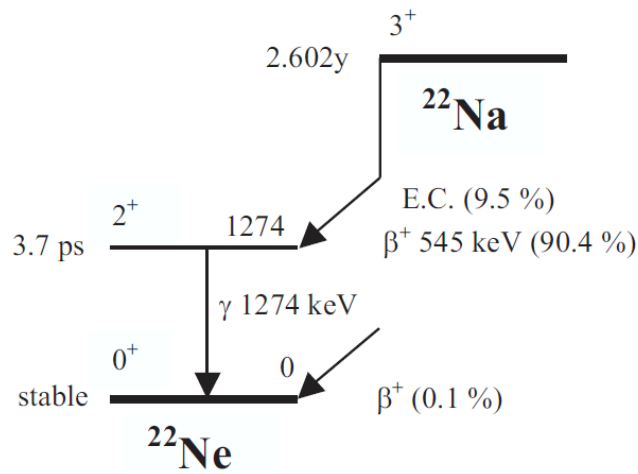


Fig. 2.8: Decay profile of ^{22}Na . (Adapted from Ref. [23])

The positrons generated in the γ decay of ^{22}Na exhibit a broad energy distribution, extending up to 0.540 MeV, allowing for deep penetration into a sample. To obtain depth profile information, especially for analyzing thin layers, mono-energetic "slow" positron beams are crucial. Fast positrons can be moderated through a moderation step. Positrons can be emitted from a surface with a negative work function. The characteristic time scales of various positron annihilation processes in materials are summarized in Table 2.3.

When positrons are introduced into a solid medium, they quickly reach thermal equilibrium with their surroundings, interact with the environment, and eventually annihilate with electrons within the material. The observable characteristics of this annihilation process provide insights into the structure of the medium. These characteristics are influenced by two main factors related to the medium's structure: Firstly, the properties of the electron involved in the annihilation depend on the local electronic environment at the annihilation site. Secondly, the state of the positron itself at the time of annihilation is influenced by medium-specific interactions preceding annihilation, which include scenarios such as a free positron, a positron captured in a trap, or different states of the positronium (Ps) atom within the medium.

Table. 2.3: Characteristic time scales of different positron annihilation processes in matter (Adapted from Ref. [23])

Positron State	Type of Process	Characteristic Lifetime
Free e^+	2γ	0.1 - 0.4 ns
Trapped e^+	2γ	0.2 - 0.5 ns
pPs	2γ , self-annihilation	0.1 ns
	2γ , pick-off process	> 1 ns
oPs	3γ , self-annihilation	140 ns
	2γ , pick-off process	> 1 ns

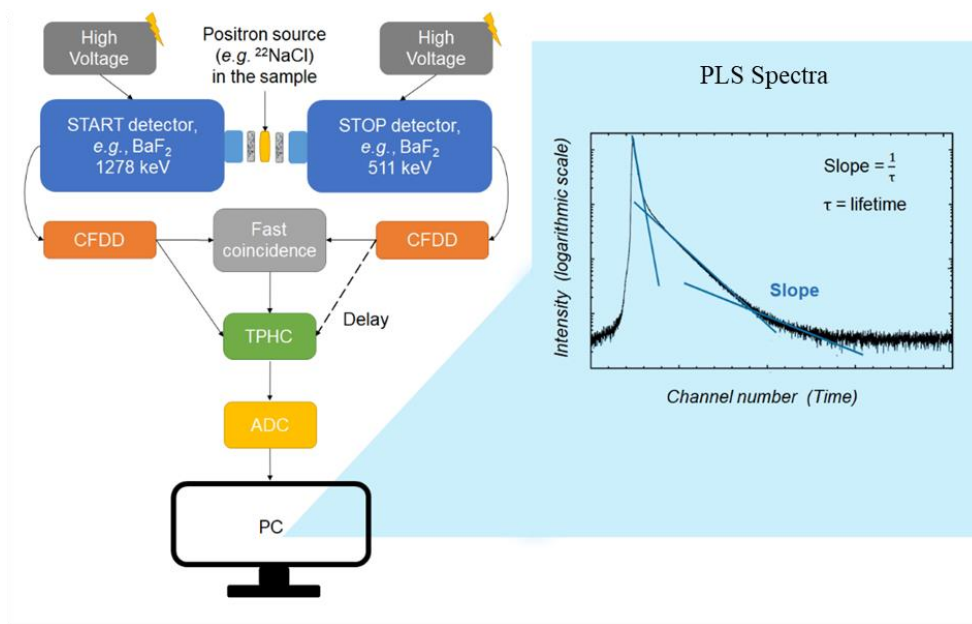


Fig. 2.9: Schematic of the PALS spectrometer and spectra. Abbreviations: ADC for analog-to-digital converter, CFDD for constant-fraction differential discriminator, TPHC for time-to-pulse height converter, PC for personal computer for experimental data collection and analysis. (Adapted from Ref. [25])

➤ Experimental Setup

The Positron Annihilation Lifetime Spectroscopy (PALS) method traditionally employs an analogue coincidence measurement setup to assess the positron lifetime within the material sample under investigation. The positron lifetime spectrum is constructed as a histogram of counts $[N(t)]$ versus time (t), representing a summation of exponentials of lifetimes within the medium. In recent times, there has been a transition towards digital oscilloscopes and fast digitizers, supplanting conventional analogue timing modules in PALS experiments. This shift has been accompanied by a growing reliance on digital signal processing, which significantly impacts time resolution in addition to the properties of scintillators [24]. The resolution function of the spectrometer, delineating its response to prompt coincidence events, typically exhibits a Gaussian-like profile, characterized by its FWHM. Here, τ represents the inverse slope of the ortho-positronium (o-Ps) component, while the intensity (I) corresponds to the area under the o-Ps slope. Data analysis in PALS can be accomplished through either direct deconvolution of the spectrum using programs employing diverse regularization strategies (e.g., CONTIN, MELT, RESOLUTION), or by fitting a theoretical model to the experimental data utilizing

spectra-fitting software (e.g., PATFIT, PositronFit, PALSfit) [25,26]. A schematic representation of the PALS spectrometer and spectra is illustrated in Fig. 2.9.

2.7.2. Doppler Broadening Spectroscopy (DBS)

The energy spectrum of annihilation radiation offers statistical insights into the annihilation surroundings. According to the laws of momentum and energy conservation, the two gamma quanta are emitted nearly in opposite directions and can be directly detected. The deviation from 180° and 511 keV is influenced by the centre-of-mass momentum of the annihilating particles and the emission direction of the quanta relative to the system momentum. Because the thermalized positron typically possesses more momentum than bound electrons, the resulting spectrum reflects the momentum distribution of electrons as sensed by the positron.

The 511 keV annihilation line undergoes Doppler broadening ($511 \pm \Delta E$) due to the longitudinal momentum component (p_L) of the annihilating positron-electron pair. In Doppler experiments, the longitudinal component p_L towards the detector is evaluated, and the change in energy (ΔE) corresponding to the momentum p_L is given by the formula $\Delta E = 1/2 p_L c$, where c represents the speed of light. The energy spectrum correlates directly with the electron momentum spectrum, with a 1 keV shift equivalent to a momentum of 0.54 a.u. High-purity Germanium (HPGe) detectors are used to discern these small energy shifts in the annihilation peak. A Full Width at Half Maximum (FWHM) of 1.2 keV at the 511 keV annihilation peak is attainable with a robust setup. Despite this resolution width being critical compared to the typical Doppler broadening peak FWHM of 3 keV, the measured spectrum reveals two main regions in the one-dimensional momentum distribution of the annihilating positron-electron pair.

These regions include: (i) a low-momentum region near the peak position (typically $0 < p_L < 3.0 \times 10^{-3} m_0 c$, where p_L is the longitudinal momentum), reflecting annihilations with valence electrons, and (ii) a high-momentum region toward the tails of the spectrum (typically $6.2 \times 10^{-3} m_0 c < p_L < 15 \times 10^{-3} m_0 c$) due to annihilation with high-momentum electrons. In cases where a positron is trapped in a vacancy, there is a probability of reduced annihilation with core electrons compared to a free positron. Doppler broadening spectroscopy has been employed to identify the precise nature of defects. The energy of the core electron participating in the annihilation process is crucial because, in a positron lifetime spectrum, the different spectra from the entire positron

states in the sample are added and cannot be resolved into components. Therefore, a Doppler broadening measurement provides more intricate data than a lifetime measurement. Doppler broadening spectroscopy is sensitive to the surroundings of a vacancy, allowing differentiation between vacancies with similar open volumes, which is challenging with lifetime measurements alone.

These regions consist of (i) a region with low momentum close to the peak position (typically $0 < p_L < 3 \times 10^{-3} m_0 c$, where p_L represents the longitudinal momentum), indicating annihilation with valence electrons, and (ii) a high-momentum region at the edges of the spectrum (typically $6.2 \times 10^{-3} m_0 c < p_L < 15 \times 10^{-3} m_0 c$) resulting from annihilation with high-momentum electrons [27]. In scenarios where a positron is trapped in a vacancy, there is a decreased likelihood of annihilation with core electrons compared to a free positron. Doppler broadening spectroscopy has been utilized to identify the specific characteristics of defects. The energy of the core electron involved in the annihilation process is crucial because, in a positron lifetime spectrum, the spectra from all positron states in the sample are combined and cannot be distinguished as individual components. Therefore, Doppler broadening measurement offers more detailed information compared to a lifetime measurement. Doppler broadening spectroscopy is sensitive to the environment of a vacancy, enabling differentiation between vacancies with similar open volumes, which is challenging with lifetime measurements alone [28].

Two critical parameters, the shape (S) parameter and the wing (W) parameter, are commonly employed to analyze the distinct regions of the spectrum, aiding in the extraction of information about the type and concentration of open-volume defects. The S parameter, which is associated with conduction electrons, represents the fraction of counts in the central region of the peak, while W, linked to core electrons, signifies the counts in the wing areas on both sides of the peak. The S parameter is determined by integrating the counts within ± 800 eV around the 511 keV annihilation line, divided by the total counts under the spectrum. Conversely, W is evaluated from an energy window (~ 5 keV) in the wing region of the Doppler broadened annihilation peak. The S parameter reflects open-volume defects, whereas W reflects the chemical environment at the annihilation site. An increase in the S parameter suggests the presence of vacancy defects where positrons are trapped, leading to localized wave functions and reduced annihilation probability with core electrons compared to valence electrons. As a result,

the momentum distribution of annihilating electrons shifts to smaller values, resulting in decreased Doppler broadening of the annihilation line. Consequently, defect-rich samples exhibit higher and narrower curves compared to defect-free samples when both are normalized to equal area, resulting in a higher S parameter for defect-rich samples [29].

References

1. F. Braun, Ann. Phys. **229**, 556 (1875).
2. S. M. Sze, Y. Li, and K. K. Ng, *Physics of Semiconductor Devices* (John Wiley & Sons, 2021).
3. W. Schottky, R. Stormer, and F. Waibel, Z. Hoch Freq. **37**, 162 (1931).
4. W. Schottky, Naturwissenschaften **26**, 843 (1938).
5. N. F. Mott, Math. Proc. Cambridge Philos. Soc. **34**, 568 (1938).
6. B. L. Sharma, *Metal-Semiconductor Schottky Barrier Junctions and Their Applications* (Springer Science & Business Media, 2013).
7. R. Kumar and S. Chand, Solid State Sci. **58**, 115 (2016).
8. J. Hass, R. Feng, T. Li, X. Li, Z. Zong, W. A. De Heer, P. N. First, E. H. Conrad, C. A. Jeffrey, and C. Berger, Appl. Phys. Lett. **89**, (2006).
9. I. Ullah, M. Shah, M. Khan, and F. Wahab, J. Electron. Mater. **45**, 1175 (2016).
10. İ. Taşcıoğlu, U. Aydemir, and Ş. Altındal, J. Appl. Phys. **108**, 064506 (2010).
11. M. Soylu and B. Abay, Phys. E Low-Dimensional Syst. Nanostructures **43**, 534 (2010).
12. K. C. Kao, *Dielectric Phenomena in Solids* (Elsevier, 2004).
13. S. Sil, A. Dey, J. Datta, M. Das, R. Jana, S. Halder, J. Dhar, D. Sanyal, and P. P. Ray, Mater. Res. Bull. **106**, 337 (2018).
14. E. Barsoukov and J. R. Macdonald, *Impedance Spectroscopy: Theory, Experiment, and Applications* (John Wiley & Sons, 2018).
15. In *Impedance Spectrosc.* (2012), pp. 1–21.
16. J. R. Macdonald and W. B. Johnson, in *Impedance Spectrosc.* (2005), pp. 1–26.
17. R. W. Siegel, Annu. Rev. Mater. Sci. **10**, 393 (1980).
18. M. Deutsch, Phys. Rev. **83**, 866 (1951).
19. P. A. M. Dirac, *The Principles of Quantum Mechanics* (Oxford university press, 1981).
20. A. E. Ruark, Phys. Rev. **68**, 278 (1945).
21. P. Asoka-Kumar, K. G. Lynn, and D. O. Welch, J. Appl. Phys. **76**, 4935 (1994).
22. P. J. Schultz and K. G. Lynn, Rev. Mod. Phys. **60**, 701 (1988).
23. I. Procházka, Mater. Struct. **8**, 55 (2001).
24. M. Fang, N. Bartholomew, and A. Di Fulvio, Nucl. Instruments Methods Phys. Res. Sect. A Accel. Spectrometers, Detect. Assoc. Equip. **943**, 162507 (2019).
25. M. M. Shokoya, B.-M. Benkő, K. Süvegh, R. Zelkó, and I. Sebe, Pharmaceuticals **16**, (2023).
26. S. Thomas, Y. Grohens, and P. Jyotishkumar, *Characterization of Polymer Blends: Miscibility, Morphology and Interfaces* (John Wiley & Sons, 2014).
27. R. S. Brusa, W. Deng, G. P. Karwasz, and A. Zecca, Nucl. Instruments Methods Phys.

Res. Sect. B Beam Interact. with Mater. Atoms **194**, 519 (2002).

28. R. S. Brusa, G. P. Karwasz, N. Tiengo, A. Zecca, F. Corni, R. Tonini, and G. Ottaviani, Phys. Rev. B **61**, 10154 (2000).

29. A. K. Mishra, S. K. Chaudhuri, S. Mukherjee, A. Priyam, A. Saha, and D. Das, J. Appl. Phys. **102**, (2007).

Exploring Reduced Graphene Oxide-Zinc
Telluride Nanocomposites for Enhanced
Charge Transfer in Optoelectronic
Devices: A Study of the Metal-
Semiconductor Interfaces via Equivalent
Circuit Model

Chapter 3

➤ *The study reported in this chapter has appeared in **J Mater Sci: Mater Electron**, 34 (2023), 1574.*

3.1. Introduction

In recent years, there has been a significant rise in the utilization of compound semiconductors in optoelectronic devices, driven by the increasing demand for solar energy solutions [1,2]. Group II-VI compound semiconductors, such as zinc oxide (ZnO), zinc selenide (ZnSe), and zinc sulfide (ZnS), have gained attention due to their favourable characteristics, including low environmental impact, cost-effectiveness, and abundant availability [2]. Amongst the various semiconductors, the brownish-red coloured zinc telluride (ZnTe), with a direct bandgap of ~ 2.26 eV, exhibits several desirable properties for optoelectronic applications, such as non-toxicity, ease of processing, high physical and thermal stability, and efficient absorption of visible light [3–5]. These qualities make ZnTe (ZT) a promising candidate for various device applications, including light-emitting diodes (LEDs) [4], solar cells [6] and sensors [7]. However, a major limitation of ZT is their tendency for fast electron-hole ($e-h^+$) recombination, leading to weak charge transport, particularly in optoelectronic applications. To address this issue, various strategies have been explored, and the synthesis of graphene-based composites has emerged as an effective approach [8,9]. Reduced graphene oxide (RGO) is particularly attractive due to its easy processability, low cost, high specific surface area, and superior conductivity [10].

In this study, we investigate the potential of ZnTe and RGO-ZnTe (abbreviated as R-ZT) for fabricating optoelectronic devices by analyzing their electrical charge transport parameters and interfacial properties. We focus on the Schottky barrier diodes as a starting point to evaluate the device performance for electronic conduction through the MS interfaces. Specifically, we fabricate Al/ZT/ITO and Al/R-ZT/ITO Schottky barrier diodes, where thin layers of ZT and R-ZT are sandwiched between aluminium (Al) and indium tin oxide (ITO) electrodes. We study the morphological properties of the ZT and R-ZT thin films to optimize the device's performance. Additionally, we investigate frequency-dependent and bias-dependent impedance spectroscopy (IS) to explore the different interfacial properties of the fabricated diodes. Moreover, the current-voltage (I-V) measurements are conducted under both dark and illumination conditions to analyze the charge transport mechanism within the MS junction and evaluate the photoresponsive properties of the fabricated Schottky devices.

3.2. Materials and Methods

3.2.1. Materials

The chemicals used in this study were zinc (Zn) powder (assay $\geq 93\%$), tellurium (Te) powder (~30 mesh, 99.997%), sodium hydroxide (NaOH) (analytical grade, $>97\%$), graphite powder (98%), H_2SO_4 , H_3PO_4 , KMnO_4 , H_2O_2 , HCl, absolute ethanol and deionized (DI) water. All the chemicals were procured from Sigma-Aldrich (India) and used as received without requiring any further purification steps.

3.2.2. Synthesis of ZnTe

The synthesis of zinc telluride (ZnTe) nanoparticles was carried out using a simple alkaline hydrothermal (HT) method [11]. In this procedure, 0.36 g of Zn powder, 0.66 g of Te powder, and 1.61 g of NaOH pellets were dissolved in 40 ml of deionized (DI) water, resulting in a homogeneous solution upon magnetic stirring for 2 hours. The solution was then transferred into a Teflon-lined HT autoclave, and additional DI water was added to achieve the desired dilution. The autoclave was subsequently placed in an oven, and the temperature was increased at a rate of $3^\circ\text{C}/\text{min}$ until a constant temperature of 160°C was reached. The thermal treatment was maintained at this temperature for 18 hours. Afterwards, the autoclave was cooled to room temperature, and the resulting grey-coloured ZnTe sediment was collected by centrifugation. The sediment was washed multiple times using DI water and absolute ethanol. Finally, the as-synthesized ZnTe nanoparticles were dried overnight in a vacuum furnace at 80°C to obtain the final product.

3.2.3. Synthesis of GO

Graphene oxide (GO) was synthesized using an improved version of Hummer's method, initially proposed by Marcano et al. [12,13]. In this procedure, a 100 mL solution of $\text{H}_2\text{SO}_4/\text{H}_3\text{PO}_4$ with a molar ratio of 9:1 was prepared. Then, 0.75 g of graphite flakes were dispersed in the solution using intense sonication. Subsequently, 4.5 g of KMnO_4 was gradually added to the acid suspension and stirred for 12 hours at 50°C . The resulting mixture was cooled to room temperature and transferred to 100 mL of ice water. To the homogeneous mixture, 0.75 mL of a 30% aqueous solution of H_2O_2 was slowly added, resulting in the formation of a golden-brown GO suspension. The obtained suspension was filtered and subjected to centrifugation at 6000 rpm for 1 hour. The resulting GO was

then washed repeatedly with deionized (DI) water, dilute HCl, and ethanol. Finally, the product was obtained by drying overnight at 100 °C.

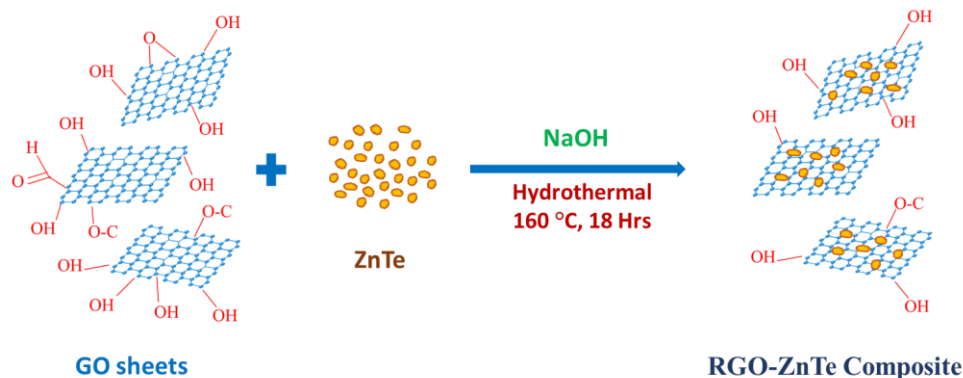


Fig. 3.1: Schematic illustration of the synthesis of the RGO-ZnTe nanocomposite.

3.2.4. Synthesis of RGO-ZnTe

The composite material RGO-ZnTe (R-ZT) was synthesized using a similar alkaline hydrothermal reaction as described for ZnTe synthesis. The synthesis procedure involved several steps. Firstly, 10 mg of graphene oxide (GO) was reduced to obtain 10 mg of reduced GO through hydrazine treatment, following the method described by Das et. al. [14]. Next, 5 mg of the reduced GO was dispersed in 30 mL of deionized (DI) water through ultrasonication for 1 hour, resulting in a well-dispersed and homogeneous solution. Subsequently, the synthesized ZnTe nanoparticles were slowly added to the RGO suspension while maintaining stirring. The mixture was further stirred for 1 hour to ensure uniform dispersion and then transferred into a hydrothermal autoclave to synthesize the R-ZT nanocomposite. During this process, the deoxygenation of RGO and the formation of the R-ZT composite occurred simultaneously in the presence of NaOH [15]. The resulting grey-coloured residue was collected through centrifugation, thoroughly washed, and dried overnight to obtain the R-ZT nanocomposite. The entire synthesis process of the RGO-ZnTe composite is collectively schemed out in Fig. 3.1.

3.2.5. Fabrication of Schottky Devices

In this report, the electrical characteristics were studied in ZnTe and RGO-ZnTe-based metal-semiconductor (MS) junction Schottky devices. To fabricate the Schottky barrier diodes, first, the ITO-coated glass substrates were cleaned using acetone, followed by 2-

propanol and distilled water. Then, on top of the cleaned ITO-coated substrate, the thin film of ZnTe and RGO-ZnTe was deposited by the spin coating unit at 1200 rpm. Subsequently, the as-prepared films were dried in a vacuum oven for 1 h. Next, as a metallic contact, aluminium (Al) was deposited onto the coated film using a vacuum coating unit (12A4D, HindHivac) under an atmospheric pressure of 3.2×10^{-6} Torr. In the deposition method, a typical quad-punch-hole shadow mask was used to control the effective contact area of the Schottky devices as $7.065 \times 10^{-6} \text{ m}^2$. The schematic diagram of the Schottky device structure is portrayed in Fig. 3.2.

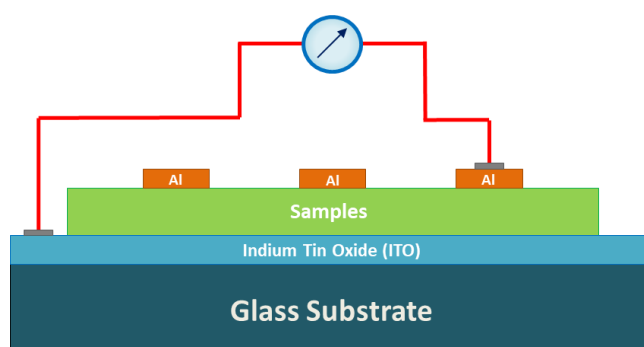


Fig. 3.2: Schematic diagram of the fabricated Schottky devices.

3.3. Material Characterizations Techniques

The crystal structure and the constituent phase(s) in the synthesized materials (ZT and R-ZT) were investigated by the X-ray diffraction (XRD) patterns acquired using a laboratory X-ray powder diffractometer (Bruker D8, $\text{Cu-K}\alpha = 1.5418 \text{ \AA}$) operated with a position-sensitive detector and a scan rate of $0.1^\circ/\text{min}$. The surface morphology of the vacuum-deposited ZT and R-ZT thin films onto the ITO was examined through field emission scanning electron microscopy (FESEM) images obtained from an FEI Inspect F50 instrument. Subsequently, atomic force microscopy (AFM) images were utilized to assess the surface topography of the MS junctions of the fabricated Schottky diodes. The impedance spectroscopy (IS) of the MS junction SDs was performed using an Agilent 4294A impedance analyzer. Further, the current-voltage (I-V) measurements of the fabricated diodes based on ZT and R-ZT were conducted using a semi-automated source measurement unit (Keithley 2635B).

3.4. Results and Discussion

3.4.1. Structural Properties

The X-ray diffraction (XRD) patterns of the as-synthesized ZT and reduced graphene oxide-zinc telluride nanocomposites (R-ZT) are shown in Fig. 3.3. The patterns reveal distinct Bragg reflections at 2θ angles $\sim 25.26^\circ$, 41.81° , 49.50° , 60.63° , 66.74° , and 76.39° , corresponding to the crystallographic planes (111), (220), (311), (400), (331), and (422) of ZnTe (black line), as identified by the JCPDS File No. 15-0746 [16]. Besides, the X-ray spectra (red line) of the R-ZT composites closely resemble those of pristine ZT, exhibiting sharp peaks that indicate higher crystallinity in the specimens. Notably, no distinct diffraction peaks corresponding to RGO are observed in the composite, which can be attributed to the low loading level of RGO and its relatively weaker diffraction peaks [17]. Furthermore, the addition of graphene oxide (GO) does not appear to have influenced the relative intensities and positions of the Bragg reflections in ZT and R-ZT, indicating the absence of new crystallographic phases.

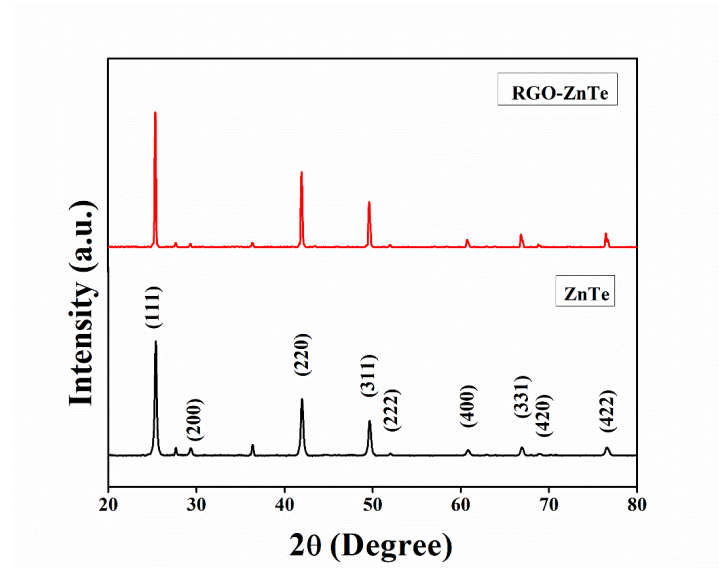


Fig. 3.3: XRD spectra of pristine ZT and R-ZT nanocomposite.

3.4.2. Morphological Studies

The surface morphology of the ZT and R-ZT composites was examined using FESEM micrographs, as illustrated in Fig. 3.4. In Fig. 3.4(a), the nanoflakes of ZT (diameter ~ 250 - 400 nm) are observed, randomly distributed across the surface. In contrast, Fig. 3.4(b)

shows the presence of RGO sheets with embedded ZT flakes, arranged over crumpled graphene layers. In certain areas, agglomeration of ZT flakes can be observed, which is likely caused by the aggregation tendency of graphene layers due to van der Waals interactions [15].

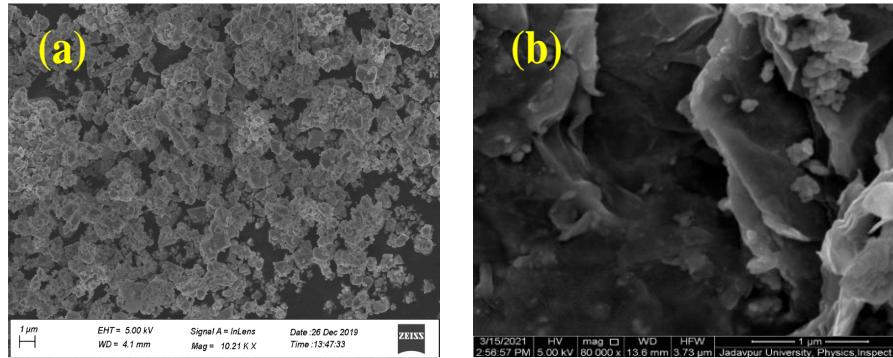


Fig. 3.4: FESEM micrographs of (a) ZT flakes and (b) R-ZT nanocomposites.

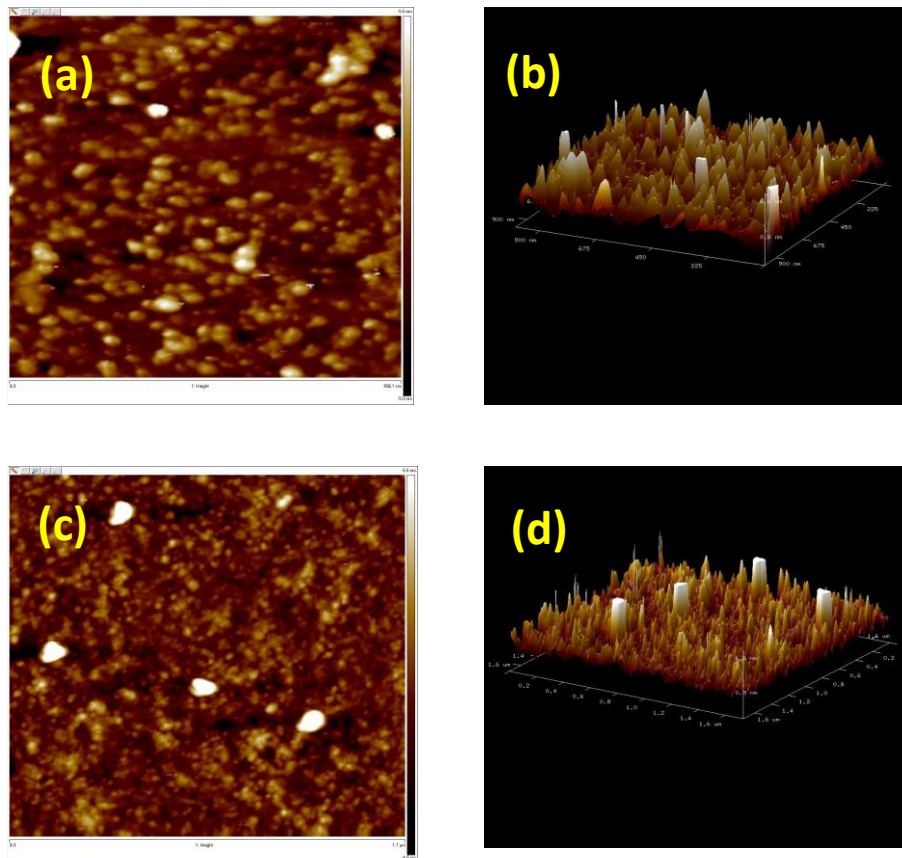


Fig. 3.5: AFM images of the (a,b) ZT/Al and (c,d) R-ZT/Al Schottky contacts.

The atomic force microscopy (AFM) images, presented in Fig. 3.5, offer valuable insights into the topography of the fabricated Schottky diodes and their interfacial structures. Examination of Fig. 3.5(a) reveals a uniform distribution of ZT flakes across the indium tin oxide (ITO) surface. This even distribution is advantageous for achieving high-quality Al/ZT Schottky contacts [18]. In the case of R-ZT-based Schottky devices, the uniformity is even higher, where the ZT flakes are seen to be randomly dispersed over the RGO layers [Fig. 3.5(c)], exposing a larger surface area to the Al contacts and facilitating efficient charge transfer. The surface roughness of both the layers on the ITO surface was measured from the 3D images, as displayed in Fig. 3.5(b) and Fig. 3.5(d), resulting in the root mean square (RMS) values of surface roughness as 1.68 nm and 1.56 nm for ZT and R-ZT-based devices, respectively. The lower roughness observed for R-ZT-based SDs indicates the formation of well-defined interfacial contacts, which enhances the charge transfer capabilities [19].

3.4.3. Impedance Spectroscopy Analysis

Impedance spectroscopy (IS) is a valuable technique that allows for the investigation of the frequency-dependent behaviour of Schottky devices incorporating metal-semiconductor (MS) junctions. In this study, we conducted measurements of bias-dependent impedance spectra to analyze the characteristics of the fabricated Schottky devices. The measurements were performed across a voltage range of -0.6 V to +0.6 V while maintaining a constant oscillating voltage of 100 mV. The frequency was varied from 50 Hz to 10 MHz. The obtained Nyquist plots, as shown in Fig. 3.6, exhibit distinctive semicircular arcs. The diameter of these arcs increases as the negative bias voltage decreases and decreases with the increase of positive biases. These observations highlight the significant impact of applied bias voltages on the impedance of the MS junctions [20].

In general, applying a negative voltage to a metal-semiconductor (MS) junction results in a decrease in the Fermi energy (E_F) of the semiconductor compared to the metal. This leads to an increase in the potential of the semiconductor, resulting in a wider depletion region and a stronger electronic charge field at the interface. Consequently, a barrier is formed at the MS interface, impeding the movement of electrons under reverse bias voltages. Conversely, under forward bias conditions, the Fermi energy level (E_F) of the semiconductor is raised above that of the metal. This causes a reduction in the

potential across the semiconductor, disrupting the relationship between diffusion and drift current [21]. As a result, a larger number of electrons diffuse towards the metal instead of drifting into the semiconductor due to the decreased barrier under forward bias voltages.

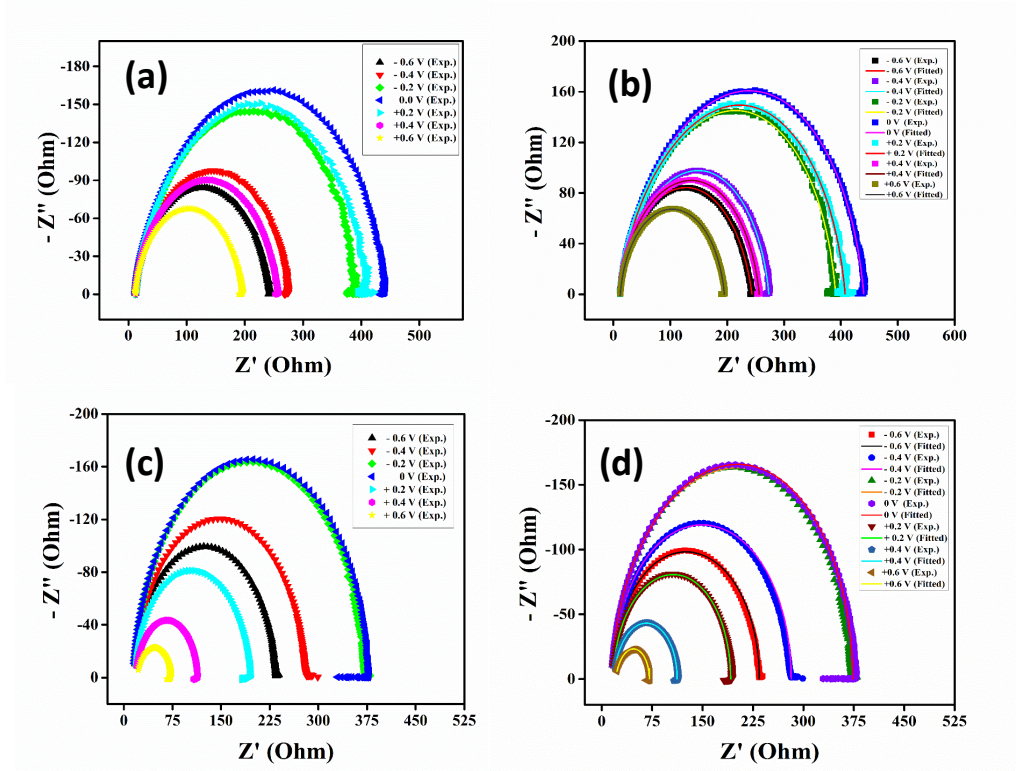


Fig. 3.6: Experimental and fitted Nyquist plots of the (a,b) ZT and (c,d) R-ZT-based SDs under different bias voltages.

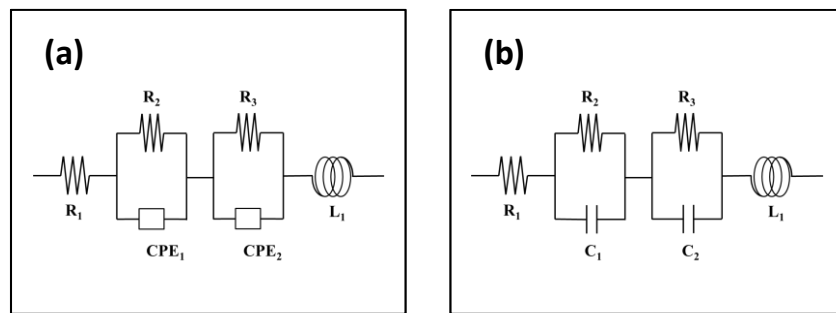


Fig. 3.7: Equivalent circuit models for the (a) Al/ZT and (b) Al/R-ZT-based MS junction SDs.

To describe the impedance spectra obtained under different bias voltages, we employed the equivalent circuit consisting of resistances (R), capacitances (C), and/or constant phase elements (CPE). Fig. 3.7(a) illustrates the equivalent circuit used for ZT-based Schottky diodes (SDs), featuring a series of resistance connected to two meshes of

resistance and constant phase elements, supplemented by a parasitic inductance. In contrast, R-ZT devices are characterized by an equivalent circuit [Fig. 3.7(b)] consisting of two parallel RC branches and a series resistance in conjunction with a parasitic inductance.

The fitted Nyquist curves for both SDs are depicted in Fig. 3.6(b) and Fig. 3.6(d), respectively. The graphical representations demonstrate a close agreement between the experimental data and the fitted curves. The summarized results of the fitting analysis are presented in Table 3.1 and Table 3.2 for ZT and R-ZT-based SDs, respectively. It is worth noting that the shunt resistance (R_1) remains consistent throughout the entire range of bias voltages. On the other hand, the series resistances, R_2 and R_3 , exhibit notable changes as the voltage transitions from reverse to forward bias. Particularly for R-ZT-based SDs, R_2 assumes significantly higher values compared to R_3 under reverse bias voltages. This observation indicates that the R_2C_1 component in the equivalent circuit corresponds to the formation of the Schottky barrier at the Al/R-ZT interface, which hinders the flow of charges across the junction. In contrast, under forward bias, R_2 experiences a sharp decline with increasing bias voltages, resulting in an enhanced current flow due to the reduced barrier. Further, the variations observed in R_3 across the entire dc bias range are relatively small, and these can be attributed to the ITO/R-ZT interface, where minor fluctuations may arise due to the presence of inhomogeneity and defects [22].

Table 3.1: Equivalent circuit parameters obtained for the ZT-based SDs.

Voltage (V)	R_1 (Ω)	R_2 (Ω)	CPE_1 (F)	R_3 (Ω)	CPE_2 (F)	L_1 (H)
-0.6	8.08	194.98	5.00×10^{-8}	40.57	2.20×10^{-8}	1.98×10^{-7}
-0.4	9.23	201.79	2.90×10^{-8}	62.24	1.81×10^{-8}	1.79×10^{-7}
-0.2	8.92	262.9	2.82×10^{-8}	135.56	5.93×10^{-8}	1.82×10^{-7}
0	8.62	284.44	3.08×10^{-8}	147.2	6.20×10^{-8}	1.83×10^{-7}
+0.2	9.09	241.37	2.35×10^{-8}	140.16	5.60×10^{-8}	1.74×10^{-7}
+0.4	8.06	137.93	4.87×10^{-8}	110.43	3.82×10^{-8}	1.95×10^{-7}
+0.6	8.48	74.19	6.11×10^{-8}	112.33	2.71×10^{-8}	1.89×10^{-7}

Table 3.2: *Equivalent circuit parameters obtained for the R-ZT-based SDs.*

Voltage (V)	R ₁ (Ω)	R ₂ (Ω)	C ₁ (F)	R ₃ (Ω)	C ₂ (F)	L ₁ (H)
-0.6	14.51	101.46	9.00×10^{-10}	118.46	2.61×10^{-9}	2.04×10^{-7}
-0.4	14.60	130.91	9.22×10^{-10}	136.25	2.45×10^{-9}	2.02×10^{-7}
-0.2	14.49	245.61	1.22×10^{-9}	112.99	1.46×10^{-9}	2.03×10^{-7}
0	14.27	277.70	1.50×10^{-9}	81.14	1.20×10^{-9}	2.03×10^{-7}
+0.2	14.15	108.54	1.13×10^{-9}	68.97	1.63×10^{-9}	2.09×10^{-7}
+0.4	13.98	51.21	2.18×10^{-9}	47.04	9.78×10^{-10}	2.12×10^{-7}
+0.6	13.67	38.08	1.39×10^{-9}	19.15	1.31×10^{-9}	2.13×10^{-7}

3.4.4. Current-Voltage (I-V) Measurement

The impedance spectroscopy analysis prompted us to delve deeper into the electrical characteristics of MS junction SDs based on ZT and R-ZT. Subsequently, the current-voltage (I-V) characteristics of the fabricated SDs were investigated under both dark and light conditions, using a bias voltage range of ± 1 V. As illustrated in Fig. 3.8, the I-V curves of the Al/ZT/ITO and Al/R-ZT/ITO configurations exhibited the typical nonlinear rectifying behaviour characteristic of Schottky barrier diodes [23]. The rectification ratio or the on-off ratio ($I_{\text{on/off}}$) of the ZT-based SDs was determined to be 13.63 under dark conditions and 21.19 under light irradiation. Similarly, the R-ZT-based SDs exhibited rectification ratios of 13.77 and 23.03 for dark and illuminated conditions, respectively. Notably, the significantly higher current observed under illumination indicates the photoresponsive nature of the devices [24]. Additionally, the conductivity of both ZT and R-ZT-based SDs was measured under dark conditions, and a substantial increase in conductivity was observed with photo-irradiation, as presented in Table 3.3. These results highlight a significant enhancement in the conductivity of the graphene composites compared to the pristine ZT-based devices [24,25].

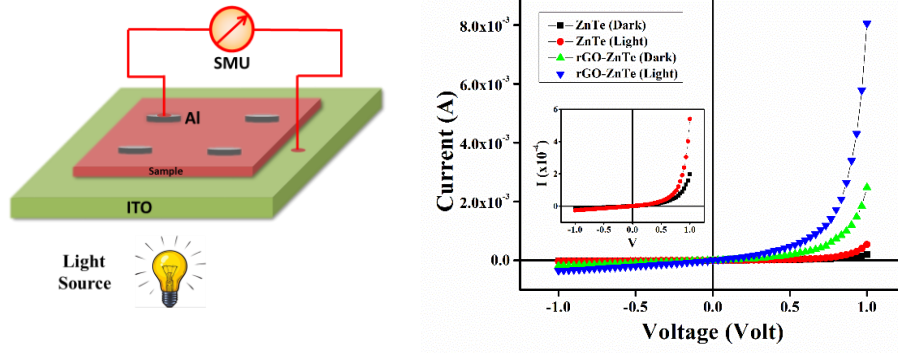


Fig. 3.8: (a) Schematic representation of I-V measurement and (b) Current-voltage (I-V) characteristics curve for the ZT and R-ZT-based SDs.

The current vs. voltage (I-V) behaviour of the SDs was further investigated using the principles of thermionic emission (TE) theory, discussed in the preceding chapter (§ 2.5.1) [26,27]. To extract various diode parameters, Cheung's equations were applied [28,29]. To quantitatively analyze the I-V curves, the following standard equations were considered:

$$J = J_0 \left[\exp \left(\frac{qV_D}{\eta kT} \right) - 1 \right] \quad (3.1)$$

where J and J_0 are the diode current density and the saturation current density, respectively, and J_0 is given by:

$$J_0 = A^* T^2 \exp \left(\frac{-\phi_B}{kT} \right) \quad (3.2)$$

Here, the symbols q , k , T , V_D , A_{eff} , η , ϕ_B and A^* represent the electronic charge, Boltzmann constant, temperature in Kelvin, voltage across the diode, effective diode area, ideality factor, barrier height and Richardson constant, respectively. Additionally, taking into account the series resistance (R_s), Eq. (3.1) can be expressed as:

$$J = J_0 \left[\exp \left\{ \frac{q(V - JA_{eff}R_s)}{\eta kT} \right\} - 1 \right] \quad (3.3)$$

In this equation, the term $JA_{eff}R_s$ represents the voltage drop across the series resistance. By applying the Cheung and Cheung analysis, the relationship between the ideality factor and the series resistance can be expressed as [24]:

$$G(J) = \frac{dV}{d(\ln J)} = \left(\frac{\eta kT}{q} \right) + A_{eff} J R_s \quad (3.4)$$

Furthermore, the effective barrier height (ϕ_B) can also be determined using the following equation:

$$H(J) = V - \left(\frac{\eta kT}{q} \right) \ln \left(\frac{J}{A^* T^2} \right) \quad (3.5)$$

By mathematical formulations, Eq. (3.5) also can be expressed as:

$$H(J) = J A_{eff} R_s + \eta \phi_B \quad (3.6)$$

In the following section, Fig. 3.9 showcases the graphical representation of $G(J)$ vs. J and $H(J)$ vs. J for both the dark and light conditions for both of the fabricated SDs. The crucial parameters, namely, ideality factor (η) and series resistance (R_s) were obtained by analyzing the intercept and slope of the linear plot of $G(J)$ vs. J , respectively. Additionally, the barrier height (ϕ_B) was estimated based on the intercept of the $H(J)$ vs. J plot.

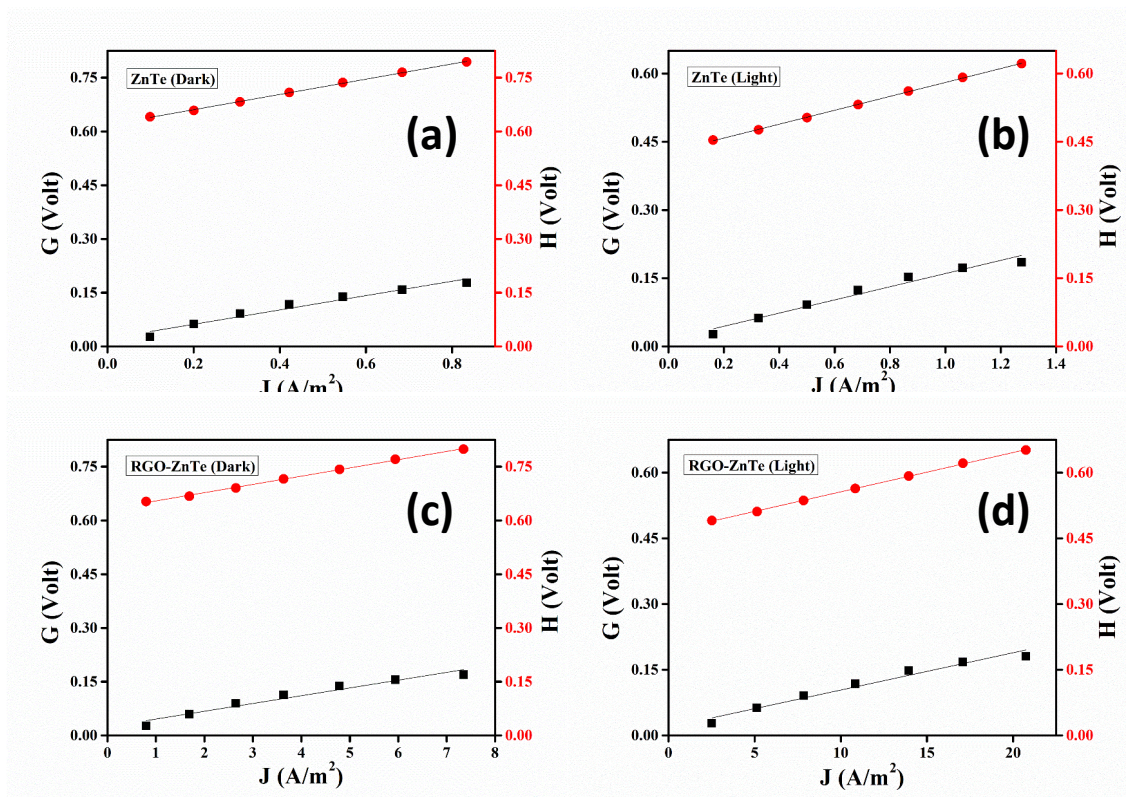


Fig. 3.9: $G(J)$ vs. J and $H(J)$ vs. J plot for the ZT (dark (a) and light (b)) and R-ZT (dark (c) and light (d)) based Schottky devices.

The findings, presented in Table 3.4, reveal that the MS junction formed in the devices deviates from ideal behaviour, primarily due to the presence of interfacial defects and the inhomogeneity present at the Schottky contacts [30]. However, exposure to light resulted in an improved ideality factor (η) approaching 1, indicating a more ideal device. Furthermore, the evaluated barrier height (ϕ_B) values suggest a slightly lower turn-on voltage when illuminated. The observed higher rectification ratio under photo irradiance could be attributed to the reduced barrier height. Notably, the series resistance exhibited a significant decrease in the presence of light, leading to a substantial increase in the photocurrent, which can be attributed to the enhanced homogeneity of Schottky contacts and reduced carrier recombination under photo illumination [31]. The summarized values of η , ϕ_B and R_s in Table 3.4 underscore the improved performance of the R-ZT-based devices following light exposure. These findings highlight the tremendous potential of R-ZT in various optoelectronic devices, solidifying their significance in the field.

Table 3.3: Charge transport parameters.

	Conductivity (σ) ($S.m^{-1}$)		Photo-sensitivity	Rectification Ratio ($I_{on/off}$)	
	Dark	Light		Dark	Light
ZT	4.36×10^{-5}	5.71×10^{-5}	1.75	13.63	21.19
R-ZT	3.96×10^{-4}	1.07×10^{-3}	2.24	13.77	23.03

Table 3.4: Schottky diode parameters.

	Ideality factor (η)		Barrier height (ϕ_B) (eV)		Series Resistance (R_s) (k Ω)	
	Dark	Light	Dark	Light	Dark	Light
ZT	0.60	0.84	0.73	0.72	28.87	20.81
R-ZT	0.72	0.93	0.68	0.64	3.12	1.22

3.5. Conclusions

In this study, we successfully synthesized ZT nanoflakes and their graphene composites through a simple hydrothermal method. Subsequently, we fabricated metal-semiconductor junction Schottky diodes using both pristine ZT and R-ZT composites and extensively investigated their device structure using FESEM and AFM micrographs. By performing a comprehensive analysis of the fabricated Schottky diodes and employing dc current-voltage measurements, we gained valuable insights into their diode behaviour at the metal-semiconductor junctions, as well as their charge conduction mechanisms. To further enhance our understanding of the interface properties within the fabricated diodes, we developed an ac equivalent circuit model. By utilizing ac impedance spectroscopy, we were able to conduct a detailed analysis of different interfaces and their charge transport properties, which would not have been feasible through dc analysis alone. Notably, the R-ZT-based Schottky diodes exhibited superior diode characteristics and enhanced charge transport properties, positioning them as promising candidates for applications in rectification and optoelectronics.

References

1. E. Shalaan, E. Ibrahim, F. Al-Marzouki, and M. Al-Dossari, *Appl. Phys. A* **126**, 852 (2020).
2. J. Wang, Y. Xing, F. Wan, C. Fu, C.-H. Xu, F.-X. Liang, and L.-B. Luo, *J. Mater. Chem. C* **10**, 12929 (2022).
3. W. Mahmood and N. A. Shah, *Phys. B Condens. Matter* **602**, 412557 (2021).
4. A.-M. Panaitescu and V.-A. Antohe, *Coatings* **13**, 208 (2023).
5. D. Suthar, Himanshu, S. L. Patel, S. Chander, M. D. Kannan, and M. S. Dhaka, *Solid State Sci.* **107**, 106346 (2020).
6. W. Wang, A. S. Lin, and J. D. Phillips, *Appl. Phys. Lett.* **95**, 11103 (2009).
7. O. I. Olusola, M. L. Madugu, N. A. Abdul-Manaf, and I. M. Dharmadasa, *Curr. Appl. Phys.* **16**, 120 (2016).
8. M. Yadav, A. Yadav, R. Fernandes, Y. Popat, M. Orlandi, A. Dashora, D. C. Kothari, A. Miotello, B. L. Ahuja, and N. Patel, *J. Environ. Manage.* **203**, 364 (2017).
9. L. Zhang, L. Du, X. Yu, S. Tan, X. Cai, P. Yang, Y. Gu, and W. Mai, *ACS Appl. Mater. Interfaces* **6**, 3623 (2014).
10. S. Saxena, T. A. Tyson, S. Shukla, E. Negusse, H. Chen, and J. Bai, *Appl. Phys. Lett.* **99**, 13104 (2011).
11. M. F. Ehsan, M. N. Ashiq, F. Bi, Y. Bi, S. Palanisamy, and T. He, *RSC Adv.* **4**, 48411 (2014).
12. W. S. J. Hummers and R. E. Offeman, *J. Am. Chem. Soc.* **80**, 1339 (1958).
13. D. C. Marcano, D. V Kosynkin, J. M. Berlin, A. Sinitskii, Z. Sun, A. Slesarev, L. B. Alemany, W. Lu, and J. M. Tour, *ACS Nano* **4**, 4806 (2010).
14. M. Das, J. Datta, A. Dey, R. Jana, A. Layek, S. Middya, and P. P. Ray, *RSC Adv.* **5**, 101582 (2015).
15. S. D. Perera, R. G. Mariano, K. Vu, N. Nour, O. Seitz, Y. Chabal, and K. J. J. Balkus, *ACS Catal.* **2**, 949 (2012).
16. M. F. Ehsan, M. N. Ashiq, and T. He, *RSC Adv.* **5**, 6186 (2015).
17. Y.-L. Chen, Z.-A. Hu, Y.-Q. Chang, H.-W. Wang, Z.-Y. Zhang, Y.-Y. Yang, and H.-Y. Wu, *J. Phys. Chem. C* **115**, 2563 (2011).
18. M. A. Khan, N. Nayan, M. K. Ahmad, S. C. Phong, and M. Tahir, *Surfaces and Interfaces* **21**, 100649 (2020).
19. A. Fernández-Pérez, C. Navarrete, R. Muñoz, E. Baradit, M. Saavedra, G. Cabello-

- Guzmán, and W. Gacitúa, Mater. Res. Express **8**, 16408 (2021).
20. C. Yim, N. McEvoy, and G. S. Duesberg, Appl. Phys. Lett. **103**, 193106 (2013).
21. Z. Benamara, B. Akkal, A. Talbi, and B. Gruzza, Mater. Sci. Eng. C **26**, 519 (2006).
22. H. Kim, M. J. Jung, and B. J. Choi, Solid State Commun. **344**, 114685 (2022).
23. M. Shah, M. H. Sayyad, K. S. Karimov, and M. Maroof-Tahir, Phys. B Condens. Matter **405**, 1188 (2010).
24. D. Das, M. Das, S. Sil, P. Sahu, and P. P. Ray, ACS Omega **7**, 26483 (2022).
25. M. Das, D. Das, S. Sil, and P. P. P. Ray, Nanoscale Adv. **5**, 3655 (2023).
26. S. M. Sze, Phys. Semicond. Devices Second Ed. (1981).
27. E. H. Rhoderick and E. H. Rhoderick, *Metal-Semiconductor Contacts* (Clarendon Press Oxford, 1978).
28. S. K. Cheung and N. W. Cheung, Appl. Phys. Lett. **49**, 85 (1986).
29. D. Das, M. Das, P. Sahu, and P. Pratim Ray, Mater. Today Proc. (2023).
30. İ. Taşcıoğlu, U. Aydemir, and Ş. Altındal, J. Appl. Phys. **108**, 064506 (2010).
31. I. Ullah, M. Shah, M. Khan, and F. Wahab, J. Electron. Mater. **45**, 1175 (2016).

Effect of Higher Carrier Mobility of
Reduced Graphene Oxide-Zinc Telluride
Nanocomposite Towards Efficient
Charge Transfer Facility and The
Photodecomposition of Rhodamine B

Chapter 4

➤ *The study reported in this chapter has appeared in ACS Omega, 7 (2022), 26483–26494.*

4.1. Introduction

Dye wastewater released into water bodies mainly by textile industries is becoming a major environmental concern, causing several ecological problems [1]. In the past few decades, different physicochemical and biological attempts based on chemical and physical adsorption techniques were made to degrade these industrial effluents, but they are not cost-effective from an economical point of view and often produce secondary pollutants [2]. Among all advanced oxidation methods known to date, the photocatalytic route based on semiconducting materials has shown considerable efficiency in wastewater decontamination processes [3]. Thus far, a large number of compound semiconductors have been investigated for organic dye decomposition since they possess an excellent larger absorbance cross-section and higher environmental stability [4,5]. The semiconductor materials though have excellent potential in the area of organic dye decolourization; they also suffer from the shortcomings of having wide bandgaps and comparatively shorter life span of excitons – limiting the usage of these semiconductors in practical applications [6]. As an example, TiO_2 , which is one of the most promising materials for the decomposition of many organic pollutants, responds only in the UV region of the electromagnetic spectrum, attributed to its wide bandgap (~ 3.2 eV) [7,8]. This causes fewer redox reactions with the pollutants and detrimentally affects its degradation efficiency [9].

On the other hand, Zinc telluride (ZnTe), which is an important group II-VI compound semiconductor having a direct bandgap ~ 2.26 eV, has shown immense potential in a wide range of applications in solar cells [10], light-emitting diodes (LED) [11], optoelectronic devices [12], CO_2 reductions [13], as well in wastewater treatment [14–16]. The solution-processed ZnTe nanostructures demonstrate a few excellent features, namely, low production cost, large surface area, good environmental stability, excellent reusability and prominent visible-light absorption - which make them a prospective photocatalyst. However, they also have an inherent shortcoming in that the fast electron (e^-)-hole (h^+) recombination in ZnTe nanomaterials is responsible for their weak photocatalytic performance, particularly under visible light irradiation. Several attempts were made to decrease the electron-hole recombination in these materials, and thus promote the electron transfer during the photocatalytic process. Among them, the synthesis of graphene-based composite is considered one of the most effective remedial techniques [17,18], wherein, the easily processed, low-cost graphene oxide (GO) and/or

reduced graphene oxide (RGO) possess high specific surface area alongside manifesting superior conductivity [19–21]. The presence of different functional groups further allows the GO sheets to exfoliate easily in water thereby producing stable dispersions. These exfoliated GO sheets owing to possessing a large surface area also provide sufficient interfacial contact with the nanoparticles, which in turn, suppress the recombination of photo-generated electron-hole pairs and thereby enhance the charge transfer facility [22]. The present work describes the synthesis of a reduced graphene oxide-zinc telluride (RGO-ZnTe) nanocomposite and identifies its potential in the degradation of organic dye (Rhodamine B) under visible-light irradiation. The associated enhancement in the transport properties of the charge carriers and the role of their mobility in dye degradation are discussed in detail in this report.

4.2. Materials and Methods

The synthesis procedure of the ZnTe and RGO-ZnTe nanocomposites and the fabrication of the Schottky diodes were discussed in detail in the previous chapter (§ 3.2).

4.3. Material Characterization Techniques

The material characterization techniques adopted in the preceding chapter (§ 3.3) have been consistently utilized in this chapter. Additional techniques include:

The surface morphology and the elemental composition were studied with the FEI Inspect F50 field emission scanning electron microscope (FESEM) and the integrated energy dispersive X-ray (EDX) analyser, respectively. The microstructural information of the nanocomposite was analysed with the JEOL JEM 2100F field emission gun (FEG) transmission electron microscope (TEM). The X-ray photoelectron spectroscopic (XPS) (Omicron Nanotechnology) measurement technique, using Al-K α radiation ($E = 1486.7$ eV) was employed to probe the surface electronic states of the existing elements and the reduction state of GO. The absorption spectra of synthesized materials and their photocatalytic behaviour were investigated using a UV-Vis spectrophotometer (Perkin Elmer, Lambda 365) and a low-cost solar simulator (Abet Technologies, Model 10500), respectively. The photo luminance spectra of the samples were collected by a spectrofluorimeter (PerkinElmer LS55). The thermal stability of both of the materials was investigated by thermogravimetric analysis (Perkin Elmer Pyris Diamond TG/DTA) in the temperature range of 25-750 °C under an N₂ atmosphere. For the interpretation of

the Brunauer-Emmett and Teller (BET) specific surface area of the nanomaterials, the N_2 adsorption-desorption was performed at 77K (Autosorb iQ2, Quantachrome Instruments, USA).

4.4. Results and Discussion

4.4.1. Structural Properties

➤ XRD Analysis

Rietveld refinement of the as-synthesized ZT and R-ZT composite was carried out using the MAUD program [23] and the fitted XRD patterns are presented in Fig. 4.1. Fig. 4.1(a) displays the observed Bragg reflections of the as-prepared ZT specimens at $2\theta \approx 25.26^\circ$, 41.81° , 49.50° , 60.63° , 66.74° and 76.39° , assigned to (111), (220), (311), (400), (331) and (422) crystallographic planes (JCPDS File No. 15-0746), were refined according to the crystal structure of ZnTe [13]. The corresponding crystal structure is also available at Crystallography Open Database (COD) entry no. 1540103, having a space group $Fm - 3m$ [24]. Additionally, a pair of very weak peaks at $2\theta \approx 27.61^\circ$ and 36.27° of zinc oxide (ZnO) and tellurium dioxide (TeO_2) respectively, were also detected in the specimens, which have corresponding COD entry nos. 2107059 and 1520934. The incidence of these two peaks could be attributed to the residual zinc and tellurium, precipitated and oxidized during hydrothermal treatment [25–27].

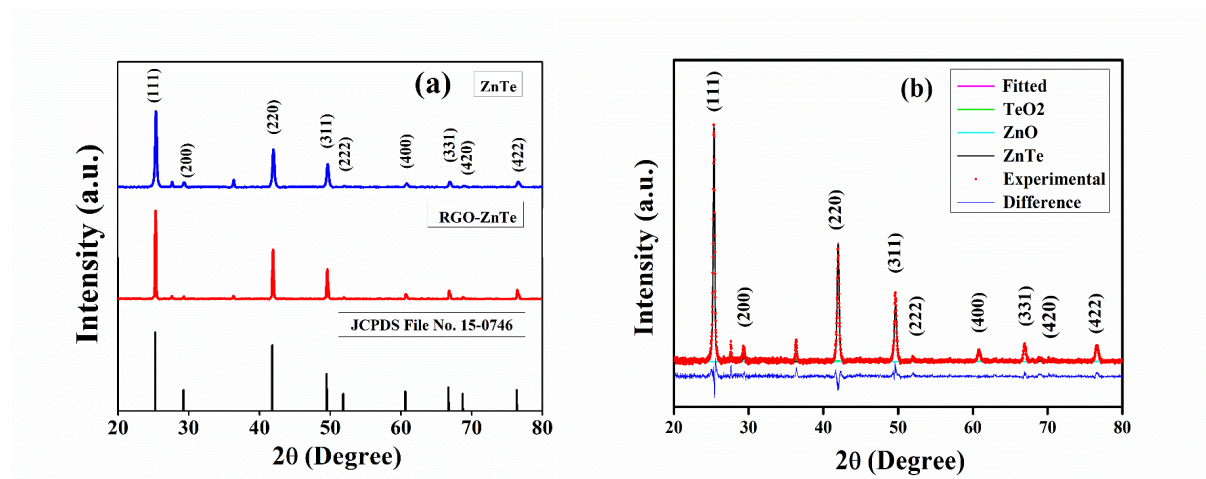


Fig. 4.1: (a) XRD spectra of as-synthesized ZT and R-ZT nanocomposite. (b) Rietveld refinement of the ZT specimen.

The quality of refinements in Fig. 4.1(b) was ascertained from the ‘goodness of fit’ parameter values lying close to unity, which is standard practice while carrying out

Rietveld structure refinement. The presence of a trace amount of secondary phases is easily discernible from the deconvoluted XRD pattern in Fig. 4.1(b), presented as a representative of the pure ZT specimen. The refinement yields a lattice constant value of $a = 6.1031 \text{ \AA}$ for pure ZT, increasing to $a = 6.1048 \text{ \AA}$ for the R-ZT composite, indicating an insignificant lattice expansion $\sim 0.03\%$ due to the incorporation of RGO with ZT. Interestingly, although the R-ZT composite XRD pattern in Fig. 4.1(a) resembles closely that of pure ZT, including the presence of trace ZnO and TeO_2 phases, they reveal markedly, sharp peaks, suggesting the higher crystallinity in the specimens. A further observation from Fig. 4.1(a) is that the addition of RGO did not affect the relative intensities and positions of the Bragg reflections in ZT and R-ZT which could result in the growth of new crystallographic phases. Also, no characteristic diffraction peaks for RGO were noticed in the composite, which is attributed to the low level of loading and comparatively weaker diffraction peaks of GO [28]. The interplanar spacing (d) of the ZT crystal is measured from Bragg's equation ($2d\sin\theta = n\lambda$) as 3.50 \AA corresponding to (111) lattice planes. Moreover, the X-ray diffraction was performed for the synthesized Graphene oxide (GO) and reduced graphene oxide (RGO). The signature peak of the graphene oxide was found at 10.9° in the XRD pattern in Fig. 4.2(a). This authenticates the successful formation of GO from the graphite powder. After hydrazine treatment, the peak at 10.9° was almost diminished and a new and wide peak at 24.7° is observed in Fig. 4.2(b), indicating the reduction of GO [29].

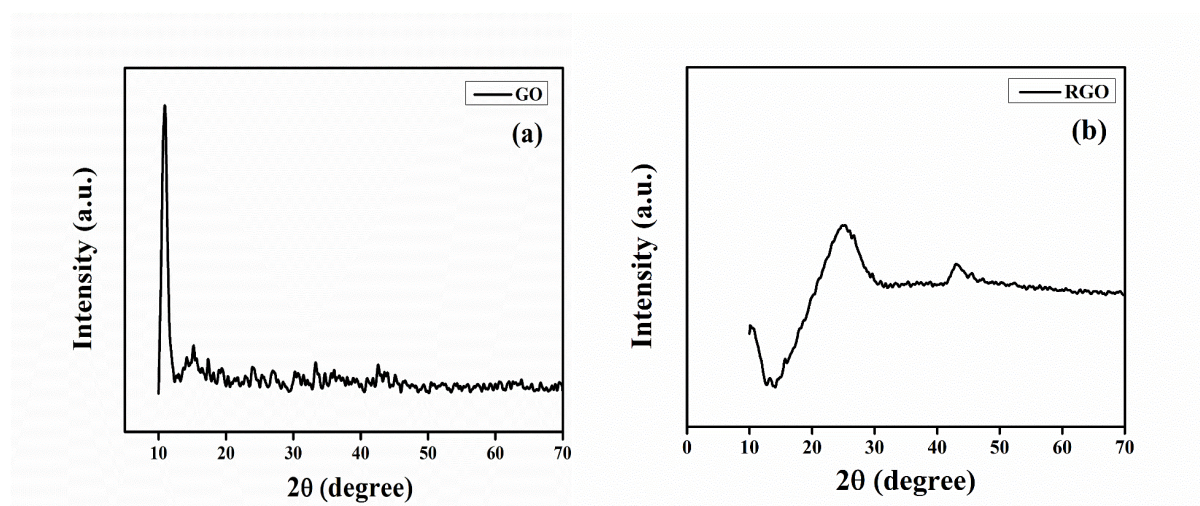


Fig. 4.2: XRD spectra of (a) GO and (b) RGO.

➤ FESEM Study

The morphology and microstructural information of the synthesized materials were also confirmed by electron microscopy studies. Firstly, the FESEM image presented in Fig. 4.3(a) displays the distribution of ZT nanoparticles over the crumpled graphene layers in the R-ZT composite. Some random agglomeration of ZT nanoparticles is also observed, which might occur from the aggregation tendency of the graphene layers due to the van der Waals interaction [29]. The corresponding EDX spectra presented alongside in Fig. 4.3(b) confirm the presence of constituting elements (Zn, Te, C and O) in the nanocomposite. Furthermore, the quantitative analysis of the EDX reveals that the molar ratio of Zn to Te of the synthesized material was very close to unity, suggesting the formation of stoichiometric ZT nanoparticles.

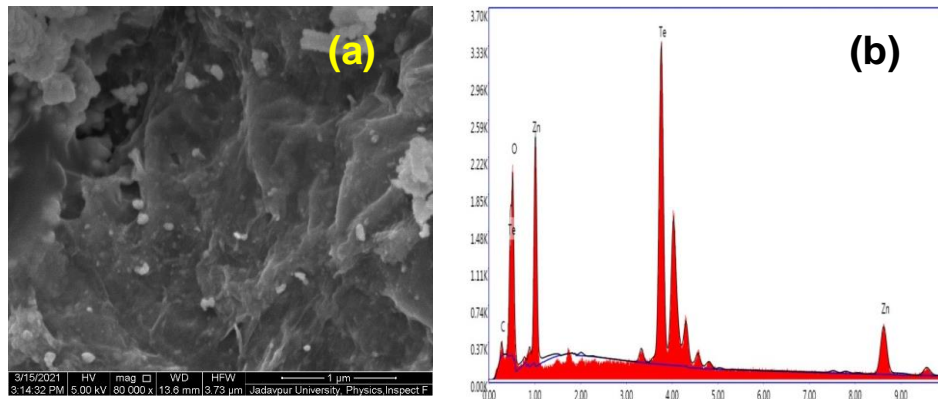


Fig. 4.3: (a) FESEM image and (b) EDX spectra of the R-ZT nanocomposite.

➤ TEM Study

The TEM microstructures in Fig. 4.4(a) and Fig. 4.4(b) are under different magnifications, wherein, the ZT are nearly spherical nanometric-sized particles and they are dispersed uniformly over the wrinkled 2D RGO layers [30]. This kind of situation would help in establishing a close interface with minimal aggregation of the particles and an intimate bond is formed between the ZT and the RGO layers [31]. The formation of the intimate bonding between the ZT and RGO layers would assist the transfer of charge carriers and thereby should inhibit their recombination. The high-resolution transmission electron microscopy (HRTEM) image shown in Fig. 4.4(c) corresponds to an interplanar spacing of ~ 3.49 Å fringe spacing for the (111) crystallographic planes of cubic ZT lattice, agreeing reasonably well with ~ 3.50 Å obtained from the XRD analysis. Fig. 4.4(d) shows

the selected area electron diffraction (SAED) pattern of the ZT nanoparticles with concentric diffraction rings, indicating the polycrystalline nature of the specimen.

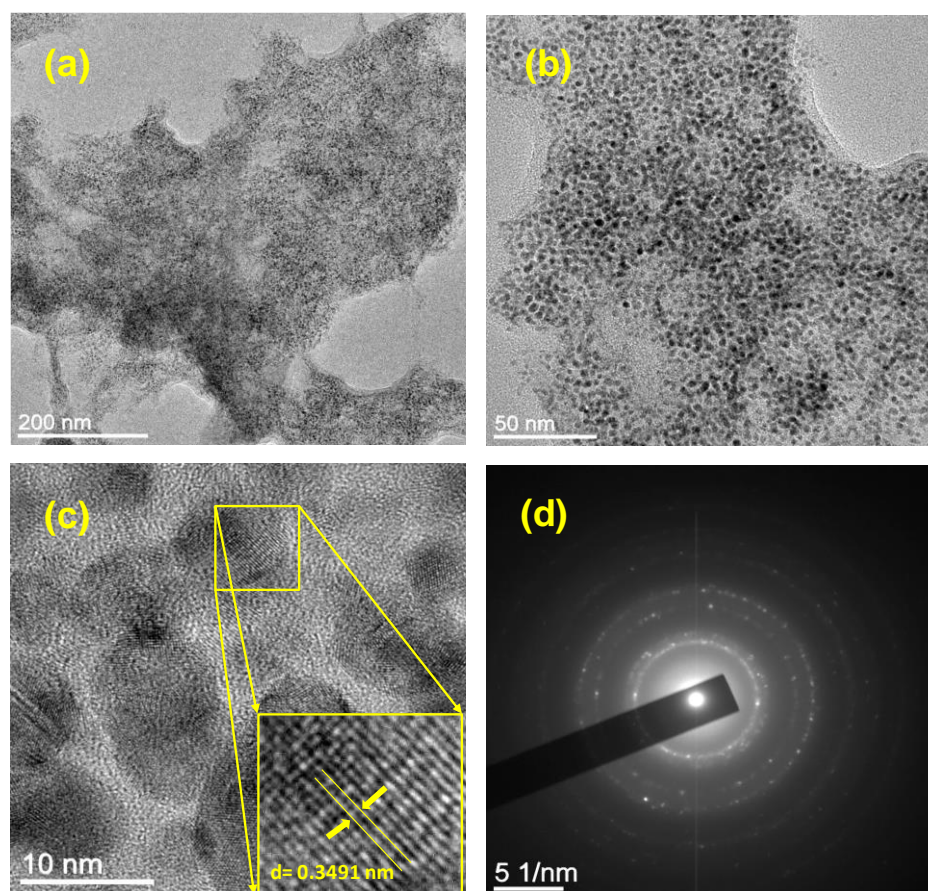


Fig. 4.4: (a) and (b) TEM images of the R-ZT nanocomposite. (c) High-resolution TEM and (d) SAED pattern of ZT nanoparticles over RGO layers.

➤ XPS Study

X-ray Photoelectron Spectroscopy (XPS) study of the R-ZT nanostructures was performed to examine the chemical composition of the surface and oxidation state of the metallic ions. The presence of the Zn, Te, C and O in the R-ZT nanocomposite was validated by the survey spectrum in the energy range of 0-1200 eV and shown in Fig. 4.5(a). The XPS peak of C 1s for the R-ZT composite was deconvoluted into four constituent Gaussian peaks in Fig. 4.5(b), and they are centred around the binding energies: 283.76, 285.07, 287.16 and 290.07 eV, which are ascribed to the C=C, C-OH, C=O and O-C=O bonds, respectively [32]. The incidence of relatively low intense oxygenated functional groups implicates their partial elimination, besides the existence of the restored graphitic segment in the composite material [29]. This, on one hand, has an obvious ramification in that the restored graphitic layers favour the electron transfer,

while on the other hand, the O₂ containing functional groups would incite establishing a strong interaction among the nanocomposite and the aqueous solution during the photocatalytic degradation [33,34].

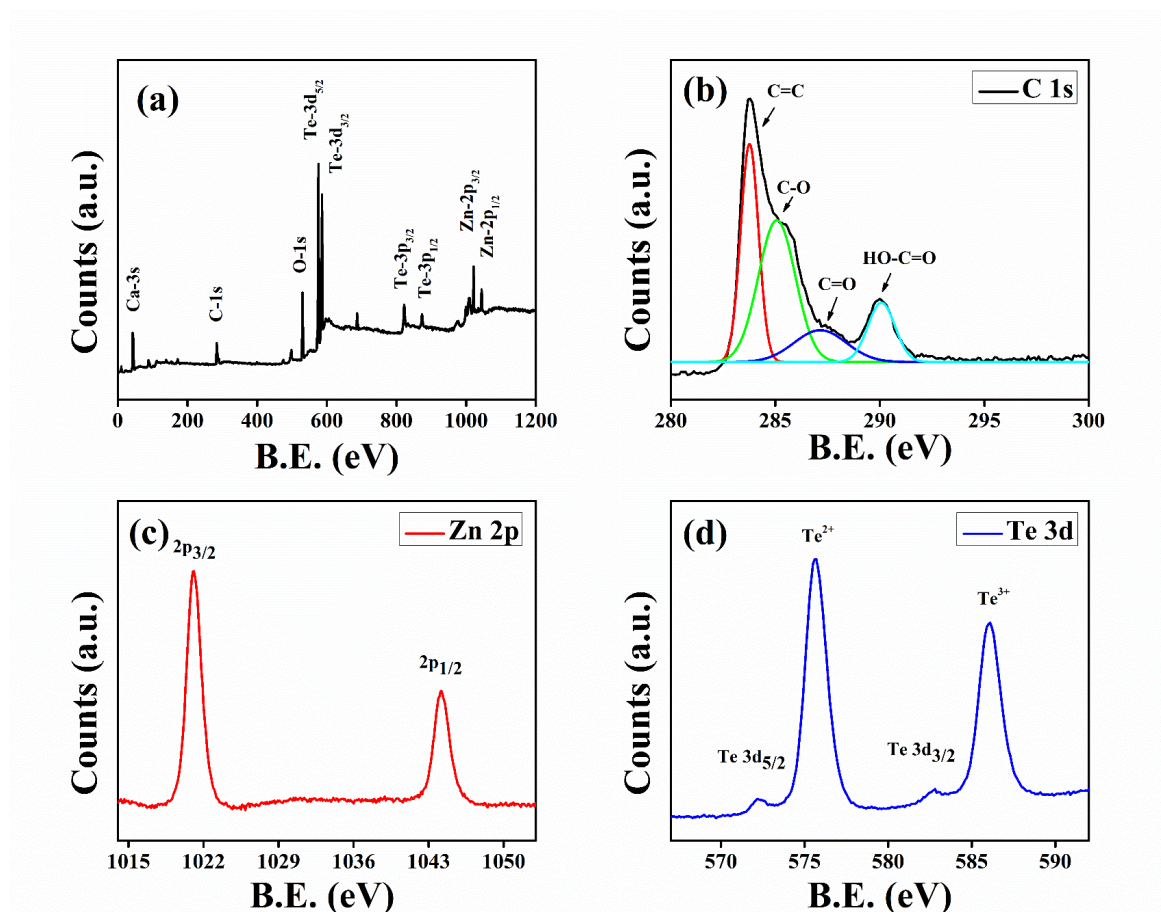


Fig. 4.5: (a) XPS survey and (b) C 1s spectrum of the R-ZT nanocomposite. The HR-XPS spectrum of (c) Zn-2p and (d) Te-3d states.

Fig. 4.5(c) further shows the high-resolution XPS spectrum corresponding to the Zn 2p doublet. The splitting of the 23.1 eV core level into Zn-2p_{3/2} and Zn-2p_{1/2} levels indicates the 2⁺ oxidation state of Zn. On the other hand, two peaks corresponding to Te are identified in Fig. 4.5(d) at binding energies: 573 and 583.1 eV, respectively representing the 3d_{5/2} and 3d_{3/2} transitions and thereby validating the establishment of Zn-Te bonding. Additionally, it is also discernible that the two Te peaks are accompanied by a pair of small, but prominent peaks corresponding to energies: 576.1 eV and 586.8 eV, arising out of the 3d_{5/2} and 3d_{3/2} transitions due to the incidence of other tellurium oxides (TeO₂ and TeO₃), respectively. The existence of secondary tellurium oxides in the present study has also been confirmed in the XRD patterns fitted according to Rietveld

refinement [Fig. 4.1(b)], which has been accredited to the oxidation of tellurium-rich phases of ZT during the hydrothermal process [35,36]. Nevertheless, Baghchesara et al. reckon that these oxidation states of Te could be diminished by growing the ZT at a relatively higher temperature [37].

4.4.2. Optical Properties

➤ UV-visible Spectroscopy

The UV-visible absorbance spectra of as-synthesized ZT and R-ZT nanocomposite presented in Fig. 4.6(a) were recorded in the wavelength range 200-900 nm to study their optical properties. The optical band gap (E_g) of the nano-catalysts was derived employing Tauc's equation (Eq. 4.1) in the fundamental absorption edge of the UV-visible absorption spectroscopy. According to Tauc's equation [38]:

$$(\alpha h\nu)^n = A(h\nu - E_g) \quad (4.1)$$

where α is the absorption coefficient, E_g is the bandgap, h is Planck's constant, ν is frequency, A is a constant, and $n = 2$ and $\frac{1}{2}$ corresponds to the allowed direct and indirect optical transition respectively.

The estimated value of the bandgap of pure ZT nanoparticles using Tauc's plot [Fig. 4.6(b)] was 2.11 eV, which is in good agreement with the previously reported value [39]. The broadness of the absorption band of the R-ZT composite material as compared

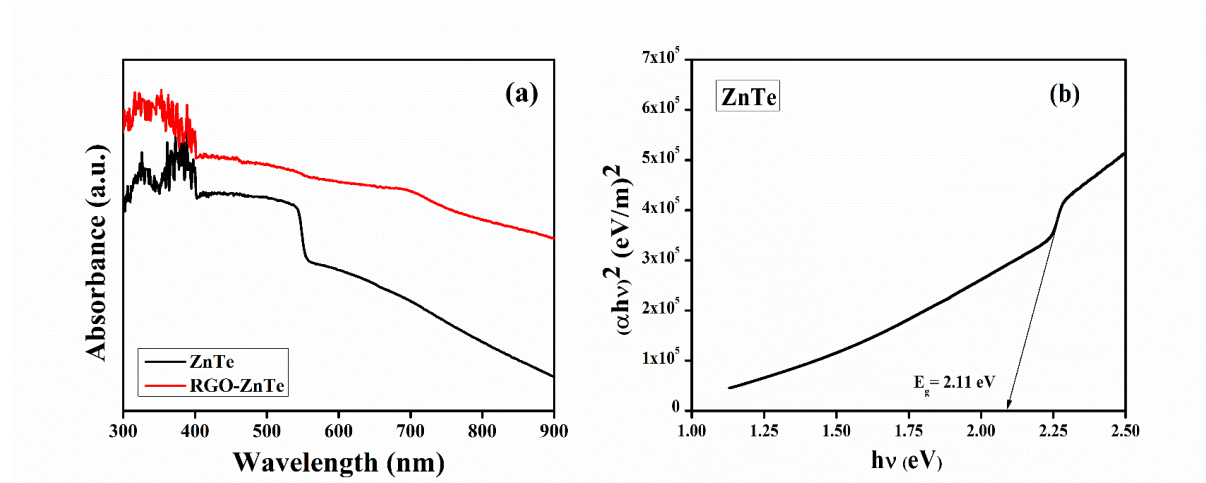


Fig. 4.6: (a) Optical absorption spectra of pure ZT and R-ZT composite. (b) Tauc's plot for the optical band gap of pure ZT.

to pristine ZT indicates improvement in the photon absorption and proliferation of the electron-hole pair in the photocatalytic experiment.

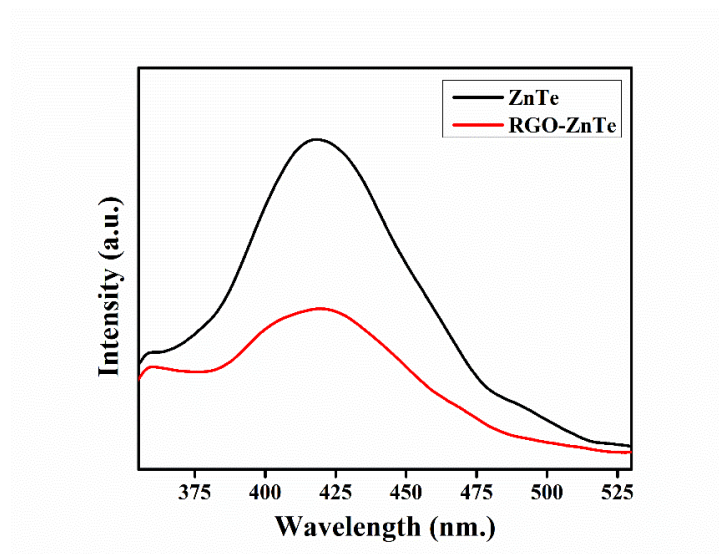


Fig. 4.7: Photoluminescence spectra of ZT and R-ZT nanocomposite.

☞ *Photoluminescence (PL) Spectroscopy*

Photoluminescence (PL) spectroscopy is a useful tool to reveal the interaction between the electrons and holes that are generated by photon excitation. Fig. 4.7 shows the PL spectra of as-synthesized ZT and R-ZT nanocomposite under 315 nm excitation. The pristine ZT exhibits a prominent emission centred around 418 nm, whose intensity significantly diminishes after loading GO sheets - due to the existence of strong interfacial interaction in the composite material, which renders a dedicated pathway to the electrons and holes for establishing interaction between the ZT and GO layers [40,41]. The electrons thus could easily migrate from the excited ZT and the ‘quenching’ of fluorescence occurs. Such extended separation between the photo-generated charge carriers and their swift transportation essentially enhances the photocatalytic processes [42,43].

4.4.3. Thermal Stability Study

The thermal stabilities of the as-synthesized ZT and R-ZT nanocomposite were probed by the thermogravimetric analysis (TGA), performed at gradually increasing temperatures (10 °C/min) from 25 °C to 750 °C in an N₂ atmosphere. Fig. 4.8 depicts the TGA spectrum of the R-ZT composite, exhibiting two distinct stages of weight loss with 99.65% residue

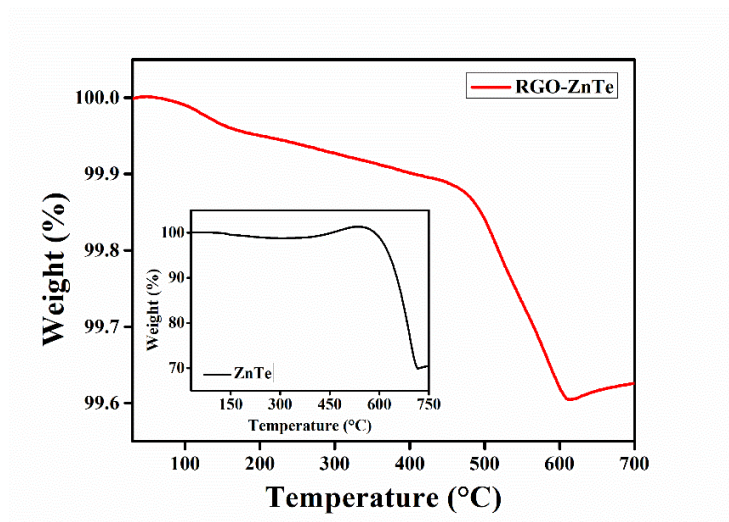


Fig. 4.8: TGA curves of pure ZT (inset) and R-ZT nanocomposite.

up to 700 °C. The first weight loss took place approximately at 65-185 °C, indicating the desorption of solvents and absorbed moisture, followed by a step-like second stage (435-625 °C), wherein the oxidation of RGO and phase transformation of ZT occurs. On the other hand, the pure ZT also underwent a rapid weight loss in the temperature range of 510-715 °C, thereby leaving about 70% residue [44]. These results reveal that RGO loading imparts higher stability to the R-ZT composites, as compared to the pristine ZT.

4.4.4. BET Surface Area Studies

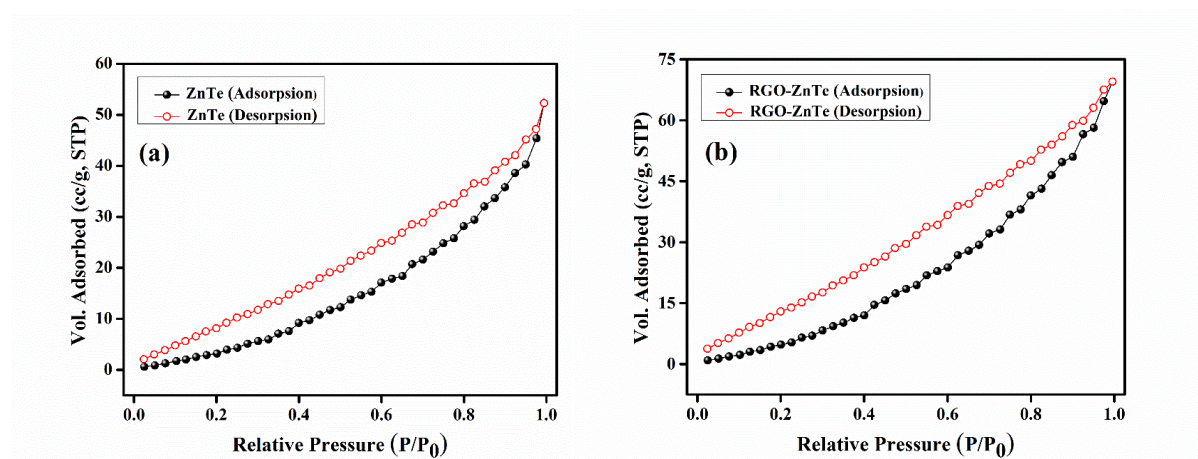


Fig. 4.9: N₂ adsorption-desorption isotherms for (a) ZT and (b) R-ZT nanocomposite.

The N₂ adsorption-desorption isotherms (Fig. 4.9) at 77 K (-196 °C) were also recorded to obtain information about the Brunauer-Emmett-Teller (BET) specific surface for the

pure ZT and R-ZT nanocomposite [45]. The BET analysis estimates that the specific surface area of pristine ZT and R-ZT composites were $24.58 \text{ m}^2\text{g}^{-1}$ and $36.31 \text{ m}^2\text{g}^{-1}$, respectively, expectedly indicating a higher surface area in the graphene-based composite [13]. In photocatalytic applications, a higher absorbance cross-section is always desirable since the larger the surface area, the higher will be the photo-absorption and consequently, the diffusion of molecules is also enhanced. Fig. 4.9, therefore, indicates that the graphene composite is expected to fulfil those requirements, which is now demonstrated in the following.

4.4.5. Electrical Properties

➤ *Current-Voltage (I-V) Measurements*

To interpret the electronic charge transport properties of the synthesized materials, the current-voltage (I-V) characteristics for the fabricated Schottky devices (Al/ZT/ITO and Al/R-ZT/ITO), as displayed in the previous Chapter (§ 3.3.4), were studied by applying a dc bias voltage of $\pm 1 \text{ V}$ at room temperature under dark and light ($\sim 1000 \text{ W/m}^2$) conditions. The dc conductivity (σ), which is a measure of the charge flow, was estimated from the linear region of the diode characteristic curves [Fig. 4.10(a)] for both the devices studied under different conditions (Table 4.1). The significant rise in current density after light irradiation indicates the photo-responsive nature of the materials. The Photosensitivity (S), defined as $S = I_v/I_d$ (where $I_v = I_l - I_d$ is the photo-induced current and I_d is the current under dark) was further deduced for both devices [46]. The graphene-based device, which possesses a strong absorption ability, displayed higher sensitivity than its counterpart with pristine ZT (Table 4.1). Also, the higher conductivity of the composite material in Table 4.1 implicates enhancement in charge transportation alongside improved mobility. For any semiconducting material, carrier mobility is very important because it decides how fast a carrier, i.e., electrons and/or holes would advance through its complex network before reaching the active sites, wherein, they finally recombine with each other. Since RGO offers higher electron mobility ($\sim 10^4 \text{ cm}^2/\text{Vs}$ at 300K), it is expected to also assist their passage and electron-hole pair separation through its high-grade 2D network [47].

To elucidate the inclusive influence of RGO in the charge transport mechanism and photodegradation process, the I-V characteristics were further analysed by interpreting the carrier's mobility (μ_{eff}) and lifetime (τ) based on semiconductor theory. For this

purpose, the $\log(I)$ against $\log(V)$ for positive voltages are plotted in Fig. 4.10(b), wherein, three distinct linear regions can be delineated implying different conduction mechanisms.

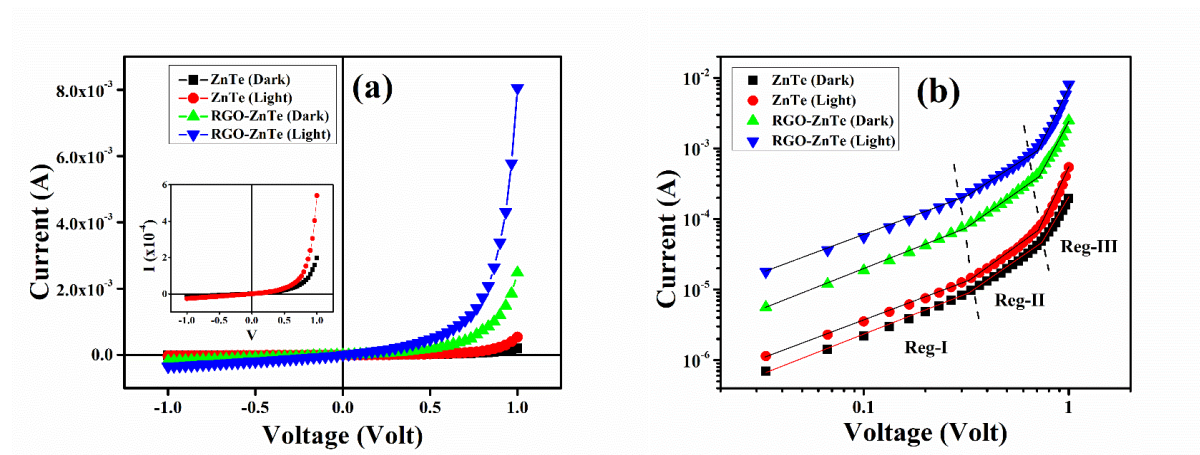


Fig. 4.10: (a) Current-voltage (I-V) characteristic curves and (b) I-V plot in logarithmic scale for the pure ZT and R-ZT composite-based Schottky diodes under the dark and light conditions.

Mainly, in a metal-semiconductor junction, the interfacial trap states alter the conduction of charge carriers and thus reform the I-V characteristic curves. At low bias (region-I), the Ohmic behaviour ($I \propto V$) with a slope about unity is observed. In this region, the current is mainly driven by the charge carriers that are intrinsic to the material under investigation [48]. Moving on to region II in Fig. 4.10(b), the injected carriers from the contacts are spread over the intrinsic ones for intermediate potential difference values and they develop a spatially distributed charge field. The charge carriers are then governed by this field and their 'mobility' predominantly controls the quadratic current ($I \propto V^2$) in this region [49,50]. Finally, for even higher applied voltages, the device surpasses the trap-filled limit when the injection level of electrons is so high that the conduction is due to the 'trap-free space-charge limited current' followed by the power-law ($I \propto V^n$, where $n > 2$) and that this corresponds to region III in Fig. 4.10(b) [50].

➡ Estimation of the Charge Transport Parameters

To obtain a better understanding of the charge transport mechanism, the I-V characteristics were further analysed by deciphering the effective carrier's mobility (μ_{eff}) and lifetime (τ) from region II [Fig. 4.10(b)] based on the space-charge limited current (SCLC) theory [49]. Fig. 4.11(a) and Fig. 4.11(b) display the current (I) vs. voltage² (V^2) plot for the SCLC region for ZT and R-ZT composite, respectively. The dielectric constant

of the synthesized materials (ϵ_r), the mobility (μ_{eff}), and the lifetime or transient time (τ) of the charge carriers were estimated employing the following equations:

$$\epsilon_r = \frac{C_0 d}{\epsilon_0 A_{\text{eff}}} \quad (4.2)$$

$$I = \frac{9 \mu_{\text{eff}} \epsilon_0 \epsilon_r A_{\text{eff}}}{8} \left(\frac{V^2}{d^3} \right) \quad (4.3)$$

$$\tau = \frac{9 \epsilon_0 \epsilon_r A_{\text{eff}}}{8 d} \left(\frac{V}{I} \right) \quad (4.4)$$

The detailed elucidation of all the symbols used in the aforementioned equations was provided in Chapter 2 (§ 2.5.2). Also, the plot illustrating the capacitance (C) vs. frequency (f) characteristics for both ZnTe and RGO-ZnTe films is presented in Fig. 4.12.

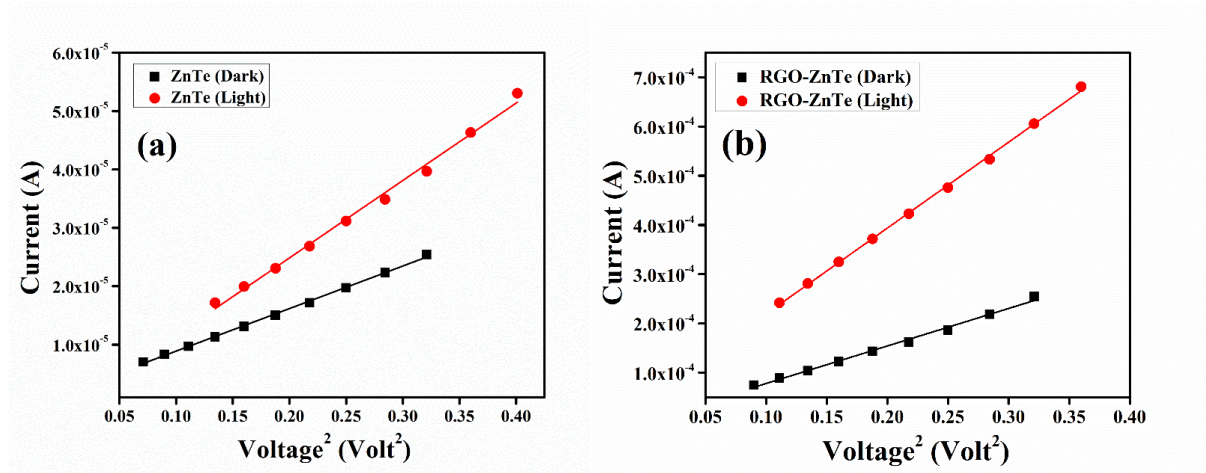


Fig. 4.11: The current (I) vs. voltage² (V²) plot for the SCLC region for (a) ZT and (b) R-ZT composite.

The estimated values of μ_{eff} and τ are also presented in Table 4.1. The higher mobility of graphene and its impressive contribution to the smooth transfer of charge carriers was portrayed in our results. The graphene-based composite exhibited better carrier mobility and lifetime than the as-synthesized ZT nanoparticles. The results are consistent with the previously reported data for the RGO-based inorganic composite [53,54]: For both dark and light conditions, the mobility of the carriers was significantly increased by almost 10-12 times (Table 4.1). This enrichment in mobility as well as in lifetime could enhance the charge transfer efficiency and thus, the photocatalytic activity.

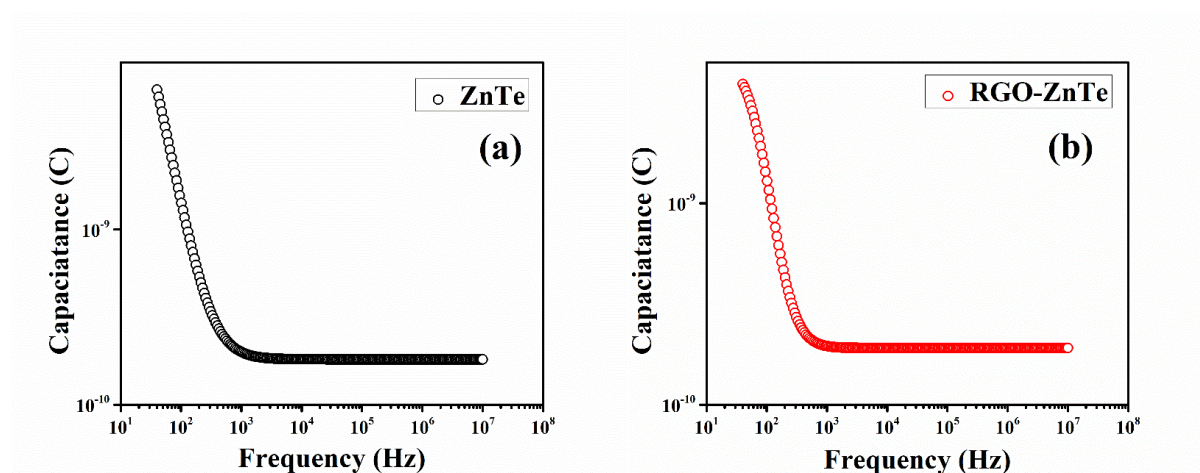


Fig. 4.12: Capacitance (C) vs. frequency (f) plot for (a) ZnTe and (b) RGO-ZnTe thin film.

Table 4.1: Charge transport parameters.

Sample	Photo-sensitivity	Conductivity (σ) (Sm^{-1})		Mobility (μ_{eff}) ($\text{cm}^2\text{V}^{-1}\text{s}^{-1}$)		Lifetime (τ) (s)	
Condition	-	Dark	Light	Dark	Light	Dark	Light
ZT	1.75	4.36×10^{-5}	5.71×10^{-5}	3.56×10^{-3}	6.49×10^{-3}	2.91×10^{-6}	1.81×10^{-6}
R-ZT	2.24	3.96×10^{-4}	1.07×10^{-3}	3.54×10^{-2}	8.13×10^{-2}	3.11×10^{-7}	1.39×10^{-7}

➤ Transient Photocurrent Measurements and Nyquist Plots

To investigate the photo-electrochemical properties of the as-prepared catalysts, the transient photo-response spectra and EIS Nyquist plots were obtained and displayed in Fig. 4.13(a) and Fig. 4.13(b), respectively [55]. As expected, the photocurrent intensity of the R-ZT composite was found to be much higher than the pristine ZT. This result indicates that the incorporation of RGO into the ZT nanoparticles could facilitate the separation of the photo-generated electrons and holes and their swift transfer through the 2D graphene channels [56]. Furthermore, the EIS Nyquist spectra, which is also a powerful tool to investigate the conductance and charge transfer facility, showed a much smaller diameter of the semi-circular arc for the R-ZT composite than the pristine ZT [Fig. 4.13(b)]. This result affirms that the introduction of RGO significantly decreased the charge transfer resistance in the composite material, facilitating the migration of

electrons and holes to the active sites during the degradation process, as discussed below [5,57].

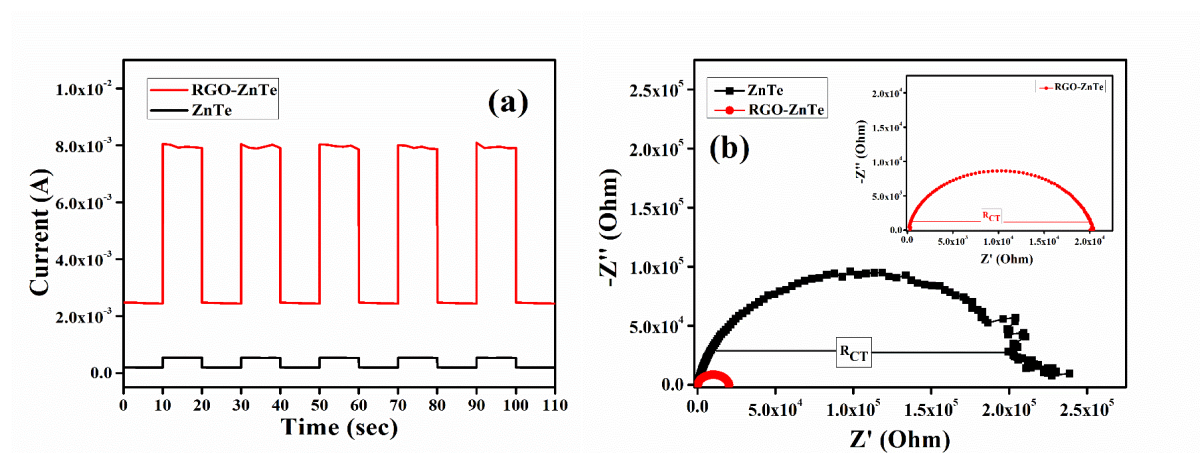


Fig. 4.13: (a) Transient photocurrent response and (b) EIS Nyquist plots of pristine ZT (inset) and R-ZT composite.

4.4.6. Photocatalytic Activity

➤ Photo-degradation Process

The photocatalytic performance of the as-prepared samples was measured by photocatalytic degradation of RhB under solar-simulated visible light irradiation. In the typical experiment, 30 mg of the samples and 1 mL H_2O_2 were dispersed in 100 mL of RhB aqueous solution (100 ppm). The mixed suspensions were magnetically stirred for 30 minutes in the dark condition to attain an adsorption-desorption equilibrium. Under ambient conditions and stirring, the mixed suspensions were exposed to visible light produced by a solar simulator (Abet Technologies, Model 10500). At regular time intervals, 3 ml of the suspensions under investigation were extracted and centrifuged to remove the suspended impurities. The absorption of RhB in the filtrate was then examined using a UV-Vis spectrometer and the degradation process was analysed.

For the recyclability test, the catalyst was extracted after the degradation cycle by centrifugation and washed with isopropyl alcohol followed by Millipore water and reused in the next cycle. In this study, all the experiments have been repeated three times to find their catalytic activity.

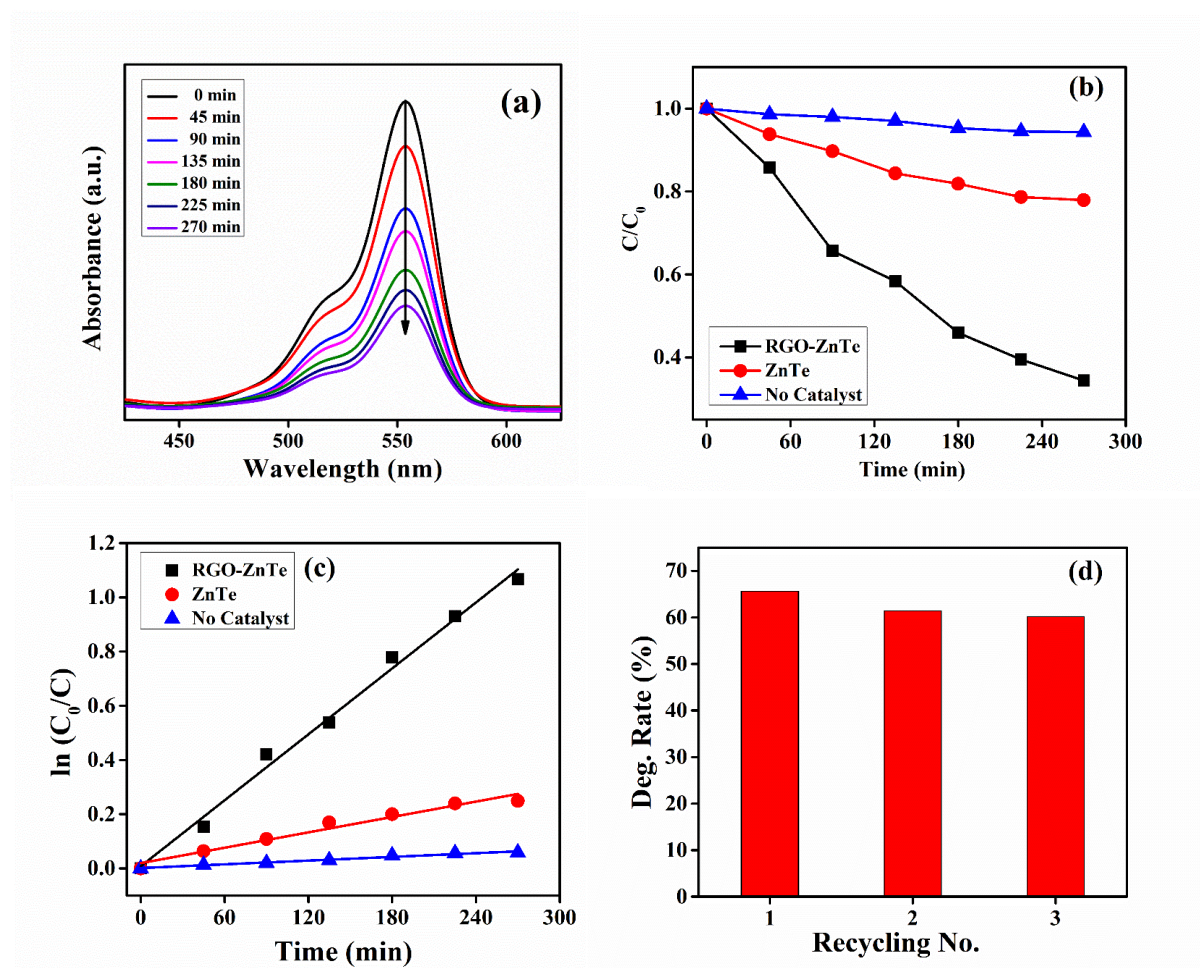


Fig. 4.14: (a) Absorption spectra of aqueous RhB solution for different time intervals in the presence of R-ZT nanocomposite under the solar simulator. (b) Photocatalytic decomposition behaviour and (c) plot of $\ln(C_0/C)$ vs. irradiation time for RhB solution in the presence of different catalysts. (d) Recycling performance of R-ZT catalyst for RhB degradation.

☞ Photo-degradation Behaviour and Performances

The photocatalytic degradation of RhB under simulated solar light irradiation is used to study the photocatalytic behaviour of pristine ZT and R-ZT nanocomposite. The degradation process was studied by monitoring the major absorption peak of RhB aqueous solution centred at 553.5 nm with the help of a UV-Vis spectrometer [Fig. 4.14(a)] and the degradation process was analysed by the following equation:

$$\text{Degradation} = \left(\frac{C_0 - C_t}{C_0} \times 100 \right) \% \quad (4.5)$$

where C_0 and C_t represent the concentration of RhB at the time zero and 't', respectively [58]. The linearity of the $\ln(C_0/C)$ vs. illumination time (min) [Fig. 4.14(c)] for both pure

ZT and R-ZT composite demonstrates the existence of pseudo-first-order degradation kinetics [59]. Under solar light irradiation for 270 minutes, no considerable change in the RhB concentrations was observed for catalyst-free suspensions. After adding the pure ZT catalyst, the RhB solution was found to be bleached up to 23% of its initial concentration. On the other hand, the R-ZT nanocomposite exhibited an enhanced degradation of 66% due to the synergistic effect of ZT nanoparticles and RGO [Fig. 4.14(b)]. Further, the recycling test [Fig. 4.14(d)] showed that the degradation efficiency of the R-ZT catalyst does not change conspicuously even after repetitive usage up to three cycles.

➤ Adsorption of RhB by the Photocatalysts

The adsorption of RhB on the photocatalysts was measured before the degradation experiments since the pre-adsorption of the dyes aids the migration of the charge carriers. The adsorption experiments were performed by continuously stirring 100 mL of aqueous RhB solution with 30 mg of each catalyst (ZT and R-ZT) for 30 min in the dark condition [60]. Fig. 4.15 displays the adsorption profiles of aqueous RhB solution as a function of time in the dark on the pristine ZT and the R-ZT composite, respectively. The pristine ZT demonstrated no adsorption in the dark, as the concentration of the RhB solution remained almost unchanged. In addition, the R-ZT composite also showed negligible adsorption behaviour to RhB, which was less than 1% for 30 min of stirring. These results indicate that the adsorption of RhB by the catalysts would not significantly impact the photo-induced degradation process, which is discussed in the following

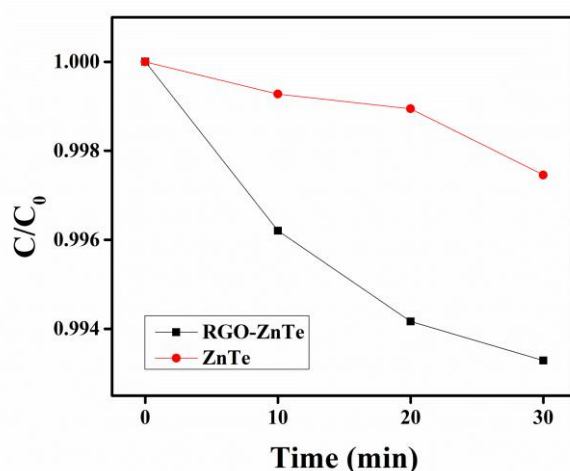


Fig. 4.15: The adsorption profiles of aqueous RhB solution on the pristine ZT and the R-ZT composite, as a function of time in the dark.

➤ Identifications of Reactive Species

The reactive species in the photocatalytic degradation process were identified by the in situ capture experiments. In these tests, isopropyl alcohol (IPA), disodium ethylenediaminetetraacetate (EDTA- Na_2) and N_2 atmosphere were used as scavengers in the degradation process. The absorption plots of the degraded RhB by R-ZT in the presence of different scavengers are shown in Fig. 4.16. The role of the active species was determined from the variation of C/C_0 with irradiation time (Fig. 4.17) of RhB after the scavengers were added to the photocatalytic system [61].

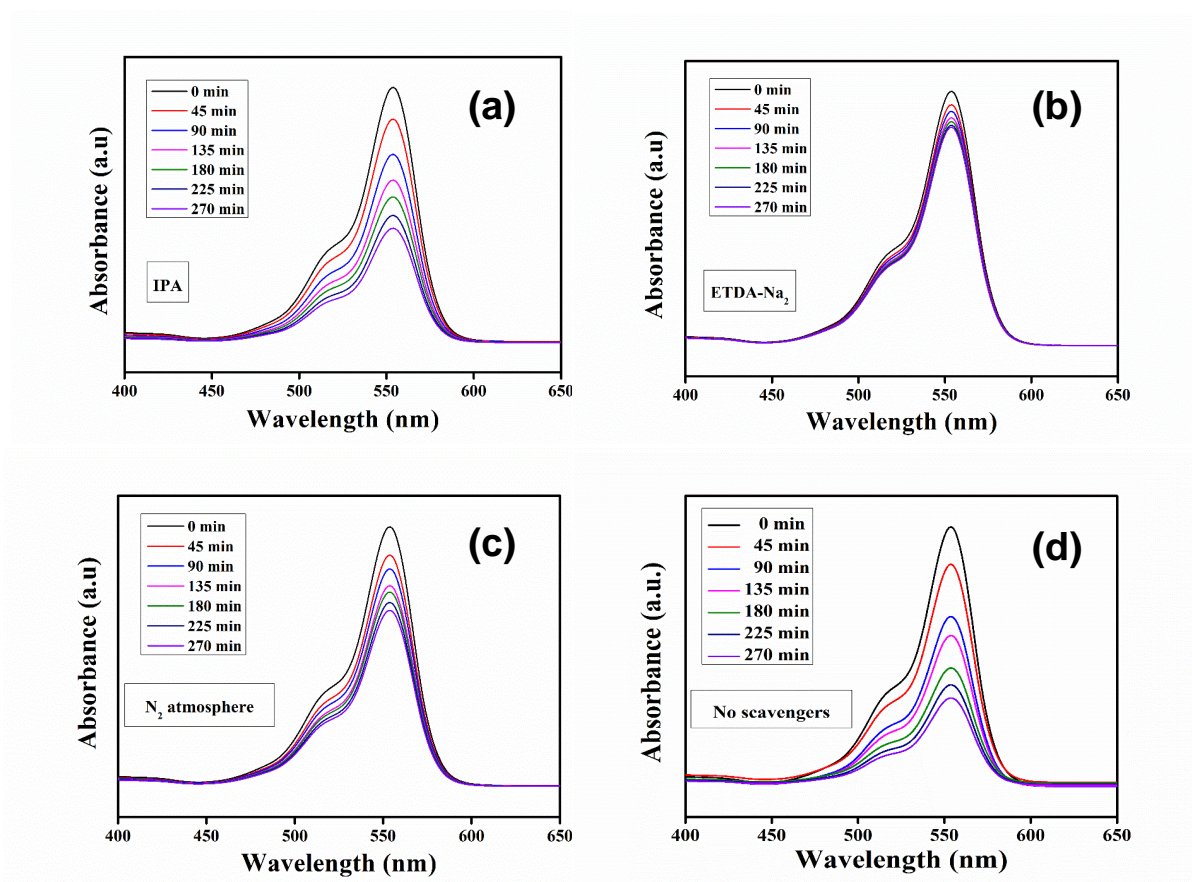


Fig. 4.16: UV-vis absorption spectra of degraded RhB aqueous solution by R-ZT in the presence of (a) Isopropyl alcohol (b) EDTA- Na_2 (c) N_2 atmosphere and (d) No scavengers.

As seen in Fig. 4.17, the RhB solution degraded up to 45% of its initial concentration for 270 min irradiation time. It demonstrates that the decomposition of RhB was slightly suppressed in the presence of IPA, a hydroxyl (OH^\bullet) quencher, as compared to 34% in the absence of scavengers. This finding indicates that OH^\bullet has a mild effect on the photocatalytic degradation of RhB using the R-ZT catalyst. In the case of EDTA- Na_2 , a quencher of h^+ , the value of C/C_0 was not reduced below 86%, indicating that

holes play a significant role in the RhB degradation. On the other hand, the normalised concentration (C/C_0) was moderately diminished up to 68% when the reaction was carried out in an N_2 atmosphere, a quencher of $O_2^{\bullet-}$. This suggests that the $O_2^{\bullet-}$ radical is also markedly responsible for the photocatalytic degradation of RhB. The above observations suggest that although all the reactive species contribute to some extent, h^+ and $O_2^{\bullet-}$ radicals play a pivotal role in the photodegradation of RhB [60].

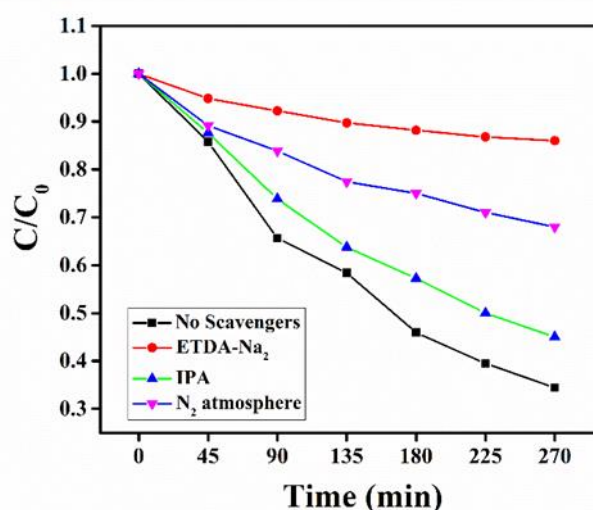


Fig. 4.17: Photocatalytic degradation of RhB aqueous solution by R-ZT in the presence of IPA, EDTA- Na_2 , N_2 atmosphere and no scavengers.

➤ Optimization of the RGO Content in the Composites

To determine the optimum composite photocatalyst for achieving the highest photocatalytic activity, the R-ZT composites with different RGO content were prepared and they were labelled as “R (x%)-ZT”, where x stands for the weight % of the RGO (0%, 2%, 5% and 6.67%). Fig. 4.18 shows the variation of RhB concentration (C/C_0) with time in the presence of different catalysts under visible-light irradiation for 270 min irradiation. It was seen that no considerable change in the RhB concentration was observed for catalyst-free suspensions. After adding the pristine ZT catalyst, the RhB solution was found to be bleached up to 23% of its initial concentration. On the other hand, the RhB solution was degraded up to 51%, 66% and 62% with the R(2%)-ZT, R(5%)-ZT, R(6.67%)-ZT, respectively. The result demonstrates that the photocatalytic activity of R-ZT composites was first enhanced and then diminished with the increasing

amount of RGO. Among the prepared samples, the composite with 5% RGO content showed the highest photocatalytic activity (66%).

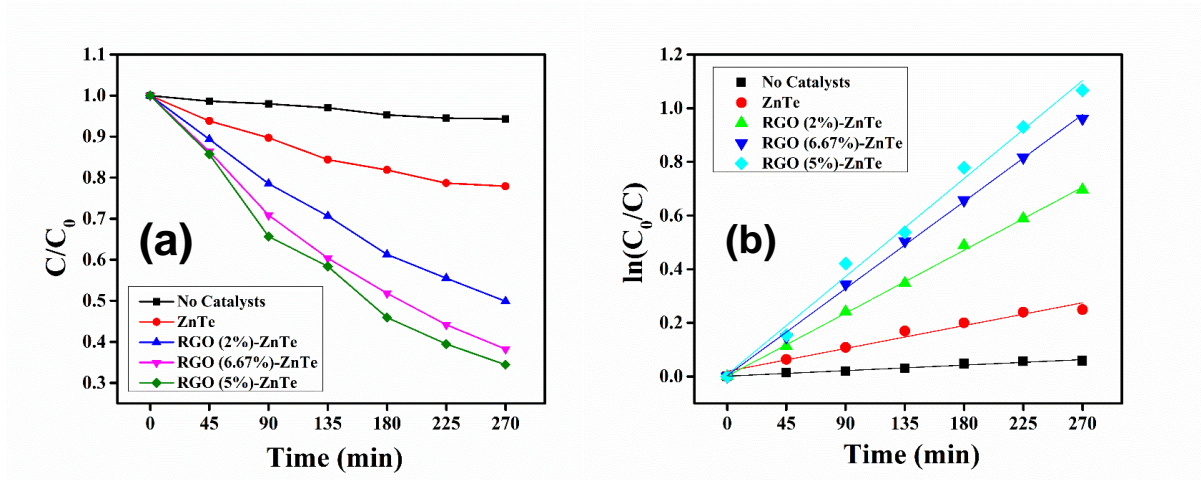


Fig. 4.18: (a) Changes in concentration vs. time and (b) $\ln(C_0/C)$ vs. time plot in the presence of different catalysts under visible-light irradiation.

➤ Photo-degradation Mechanism

To explain the synergy between RGO and ZT in the composite material, the photocatalytic decomposition process was analyzed. Under visible light irradiation, interfacial excitons originated over the surface of ZT nanoparticles and subsequently, separated into free electrons and holes in the conduction band (CB) and valence band (VB) respectively. However, these photogenerated electrons and holes tend to recombine before appearing at the active sites and thus, a poor photocatalytic reaction is observed. When ZT nanoparticles are attached to the RGO, the photoinduced electron in the CB of ZT could be efficiently separated at the graphene interface leaving behind a hole in the VB of ZT due to their preferable energy levels (Fig. 4.19) [39,62]. Thus, the photogenerated electrons in ZT can easily reach the active sites through the RGO platform and reduce the dissolved O_2 present in the aqueous medium to generate the highly reactive superoxide radical anion ($O_2^{\bullet-}$), which can further react with H_2O to form hydroxyl (OH^\bullet) radical [63]. Meanwhile, the photoinduced holes may also react with H_2O or OH^- and oxidize them into OH^\bullet [64]. These $O_2^{\bullet-}$, OH^\bullet and the photogenerated holes cooperatively participate in the decomposition process of the RhB solution [65,66]. A schematic representation of the photocatalytic mechanism of the R-ZT photocatalysts is displayed in Fig. 4.19.

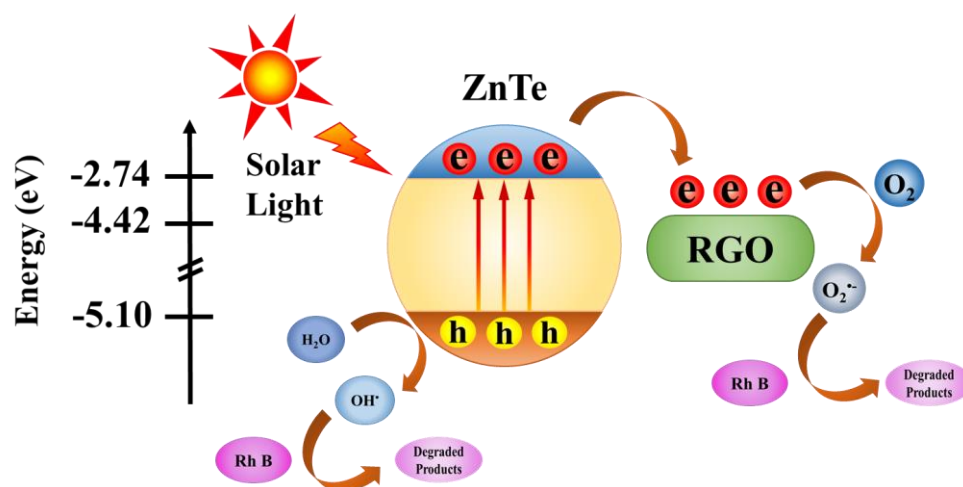


Fig. 4.19: A plausible mechanism of the photocatalytic degradation process of RhB containing R-ZT catalyst under solar light irradiation.

4.5. Conclusion

The ZT nanoparticles were successfully synthesized and the incorporation of the RGO sheet with ZT was supported by XRD, TEM, FESEM, XPS, PL and UV-Vis spectroscopic data. The charge transport dynamics and the significance of higher carrier mobility of the photocatalysts in the degradation RhB were studied. The graphene composite exhibited relatively higher photocatalytic activity than the bare ZT under visible-light irradiation. The higher mobility of the graphene-based composite material assisted the photoinduced charges in swiftly travelling between active sites and target molecules during the degradation process. The strong interfacial contact, along with higher visible light absorption and low electron-hole pair recombination mainly contributed to the enhanced photocatalytic performance of the composite materials. Conclusively, our findings have shed light upon the design and the charge transfer mechanism of graphene-semiconductor-based R-ZT composite material, which could be a promising photocatalyst finding diversified applications in wastewater treatment.

References

1. R. Al-Tohamy, S. S. Ali, F. Li, K. M. Okasha, Y. A. G. Mahmoud, T. Elsamahy, H. Jiao, Y. Fu, and J. Sun, *Ecotoxicol. Environ. Saf.* **231**, 113160 (2022).
2. V. Selvaraj, T. Swarna Karthika, C. Mansiya, and M. Alagar, *J. Mol. Struct.* **1224**, 129195 (2021).
3. D. Liu, C. Li, C. Zhao, Q. Zhao, T. Niu, L. Pan, P. Xu, F. Zhang, W. Wu, and T. Ni, *Chem. Eng. J.* **438**, 135623 (2022).
4. Y. Zhao, R. Li, L. Mu, and C. Li, *Cryst. Growth Des.* **17**, 2923 (2017).
5. T. Ni, Z. Yang, H. Zhang, L. Zhou, W. Guo, L. Pan, Z. Yang, K. Chang, C. Ge, and D. Liu, *J. Colloid Interface Sci.* **615**, 650 (2022).
6. Z. Zhang, W. Wang, L. Wang, and S. Sun, *ACS Appl. Mater. Interfaces* **4**, 593 (2012).
7. U. G. Akpan and B. H. Hameed, *J. Hazard. Mater.* **170**, 520 (2009).
8. D. Liu, H. Li, R. Gao, Q. Zhao, Z. Yang, X. Gao, Z. Wang, F. Zhang, and W. Wu, *J. Hazard. Mater.* **406**, 124309 (2021).
9. T. Aarthi and G. Madras, *Ind. Eng. Chem. Res.* **46**, 7 (2007).
10. K. S. Lee, G. Oh, and E. K. Kim, *Sol. Energy* **164**, 262 (2018).
11. M. Son, S. Kim, Y. Lee, and J. Bang, *J. Alloys Compd.* **886**, 161233 (2021).
12. O. I. Olusola, S. S. Oluyamo, and O. A. Ajayi, *Mater. Sci. Semicond. Process.* **123**, 105494 (2021).
13. M. F. Ehsan, M. N. Ashiq, and T. He, *RSC Adv.* **5**, 6186 (2015).
14. X. P. Wu, J. Gu, S. M. Zhou, X.-Y. Li, S. L. Wang, L. Jin, H. Chen, and J. J. Shi, *J. Alloys Compd.* **627**, 166 (2015).
15. Y. Sun, Q. Zhao, J. Gao, Y. Ye, W. Wang, R. Zhu, J. Xu, L. Chen, J. Yang, and L. Dai, *Nanoscale* **3**, 4418 (2011).
16. N. Raza, W. Raza, H. Gul, and K.-H. Kim, *Environ. Res.* **194**, 110499 (2021).
17. H. Sun, S. Liu, G. Zhou, H. M. Ang, M. O. Tadé, and S. Wang, *ACS Appl. Mater. Interfaces* **4**, 5466 (2012).
18. K. Thakur and B. Kandasubramanian, *J. Chem. Eng. Data* **64**, 833 (2019).
19. S. Saxena, T. A. Tyson, S. Shukla, E. Negusse, H. Chen, and J. Bai, *Appl. Phys. Lett.* **99**, 13104 (2011).
20. D. Li, M. B. Müller, S. Gilje, R. B. Kaner, and G. G. Wallace, *Nat. Nanotechnol.* **3**, 101 (2008).
21. W. Liu, J. Cai, and Z. Li, *ACS Sustain. Chem. Eng.* **3**, 277 (2015).
22. B. Liu, X. Liu, J. Liu, C. Feng, Z. Li, C. Li, Y. Gong, L. Pan, S. Xu, and C. Q. Sun, *Appl. Catal. B Environ.* **226**, 234 (2018).

23. H. M. Rietveld, *J. Appl. Crystallogr.* **2**, 65 (1969).
24. H. J. Holland and K. Beck, *J. Appl. Phys.* **39**, 3498 (1968).
25. Q. Meng, C. Jiang, and S. X. Mao, *J. Cryst. Growth* **310**, 4481 (2008).
26. B. B. Wang, M. K. Zhu, H. Wang, G. B. Dong, and H. L. Xie, *Mater. Sci. Semicond. Process.* **15**, 131 (2012).
27. B. B. Wang and X. Z. Xu, *J. Cryst. Growth* **311**, 4759 (2009).
28. Y. L. Chen, Z.-A. Hu, Y. Q. Chang, H. W. Wang, Z. Y. Zhang, Y. Y. Yang, and H. Y. Wu, *J. Phys. Chem. C* **115**, 2563 (2011).
29. S. D. Perera, R. G. Mariano, K. Vu, N. Nour, O. Seitz, Y. Chabal, and K. J. J. Balkus, *ACS Catal.* **2**, 949 (2012).
30. J. Zhang, K. Sun, A. Kumbhar, and J. Fang, *J. Phys. Chem. C* **112**, 5454 (2008).
31. S. Pan and X. Liu, *J. Solid State Chem.* **191**, 51 (2012).
32. C. Xu, X. Wang, and J. Zhu, *J. Phys. Chem. C* **112**, 19841 (2008).
33. Q. Li, B. Guo, J. Yu, J. Ran, B. Zhang, H. Yan, and J. R. Gong, *J. Am. Chem. Soc.* **133**, 10878 (2011).
34. M. Gao, X. Wu, H. Qiu, Q. Zhang, K. Huang, S. Feng, Y. Yang, T. Wang, B. Zhao, and Z. Liu, *RSC Adv.* **8**, 20661 (2018).
35. Z. T. Kang, H. Menkara, B. K. Wagner, C. J. Summers, R. Durst, Y. Diawara, G. Mednikova, and T. Thorson, *J. Lumin.* **117**, 156 (2006).
36. T. Potlog, D. Duca, and M. Dobromir, *Appl. Surf. Sci.* **352**, 33 (2015).
37. M. Amin Baghchesara, M. Cheraghizade, and R. Yousefi, *Mater. Lett.* **162**, 195 (2016).
38. J. Tauc, R. Grigorovici, and A. Vancu, *Phys. Status Solidi* **15**, 627 (1966).
39. S. Rawalekar, S. Kaniyankandy, S. Verma, and H. N. Ghosh, *J. Phys. Chem. C* **115**, 12335 (2011).
40. T. Cheng, D. Li, J. Li, B. Ren, G. Wang, and J. Cheng, *J. Mater. Sci. Mater. Electron.* **26**, 4062 (2015).
41. H. X. Wang, R. Wu, S.-H. Wei, L.-R. Yu, J. K. Jian, J. Hou, J. Wang, H. Y. Zhang, and Y. F. Sun, *Chinese Chem. Lett.* **27**, 1572 (2016).
42. Z. Chen, S. Berciaud, C. Nuckolls, T. F. Heinz, and L. E. Brus, *ACS Nano* **4**, 2964 (2010).
43. S. Kumar, T. Surendar, A. Baruah, and V. Shanker, *J. Mater. Chem. A* **1**, 5333 (2013).
44. B. Wan, C. Hu, B. Feng, J. Xu, Y. Zhang, and Y. Tian, *Mater. Sci. Eng. B* **171**, 11 (2010).
45. P. Madhusudan, J. Zhang, B. Cheng, and G. Liu, *CrystEngComm* **15**, 231 (2013).
46. Q. Yang, X. Guo, W. Wang, Y. Zhang, S. Xu, D. H. Lien, and Z. L. Wang, *ACS Nano* **4**, 6285 (2010).
47. S. Sun, L. Gao, and Y. Liu, *Appl. Phys. Lett.* **96**, (2010).

48. İ. Taşcıoğlu, U. Aydemir, and Ş. Altındal, J. Appl. Phys. **108**, 064506 (2010).
49. I. Ullah, M. Shah, M. Khan, and F. Wahab, J. Electron. Mater. **45**, 1175 (2016).
50. M. Soylu and B. Abay, Phys. E Low-Dimensional Syst. Nanostructures **43**, 534 (2010).
51. K. C. Kao, *Dielectric Phenomena in Solids* (Elsevier, 2004).
52. S. Sil, A. Dey, J. Datta, M. Das, R. Jana, S. Halder, J. Dhar, D. Sanyal, and P. P. Ray, Mater. Res. Bull. **106**, 337 (2018).
53. M. Das, J. Datta, A. Dey, R. Jana, A. Layek, S. Middya, and P. P. Ray, RSC Adv. **5**, 101582 (2015).
54. M. Das, J. Datta, R. Jana, S. Sil, S. Halder, and P. P. Ray, New J. Chem. **41**, 5476 (2017).
55. D. Liu, C. Li, T. Ni, R. Gao, J. Ge, F. Zhang, W. Wu, J. Li, and Q. Zhao, Appl. Surf. Sci. **555**, 149677 (2021).
56. D. Liu, C. Li, J. Ge, C. Zhao, Q. Zhao, F. Zhang, T. Ni, and W. Wu, Appl. Surf. Sci. **579**, 152180 (2022).
57. T. Cheng, H. Gao, G. Liu, Z. Pu, S. Wang, Z. Yi, X. Wu, and H. Yang, Colloids Surfaces A Physicochem. Eng. Asp. **633**, 127918 (2022).
58. S. Khanchandani, S. Kundu, A. Patra, and A. K. Ganguli, J. Phys. Chem. C **117**, 5558 (2013).
59. J. M. Herrmann, Catal. Today **53**, 115 (1999).
60. T. Liu, L. Wang, X. Lu, J. Fan, X. Cai, B. Gao, R. Miao, J. Wang, and Y. Lv, RSC Adv. **7**, 12292 (2017).
61. L. Li, X. Sun, T. Xian, H. Gao, S. Wang, Z. Yi, X. Wu, and H. Yang, Phys. Chem. Chem. Phys. **24**, 8279 (2022).
62. D. K. Padhi and K. Parida, J. Mater. Chem. A **2**, 10300 (2014).
63. L. Huang, F. Peng, H. Yu, and H. Wang, Solid State Sci. **11**, 129 (2009).
64. M. Wang, L. Sun, Z. Lin, J. Cai, K. Xie, and C. Lin, Energy Environ. Sci. **6**, 1211 (2013).
65. H. Wang, Y. Wu, P. Wu, S. Chen, X. Guo, G. Meng, B. Peng, J. Wu, and Z. Liu, Front. Mater. Sci. **11**, 130 (2017).
66. Z. Zhang, S. Zhai, M. Wang, H. Ji, L. He, C. Ye, C. Wang, S. Fang, and H. Zhang, J. Alloys Compd. **659**, 101 (2016).

Investigating Carrier Mobility in Hollow and Mesoporous ZnSe/ZnTe Heterostructures: Microscopic Observations of Swift Charge Transfer and Visible-Light-Driven Dye Decomposition

Chapter 5

➤ The study reported in this chapter has appeared in *J. Photochem. Photobiol., A*, 449 (2024), 115421.

5.1. Introduction

Wastewater released by the textile industry is a major cause of ecological imbalances and environmental concerns. Azo dyes, commonly used in textile production, contain high levels of aromatic rings and strong colours, making them harmful and carcinogenic to both humans and animals [1]. In recent decades, various biological and physio-chemical methods have been adopted to degrade these complex dyes; however, many of these methods are not cost-effective and they often produce hazardous by-products [2]. Among the various Advanced Oxidation Processes (AOPs), photo-induced catalytic decomposition has garnered significant attention from researchers due to its economical and green approach to environmental remediation. Metal oxides and sulphides, including TiO_2 [3], ZnO [4], ZnS [5], CdS [6], ZnSe [7], WO_3 [8] and CeO_2 [9] have been employed to bleach the industrial effluents through photocatalytic decomposition methods. However, these single metal oxides or sulphides suffer from several shortcomings, such as a low surface-to-volume ratio, broad optical bandgaps, and short lifetimes of photo-generated electron-hole pairs that limit the number of excitons produced upon light illumination [10]. Even if the excitons are produced, their rapid recombination hinders an efficient degradation process. For example, ZnO , despite having a higher hydroxyl ion-generating ability, suffers from fast electron-hole pair recombination for catalytic activities [11]; while TiO_2 , despite being an excellent candidate for dye degradation, only responds only in the UV region of electromagnetic radiations due to its wide bandgap ($\sim 4.1\text{eV}$) [12].

It is therefore imperative to design a rational architecture that could overcome the aforementioned limitations of using single metal oxides or chalcogenides. One effective approach we found was to synthesize the graphene-based composites using the single metal chalcogenide (ZnTe), as discussed in the previous chapter. Is there any alternative approach? Yes, the synthesis of micro-sized and hollow heterostructures of two compound semiconductors, such as ZnO/ZnTe [13], ZnS/ZnSe [14], ZnO/ZnS [15], ZnO/ZnSe was identified to be an effective strategy [16]. Since the last few years, several such 3D hierarchical architectures have been synthesized and reported to degrade industrial effluents. In this chapter, we present the synthesis of ZnSe/ZnTe common cation heterostructures via an in-situ hydrothermal route [17], wherein, ZnSe is one of the type II-VI semiconductors having a direct bandgap of $\sim 2.60\text{-}2.65\text{ eV}$ and has been used in various solar energy conversions applications, such as blue-laser diodes, lasers, photodetectors, catalysis, water-splitting, and biomedical sensors [18]. On the other

hand, Zinc telluride (ZnTe) exhibits a direct bandgap in the range of 2.17-2.26 eV and significant potential in diversified areas, including solar cell technology, light-emitting diodes, optoelectronics, CO₂ mitigation, and wastewater treatment [19]. Despite significant research publications existing on the catalytic performances of single metal halides such as ZnSe and ZnTe – they primarily discuss the dependence of macroscopic parameters (particle size, shapes, surface area, or morphology of the catalysts) on the degradation of pollutants. To the best of our knowledge, very few publications [20,21], are concerned about enlightening the role of microscopic parameters such as mobility or transit time (lifetime or travel time) in governing the catalytic degradation. Therefore, a detailed survey of the photo-responsivity and conductivity of the catalysts under solar light-illuminated conditions is warranted to better understand the photocatalytic process. This study is thus aimed to synthesize ZnSe/ZnTe microstructures and investigate their role in the degradation of azo dyes with an emphasis on the morphology and surface area of the hybrid ZnSe/ZnTe catalysts in the first half of the report. In the latter part, we extract the mobility of each catalyst using the spatial-charge-limited conduction (SCLC) theory and comprehensively discuss how the mobility of the charge carriers affects the degradation efficiency of the photocatalysts.

5.2. Experimental Section

5.2.1. Materials

The chemicals used in this study included zinc (Zn) powder (assay $\geq 93\%$), selenium (Se) powder, tellurium (Te) powder (~ 30 mesh, 99.997%), potassium hydroxide (KOH) (analytical grade, $>97\%$), hydrochloric acid (HCl), absolute ethanol, and deionized (DI) water. All the reagents used in the experiments were procured from Sigma-Aldrich, India and utilized without any additional purification.

5.2.2. Synthesis of ZnSe/ZnTe Heterostructures

We synthesized five different catalysts using a one-pot alkaline hydrothermal (OHT) route [20]. The catalysts consisted of bare ZnSe and ZnTe, labelled as ZS and ZT respectively, as well as three ZnSe/ZnTe hybrids (ZST-1, ZST-2, and ZST-3). To synthesize these catalysts, we dispersed 0.1 M Zn powder and varying concentrations of Se and Te powders (as presented in Table 5.1) into 3 M KOH solutions adopting a typical OHT method [22]. After magnetic stirring for 1 h, the resulting solutions were transferred into

a Teflon-lined high-pressure autoclave and subjected to thermal treatment at a constant temperature of 160 °C for 18 h, in an oven with a heat flow rate of 3 °C/min. Upon completion of the thermal treatment, the autoclave was allowed to cool down to room temperature. The precipitates were collected by centrifugation, and subsequent washing steps included rinsing with deionized water, diluted HCl, and absolute ethanol. The photocatalysts were finally dried overnight in a vacuum furnace at 80°C, collected, and subsequently stored for further analysis and characterization.

Table 5.1: Preparation of ZnSe/ZnTe Heterostructures.

Sample Name	Zn (M)	Se (M)	Te (M)	Time and Temperature
ZS	0.1	0.1	0.0	18 h, 160°C
ZST-1	0.1	0.075	0.025	18 h, 160°C
ZST-2	0.1	0.050	0.050	18 h, 160°C
ZST-3	0.1	0.025	0.075	18 h, 160°C
ZT	0.1	0.0	0.1	18 h, 160°C

5.2.3. Fabrication of Schottky Devices

The fabrication of the Schottky diodes was discussed in detail in Chapter 3 (§ 3.2).

5.3. Materials Characterization Techniques

The material characterization techniques employed in the previous chapters (§ 3.3 and § 4.3) have been consistently applied in this chapter. Additional methodologies encompass:

The core level XPS peaks were fitted with the help of the XPS Peakfit41 programme, considering the ‘Shirley’ type background. The absorbance spectra and reflectance spectra of the synthesized materials were studied using a UV-Vis spectrophotometer (Perkin Elmer, Lambda 365). To obtain precise information about the valence band (HOMO) and conduction band (LUMO) position of the individual photocatalyst, electrochemical techniques (Cyclic Voltammetry, AUTOLAB) were employed.

5.4. Results and Discussion

5.4.1. Structural Properties

☞ XRD Analysis

The crystal structures of the as-synthesized heterostructured photocatalysts were thoroughly investigated using X-ray diffraction (XRD) analysis, and the comprehensive results are illustrated in Fig. 5.1(a). The XRD patterns for ZnSe and ZnTe demonstrated an excellent match with the reference diffraction patterns available in the JCPDS database, specifically JCPDS Card No. 37-1463 for ZS and JCPDS Card No. 15-0746 for ZT [22,23]. In the XRD spectrum of ZT, distinctive Bragg reflections were observed at $2\theta \approx 25.26^\circ$, 29.31° , 41.81° , 49.50° , 60.63° , 66.74° , and 76.39° , which correspond to the crystallographic planes (111), (200), (220), (311), (400), (331), and (422), respectively, thereby confirming the cubic phase of ZT, with lattice constant (a) = 6.102 Å [23]. Additionally, two minor peaks at $2\theta \approx 23.15^\circ$ and 27.63° were detected, which can be attributed to the presence of residual Te (100) (JCPDS #65-3358) and (011) planes (JCPDS #65-3370). This residual Te might have precipitated during the hydrothermal treatment at low growth temperatures [24,25]. Conversely, the XRD pattern for ZS exhibited diffraction peaks at $2\theta \approx 27.19^\circ$, 45.21° , 53.56° , 65.91° , and 72.63° , corresponding to the crystallographic planes (111), (220), (311), (400), and (331), respectively. This observation confirms the cubic crystal structure of ZS with lattice constant (a) = 5.668 Å, in agreement with JCPDS Card No. 37-1463 [26]. Similar to ZT, a weak peak at about $2\theta \approx 29.65^\circ$ was also present in the XRD spectrum of ZS, which can be

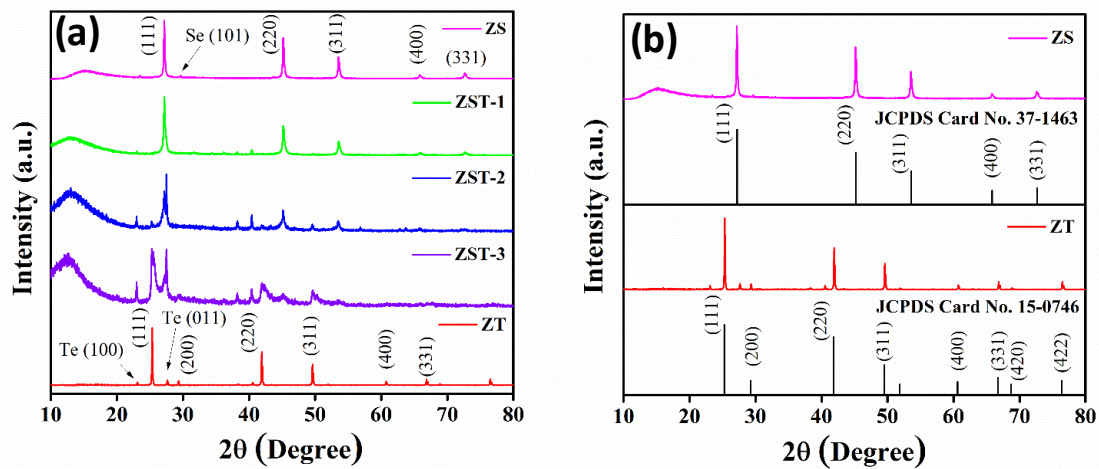


Fig. 5.1: (a) XRD spectra of as-synthesized photocatalysts and (b) peak-to-peak comparison of the ZS and ZT samples with JCPDS cards.

attributed to the Se (101) plane (JCPDS card No. 06-0362), arising from excess Se in the hydrothermal method. Wang et al. have previously demonstrated that these residual peaks can be minimized by increasing the growth time and temperature [26].

Consequently, both synthesized materials, ZS and ZT, exhibit excellent crystallinity, evident from the sharp and characteristic Bragg reflections in their respective XRD patterns. Fig. 5.1(b) showcases the corresponding Bragg reflections and the available diffraction patterns from JCPDS, facilitating a peak-to-peak comparison. On the other hand, the XRD patterns corresponding to the heterostructures (ZST-1 to ZST-3) reveal that the observed peaks can be attributed to either the cubic ZS phase or the ZT phase. Furthermore, the XRD patterns exhibit an intriguing trend: the relative intensity of the (111) peaks of ZnTe increases as we move downward in Fig. 5.1(a), which can be attributed to the incremental Te content during in-situ synthesis (as detailed in Table 5.1), while the intensity of the (111) peak corresponding to ZS predictably decreases. Notably, no additional Bragg reflections were observed, apart from those related to residual Te and Se, confirming the phase purity and successful synthesis through simple variation of the precursor concentrations. This observation provides valuable insights into the composition and structure of the heterostructures, corroborating the successful formation of the ZnSe/ZnTe hybrid photocatalysts.

➤ FESEM and EDX Analysis

The morphological properties of the synthesized catalysts were analyzed using FESEM, and the obtained images are presented below. Fig. 5.2(a) and Fig. 5.2(b) display the ZS microspheres with an average diameter of 1-1.5 micrometres, also revealing their hollow

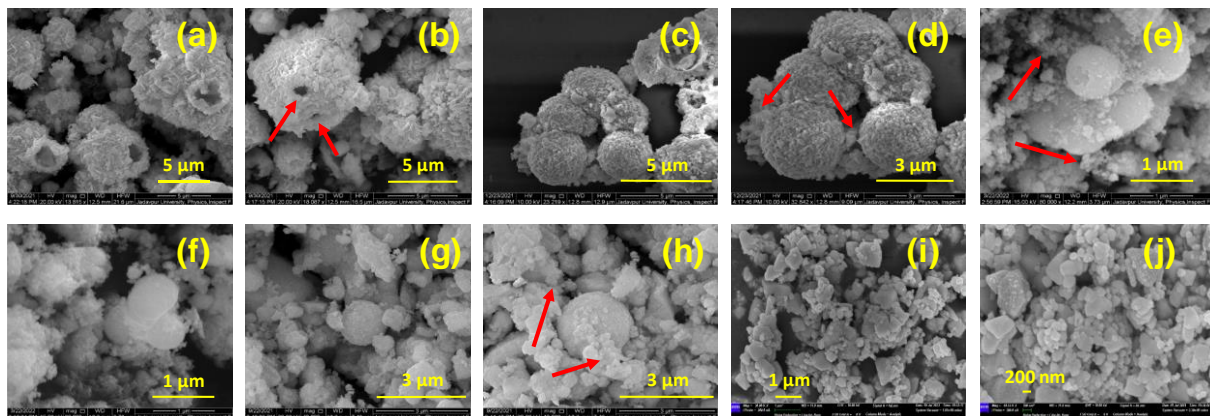


Fig. 5.2: FESEM images of the (a,b) ZS, (c,d) ZST-1, (e,f) ZST-2, (g,h) ZST-3 and (i,j) ZT microstructures.

structure, wherein the holes on the surface of the three-dimensional ZS spheres are evident and indicated using red arrowheads. This unique structure provides a significantly larger surface area for target molecules to be decomposed [27,28]. In Fig. 5.2(c) and Fig. 5.2(d), the morphologies of the hybrid catalyst ZST-1 are presented, and therein, the ZS microspheres are seen to be surrounded by irregular and agglomerated plate-like ZT particles, delineated using red arrows. The next hybrid structure, i.e. the ZST-2 catalysts, as displayed in Fig. 5.2(e) and Fig. 5.2(f), demonstrates a situation wherein the ZS microspheres are significantly screened by ZT particles. This is due to the increased weight % of ZT in ZST-2, approaching $\sim 50\%$, which only was $\sim 25\%$ in the case of ZST-1. Notably, for the ZST-2 catalyst, the BET surface area (discussed later) was found to be the largest one since the unoccupied spaces between the ZS microspheres are now filled with ZT particles – providing a larger surface area that would be advantageous during any catalytic degradation process. Furthermore, when the weight % of ZT was further increased up to 75% for the ZST-3 catalysts shown in Fig. 5.2(g) and Fig. 5.2(h), which leaves the scope of only $\sim 25\%$ ZS incorporation, the microstructures indicate that ZT particles completely occupy the volume - hardly leaving any room for the ZS microspheres. Finally, the last two images [Fig. 5.2(i) and Fig. 5.2(j)] display only irregularly shaped structures, which are identified as plate-like pristine ZT particles.

Furthermore, to address the distribution of the constituent elements (i.e. Zn, Se and Te) in the heterojunction photocatalysts, we performed elemental mapping using

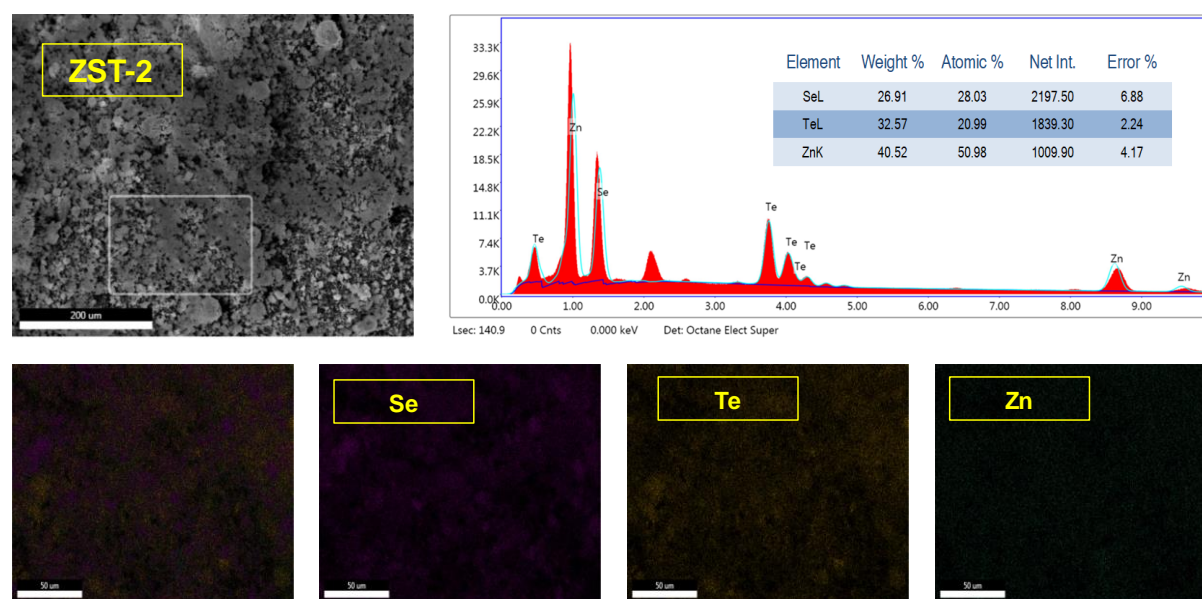


Fig. 5.3: Elemental mapping and EDX spectra of ZST-2 photocatalyst.

Energy Dispersive X-ray Spectroscopy (EDX). The EDX spectra of the catalysts confirmed that the samples maintained their stoichiometric ratio. In particular, we focused on the ZST-2 sample, and its elemental mapping results are displayed in Fig. 5.3; along with the corresponding EDX spectra. The obtained elemental mapping demonstrates the even distribution of Se and Te along with Zn within the ZST-2 heterojunction photocatalyst.

☞ TEM Analysis

TEM images of the ZnSe/ZnTe heterostructures synthesized in this study are depicted in Fig. 5.4 (a-e). Despite the challenges posed by the micrometre-sized catalysts, extensive efforts were made to acquire high-quality TEM images. However, due to the larger size of the particles, the electron beam transparency through the microspheres was limited – resulting in darker regions in the images [23]. Nevertheless, Fig. 5.4(a) showcases a clear image of a ZS microsphere with distinct holes, indicated by red arrowheads, thereby confirming the hollowness of the structures, consistent with the observations from FESEM micrographs. Transitioning to Fig. 5.4(b) and Fig. 5.4(c), they illustrate TEM images of ZST-1 and ZST-2 catalysts, respectively. In Fig. 5.4(b), the presence of a dark circular region with scattered bright patches corresponds to the ZS microspheres. Additionally, the image also reveals the presence of ZT particles (highlighted by red arrowheads) in small quantities surrounding the ZS microspheres, affirming the successful incorporation of ZT with ZS. In Fig. 5.4(c), both ZS microspheres and ZT particles are evident, with an increased proportion of ZT (50%) compared to that in ZST-1 (25%), as detailed in Table 5.1. Moving forward, Fig. 5.4(d) displays the TEM micrograph of the ZST-3 catalyst, demonstrating the ZT particles predominantly covering the ZS microspheres, attributed to the higher ZT weight percentage in ZST-3 (~75%), as presented in Table 5.1. Lastly, Fig. 5.4(e) solely displays the plate-like ZT particles, with some appearing to have agglomerated in certain regions, possibly due to challenges during sample preparation.

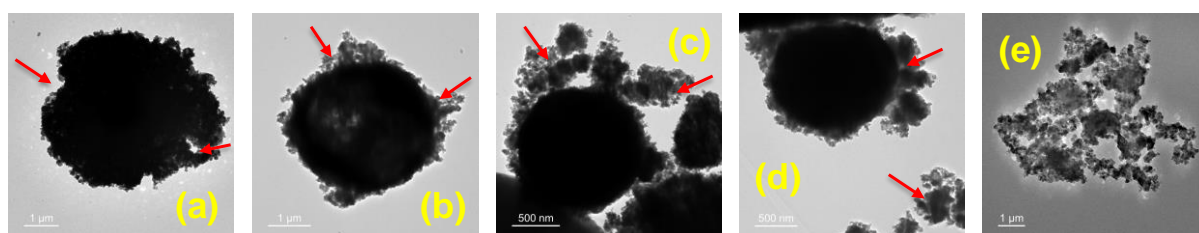


Fig. 5.4: TEM images of the (a) ZS, (b) ZST-1, (c) ZST-2, (d) ZST-3 and (e) ZT microstructures.

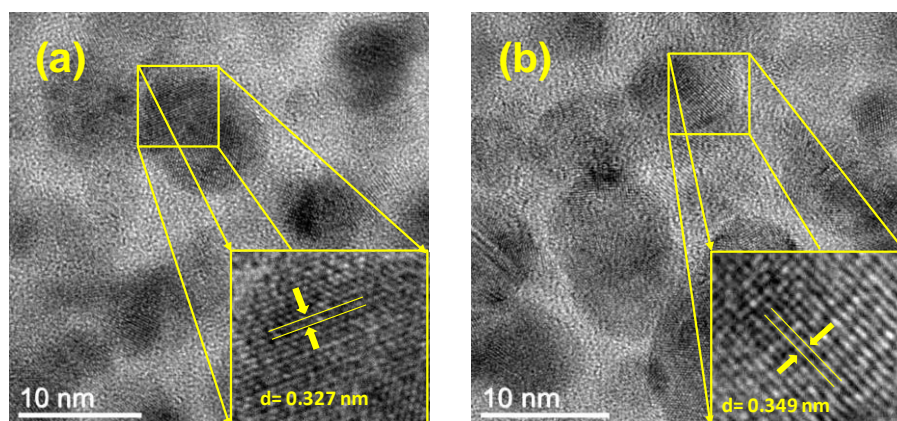


Fig. 5.5: High-resolution TEM images of (a) ZS and (b) ZT photocatalyst.

Despite this, all TEM images consistently reveal the microstructures of the heterojunction photocatalysts, further reinforcing the congruence with the SEM micrographs presented earlier. In addition, the interplanar distance (d-spacing) of the ZS and ZT specimen was estimated from the High-resolution TEM images (Fig. 5.5) and they were found to be 0.327 nm and 0.349 nm for ZS and ZT, respectively – assigned to the (111) planes for both the samples.

➤ XPS Studies

X-ray Photoelectron Spectroscopy (XPS) was employed to investigate the elemental composition, the chemical and the electronic states of the as-synthesized microstructure. The survey spectrum of the ZST-2 photocatalyst, depicted in Fig. 5.6(a), covers an energy range of 0-1200 eV, confirming the presence of Zn, Te, and Se in the heterostructure. Fig. 5.6(b) presents the high-resolution XPS spectrum of the Zn-2p core level, revealing two spin-orbit doublet peaks ($2p_{1/2}$ and $2p_{3/2}$) centred at 1044.41 eV and 1021.34 eV, respectively, with a significant splitting (Δ) of 23.07 eV. This spin-orbit separation aligns with established literature, indicating the 2^+ oxidation state of Zn within the ZST-2 heterostructure [29]. Furthermore, satellite peak appeared in the Zn 2p spectrum within the binding energy range of 1040-1025 eV, with their central position at ~ 1037 eV; which could be attributed to various physical processes, such as shake-up excitations, Auger electron energy decay, or other interactions taking place within the spatial environment during the photoemission process [30,31]. Similarly, Fig. 5.6(c) illustrates the deconvoluted spin-orbit doublet of Te 3d ($j = 3/2, 5/2$), centred at binding energies

of 582.74 eV (Te 3d_{3/2}) and 572.34 eV (Te 3d_{5/2}), with an energy separation of 10.39 eV, elucidating the 2⁺ oxidation state of Te in ZnTe [29,32].

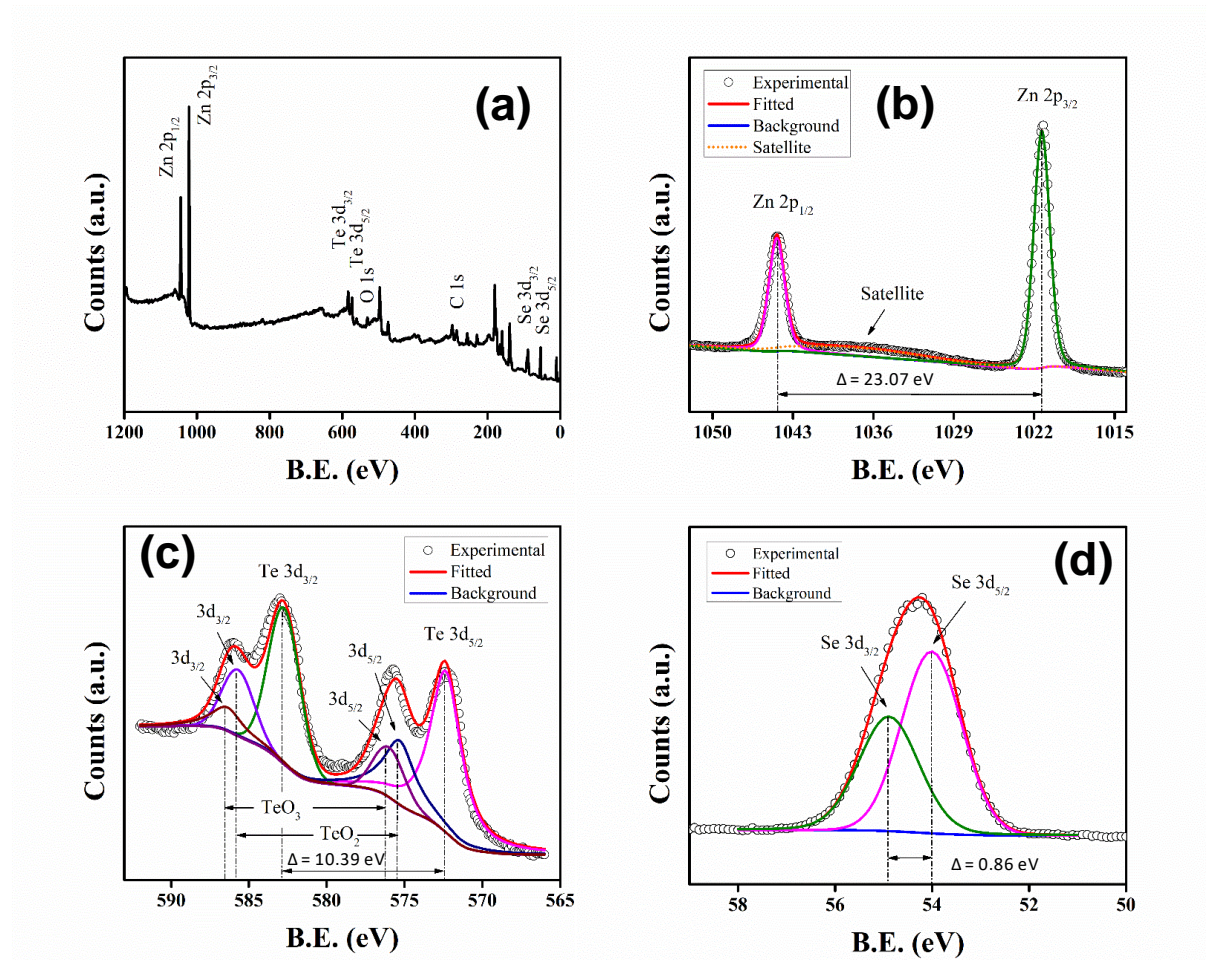


Fig. 5.6: (a) XPS full scan spectrum of ZST-2 photocatalyst. Narrow scan XPS spectrum of (b) Zn 2p, (c) Te 3d and (d) Se 3d.

Furthermore, the deconvolution of these peaks resulted in two sub-peaks for each doublet. The pair of peaks at 585.69 eV ($j=3/2$) and 575.30 ($j=5/2$) eV, with a peak separation of 10.39 eV, is consistent with existing literature [29], affirming the presence of the TeO₂ phase in the sample. Meanwhile, the pair of peaks at 586.38 eV ($j=3/2$) and 575.99 ($j=5/2$) eV, featuring a spin-orbit splitting of 10.39 eV, are attributed to the presence of the TeO₃ phase. These partially surface oxidized phases (TeO₂ and TeO₃) may form in very trace amounts during the hydrothermal process or sample preparation, but no compelling evidence of their presence was detected using other characterization techniques. It has been suggested that increasing the growth temperature might mitigate the observed oxidation states of Te [32]. Lastly, Fig. 5.6(d) showcases the narrow scan of

the Se 3d core level, deconvoluted into two doublets due to spin-orbit coupling ($j = 3/2, 5/2$) with a splitting of 0.86 eV, occurring at binding energies of 54.86 and 54 eV, respectively. These findings are in accord with the reported literature, affirming the 2⁺ oxidation state of Se in ZnSe [29,33]. Thus, the XPS analysis affirms the chemical purity of the sample, while the electronic states of the elements validate the formation of a ZST-2 heterostructure. Furthermore, the XPS analysis provides insight into the surface chemical states of Zn, Te, and Se, which together constitute our heterostructure photocatalyst, that could serve as an electron capture and transfer medium during the photocatalytic degradation process, which will be discussed in the following section.

5.4.2. Optical Properties

☞ UV-visible Spectroscopy

The optical properties of the as-synthesized catalysts were investigated through UV-visible absorbance and reflectance spectra, covering a wavelength range of 300-900 nm. The absorbance spectra of all samples are presented in Fig. 5.7(a). To establish the energy diagrams of the ZnSe/ZnTe heterostructures, we obtained the optical band gaps of the ZS and ZT catalysts using the reflectance spectra, by employing the Kubelka-Munk function [34]. For band gap estimation, we plotted the values of $\{F(R) hv\}^2$ against the $h\nu$ axis, where $F(R) = k/S$ represents the Kubelka-Munk function, with $k = (1-R)^2$, denoting the molar absorption coefficient and $S = 2R$ as the scattering factor, where R is the reflectance. Additionally, h represents Planck's constant, and ν corresponds to the frequency of the radiation.

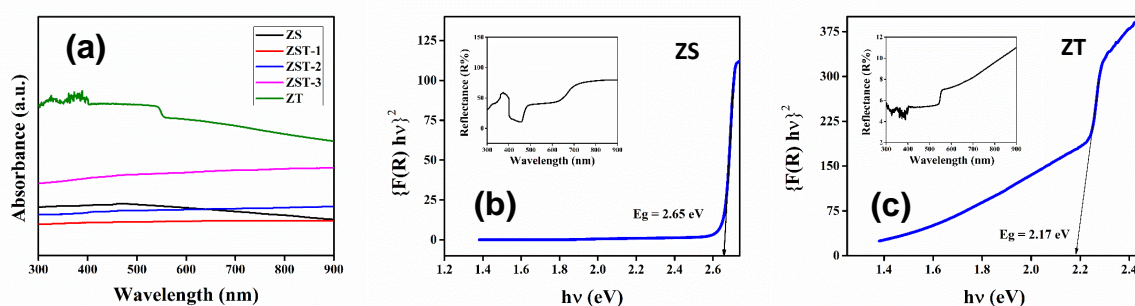


Fig. 5.7: (a) Absorbance spectra of all the catalysts. Kubelka-Munk plot and the corresponding UV-vis reflectance spectrum (inset) of (b) ZS and (c) ZT catalysts.

The corresponding reflectance spectra of ZS and ZT catalysts are displayed in the inset of Fig. 7(b) and Fig. 7(c), respectively. The ZS catalysts exhibited significant light

reflectance at around 487 nm, indicating a direct bandgap energy of 2.65 eV [Fig. 5.7(b)], while the ZT catalyst displayed a strong reflection edge at approximately 559 nm, corresponding to a direct bandgap value of 2.17 eV [Fig. 5.7(c)]. These measured bandgap values are in close agreement with previously reported data [14,20].

5.4.3. Cyclic Voltammetry and Alignment of Energy Levels

Cyclic Voltammetry (CV) was employed to determine the electrochemical properties of the ZS and ZT samples, specifically the positions of their valence band (V.B.) and conduction band (C.B.). The electrical bandgap (ΔE) was calculated as the difference between the energy levels of the valence band (E_{VB}) and the conduction band (E_{CB}), providing the electronic properties of the materials. Typically, the valence band level (E_{VB}) of a solid material correlates with its oxidation potential (E_{ox}), while the conduction band level (E_{CB}) corresponds to its reduction potential (E_{red}), as expressed by the following equations [35]:

$$E_{VB} = -(E_{ox} + 4.14) \text{ eV} \quad (5.1)$$

$$E_{CB} = -(E_{red} + 4.14) \text{ eV} \quad (5.2)$$

$$\Delta E = E_{CB} - E_{VB} \quad (5.3)$$

The cyclic voltammetry curves of the samples were obtained in anhydrous dimethylformamide (DMF) medium, employing glassy carbon, Ag/AgCl, and platinum electrodes as the working electrode, reference electrode, and counter electrode, respectively. Tetrabutylammonium perchlorate (TBAP) served as the electrolyte, and a scan rate of 0.1 V/s was applied. The oxidation onset of ZS and ZT was observed at 1.52 V and 0.82 V, respectively (Fig. 5.8). These values corresponded to valence band levels of 5.66 eV for ZS and 4.96 eV for ZT. Additionally, the conduction band levels of ZS and ZT were estimated at 3.06 eV and 2.72 eV, respectively, calculated from their reduction onset at -1.08 V and -1.42 V, respectively. Consequently, the bandgap values for ZS and ZT were determined using the above equations, resulting in bandgap values of 2.60 eV for ZS and 2.24 eV for ZT.

The activity and selectivity of a heterostructured photocatalyst for the decomposition of a dye strongly depend on the alignment of its energy levels. To illustrate this alignment, we constructed an energy diagram for the hybrid photocatalyst using the HOMO (valence band) and LUMO (conduction band) positions of individual materials.

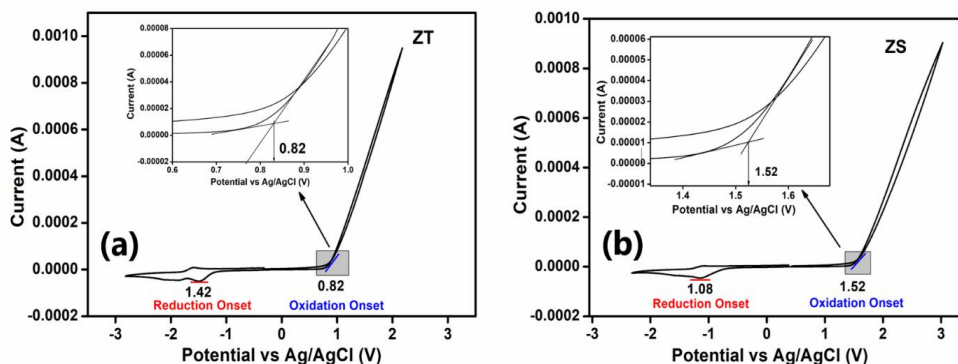


Fig. 5.8: Cyclic-voltammetry of (a) ZnTe and (b) ZnSe.

Electrochemical techniques, specifically Cyclic Voltammetry (CV), were employed to obtain the band positions of the individual materials, which are presented in Fig. 5.8. The valence band and conduction band positions of ZnTe were determined to be 0.52 V and -1.72 V (vs. SHE), respectively [36], while for ZnSe, the valence band position was deduced as 1.22 V (vs. SHE) and the conduction band position as -1.38 V (vs. SHE) [37]. Using these values, we generated a band diagram for the ZnSe/ZnTe hybrid heterostructures, both against the Standard Hydrogen Electrode (SHE) and against the Vacuum level. The resulting band diagram, depicted in Fig. 5.16, enables us to gain insight into and predict the photocatalytic behaviour of the hybrid system. This comprehensive understanding of charge transfer processes is instrumental in optimizing the photocatalytic efficiency for dye decomposition applications.

5.4.4. Surface Area (BET) Analysis

The N_2 adsorption-desorption isotherms, as shown in Fig. 5.9, were obtained at a temperature of 77 K to estimate the Brunauer-Emmett-Teller (BET) specific surface areas for all the synthesized photocatalysts. The measured surface areas of the catalysts are listed in Table 5.2 and it was observed that the ZST-2 hybrid microstructures possess the largest surface area among all five catalysts, which also is in excellent agreement with the FESEM observations (Fig. 5.2). In contrast, ZST-1 and ZST-3 possess the almost comparable value of the surface area, which could be attributed to the 'shielding effect' of the ZS microspheres by the ZT particles. Furthermore, the bare and hollow ZS microspheres showed a slightly higher surface area than the pristine ZT catalysts, despite the plate-like morphology being observed in ZT [Fig 3(i) and 3(j)]. This result could be due to the agglomeration of the ZT particles and the formation of 'clusters' in the process

[15]. In photocatalytic processes, it is generally preferred to have a larger surface area since it also leads to a higher absorbance cross-section, resulting in increased photo absorption and greater diffusion of molecules, ultimately leading to improved performance. Therefore, Table 5.2 indicates that the ZST-2 heterostructures are expected to be superior compared to the other heterostructures, which is now demonstrated in the following.

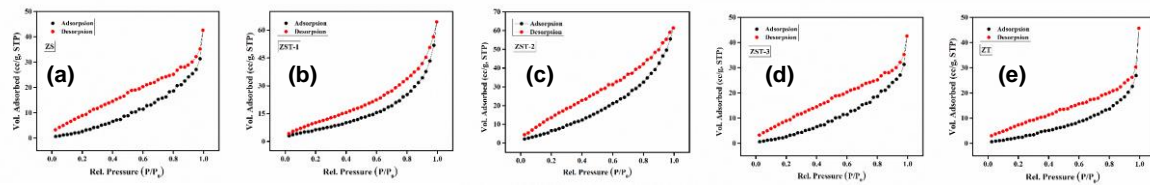


Fig. 5.9: N_2 adsorption-desorption isotherms for (a) ZS, (b) ZST-1, (c) ZST-2, (d) ZST-3 and (e) ZT catalysts.

5.4.5. Electrical Study

To investigate the electronic charge transport properties of the synthesized catalysts, the current-voltage (I-V) characteristics of the fabricated Schottky devices (Al/photocatalyst/ITO, as displayed in Fig. 3.8) were examined by applying a bias voltage of ± 1 V at room temperature under both dark and illuminated conditions (light intensity ~ 1000 W/m²) [38].

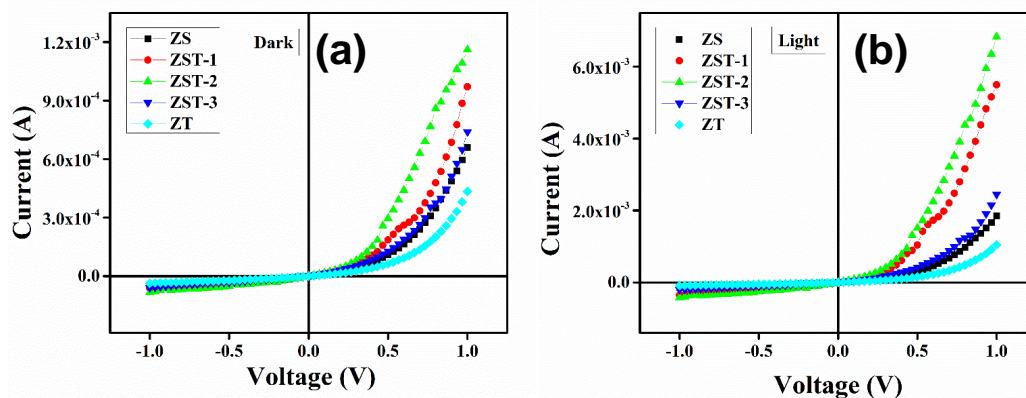


Fig. 5.10: Current-voltage (I-V) characteristic curves for all the photocatalysts-based Schottky diodes under (a) dark and (b) light conditions.

The conductivity of different catalysts, which indicates the flow of charge, was evaluated using the diode characteristic curves (Fig. 5.10). The substantial increase in current density following light irradiation established the photo-responsiveness of the hybrid

materials. Photosensitivity (S_P), being a key parameter of the catalysts to be exposed to solar radiation, must be interpreted before evaluating the photocatalytic activities and it is defined as the ratio of photo-induced current (I_{ph}) to the current under dark conditions (I_d) [39]. The S_P parameter, as discussed in the previous chapter (§ 4.4.5), was determined for all the catalysts synthesised in the present study and displayed in Table 5.2. Among all the hybrid catalysts, the ZST-2 microstructures demonstrated the highest conductivity and photosensitivity. The greater conductivity of the hybrid microstructures implies enhanced charge transfer as well as mobility in this catalyst (ZST-2).

Table 5.2: Surface Area and Photo-Responsive Parameters.

Sample	Surface Area (m^2/g)	Photosensitivity (S_P)	Conductivity (σ) (Sm^{-1})	
Condition	-	-	Dark	Light
ZS	23.05	1.81	3.82×10^{-5}	1.07×10^{-4}
ZST-1	27.37	4.65	6.39×10^{-5}	4.32×10^{-4}
ZST-2	37.92	4.88	1.01×10^{-4}	5.18×10^{-4}
ZST-3	26.43	2.31	4.48×10^{-5}	1.48×10^{-4}
ZT	16.68	1.41	2.23×10^{-5}	5.39×10^{-5}

The carrier mobility is crucial for any semiconducting material because it determines how quickly a carrier, such as an electron or a hole, will move through its complex network of hybrid molecules before arriving at the active sites, wherein they finally recombine. Thus, the I-V characteristics of Fig. 5.10 were further analyzed by interpreting the carriers' mobility (μ_{eff}) and lifetime (τ) based on the spatial-charge-limited conduction (SCLC) mechanism for Schottky diodes [40,41]. The aim was to gain insight into the synergistic effect of ZS and ZT on the charge transport mechanism and photodegradation process and the $\log(I)$ vs. $\log(V)$ variations are plotted in Fig. 5.11(a) and 10b for positive voltages, which showed three distinctly different regions arising out of the interfacial trap that alters the conduction of charge carriers at a metal-semiconductor junction, thereby reforming the I-V characteristic curves. Each of these regions indicates a different conduction process and is explained in Chapter 2 (§ 2.5.2).

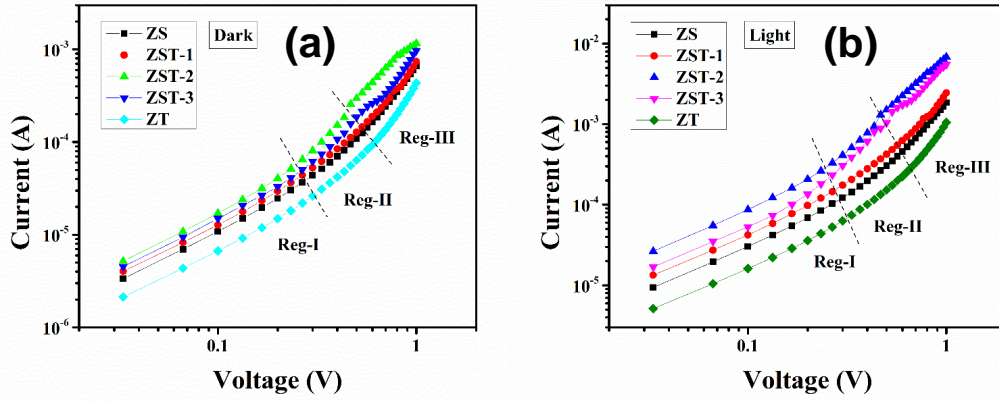


Fig. 5.11: Log (I) vs. log (V) plot for all the photocatalysts-based Schottky diodes under (a) dark and (b) light conditions.

➔ Estimation of the Charge Transport Parameters

The I-V characteristics were further analysed by estimating the effective carrier's mobility (μ_{eff}) and lifetime (τ) from region II [Fig. 5.11(b)] based on the space-charge limited current (SCLC) theory to obtain a better understanding of the charge transport mechanism. The dielectric constant of the synthesized materials (ϵ_r), the mobility (μ_{eff}), and the lifetime or transient time (τ) of the charge carriers were determined employing the following equations:

$$\epsilon_r = \frac{C_0 d}{\epsilon_0 A_{\text{eff}}} \quad (5.4)$$

$$I = \frac{9\mu_{\text{eff}}\epsilon_0\epsilon_r A_{\text{eff}}}{8} \left(\frac{V^2}{d^3} \right) \quad (5.5)$$

$$\tau = \frac{9\epsilon_0\epsilon_r A_{\text{eff}}}{8d} \left(\frac{V}{I} \right) \quad (5.6)$$

A detailed discussion of all the symbols used in the above equations was provided in Chapter 2 (§ 2.5.2). Also, The capacitance (C) vs. frequency (f) plot for all the synthesized photocatalysts is displayed in Fig. 5.12 below.

The estimated values of μ_{eff} and τ are listed in Table 5.3. The higher mobility of the ZnSe/ZnTe heterostructures and its significant contribution towards the efficient conduction of charge carriers were shown in our results. Among all the produced catalysts, the ZST-2 catalyst demonstrated the highest carrier mobility and the shortest transit time. The mobility of the carriers was improved nearly 5-6 times for both dark

and irradiated environments. This improvement in lifetime and mobility is particularly advantageous for the effective transfer of the charge carriers and therefore an enhancement in the photocatalytic activity is expected, which is discussed below in detail.

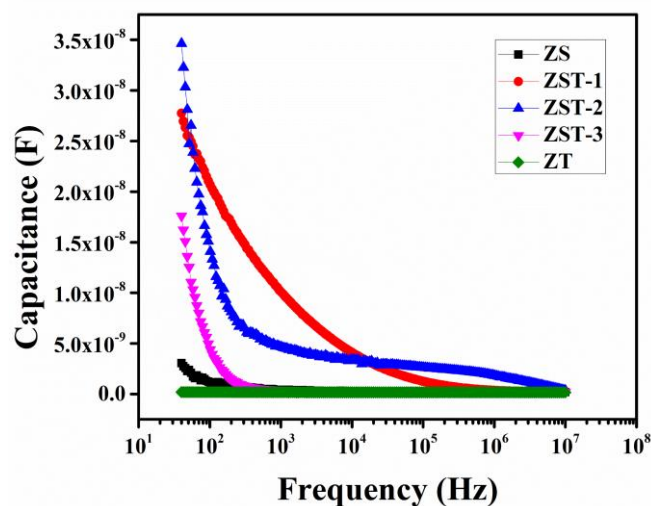


Fig. 5.12: Capacitance (C) vs. frequency (f) plot for the synthesized photocatalysts.

Table 5.3: Charge Transport Parameters.

Sample	Mobility (μ_{eff})		Lifetime (τ)	
	(m ² V ⁻¹ s ⁻¹)		(s)	
Condition	Dark	Light	Dark	Light
ZS	1.80×10^{-6}	5.05×10^{-6}	6.92×10^{-7}	2.46×10^{-7}
ZST-1	2.69×10^{-6}	1.63×10^{-5}	4.65×10^{-7}	7.63×10^{-8}
ZST-2	3.36×10^{-6}	1.70×10^{-5}	3.72×10^{-7}	7.35×10^{-8}
ZST-3	2.00×10^{-6}	6.64×10^{-6}	6.22×10^{-7}	1.87×10^{-7}
ZT	1.18×10^{-6}	2.82×10^{-6}	1.05×10^{-6}	4.37×10^{-7}

5.4.6. Photocatalytic Activity

☞ Photo-degradation Process

The photo-degradation process was discussed in detail in the previous chapter (§ 4.4.6).

➤ Photo-degradation Behaviour and Performances

The photocatalytic behaviour of synthesized catalysts was studied by investigating the decomposition of RhB aqueous solution under simulated solar light irradiation. The degradation process was monitored by measuring the absorption peak of the RhB solution at 554 nm using a UV-Vis spectrometer, as displayed in Fig. 5.13 and Fig. 5.14(a). The degradation process of RhB solution by all the synthesized catalysts was analyzed using Eq. (5.7):

$$\text{Degradation} = \left(\frac{C_0 - C_t}{C_0} \times 100 \right) \% \quad (5.7)$$

where, C_0 and C_t represent the RhB concentration at zero and 't' time, respectively [45].

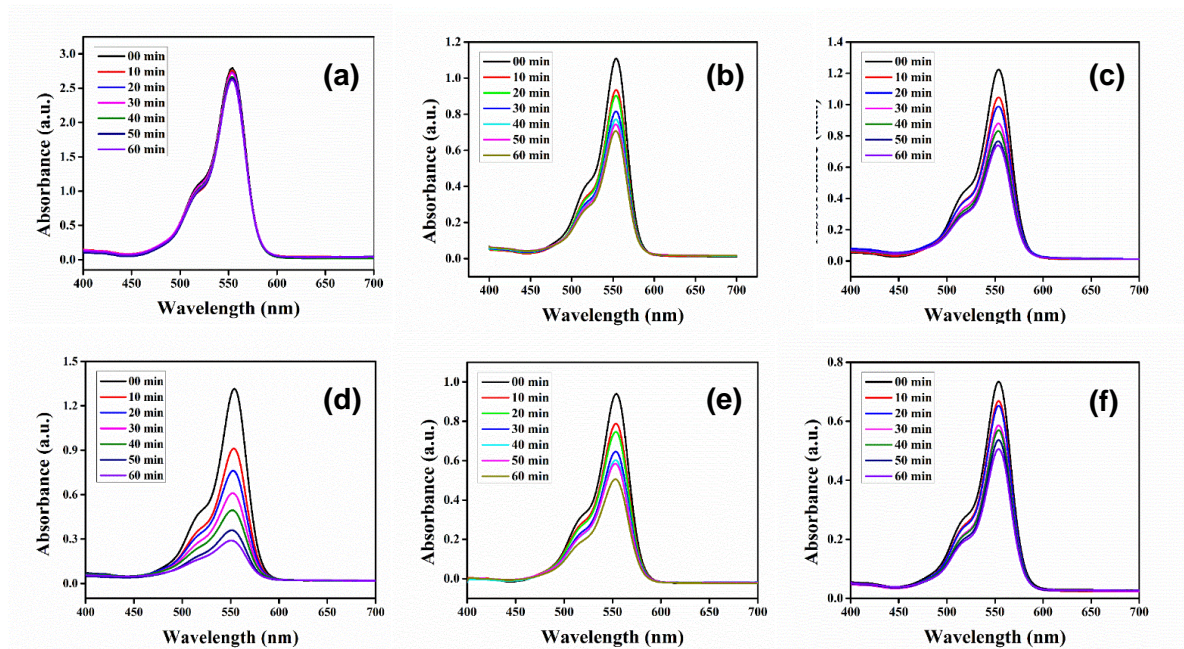


Fig. 5.13: Absorption spectra of RhB aqueous solution at different time intervals in the presence of (a) no catalyst, (b) ZS, (c) ZST-1, (d) ZST-2, (e) ZST-3 and (f) ZT catalyst.

Before initiating the photocatalytic degradation process, we conducted the adsorption test of RhB in dark conditions for 30 minutes. However, the adsorption experiment showed minimal impact on RhB removal, with less than 1% effect, as displayed in Fig. 5.14(a) as well as in Fig. 5.14(b). For a 60-minute irradiation time, no significant change in RhB concentration was noted for catalyst-free suspensions. However, the addition of the catalysts gradually bleached the RhB solution, and the degradation efficiency is shown in Fig. 5.14(b). The plot of $\ln(C_0/C)$ vs. irradiation time

(min) in Fig. 5.14(c) demonstrates the existence of pseudo-first-order degradation kinetics [21]. Among all five catalysts, ZST-2 exhibited the highest efficiency of degradation (78%), which could be accredited to the higher mobility of the charge carriers in the hybrid ZnSe/ZnTe structure. As discussed in the previous section, the high mobile charges attain an extra path length before any recombination and thus, a large volume of charges can reach the active sites and trigger the degradation process. Table 5.3 shows that the mobility of ZST-2 heterostructures was the highest among the five catalysts, while the transit time was the lowest. These values adequately demonstrate how the microscopic parameters, i.e. mobility and transit time influence the macroscopic performance in catalytic activity. The sustainability of the catalysts was also probed by recycling tests, with all the recycling bar diagrams for different catalysts displayed in Fig. 5.14(d) and Fig. 5.15, indicating that the catalytic performance of ZST-2 remains largely unchanged even after repeated use for up to three cycles.

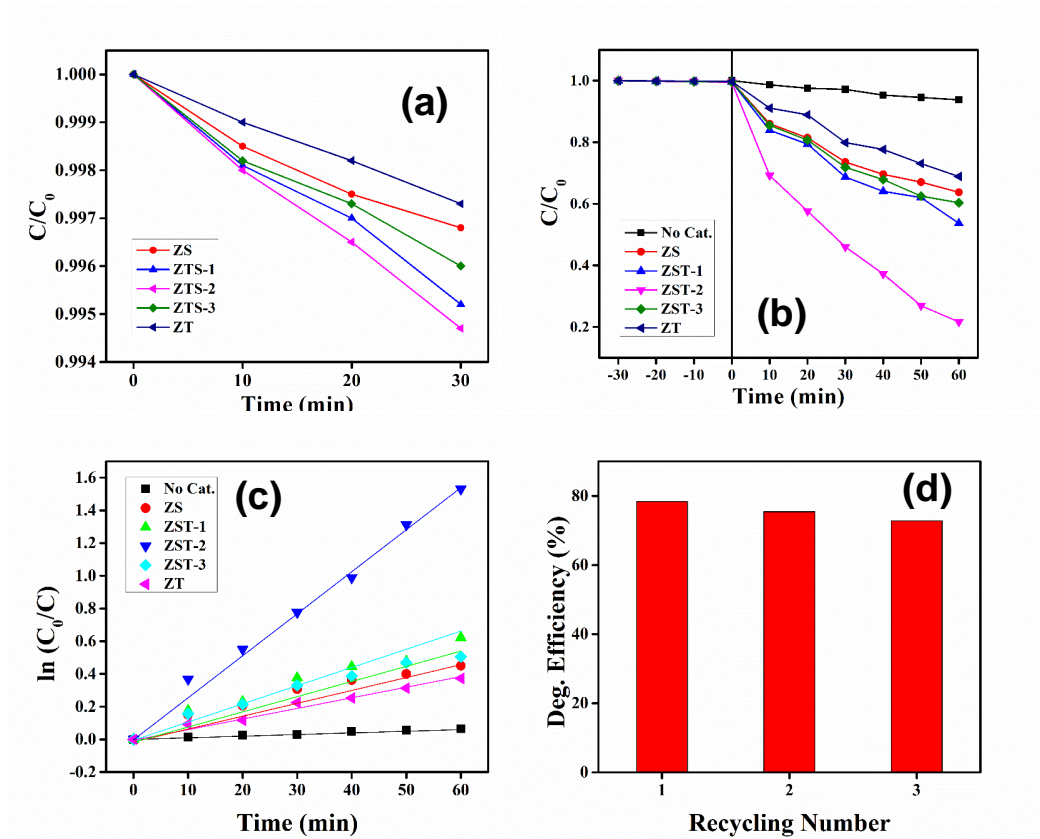


Fig. 5.14: (a) Adsorption tests, (b) Photocatalytic degradation behaviour and (c) $\ln(C_0/C)$ vs. time (t) plot for RhB solution at different time intervals in the presence of (i) no catalyst, (ii) ZS, (iii) ZST-1, (iv) ZST-2, (v) ZST-3 and (vi) ZT catalyst. Recycling test of the ZST-2 catalyst for RhB degradation.

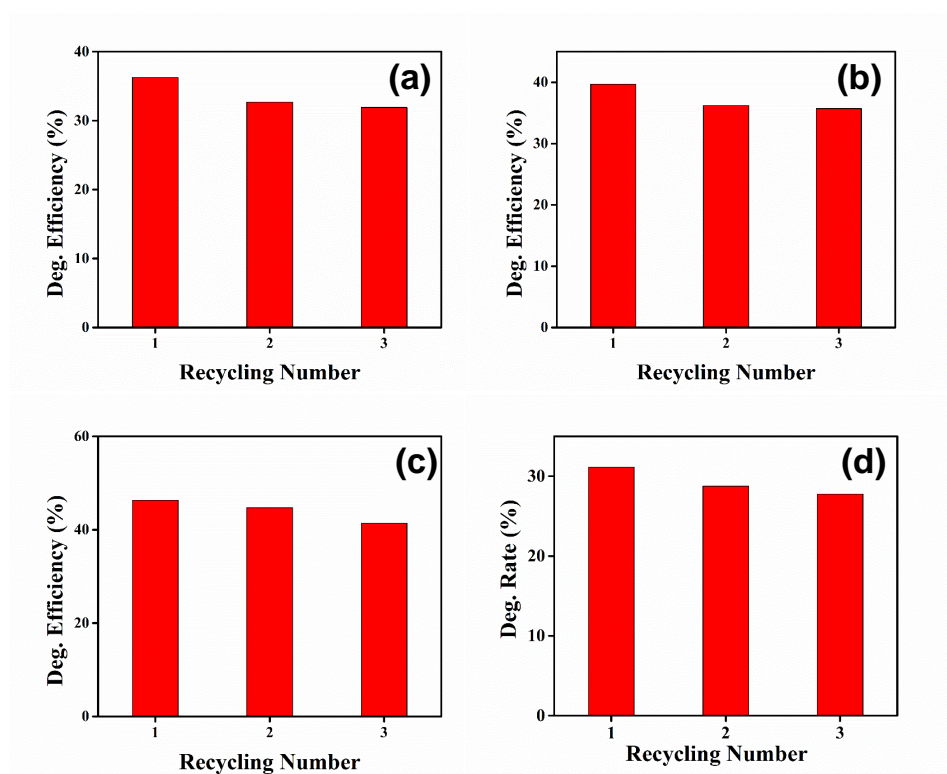


Fig. 5.15: Recycling test of the (a) ZS, (b) ZST-1, (c) ZST-3 and (d) ZT catalyst for RhB degradation.

☞ *Photo-degradation Mechanism*

In examining the synergistic effect and interaction between ZS and ZT in composite materials, we conducted a thorough analysis of the photocatalytic decomposition process. Upon light irradiation, the interfacial excitons are produced at the surface of ZT nanoparticles, and subsequently free electrons and holes are produced in the conduction and valence bands, respectively. Further, owing to the low mobility of these photogenerated electrons (e^-) and holes (h^+), they often recombine before reaching the active sites, thereby impeding the photocatalytic activity. However, the addition of ZS to ZT could facilitate the efficient separation of photoinduced electrons in the conduction bands due to their preferable energy levels [37,46], and it leaves behind a hole (h^+) in the valence band of ZT. Consequently, the photogenerated electrons from ZT could efficiently reach the active sites through the ZS platform and reduce dissolved O_2 in the aqueous medium, generating the highly reactive superoxide radical anion ($O_2^{\bullet-}$). The generation of this intermediate is thermodynamically feasible since the reduction potential of the superoxide radical ($E^0, O_2/O_2^{\bullet-} = -0.33$ V vs. SHE) is less negative than the conduction band edge of ZT ($E_{CB} = -1.72$ V, vs. SHE) [47]. This highly reactive $O_2^{\bullet-}$ is expected to play

a pivotal role in RhB degradation [45,48]. Meanwhile, the h^+ in the valence band is also a strong agent that could oxidize the pollutants through direct electron transfer and execute the degradation process. Thus, the superoxide radical anion ($O_2^{\bullet-}$) and the holes (h^+) could cooperatively participate in the decomposition process of the RhB solution [49–51]. Fig. 5.16 presents a plausible mechanism for the photocatalytic degradation process of RhB using the ZST-2 catalyst under irradiation by solar light.

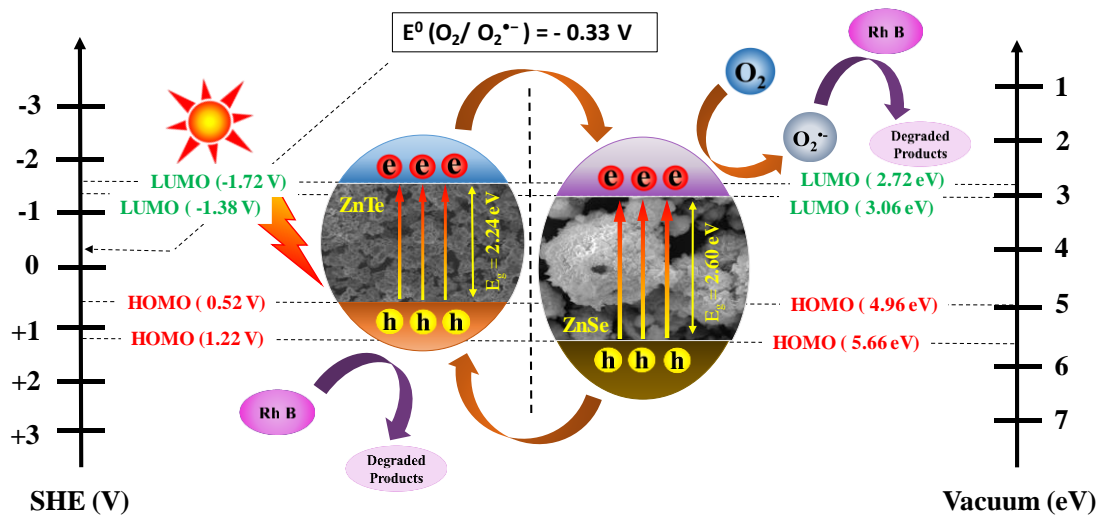


Fig. 5.16: Alignment of the energy levels and the plausible mechanism of the photocatalytic degradation of RhB by ZST-2 catalyst under solar light irradiation.

➤ Influence of the Surface Species on the Photocatalytic Performance

It is noteworthy that the XPS technique, as discussed earlier, detected trace amounts of Te oxides on the surface of ZnSe/ZnTe, which can influence the photocatalytic degradation process. The presence of Te oxides can lead to the recombination of charge carriers (electron/hole) at the surface, resulting in a fractional decrease in the degradation performance. In other words, the observed photocatalytic performance of ZnSe/ZnTe includes a contribution from Te oxides, as they participate alongside ZnSe/ZnTe in the degradation of RhB. While quantitative analysis proves challenging in this scenario, qualitative insights can still be gained. A relevant study in the literature reports a transient photocurrent density of approximately 0.2 mA/cm^2 for TeO_2 , nearly 100 times smaller than the photocurrent intensity observed in our ZnSe/ZnTe heterojunction photocatalysts ($\sim 16.43\text{ mA/cm}^2$ in the dark and 96.74 mA/cm^2 in the light) [52]. Notably, photocurrent intensity serves as a measure of the carrier's mobility,

a critical factor governing charge conduction in the photocatalytic degradation process. Thus, considering the charge mobility, the separation of electron-hole pairs due to the Te oxides is anticipated to be significantly limited, resulting in a substantial portion of the electron-hole pairs reaching the surface and subsequently recombining. This indicates that Te oxides do impact the photo-induced degradation of RhB, but their influence is much smaller compared to the ZnSe/ZnTe heterostructure. Essentially, the species present on the surface of the photocatalyst actively participate and influence the photocatalytic performance.

➤ *Comparison of the Present Study with Reported Literature*

In addition, to explore the potential application of the synthesized heterostructured photocatalyst, its performance was evaluated based on several factors, including dosage, reaction time, and degradation efficiency, in comparison to other catalysts, as summarized in Table 5.4. Remarkably, our photocatalyst exhibited the highest performance, achieving an impressive degradation efficiency of approximately 78% - surpassing all other cases listed in Table 5.4. This outstanding result can be accredited to the synergistic effects of various crucial attributes, such as particle size, shape, surface area, and mobility, which render ZST-2 an exceptionally attractive photocatalytic material for the efficient degradation of dye pollutants, addressing environmental concerns.

Table 5.4: *Comparison of the Present Study with Reported Literature.*

Sl. No.	Photo-catalyst	Photo-catalyst dosage (mg)	Light source	Pollutant (RhB) Concentration	Time (min)	Degradation efficiency (%)	Reference
1.	Graphitic g-C ₃ N ₄	50	Visible light (300W Xenon lamp)	1×10^{-5} mol/L	30	67	[53]
2.	Zn doped CoFe ₂ O ₄	0.31	Visible light (150W Halide lamp)	-	180	77.2	[54]
3.	BiOI	50	Visible light	-	240	71	[55]

4.	Ag/AgBr /ZnO composit es	100	Visible light (300W iodine tungsten lamp)	5 mg/L	60	~ 61	[56]
5.	Graphitic g- C ₃ N ₄ /Bi ₂ O ₂ CO ₃	50	Visible light (1000W Xenon lamp)	1×10^{-5} mol/L	240	45	[57]
6.	ZnO- graphene -TiO ₂ composit e	0.1	Visible light (8 W lamp, λ > 420 nm)	1×10^{-5} mol/L	60	~ 59	[58]
7.	Core- shell TiO ₂ @g- C ₃ N ₄ composit es	40	Visible light (300W Xe arc lamp)	1×10^{-5} M	60	~ 65	[59]
8.	ZnSe/Zn Te microsph ere	30	Visible light (Solar simulator, Abet Technologies , Model 10500)	0.1 mg/ml	60	78	Prese nt study

5.5. Conclusion

Our investigation involved the synthesis of five distinct catalysts via a one-pot hydrothermal method, evaluating their performance in the visible-light-driven degradation of RhB. We observed that the catalytic efficiency of the dye was significantly impacted by both macroscopic and microscopic parameters. Specifically, macroscopic factors, such as the hollowness of the ZS spheres and the plate-like nature of the ZT particles, along with their integrated surface area, played a crucial role. Moreover, microscopic parameters, such as the mobility and transit time of the charge carriers, were

also found to be critical in determining catalytic activity. Our study revealed that the ZST-2 catalyst, comprising 50% ZnSe and 50% ZnTe, demonstrated the highest catalytic activity owing to its larger surface area and enhanced mobility of charge carriers. This improved mobility, coupled with the synergistic effect of ZnSe and ZnTe in the ZST-2 heterostructure, effectively addressed the limitation of having short lifetimes of photo-generated electron-hole pairs observed in the single materials. Thus, our study not only underscores the interdependence between microscopic and macroscopic parameters but also offers valuable insights into the design and optimization of common cation-based photocatalysts, with potential applications in environmental remediation and energy conversion.

References

1. R. Al-Tohamy, S. S. Ali, F. Li, K. M. Okasha, Y. A. G. Mahmoud, T. Elsamahy, H. Jiao, Y. Fu, and J. Sun, *Ecotoxicol. Environ. Saf.* **231**, 113160 (2022).
2. V. Selvaraj, T. Swarna Karthika, C. Mansiya, and M. Alagar, *J. Mol. Struct.* **1224**, 129195 (2021).
3. D. A. Panayotov, A. I. Frenkel, and J. R. Morris, *ACS Energy Lett.* **2**, 1223 (2017).
4. Z. Mirzaeifard, Z. Shariatinia, M. Jourshabani, and S. M. Rezaei Darvishi, *Ind. Eng. Chem. Res.* **59**, 15894 (2020).
5. Z. Ye, L. Kong, F. Chen, Z. Chen, Y. Lin, and C. Liu, *Optik (Stuttg.)*. **164**, 345 (2018).
6. Y. Chen, W. Zhong, F. Chen, P. Wang, J. Fan, and H. Yu, *J. Mater. Sci. Technol.* **121**, 19 (2022).
7. A. Chauhan, A. Sudhaik, P. Raizada, A. A. P. Khan, A. Singh, Q. Van Le, V.-H. Nguyen, T. Ahamad, S. Thakur, P. Singh, and A. M. Asiri, *Process Saf. Environ. Prot.* **170**, 415 (2023).
8. P. Shandilya, S. Sambyal, R. Sharma, P. Mandyal, and B. Fang, *J. Hazard. Mater.* **428**, 128218 (2022).
9. A. A. Fauzi, A. A. Jalil, N. S. Hassan, F. F. A. Aziz, M. S. Azami, I. Hussain, R. Saravanan, and D. V. N. Vo, *Chemosphere* **286**, 131651 (2022).
10. Z. Zhang, W. Wang, L. Wang, and S. Sun, *ACS Appl. Mater. Interfaces* **4**, 593 (2012).
11. G. Meenakshi and A. Sivasamy, *Colloids Surfaces A Physicochem. Eng. Asp.* **645**, 128920 (2022).
12. U. G. Akpan and B. H. Hameed, *J. Hazard. Mater.* **170**, 520 (2009).
13. N. Raza, W. Raza, H. Gul, and K. H. Kim, *Environ. Res.* **194**, 110499 (2021).
14. Y. Feng, M. Xu, P. L. Tremblay, and T. Zhang, *Int. J. Hydrogen Energy* **46**, 21901 (2021).
15. S. Khan, V. Poliukhova, N. Tamir, J. Park, N. Suzuki, C. Terashima, K. I. Katsumata, and S.-H. Cho, *Int. J. Hydrogen Energy* **48**, 9713 (2023).
16. N. Al Abass, T. F. Qahtan, M. A. Gondal, R. A. Moqbel, and A. Bubshait, *Int. J. Hydrogen Energy* **45**, 22938 (2020).
17. X. Liu, D. Li, W. Yang, S. Tang, X. Li, L. Fan, and Y. Li, *J. Mater. Sci.* **51**, 11021 (2016).
18. Q. Zhang, H. Li, Y. Ma, and T. Zhai, *Prog. Mater. Sci.* **83**, 472 (2016).
19. O. I. Olusola, M. L. Madugu, N. A. Abdul-Manaf, and I. M. Dharmadasa, *Curr. Appl. Phys.* **16**, 120 (2016).
20. M. F. Ehsan, M. N. Ashiq, F. Bi, Y. Bi, S. Palanisamy, and T. He, *RSC Adv.* **4**, 48411 (2014).
21. K. Chakraborty, T. Pal, and S. Ghosh, *ACS Appl. Nano Mater.* **1**, 3137 (2018).
22. M. F. Ehsan, S. Qudoos, Z. Ahmad, S. Hamid, M. Arfan, A. Zia, K. Umbreen, M. N. Ashiq,

and D. Tyagi, SN Appl. Sci. **1**, 197 (2019).

23. M. F. Ehsan, M. N. Ashiq, and T. He, RSC Adv. **5**, 6186 (2015).

24. B. B. Wang, M. K. Zhu, H. Wang, and G. B. Dong, Opt. Mater. (Amst). **34**, 42 (2011).

25. B. B. Wang, M. K. Zhu, H. Wang, G. B. Dong, and H. L. Xie, Mater. Sci. Semicond. Process. **15**, 131 (2012).

26. B. B. Wang and X. Z. Xu, J. Cryst. Growth **311**, 4759 (2009).

27. C. Tang, X. Wei, X. Cai, Q. An, P. Hu, J. Sheng, J. Zhu, S. Chou, L. Wu, and L. Mai, ACS Appl. Mater. Interfaces **10**, 19626 (2018).

28. M. Das, D. Das, S. Sil, and P. P. P. Ray, Nanoscale Adv. **5**, 3655 (2023).

29. J. Chastain and R. C. King Jr, Perkin-Elmer Corp. **40**, 221 (1992).

30. C. R. Brundle and B. V. Crist, J. Vac. Sci. Technol. A **38**, 41001 (2020).

31. H. A. Elbadawy, A. E.-D. Ali, A. A. Elkashef, S. Foro, and D. S. El-Sayed, Appl. Organomet. Chem. **36**, e6793 (2022).

32. M. Amin Baghchesara, M. Cheraghizade, and R. Yousefi, Mater. Lett. **162**, 195 (2016).

33. Z. Zhu, Z. Li, X. Xiong, X. Hu, X. Wang, N. Li, T. Jin, and Y. Chen, J. Alloys Compd. **906**, 164316 (2022).

34. A. Kumar, R. Kumar, N. Verma, A. V Anupama, H. K. Choudhary, R. Philip, and B. Sahoo, Opt. Mater. (Amst). **108**, 110163 (2020).

35. S. Sil, A. Dey, J. Datta, M. Das, R. Jana, S. Halder, J. Dhar, D. Sanyal, and P. P. Ray, Mater. Res. Bull. **106**, 337 (2018).

36. S. allah Khelifi, M. Blal, R. Dabou, A. Ziane, A. Rouabhia, S. Lachtar, M. Mostefaoui, A. Neçaibia, A. Bouraiou, A. Slimani, and B. Tidjar, Phys. B Condens. Matter **647**, 414362 (2022).

37. M. F. Ehsan, M. Shafiq, S. Hamid, A. Shafiee, M. Usman, I. Khan, M. N. Ashiq, and M. Arfan, Appl. Surf. Sci. **532**, 147418 (2020).

38. Q. Yang, X. Guo, W. Wang, Y. Zhang, S. Xu, D. H. Lien, and Z. L. Wang, ACS Nano **4**, 6285 (2010).

39. D. Das, M. Das, S. Sil, P. Sahu, and P. P. Ray, ACS Omega **7**, 26483 (2022).

40. İ. Taşcıoğlu, U. Aydemir, and Ş. Altındal, J. Appl. Phys. **108**, 064506 (2010).

41. I. Ullah, M. Shah, M. Khan, and F. Wahab, J. Electron. Mater. **45**, 1175 (2016).

42. M. Soylu and B. Abay, Phys. E Low-Dimensional Syst. Nanostructures **43**, 534 (2010).

43. K. C. Kao, *Dielectric Phenomena in Solids* (Elsevier, 2004).

44. D. Das, M. Das, P. Sahu, and P. Pratim Ray, Mater. Today Proc. (2023).

45. S. Khanchandani, S. Kundu, A. Patra, and A. K. Ganguli, J. Phys. Chem. C **117**, 5558 (2013).

46. S. Rawalekar, S. Kaniyankandy, S. Verma, and H. N. Ghosh, *J. Phys. Chem. C* **115**, 12335 (2011).
47. J. Liu, J. Shi, and H. Deng, *J. Environ. Chem. Eng.* **11**, 110311 (2023).
48. L. Huang, F. Peng, H. Yu, and H. Wang, *Solid State Sci.* **11**, 129 (2009).
49. H. Wang, Y. Wu, P. Wu, S. Chen, X. Guo, G. Meng, B. Peng, J. Wu, and Z. Liu, *Front. Mater. Sci.* **11**, 130 (2017).
50. M. Wang, L. Sun, Z. Lin, J. Cai, K. Xie, and C. Lin, *Energy Environ. Sci.* **6**, 1211 (2013).
51. Z. Zhang, S. Zhai, M. Wang, H. Ji, L. He, C. Ye, C. Wang, S. Fang, and H. Zhang, *J. Alloys Compd.* **659**, 101 (2016).
52. S. M. Albukhari and A. Shawky, *J. Mol. Liq.* **336**, 116870 (2021).
53. B. Chai, J. Yan, C. Wang, Z. Ren, and Y. Zhu, *Appl. Surf. Sci.* **391**, 376 (2017).
54. M. Sundararajan, V. Sailaja, L. John Kennedy, and J. Judith Vijaya, *Ceram. Int.* **43**, 540 (2017).
55. T. Narenuch, T. Senasu, T. Chankhanittha, and S. Nanan, *Molecules* **26**, (2021).
56. L. Shi, L. Liang, J. Ma, Y. Meng, S. Zhong, F. Wang, and J. Sun, *Ceram. Int.* **40**, 3495 (2014).
57. N. Tian, H. Huang, Y. Guo, Y. He, and Y. Zhang, *Appl. Surf. Sci.* **322**, 249 (2014).
58. P. Nuengmatcha, S. Chanthai, R. Mahachai, and W.-C. Oh, *J. Environ. Chem. Eng.* **4**, 2170 (2016).
59. L. Ma, G. Wang, C. Jiang, H. Bao, and Q. Xu, *Appl. Surf. Sci.* **430**, 263 (2018).

From Electron Density to Defect Insights:
A Comprehensive Study of ZnSe/ZnTe
Heterostructures via Positron Annihilation
Spectroscopy

Chapter 6

6.1. Introduction

The rapid advancements in semiconductor technology have catalyzed the exploration of novel materials and structures for various electronic and photo-induced applications, namely photoconductor devices, photovoltaic cells, optical switches and many more. In the preceding chapter, it was observed that ZnSe/ZnTe heterostructures have emerged as intriguing candidates due to their potential for high performance in the photocatalytic degradation of azo dyes [1]. These heterostructures exhibit unique electronic behaviour governed by the inherent characteristics of ZnSe and ZnTe constituents. Specifically, it was noted that heterostructure with a composition of 50% ZnSe and 50% ZnTe displayed the highest conductivity and superior electron mobility, attributing to their exceptional catalytic performance [2]. Indeed, electron mobility, as a microscopic parameter, played a pivotal role in the degradation mechanism. However, an investigation into the distribution of charge carriers or the presence of defects in their pathways remained unexplored. Thus, this chapter aims to elucidate the electron densities not from a theoretical standpoint but through experimental means, employing the Positron Annihilation Spectroscopy (PAS) technique.

The utilization of Positron Annihilation Lifetime Spectroscopy (PALS) as a non-destructive radiological method is widespread in materials science research due to its exceptional sensitivity to the free volume within materials. This technique relies on assessing the lifetime and intensity of ortho-positronium (o-Ps) atoms within free volumes of various structures. Positronium (Ps) trapping in vacancies provides insights into the size of vacancy clusters, thereby offering valuable information regarding the structural properties of solids, liquids, and semi-solid materials [3]. PALS finds application across diverse sectors including crystals, composites, nano-materials and soft condensed matter systems, and the examination of defects and pores in metals, ceramics, and polymers.

The methodology involves employing positrons as probes, which, due to their positive electric charge, become preferentially localized within atom-sized regions of the material, making them adept at discerning voids and defects within this size range. Typically, positrons are generated from a radioactive isotope, such as ^{22}Na , which decays into ^{22}Ne through β^+ decay, emitting an energetic 1.28 MeV gamma ray as a signature of positron creation. Upon injection into a sample, positrons undergo inelastic collisions with their surroundings, eventually reaching thermal equilibrium. Following

thermalization, positrons can either freely annihilate with electrons within the material or transition into a quasi-stationary state known as Positronium (Ps). The annihilation process can occur in different modes depending on the spins of the participating particles, each mode characterized by a specific lifetime, as detailed in Chapter 2 (§ 2.7.1). Within the material, o-Ps tend to accumulate in regions of low electron density, such as the cores of voids, where they undergo annihilation via "pick-off" annihilation, producing two 0.511 MeV annihilation photons. Through the measurement of annihilation lifetime, which represents the survival time of the positron in the medium, valuable information about the 'electron density' experienced by the positron can be directly obtained [3]. The lifetime of ortho-positronium (o-Ps) serves as an indicator of the proximity of Ps to the local environment, with the time elapsed between positron creation and annihilation photon detection offering insights into the positronium lifetime within the material being studied. The o-Ps lifetimes and intensities are indicative of the 'electron density' at the annihilation site and can provide valuable information regarding atomic-scale level 'defects', such as vacancies or dislocations. Thus, this study endeavours to unravel the intricate relationship between charge transport and carrier dynamics, i.e., the conductivities and mobilities with the 'electron densities' and the presence of 'defects' within these heterostructures.

6.2. Experimental

The synthesis procedure of the ZnSe/ZnTe heterojunction microstructures was discussed in detail in the previous chapter (§ 5.2.2).

6.3. Materials Characterization Techniques

The material characterization techniques employed in the previous chapters (§ 3.3, § 4.3 and § 5.3) have been consistently applied in this chapter. Additional methodology is the Positron Annihilation Lifetime Spectroscopy (PALS), in which a sealed $^{22}\text{NaCl}$ source with a radioactivity of approximately 10 μCi was enclosed in a 1.5 μm thick nickel foil and inserted between two identical plane-faced samples (12 mm diameter pellets). The positron lifetime measurement system employed a conventional fast-fast coincidence assembly featuring two gamma-ray detectors - one measuring 25 mm in length, and the other tapering from 25 mm to a 13 mm diameter BaF_2 scintillator, optically connected with an XP2020 Q photomultiplier tube [4,5]. The spectrometer, assessed via the prompt

gamma-ray of a ^{60}Co source, exhibited a timing resolution (FWHM) of approximately 220 ps. More than ten million coincidence events were detected and recorded using a multichannel analyzer. The acquired lifetime spectrum was then analyzed using the computer program PATFIT-88, which includes corrections for source-related factors [6]. A schematic representation of the PALS spectrometer and spectra is illustrated in Chapter 2 (Fig. 2.9).

6.4. Results and Discussion

6.4.1. Structural Properties

The crystal structures of the synthesized heterostructured samples (ZS, ZST-1, ZST-2, ZST-3 and ZT) were comprehensively probed through X-ray diffraction (XRD) analysis, with detailed results presented in the previous chapter (§ 5.4.1). Notably, no additional Bragg reflections were observed, confirming phase purity and successful synthesis through the variation of the precursor concentration.

6.4.2. Positron Annihilation Lifetime Spectroscopy (PALS)

The positron annihilation lifetime spectrum (PALS) provides crucial insights into the nature of lattice defects by evaluating the lifetime of the positron upon its injection into the sample [7]. In this context, we examine the positron lifetimes of our synthesized samples to establish correlations, notably considering properties such as the conductivity profile from the Schottky diodes performance standpoint, as discussed in the previous chapters. The positron lifetime spectra were fitted using the computer program PATFIT 88 [8], and the resulting spectrum was best fitted (with a variance of fit ≤ 1 per channel) using a three-component model. The values of these lifetime components denoted as τ_1 , τ_2 , and τ_3 , are tabulated in Table. 6.1.

The initial lifetime component (τ_1) is attributed to the free annihilation of positrons in the material's bulk, while the longer lifetime component (τ_3), typically exceeding 1 ns, originates from the formation of 'positronium' (a short-lived hydrogen-like atom, comprising an electron and a positron) in large voids or at the grain surfaces of the sample. The intermediate lifetime (τ_2) arises from the positron annihilation at defect sites. Given that positrons are predominantly trapped in cation-type vacancies and experience slightly longer lifetimes than the bulk of the sample, this phenomenon implies a lower electron density near the positron. As a result, the lifetime of a positron at a defect

site is consistently greater than the bulk lifetime. Additionally, the average lifetime (τ_{avg}) is given by:

$$\tau_{avg} = \left(\frac{\tau_1 I_1 + \tau_2 I_2}{I_1 + I_2} \right) \quad (6.1)$$

The correlation between positron lifetime and electrical conductivity arises from their interaction with the defect structure within materials. Positron annihilation spectroscopy (PAS) serves as a valuable method for investigating defects by detecting positron-electron annihilation processes. Defects such as vacancies, dislocations, and impurities act as trapping sites for positrons [9], leading to a higher annihilation probability compared to interactions within a perfect crystal lattice. The lifetime of positrons before annihilation reflects the concentration and nature of these defects. Conversely, electrical conductivity is associated with the mobility of charge carriers (electrons or holes) within the material. Defects can impede the mobility of charge carriers through scattering or trapping mechanisms, thereby influencing conductivity.

Table. 6.1: Positron Annihilation lifetime component of all the samples.

Sample	τ_1 (ps)	I_1 (%)	τ_2 (ps)	I_2 (%)	τ_{av} (ps)	τ_3 (ps)	I_3 (%)
ZS	211 ± 2	52 ± 2	423 ± 8	46 ± 2	310	1861 ± 169	2 ± 0.1
ZST-1	176 ± 3	28 ± 2	370 ± 5	70 ± 2	314	1525 ± 69	2 ± 0.1
ZST-2	179 ± 4	19 ± 2	321 ± 6	80 ± 2	293	2743 ± 180	1 ± 0.1
ZST-3	176 ± 4	41 ± 2	382 ± 7	58 ± 2	296	2031 ± 210	1 ± 0.1
ZT	230 ± 3	61 ± 2	437 ± 5	38 ± 2	309	1952 ± 191	1 ± 0.1

Analysis of Table 6.1 reveals that the intermediate positron lifetime (τ_2) of the ZST-2 sample is notably shorter compared to the other samples. This observation suggests that injected positrons undergo rapid annihilation within the volume of the sample, indicating a lower anticipated presence of defects compared to other samples [10]. Positively charged defects could potentially scatter injected positrons, leading to longer positron lifetimes. Thus, a shorter positron lifetime in the ZST-2 heterostructure

implies a relatively defect-free material. Additionally, a shorter positron lifetime suggests a higher density of electrons, which typically serve as charge carriers for various electronic and photo-induced applications. Consequently, through PAS-based lifetime studies, it becomes feasible to correlate higher charge conductivity or mobility with the defects and electron density of materials.

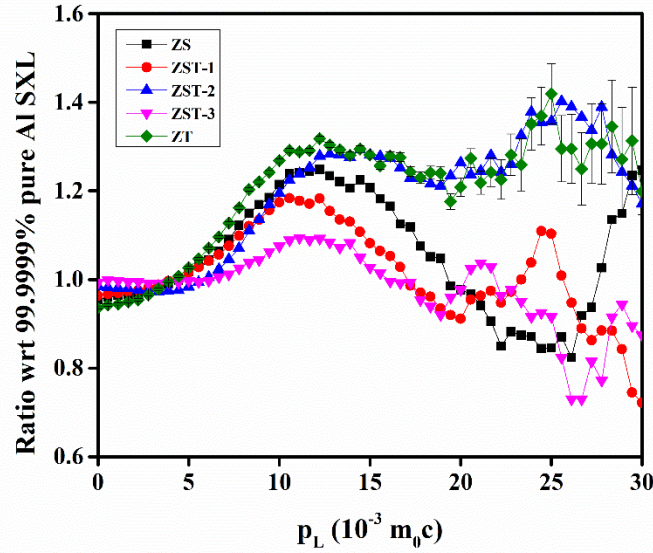


Fig. 6.1: Area-normalized ratio curve of CDB spectra of synthesized heterostructured materials constructed relative to CDB spectrum of defect-free Al single crystal (purity ~ 99.9999%).

6.4.3. Coincidence Doppler Broadening (CDB) Spectroscopy

CDB is another method employed for defect analysis in materials. This technique involves measuring pairs of back-to-back annihilation γ rays resulting from the interaction between a positron and an electron. The energy distribution of these gamma rays reflects the momentum distribution of the annihilating positron-electron pairs. Similar to positron lifetime spectroscopy, coincidence Doppler broadening spectroscopy is sensitive to the defect structure of materials. Interactions between positrons and defects in the material influence the momentum distribution of positron-electron pairs, leading to Doppler broadening of annihilation gamma rays. The correlation between coincidence Doppler broadening and electrical conductivity stems from their shared sensitivity to defects in materials. Vacancies, dislocations, and impurities affect the mobility of charge carriers, resulting in changes in electrical conductivity. These defects also impact the momentum distribution of positron-electron pairs, thereby influencing the Doppler

broadening of annihilation gamma rays. This Coincidence Doppler Broadening Spectrum (CDB) is used to elucidate the nature of defect sites, specifically using the "ratio curve," which compares the area-normalized CDB spectrum of our synthesized samples with that of a defect-free (99.9999% pure) Al single-crystal sample [11]. Fig. 6.1 displays the individual ratio curves for all samples, providing further insights into the characterization of lattice defects and material properties.

6.5. Conclusion

We synthesized various ZnSe/ZnTe heterostructures and assessed their efficacy in the context of photo-induced dye degradation in the preceding chapter. Among the five distinct heterostructures examined, ZST-2 emerged as the most promising, exhibiting notable improvements in electrical conductivity and charge transfer characteristics. Notably, the ZST-2 sample demonstrated the highest mobility, a crucial parameter influencing electronic conductivity within the material. Our investigation further involved measuring the positron lifetimes of all samples, with ZST-2 displaying the shortest lifetime for bombarded positrons. This observed lower positron lifetime suggests a reduced defect density within the ZST-2 material, aligning with our earlier findings of enhanced electrical mobility and charge transfer efficiency. Moreover, the PAS also indicates a higher electron density within the material. Thus, the integration of charge conduction and positron annihilation spectroscopy for a comprehensive understanding of ZnSe/ZnTe heterostructures and their superior catalytic behaviour was possible in this study. By analyzing positron lifetime measurements and coincidence Doppler broadening spectra alongside electrical conductivity measurements, researchers can glean insights into the defect structure of materials and its impact on their electronic properties. This correlation is particularly invaluable in materials science and engineering for optimizing the performance of electronic and optoelectronic devices.

References

1. D. Suthar, Himanshu, S. L. Patel, S. Chander, M. D. Kannan, and M. S. Dhaka, *Solid State Sci.* **107**, 106346 (2020).
2. L. Zhang, H. Yang, J. Yu, F. Shao, L. Li, F. Zhang, and H. Zhao, *J. Phys. Chem. C* **113**, 5434 (2009).
3. M. M. Shokoya, B.-M. Benkő, K. Süvegh, R. Zelkó, and I. Sebe, *Pharmaceuticals* **16**, (2023).
4. A. Sarkar, M. Chakrabarti, S. K. Ray, D. Bhowmick, and D. Sanyal, *J. Phys. Condens. Matter* **23**, 155801 (2011).
5. J. Dhar, S. Sil, A. Dey, D. Sanyal, and P. P. Ray, *J. Phys. Chem. C* **121**, 5515 (2017).
6. M. Chakrabarti, A. Sarkar, S. Chattapadhyay, D. Sanyal, A. K. Pradhan, R. Bhattacharya, and D. Banerjee, *Solid State Commun.* **128**, 321 (2003).
7. J. Dhar, S. Sil, N. A. Hoque, A. Dey, S. Das, P. P. Ray, and D. Sanyal, *ChemistrySelect* **3**, 5304 (2018).
8. P. Kirkegaard, N. J. Pederson, and M. Eldrup, *Riso Natl. Lab. Riso* (1989).
9. S. Moshat, P. P. Ray, S. Sil, J. Dhar, and D. Sanyal, *Phys. Scr.* **98**, 35822 (2023).
10. Y. Yuan, Q. Wang, Y. Shao, H. Lu, T. Li, A. Gruverman, and J. Huang, *Adv. Energy Mater.* **6**, 1501803 (2016).
11. S. Sil, S. Moshat, P. P. Ray, J. Dhar, and D. Sanyal, *J. Phys. D. Appl. Phys.* **54**, 465502 (2021).

Summary and Future Outlook

Chapter 7

7.1. Summary

In the culmination of the thesis, encompassing six comprehensive chapters, we have meticulously explored various facets of material science, focusing particularly on charge transport kinetics and photocatalytic degradation - a realm that remains relatively underexplored. Despite the breadth of material science, our endeavour aimed to effectively communicate our experimental findings and the underlying rationale behind the results through a systematic examination presented across the six chapters.

The significance of graphene as a versatile material with multifaceted applications has been widely recognized in the modern scientific landscape. Over the past decade, extensive research has uncovered its vast potential, yet much remains to be explored. Therefore, a detailed understanding of graphene properties is imperative for its effective utilization across diverse fields such as solar cells, supercapacitors, and photocatalysis. In this pursuit, we endeavoured to gain a comprehensive understanding of graphene oxide, including its production methods, reduction techniques, and its integration with other compound semiconductors.

Our investigation was motivated by a noticeable gap in the literature concerning the direct interpretation of graphene oxide's conductivity and mobility. While numerous studies have explored graphene oxide composites for various photo-induced applications, the underlying reasons for graphene oxide's unique characteristics often remain unexplored. By elucidating these fundamental aspects, we aimed to provide researchers with a scientific and strategic framework for the application of graphene oxide in diverse fields.

Central to our research was the exploration of graphene oxide's applicability in composites and its potential benefits. Before its application, we sought to extract charge transport parameters, particularly the mobility (μ) of charge carriers. This necessitated the fabrication of metal-semiconductor junction-based Schottky diodes for the synthesized materials. By analyzing current-voltage (I-V) characteristics and applying thermionic emission (TE) theory, we estimated the mobility and lifetime or transit times (τ) of charge carriers. These parameters played a crucial role in determining the efficacy of incorporating graphene oxide in various photo-induced applications, especially in the decolourization of dye wastewater. Our investigation extended to the degradation of wastewater through two approaches: synthesizing reduced graphene oxide-zinc telluride composites (RGO-ZnTe) and developing heterostructures (ZnSe/ZnTe) comprising

different ratios of ZnSe and ZnTe. However, before applying these materials, a foundational understanding of graphene oxide and other materials was essential. Hence, in Chapter 1, we provided an extensive overview of graphene and its derivatives, group II-VI semiconductors, and their composites, setting the stage for our subsequent analyses.

In Chapter 2, we conducted an in-depth exploration of Schottky barrier diodes (SBDs), encompassing their theoretical principles, fabrication techniques, and insights into electrical studies, impedance spectroscopy, and positron annihilation spectroscopy. This chapter provided a thorough understanding of SBDs, from their theoretical underpinnings to practical applications, setting the stage for further analysis.

Continuing our journey, Chapter 3 focused on the investigation of reduced graphene oxide-zinc telluride (RGO-ZnTe) nanocomposites, aimed at enhancing charge transfer in optoelectronic devices. Through the lens of an equivalent circuit model, we examined the metal-semiconductor interfaces, shedding light on the intricate interplay between materials and charge transfer mechanisms.

In Chapter 4, we delved into the impact of higher carrier mobility in RGO-ZnTe nanocomposites on efficient charge transfer and the photodecomposition of Rhodamine B. Through a comprehensive analysis of structural, optical, thermal, and electrical properties, we elucidated the underlying mechanisms governing charge transport and photocatalytic activity in these nanocomposites. We investigated the charge transport dynamics and highlighted the importance of higher carrier mobility in the photocatalytic degradation of RhB. Our results revealed that the graphene composite exhibited superior photocatalytic activity compared to bare ZnTe under visible-light irradiation. This enhanced performance was attributed to the higher mobility of the graphene-based composite, facilitating the rapid movement of photoinduced charges between active sites and target molecules during the degradation process.

Chapter 5 extended our exploration to carrier mobility in hollow and mesoporous ZnSe/ZnTe heterostructures, with a focus on microscopic observations of swift charge transfer and visible-light-driven dye decomposition. By employing an array of material characterization techniques, we gained insights into the structural, optical, and electrical properties of these heterostructures, illuminating their potential in wastewater treatment. We found that the catalytic performance of the dye degradation process was influenced significantly by both macroscopic and microscopic characteristics. Notably, macroscopic features such as the hollow structure of zinc selenide (ZnSe) spheres and

the plate-like morphology of zinc telluride (ZnTe) particles, along with their collective surface area, played a pivotal role in determining catalytic efficiency. Additionally, microscopic parameters including charge carrier mobility and transit time were identified as crucial factors affecting catalytic activity. This heightened mobility, combined with the synergistic interaction between ZnSe and ZnTe within the heterostructure, effectively mitigated the challenge of short lifetimes observed in photo-generated electron-hole pairs within individual materials.

Finally, in Chapter 6, we undertook a comprehensive examination of ZnSe/ZnTe heterostructures using Positron Annihilation Spectroscopy (PAS), elucidating the electron density and defect insights to correlate the outcomes we observed in the preceding chapter. Through the analysis of Positron Annihilation Lifetime Spectroscopy (PALS) and Coincidence Doppler Broadening (CDB) Spectroscopy, we unravelled the behaviour of positrons within the material, offering valuable insights into defect structures.

In summation, our thesis endeavours to contribute to the ever-evolving landscape of material science by unravelling the intricacies of graphene composites and group II-VI-based semiconductor heterostructures. Through a multidisciplinary approach encompassing theoretical insights, experimental investigations, and advanced characterization techniques, we aim to pave the way for the development of novel materials with enhanced functionalities and applications across diverse fields.

7.2. Future Outlook

We intend to expand our research to delve deeper into the various conduction mechanisms of Schottky contacts, emphasizing the critical importance of precise understanding regarding the Schottky interface. In Chapter 5, we departed from the traditional approach of employing direct current (dc) measurement techniques to evaluate the electrical properties of ZnSe/ZnTe-based Schottky devices. Instead, our focus shifted towards employing impedance spectroscopy (IS), a technique often underappreciated and scarcely documented in the existing literature.

➤ *Impedance Spectroscopy (IS) and Development of Equivalent Circuit Models*

The primary objective is to extend the study beyond conventional direct current (dc) techniques and utilize impedance spectroscopy (IS) to comprehensively assess the

electrical properties of ZnSe/ZnTe-based Schottky devices. By employing IS, this research aims to gain a deeper understanding of charge transport mechanisms within the devices, particularly focusing on the dynamics of mobile charges in both bulk and interfacial regions. We aim to develop and simulate complex equivalent circuit models to analyze the impedance spectra obtained from the Schottky devices under different bias conditions. By modelling the devices with precise equivalent circuits, the research aims to differentiate individual interface resistances, particularly between Al and (ZnSe/ZnTe)/ITO interfaces, shedding light on the influence of interface properties on the electrical behaviour of the devices.

➤ *Differentiation of Interface Resistances*

The study further aims to differentiate interface resistances using ac impedance analysis, emphasizing the importance of understanding the electrical characteristics beyond conventional current-voltage (I-V) analysis. By discerning the contributions of individual interface resistances, the research seeks to elucidate the underlying mechanisms governing charge transport across metal-semiconductor interfaces.

➤ *Estimation of Electron Lifetime and Interface Impedance*

An objective is to estimate parameters such as electron recombination lifetime (τ_r) and interface impedance from impedance spectra, providing valuable insights into the performance and suitability of the fabricated Schottky devices using the ZnSe/ZnTe heterostructures. By analyzing these parameters, the research aims to identify optimal device configurations for various applications, such as solar cells and photodetectors.

➤ *Capacitance-Voltage (C-V) Characteristics*

Additionally, our research aims to conduct the capacitance-voltage (C-V) characteristics of the Schottky devices to gather supportive evidence regarding their electrical properties. By analyzing parameters such as charge carrier density (N_D), barrier height $\{\Phi_b\}$ (C-V), and depletion layer thickness (W_D), the study seeks to provide comprehensive insights into the performance of the devices.

➤ *Comparison with Theoretical Models*

Lastly, the research aims to compare experimentally derived electrical properties, such as barrier height, with theoretical considerations based on energy band diagrams. By conducting this comparison, the study aims to identify potential discrepancies and

factors influencing barrier height determination, thereby refining theoretical models and enhancing the understanding of metal-semiconductor interactions.

Overall, the objectives of this research endeavour are to advance the understanding of charge transport mechanisms and interface properties in ZnSe/ZnTe-based Schottky diode devices through advanced characterization techniques, with the ultimate goal of optimizing device performance for various electronic and optoelectronic applications.

List of Publications, Conferences and Workshops

List of Publications

▪ Journal Publications

1. "Effect of Higher Carrier Mobility of the Reduced Graphene Oxide-Zinc Telluride Nanocomposite on Efficient Charge Transfer Facility and the Photodecomposition of Rhodamine B" - **Dhananjoy Das**, Mainak Das, Sayantan Sil, Puspendu Sahu, and Partha Pratim Ray; *ACS Omega*, 7 (2022): 26483-94.
2. "Investigating carrier mobility in hollow and mesoporous ZnSe/ZnTe heterostructures: microscopic observations of swift charge transfer and visible-light-driven dye decomposition" - **Dhananjoy Das**, Mainak Das, Saikat Shyamal, Sayantan Sil, Puspendu Sahu, Partha Pratim Ray, *Journal of Photochemistry and Photobiology A: Chemistry*, 449 (2024): 115421.
3. "Exploring reduced graphene oxide-zinc telluride nanocomposites for enhanced charge transfer in optoelectronic devices: a study of the metal-semiconductor interfaces via equivalent circuit model"- **Dhananjoy Das**, Mainak Das, Animesh Biswas, Puspendu Sahu, and Partha Pratim Ray, *Journal of Materials Science: Materials in Electronics*, 34 (2023): 1574.
4. "Development of hierarchical copper sulfide-carbon nanotube (CuS-CNT) composites and utilization of their superior carrier mobility in efficient charge transport towards photodegradation of Rhodamine B under visible light" - Mainak Das, **Dhananjoy Das**, Sayantan Sil, Partha Pratim Ray, *Nanoscale Advances*, 5 (2023): 3655-3663.
5. "Phenoxo-bridged dinuclear mixed valence cobalt(iii/ii) complexes with reduced Schiff base ligands: synthesis, characterization, band gap measurements and fabrication of Schottky barrier diodes" - Abhisek Banerjee, **Dhananjoy Das**, Partha Pratim Ray, Snehasis Banerjee, and Shouvik Chattopadhyay; *Dalton Transactions*, 50 (2021): 1721-32.
6. "Synthesis, characterization, self-assembly and non-ohmic Schottky barrier diode behaviors of two iron(iii) based semiconductors with theoretical insight" - Tanmoy Basak, **Dhananjoy Das**, Partha Pratim Ray, Snehasis Banerjee, and Shouvik Chattopadhyay; *CrystEngComm*, 22 (2020): 5170-81.
7. "Investigation of conduction kinetics in Al/CuInSe₂ Schottky device utilizing impedance spectroscopy (IS) measurement and study of its photosensing behaviour" - Animesh Biswas, Sayantan Sil, Arka Dey, Joydeep Datta, **Dhananjoy Das**, and Partha Pratim Ray; *Journal of Physics and Chemistry of Solids*, 150 (2021): 109878.

8. "Electrical and photocatalytic properties of composites of manganese and titanium oxides" - Bharati Debi Biswas, Joydeep Datta, Moushumi Dutta Purkayastha, **Dhananjoy Das**, Partha Pratim Ray, Abhigyan Dutta, and Tapas Pal Majumder; *Surfaces and Interfaces*, 20 (2020): 100606.
9. "Cd(II) coordination polymer of fumaric acid and pyridyl-hydrazide Schiff base: Structure, photoconductivity and theoretical interpretation" - Angeera Chandra, **Dhananjoy Das**, Joaquín-Ortega Castro, Kaushik Naskar, Srikanta Jana, Antonio Frontera, Partha Pratim Ray, and Chittaranjan Sinha; *Inorganica Chimica Acta*, 518 (2021): 120253.
10. "Improved electrical conductivity of Co(ii) and Cu(ii) ladder polymers in the fabrication of photoresponsive Schottky devices" - Basudeb Dutta, **Dhananjoy Das**, Kumari Raksha, Chittaranjan Sinha, Sumit Khanra, Partha Pratim Ray, and Mohammad Hedayetullah Mir; *Materials Advances*, 4 (2023): 215-22.
11. "Findings of inhomogeneity in barrier height of Schottky junction Al/rGO-SnO₂ having anomaly in theoretical and experimental value of Richardson constant: A Gaussian approach" - Pubali Das, Baishakhi Pal, Mrinmay Das, Sayantan Sil, **Dhananjoy Das**, Animesh Layek and Partha Pratim Ray; *Results in Physics*, 42 (2022): 105996.
12. "Designing of a Zn(ii)-isonicotinohydrazido thiophenyl based 2D coordination polymer: structure, augmented photoconductivity and superior biological activity" - Kingshuk Debsharma, Sunanda Dey, **Dhananjoy Das**, Satyajit Halder, Joaquin Ortega-Castro, Sarita Sarkar, Basudeb Dutta, Suwendu Maity, Kuladip Jana, Antonio Frontera, Partha Pratim Ray, and Chittaranjan Sinha; *CrystEngComm*, 25 (2023): 162-72.
13. "Synthesis of a Zn(ii)-based 1D zigzag coordination polymer for the fabrication of optoelectronic devices with remarkably high photosensitivity" - Basudeb Dutta, **Dhananjoy Das**, Joydeep Datta, Angeera Chandra, Srikanta Jana, Chittaranjan Sinha, Partha Pratim Ray, and Mohammad Hedayetullah Mir; *Inorganic Chemistry Frontiers*, 6 (2019): 1245-52.
14. "Elucidation of Inhomogeneous Heterojunction Performance of Al/Cu₅FeS₄ Schottky Diode With a Gaussian Distribution of Barrier Heights" - Sayantan Sil, Rajkumar Jana, Animesh Biswas, **Dhananjoy Das**, Arka Dey, Joydeep Datta, Dirtha Sanyal, and Partha Pratim Ray; *IEEE Transactions on Electron Devices*, 67 (2020): 2082-87.
15. "Intriguing π -interactions involving aromatic neutrals, aromatic cations and semiconducting behavior in a pyridinium-carboxylate salt"- Prantika Das, Samiul Islam, **Dhananjoy Das**, Partha Pratim Ray, Saikat Kumar Seth, *Journal of Molecular Structure*, 1284 (2023): 135326.

16. "Improved device performance of rod like ZnO in a Schottky type photosensor compared to particle like ZnO: Analysis of charge transport" - Mrinmay Das, Pubali Das, Joydeep Datta, **Dhananjoy Das**, Somobrata Acharya, and Partha Pratim Ray; *Materials Science in Semiconductor Processing*, 130 (2021): 105799.
17. "Crystallographic, theoretical and conductivity studies of two new complexes [Ni(II) and Cu(II)] based on mixed ligands approach"- Nirvik Ghosh, Mohd Afzal, **Dhananjoy Das**, Partha Pratim Ray, Samit Pramanik, Sudipta Pathak, Kinsuk Das, Rosa M. Gomila, Antonio Frontera, Subrata Mukhopadhyay; *Journal of Molecular Structure*, 1298 (2024): 137106.

▪ Conference Proceedings

1. "Investigation of the metal–semiconductor interface by equivalent circuit model in zinc phthalocyanine (ZnPc) based Schottky diodes and its charge transport properties"- **Dhananjoy Das**, Mainak Das, Puspendu Sahu, Partha Pratim Ray; *Materials Today: Proceedings*, (2023), In Press, Corrected Proof.

▪ List of Conferences Attended

1. "An approach for hydrothermally synthesized CuFeS₂ nanocomposite for potential application as an acceptor in hybrid solar cell" – participated in the ***International Conference on Current Trends in Materials Science and Engineering (CTMSE-2021)***, organized by the Institute of Engineering & Management, Salt Lake during 11th to 13th March 2021.
2. "Analysis of equivalent circuit model and charge transport phenomena of metal-semiconductor interfaces in Zinc Phthalocyanine (ZnPc) based heterojunction Schottky diode" – presented in the ***International Conference on Renewable Energy (ICRE-2022)***, organized by the Centre for Non-Conventional Energy Resources (CNCER), University of Rajasthan, Jaipur, India in association with International Association for Hydrogen Energy (IAHE), USA & MRSI, Rajasthan Chapter, during February 25-27, 2022.
3. "Analysis of the Charge Transport Phenomena and Equivalent Circuit Model of the Metal-Semiconductor Interfaces in Zinc Phthalocyanine (ZnPc) based Schottky Diodes" - participated and presented in the ***International Conference on Nanotechnology: Opportunities & Challenges (ICNOC-2022)***, organized by the Department of Applied Sciences & Humanities, Faculty of Engineering & Technology, Jamia Millia Islamia, New Delhi, India on November 28-30, 2022.
4. "Investigation of the metal-semiconductor interfaces by equivalent circuit model in Zinc Phthalocyanine (ZnPc) based Schottky diodes and its charge transport properties" – presented in the ***International Conference on Advances in Smart Materials, Chemical & Biochemical Engineering (CHEMSMART-22)***, organized By the Department of Chemical Engineering, National Institute of Technology Rourkela, Rourkela, India, on 16-18 December 2022.
5. "Effect of higher carrier mobility of reduced graphene oxide-zinc telluride nanocomposite towards efficient charge transfer facility and the photodecomposition of Rhodamine B"- presented in the ***7th International Conference on Nanoscience and Nanotechnology (ICONN- 2023)***, organised by the Department of Physics and Nanotechnology, SRM Institute of Science and Technology, India, during March 27-29, 2023.

▪ Workshops Attended

1. ***"1st DFT-M: Workshop/Hands-on-Training on Density Functional Theory Modelling of Materials: Nanoparticles, Thin Films, Unit cells using Quantum Espresso"***- organized by Centre for Advanced Computational Studies, New Delhi, India; during 14th September - 20th September 2023.
2. ***"1st Workshop/Hands-on-Training on Rietveld Refinement of X-Ray Diffraction data (RRD) (using FullProf Software Package)"***- organized by Centre for Advanced Computational Studies, New Delhi, India; during 1st – 7th January 2024 via Online Mode.

Publications, Conference and Workshop Certificates

Effect of Higher Carrier Mobility of the Reduced Graphene Oxide–Zinc Telluride Nanocomposite on Efficient Charge Transfer Facility and the Photodecomposition of Rhodamine B

Dhananjoy Das,[§] Mainak Das,[§] Sayantan Sil,[§] Puspendu Sahu,[§] and Partha Pratim Ray^{*,§}



Cite This: *ACS Omega* 2022, 7, 26483–26494



Read Online

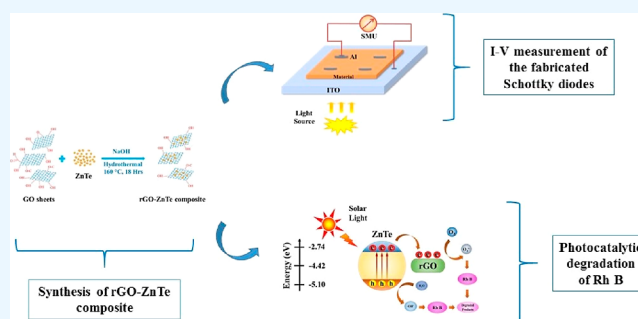
ACCESS |

Metrics & More

Article Recommendations

Supporting Information

ABSTRACT: The synthesis of solar-light-responsive zinc telluride (ZnTe) nanoparticles and their composite with reduced graphene oxide (rGO–ZnTe) via a simple hydrothermal reaction is reported. The synthesized nanostructures were comprehensively characterized by a combination of X-ray diffraction and photoelectron spectroscopy, electron microscopy, UV–vis spectroscopy, photoluminescence spectroscopy and thermogravimetric analysis. The effects of graphene oxide on the crystallinity, microstructure, photo-excitation, light absorption, surface area and thermal stability of ZnTe were studied. The current–voltage (I – V) characteristics for both as-synthesized ZnTe and rGO–ZnTe composite-based Schottky devices were measured to estimate the charge transport parameters such as dc conductivity, photosensitivity, carrier's mobility and lifetime. The photocatalytic performance of both the materials in the degradation of an azo dye (Rhodamine B) was subsequently investigated using simulated solar light. The rGO–ZnTe composite exhibited a higher photocatalytic activity (66%) as compared to the as-synthesized ZnTe (23%), essentially due to the synergy between rGO sheets and ZnTe nanoparticles. The role of the carrier's mobility in the transportation of photo-induced charges (electrons and holes) through the complex network of the composite materials and thus facilitating the photo-degradation process is explained. In the end, the responsible reactive species for the decomposition of Rhodamine B was also interpreted.



INTRODUCTION

Dye wastewater released into water bodies mainly by textile industries is becoming a major environmental concern, causing several ecological problems.¹ In the past few decades, different physicochemical and biological attempts based on chemical and physical adsorption techniques have been made to degrade these industrial effluents, but they are not cost-effective from an economical point of view and often produce secondary pollutants.² Among all advanced oxidation methods known to date, the photocatalytic route based on semiconducting materials has shown considerable efficiency in wastewater decontamination processes.³ Thus far, a large number of compound semiconductors have been investigated for organic dye decomposition since they possess an excellent larger absorbance cross-section and higher environmental stability.⁴ Although the semiconductor materials have excellent potential in the area of organic dye decolorization, they suffer from the shortcomings of having wide band gaps and a comparatively shorter life span of excitons, limiting the usage of these semiconductors in practical applications.⁵ As an example, TiO_2 , which is one of the most promising materials for the decomposition of many organic pollutants, responds only in the UV region of the electromagnetic spectrum, attributed to its wide band gap (~ 3.2 eV).⁶ This causes fewer redox

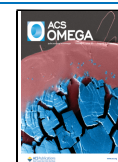
reactions with the pollutants and detrimentally affects its degradation efficiency.⁷

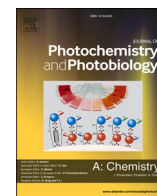
On the other hand, zinc telluride (ZnTe), which is an important group II–VI compound semiconductor having a direct band gap of ~ 2.26 eV, has shown immense potential in a wide range of applications in solar cells,⁸ light-emitting diodes,⁹ optoelectronic devices,¹⁰ CO_2 reductions,¹¹ and in wastewater treatment.¹² The solution-processed ZnTe nanostructures demonstrate a few excellent features, namely, low production cost, large surface area, good environmental stability, excellent reusability and prominent visible-light absorption, which make them a prospective photocatalyst. However, they also have an inherent shortcoming that the fast electron (e^-)–hole (h^+) recombination in ZnTe nanomaterials is responsible for their weak photocatalytic performance, particularly under visible light irradiation. Several attempts were made to decrease the electron–hole recombination in these materials and thus

Received: April 20, 2022

Accepted: June 14, 2022

Published: July 23, 2022





Investigating carrier mobility in hollow and mesoporous ZnSe/ZnTe heterostructures: Microscopic observations of swift charge transfer and visible-light-driven dye decomposition

Dhananjoy Das^a, Mainak Das^a, Saikat Shyamal^a, Sayantan Sil^b, Puspendu Sahu^a, Partha Pratim Ray^{a,*}

^a Department of Physics, Jadavpur University, Kolkata 700032, India

^b Department of Physics, University of Engineering and Management, University Area, Action Area III, B/5, Newtown, Kolkata 700160, India

ARTICLE INFO

Keywords:

Semiconductor
Hydrothermal
Heterostructure
Schottky diode
Mobility
Photocatalysis

ABSTRACT

We report herein a one-pot hydrothermal approach to synthesize zinc selenide (ZnSe)/zinc telluride (ZnTe) heterostructures - a set of common cation-based photocatalysts. The crystal structure and phase purity of the heterostructures were verified by powder X-ray diffraction (PXRD) analysis, while field emission scanning electron microscopy (FESEM), transmission electron microscopy (TEM), and X-ray photoelectron spectroscopy (XPS) techniques were employed to study their morphology, microstructures, and surface electronic states, respectively. Notably, a detailed XPS analysis was conducted to discern the chemical species present on the surface of the photocatalyst, providing valuable insights into the compound's stability in an aqueous medium. Furthermore, the synthesized hybrid structures were utilized to fabricate Schottky barrier diodes, enabling a study of their electrical and dielectric properties using the Spatial-charge-limited conduction (SCLC) mechanism. The key charge transport parameters for all the photocatalysts, namely, carriers' mobility and transit time, influencing the photo response and consequently, dye degradation were estimated. Notably, the ZnSe/ZnTe heterostructure, comprising 50 % ZnSe and 50 % ZnTe, exhibited the highest mobility (3.36×10^{-6} S/m in the dark, increasing to 1.70×10^{-5} S/m in light) and proved to be the most effective photocatalyst for degrading Rhodamine B (with up to ~ 78 % degradation over 60 min of solar light irradiation) - underscoring the pivotal role of carriers' mobility in governing the photocatalytic activity. Moreover, the ZnSe/ZnTe heterostructure demonstrated a remarkable reduction in the photo-corrosion process, a key challenge affecting the photocatalytic activity of numerous materials. Our discussion highlighted the efficient separation of photoinduced electron-hole pairs in the ZnSe/ZnTe heterostructure, facilitated by the synergistic effects of ZnSe and ZnTe, leading to the achievement of the highest photocatalytic performance.

1. Introduction

Wastewater released by the textile industry is a major cause of ecological imbalances and environmental concerns. Azo dyes, commonly used in textile production, contain high levels of aromatic rings and strong colours, making them harmful and carcinogenic to both humans and animals [1]. In recent decades, various biological and physio-chemical methods have been adopted to degrade these complex dyes; however, many of these methods are not cost-effective and they often produce hazardous by-products [2]. Among the various Advanced Oxidation Processes (AOPs), photo-induced catalytic decomposition has

garnered significant attention from researchers due to its economical and green approach to environmental remediation. Metal oxides and sulphides, including TiO₂ [3], ZnO [4], ZnS [5], CdS [6], ZnSe [7], WO₃ [8] and CeO₂ [9] have been employed to bleach the industrial effluents through photocatalytic decomposition methods. However, these single metal oxides or sulphides suffer from several shortcomings, such as a low surface-to-volume ratio, broad optical bandgaps, and short lifetimes of photo-generated electron-hole pairs that limit the number of excitons produced upon light illumination [10]. Even if the excitons are produced, their rapid recombination hinders an efficient degradation process. For example, ZnO, despite having a higher hydroxyl ion-generating

* Corresponding author.

E-mail address: parthap.ray@jadavpuruniversity.in (P. Pratim Ray).

<https://doi.org/10.1016/j.jphotochem.2023.115421>


Received 10 June 2023; Received in revised form 3 December 2023; Accepted 15 December 2023

Available online 17 December 2023

1010-6030/© 2023 Elsevier B.V. All rights reserved.



Exploring reduced graphene oxide-zinc telluride nanocomposites for enhanced charge transfer in optoelectronic devices: a study of the metal–semiconductor interfaces via equivalent circuit model

Dhananjoy Das¹, Mainak Das¹, Animesh Biswas^{1,2}, Puspendu Sahu¹, and Partha Pratim Ray^{1,*} 

¹Department of Physics, Jadavpur University, Kolkata 700032, India

²Department of Physics, Sreegopal Banerjee College, Mogra, Hoogly 712148, India

Received: 29 June 2023

Accepted: 10 July 2023

Published online:
24 July 2023

© The Author(s), under exclusive licence to Springer Science+Business Media, LLC, part of Springer Nature 2023

ABSTRACT

This study presents the synthesis of zinc telluride (ZnTe) nanoflakes and their composite with reduced graphene oxide (RGO-ZnTe) through a simple hydrothermal reaction. The crystal structure of the synthesized materials was characterized using X-ray Diffraction techniques. Subsequently, the Metal-Semiconductor (MS) based Schottky devices were fabricated by depositing the ZnTe and RGO-ZnTe thin films and Aluminium electrodes via vacuum coating methods. The surface morphology and topography of the deposited films were investigated using field emission scanning electron microscopy (FESEM) and atomic force microscopy (AFM) techniques, respectively, to study the formation of MS junctions. The interfacial properties of the MS junctions in the Al/ZnTe/ITO and Al/RGO-ZnTe/ITO configurations were analyzed using ac impedance spectroscopy over a frequency range of 50 Hz–10 MHz. Thereafter, the bias-dependent impedance spectrometry was also conducted within a voltage range of ± 0.6 V to establish the equivalent circuits for the fabricated MS junction Schottky diodes (SDs). The diode parameters, including on/off ratio, ideality factor, barrier height and series resistance were determined by measuring the current–voltage (I – V) characteristics of the fabricated SDs. Further, the charge transport parameters, such as dc conductivity and photosensitivity, were also estimated. The findings indicate that the Schottky devices based on the RGO-ZnTe composites exhibit enhanced device performance compared to those based on pristine ZnTe, attributed to the synergistic effects between the RGO sheets and ZnTe nanoflakes.

Address correspondence to E-mail: parthapray@yahoo.com



Contents lists available at ScienceDirect

Materials Today: Proceedings

journal homepage: www.elsevier.com/locate/matpr

Investigation of the metal–semiconductor interface by equivalent circuit model in zinc phthalocyanine (ZnPc) based Schottky diodes and its charge transport properties

Dhananjoy Das, Mainak Das, Puspendu Sahu, Partha Pratim Ray*

Department of Physics, Jadavpur University, Kolkata 700 032, India

ARTICLE INFO

Article history:
Available online xxxx

Keywords:
Phthalocyanines
Semiconductors
Schottky diodes
Impedance spectroscopy
Conductivity
Mobility

ABSTRACT

In this report, the ZnPc-based metal–semiconductor (MS) junction Schottky devices (Al/ZnPc/ITO) were fabricated using an effusion cell coating unit. To study the formation of the MS junction, the surface morphology of the deposited ZnPc thin film was investigated using field-emission scanning electron microscope (FESEM) images. The interfacial properties of the MS junction of the Al/ZnPc/ITO configuration were studied using the ac impedance spectroscopy technique within the frequency range of 50 Hz–10 MHz at room temperature (300 K). The bias-dependent impedance spectroscopy was carried out within the voltage range of ± 1 V to establish the equivalent circuit of the MS junction Schottky diodes (SDs). The current vs. voltage (I–V) measurements of the fabricated SDs were also conducted to deduce the diode parameters, namely on/off ratio, photosensitivity, ideality factor, barrier height, and series resistance. The charge transport parameters including dc conductivity, mobility and transit time of the charge carriers were also estimated employing the spatial-charge limited current (SCLC) theory, which illustrates the enhanced carrier's mobility and consequently, the device performance after light irradiation.

Copyright © 2023 Elsevier Ltd. All rights reserved.

Selection and peer-review under responsibility of the International Conference on Advances in Smart Materials, Chemical & Biochemical Engineering.

1. Introduction

In recent times, the use of organic semiconductors in optoelectronic devices has significantly increased to meet the growing demand for solar energy harvesting. Compared with their inorganic counterparts, organic materials have a low environmental impact and relatively low production costs with unlimited abundance. Among the variety of organic semiconductors, phthalocyanines (Pcs) manifest various excellent features such as non-toxicity, ease of processing, higher physical and thermal stability, and broadly visible light absorbance – which make them a promising candidate for numerous optoelectronic applications, namely, light-emitting diodes [1], solar cells [2], sensors [3]. Amidst many metal-phthalocyanines, the deep bluish-green colored zinc phthalocyanine (ZnPc) has been extensively studied as a promising

material for its excellent photoconductive and photo-responsive properties [4].

However, the potential of the organic zinc phthalocyanine (ZnPc) for prospective optoelectronic device applications still has to be investigated by examining its electrical charge transport parameters and equivalent circuit model of the interfaces present. Understanding the Schottky barrier diodes would be an excellent start to assess the electronic conduction through the metal–organic semiconductor interfaces and subsequently, the performance of the device. In this work, an analysis is reported on the charge transport properties of the ZnPc-based Schottky devices, in which a thin layer of ZnPc was sandwiched between the aluminium (Al) and indium tin oxide (ITO) electrodes. The bias-dependent impedance spectroscopy of the Al/ZnPc/ITO configuration was studied to investigate different interfacial properties. The I–V measurement was also carried out under dark and light conditions to analyze the photo-responsive properties and charge transport mechanism within the MS junction ZnPc-based Schottky devices.

* Corresponding author.

E-mail addresses: parthapray@yahoo.com, parthap.ray@jadavpuruniversity.in (P. Pratim Ray).



Cite this: *Nanoscale Adv.*, 2023, 5, 3655

Development of hierarchical copper sulfide–carbon nanotube (CuS–CNT) composites and utilization of their superior carrier mobility in efficient charge transport towards photodegradation of Rhodamine B under visible light†

Mainak Das,^a Dhananjay Das,^a Sayantan Sil^b and Partha Pratim Ray  ^{*a}

In this work, the synthesis of visible light sensitive copper sulfide (CuS) nanoparticles and their composites with carbon nanotubes (T-CuS) via a solvothermal technique is reported. The synthesized nanoparticles (NPs) and their composites were significantly characterized by powder X-ray diffraction (PXRD), scanning electron microscopy, transmission electron microscopy, X-ray photoelectron spectroscopy, UV-vis spectroscopy, photoluminescence (PL) spectroscopy and thermogravimetric analysis (TGA). The effect of carbon nanotubes (CNTs) on the crystallinity, microstructures, photo-absorption, photo-excitation, thermal stability and surface area of CuS was investigated. The current–voltage (*I* vs. *V*) characteristics of both CuS and T-CuS based Schottky diodes were measured to determine the charge transport parameters like photosensitivity, conductivity, mobility of charge carriers, and transit time. The photocatalytic performance of bare CuS and T-CuS in the decomposition of Rhodamine B dye was studied using a solar simulator. The T-CuS composite showed higher photocatalytic activity (94%) compared to bare CuS (58%). The significance of charge carrier mobility in transferring photo-induced charges (holes and electrons) through complex networks of composites and facilitating the photodegradation process is explained. Finally, the reactive species responsible for the Rhodamine B degradation were also identified.

Received 29th March 2023

Accepted 0th May 2023

DOI: 10.1039/d3na00204g

rsc.li/nanoscale-advances

Introduction

Organic dyes and pigments discharged into water sources, mostly by the paint and textile industries, are causing serious environmental issues and harming the ecosystem in other ways.¹ Over the last few decades, various biological and physicochemical experiments based on physical as well as chemical adsorption approaches have been conducted to decompose these industrial pollutants. However, these processes often produce secondary pollutants and are not cost-effective from

the economic viewpoint.² The photocatalytic approach based on semiconductor materials has demonstrated significant efficiency in wastewater purification among all advanced oxidation techniques known to exist.³ There are some well-known semiconducting photocatalysts, namely TiO₂ and ZnO, which have been widely used to decompose organic pollutants, but their use is hindered due to their wide range bandgaps, which are 3.2 eV and 3.37 eV for TiO₂ and ZnO, respectively, limiting their light absorption mainly in the ultraviolet (UV) region of the solar spectrum.^{4,5} This reduces the redox reactions with the impurities and significantly affects the rate of degradation.⁶

On the other hand, copper(II) sulfide (CuS) has a narrow direct bandgap of 2.29 eV, due to which it can efficiently capture visible light from the solar spectrum, making it practically function as a ‘visible-light-driven photocatalyst’. It also has excellent optical and electronic properties which show great potential in many fields like solar cells,⁷ energy storage,⁸ gas sensors,⁹ biosensors¹⁰ and photocatalysis.¹¹ Copper sulfide has some excellent features, such as its environmentally friendly and non-toxic nature, low cost, biocompatibility, higher physical and chemical stability and ease of recyclability which

^aDepartment of Physics, Jadavpur University, Kolkata 700032, India. E-mail: parthapray@yahoo.com

^bDepartment of Physics, University of Engineering and Management, University Area, Action Area III, B/5, Newtown, Kolkata 700160, India

† Electronic supplementary information (ESI) available: Device fabrication method, calculation of bandgap and dielectric constant, weight (%) test of CNT, charge transfer characteristics of CNT, adsorption of RhB by the catalysts, photodegradation process, function of H₂O₂ in the degradation process, optimization of the composite material with different CNT content, identification of reactive species, recycling test, photocatalytic activity of a non-azo dye, Fig. S1–S9, and eqn (S1) and (S2). See DOI: <https://doi.org/10.1039/d3na00204g>

PAPER

[View Article Online](#)
[View Journal](#) | [View Issue](#)Cite this: *Dalton Trans.*, 2021, **50**, 1721

Phenoxo-bridged dinuclear mixed valence cobalt(III/II) complexes with reduced Schiff base ligands: synthesis, characterization, band gap measurements and fabrication of Schottky barrier diodes†

Abhisek Banerjee,^a Dhananjay Das,^b Partha Pratim Ray,^b Snehasis Banerjee^c and Shouvik Chattopadhyay^{*a}

Two homometallic class-I dinuclear mixed valence cobalt complexes, [(N₃)Co^{III}L¹(μ-C₆H₄(NO₂)CO₂)Co^{II}(N₃)] (**1**) and [(N₃)Co^{III}L²(μ-C₆H₄(NO₂)CO₂)Co^{II}(N₃)] (**2**), have been synthesized using multisite N₂O₄ coordination ligands, H₂L¹ {where H₂L¹ = (2,2-dimethyl-1,3-propanediyl)bis(iminomethylene)bis(6-methoxyphenol) and H₂L² = (2,2-dimethyl-1,3-propanediyl)bis(iminomethylene)bis(6-ethoxyphenol)}. Each complex has been structurally characterized by single crystal X-ray diffraction and spectral analysis. Both the cobalt centers in these dinuclear complexes adopt a distorted-octahedral geometry, where the cobalt (III) center resides at the inner N₂O₂ cavity and the cobalt(II) center resides at the outer O₄ cavity of the reduced Schiff base. Both of them show good electrical conductivity, which has been rationalized by band gap measurements. The band gap in the solid state has been determined by experimental and DFT calculations and it confirms that each of the two complexes behaves as a semiconductor. The space-charge-limited current (SCLC) theory is employed to evaluate the charge transport parameters such as effective carrier mobility and transit time for both complexes. The difference in the conductivity values of the complexes may be correlated with the strengths of extended supramolecular interactions in the complexes. Bader's quantum theory of atoms-in-molecules (QTAIM) is applied extensively to get quantitative and qualitative insights into the physical nature of weak non-covalent interactions. In addition, the non-covalent interaction reduced density gradient (NCI-RDG) methods well support the presence of such non-covalent intermolecular interactions.

Received 27th October 2020,
Accepted 16th December 2020

DOI: 10.1039/d0dt03707a

rsc.li/dalton

Introduction

Mixed valence complexes have gained enormous attention in the field of coordination chemistry since the first synthesis of Prussian blue in 1704 due to their valence localization/delocalization character and intervalence electronic transitions.¹ According to the Robin-Day classification, mixed valence complexes are broadly divided into three major classes *viz.* class-I,

class-II and class-III. Such classifications were made in terms of electron delocalization parameters between the different metal centers.² Focussing on mixed valence chemistry, mixed valence cobalt complexes constituting both cobalt(III) and cobalt(II) ions represent a special class due to their extensive range of applications in magnetism, catalytic activity and electro-chromism.³ The most popular mixed valence complex of cobalt is Co₃O₄, a class-I type, that has long been known for its normal spinel structure where cobalt(III) centers (low spin) reside in an octahedral environment and cobalt(II) centers (high spin) are in a tetrahedral environment.⁴

The exploration of the optoelectronic properties of several complexes is one of the foremost areas of recent research.⁵ The formation of such photoconductive fragments requires the generation and transportation of photoinduced charge carriers within the network.⁶ The complexes may also be used as light-harvesting and energy transfer materials.⁷ They could also be used to fabricate Schottky barrier diodes.⁸ In the

^aDepartment of Chemistry, Inorganic Section, Jadavpur University, Kolkata-700032, India. E-mail: shouvik.chem@gmail.com^bDepartment of Physics, Jadavpur University, Kolkata-700032, India.E-mail: parthapray@yahoo.com^cGovt. College of Engineering and Leather Technology, Salt Lake Sector-III, Block-LB, Kolkata 700106, India†Electronic supplementary information (ESI) available: Hirshfeld surface analysis, Tables S1–S4 and Fig. S1–S6. CCDC 2035842 and 2035843 for **1** and **2**. For ESI and crystallographic data in CIF or other electronic format see DOI: 10.1039/d0dt03707a



Cite this: *CrystEngComm*, 2020, 22, 5170

Synthesis, characterization, self-assembly and non-ohmic Schottky barrier diode behaviors of two iron(III) based semiconductors with theoretical insight†

Tanmoy Basak,^a Dhananjay Das,^b Partha Pratim Ray,^{iD}^b Snehasis Banerjee^{iD}^c and Shouvik Chattopadhyay^{iD}^{*a}

Two mononuclear iron(III) complexes, $[\text{Fe}(\text{L}^1)(\text{N}_3)]$ and $[\text{Fe}(\text{L}^2)(\text{N}_3)]$, $\{\text{H}_2\text{L}^1 = N,N'$ -bis(3-methoxysalicylidene)diethylenetriamine and $\text{H}_2\text{L}^2 = N,N'$ -bis(3-ethoxysalicylidene)diethylenetriamine $\}$ have been synthesized and characterized by elemental, spectral and X-ray crystallographic studies. Structural features have been examined in detail that reveal the formation of interesting supramolecular networks generated through weak non-covalent interactions. The current-voltage characteristic curves for an Al/complex Schottky-barrier diode (SBD) exhibit non-ohmic behavior. Important parameters like ideality factor, barrier height and series resistance are measured with the help of thermionic emission (TE) theory. Space-charge-limited current (SCLC) theory is employed to evaluate the charge transport parameters such as effective carrier mobility and transit time for both complexes. Complex **1** is found to be more conductive. To obtain insight into the physical nature of weak non-covalent interactions, Bader's quantum theory of atoms-in-molecules (QTAIM) is used extensively. Additionally, the non-covalent interaction reduced density gradient (NCI-RDG) methods established nicely the presence of such non-covalent intermolecular interactions.

Received 13th February 2020,
Accepted 29th June 2020

DOI: 10.1039/d0ce00223b

rsc.li/crystengcomm

Introduction

Metal-organic frameworks and coordination polymers have the ability to be used in optoelectronics.¹ A Schottky diode is one of such optoelectronic devices which may be fabricated by any semiconducting material showing a rectifying nature at the metal-semiconductor junction.² In a Schottky diode, a junction is formed between metals (such as aluminum, silver or platinum) and a semiconductor.³ The device performance and reliability are dependent on the interfacial properties of metal-semiconductor junctions. Use of semiconducting inorganic complexes to fabricate a Schottky diode is also reported in the literature.⁴

Many mononuclear metal complexes have also been used to fabricate a Schottky diode.⁵ The electronic charge in these complexes may be transported *via* their supramolecular architectures, *e.g.* H-bonding network, π - π interaction assembly, *etc.*⁶ However, prior to this work, no systematic analysis was performed to check the ability of these supramolecular interactions for carrying charges in their crystalline assembly. In this work, we have synthesized two more or less similar mononuclear complexes, differing only in the pendant side arms; one contains methoxy side arms and the other contains ethoxy side arms. Thus, everything in these two complexes is practically the same, except their solid state supramolecular interactions. Our intention is to correlate electrical properties with their supramolecular interactions.

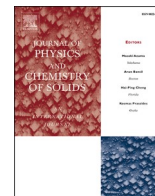
In this work, we concentrate on iron(III), because the ability of iron(III) Schiff base complexes to exhibit Schottky barrier diode behavior was not revealed as yet. So, the behavior of iron(III)-Schiff base complex based semiconductors is completely unknown. Therefore, we have synthesized two mononuclear iron(III) complexes, $[\text{Fe}(\text{L}^1)(\text{N}_3)]$ (**1**) and $[\text{Fe}(\text{L}^2)(\text{N}_3)]$ (**2**), with two similar N_3O_2 donor Schiff base ligands $[\text{H}_2\text{L}^1 = N,N'$ -bis(3-methoxysalicylidene)-diethylenetriamine and $\text{H}_2\text{L}^2 = N,N'$ -bis(3-ethoxysalicylidene)-

^a Department of Chemistry, Inorganic Section, Jadavpur University, Kolkata-700032, India. E-mail: shouvik.chem@gmail.com

^b Department of Physics, Jadavpur University, Kolkata-700032, India. E-mail: parthapray@yahoo.com

^c Govt. College of Engineering and Leather Technology, Salt Lake Sector-III, Block-LB, Kolkata 700106, India

† Electronic supplementary information (ESI) available: Contains detailed discussion of supramolecular interactions, IR spectra, device fabrication, *etc.* CCDC 1981611 and 1981612 contain the supplementary crystallographic data for complexes **1** and **2**. For ESI and crystallographic data in CIF or other electronic format see DOI: 10.1039/d0ce00223b



Investigation of conduction kinetics in Al/CuInSe₂ Schottky device utilizing impedance spectroscopy (IS) measurement and study of its photosensing behaviour

Animesh Biswas^{a,b}, Sayantan Sil^a, Arka Dey^c, Joydeep Datta^a, Dhananjay Das^a, Partha Pratim Ray^{a,*}

^a Department of Physics, Jadavpur University, Kolkata, 700032, India

^b Department of Physics, Sreegopal Banerjee College, Mogra, Hooghly, 712148, India

^c Department of Condensed Matter Physics and Material Sciences, S. N. Bose National Centre for Basic Sciences, Block JD, Sec. III, Salt Lake, Kolkata, 700106, India

ARTICLE INFO

Keywords:

Al/CuInSe₂ Schottky diode
Impedance spectroscopy (IS)
I–V Characteristics
Space charge limited current (SCLC)
Mobility

ABSTRACT

Copper Indium Selenide (CuInSe₂) has been synthesized by solvothermal synthesis method. The Schottky diode (SD) has been fabricated by using the material and the interface characteristics of Al/CuInSe₂/ITO have been investigated with the help of ac impedance spectroscopy (IS) analysis (under dark condition) and dc current-voltage (I–V) measurements (under both dark and photo condition). IS is a very important and powerful technique to investigate and analyze the impedance at the boundary regions of SDs. Ac impedance spectra of Al/CuInSe₂ SD have been recorded in the wide range of frequency from 40 Hz to 20 MHz during dc bias scanning from –0.5 V to 0.5 V under dark condition. From forward I–V characteristics, important parameters such as ideality factor (η), photosensitivity, barrier height (Φ_b), series resistance (R_s) of SD were obtained under dark and photo condition. The photosensitivity of the Al/CuInSe₂ SD was found to be 3.36. For better realization of charge transport phenomena through the MS junction, space charge limited current (SCLC) theory has been employed. The effective mobility of the carrier is evaluated in dark and photo condition as $0.42 \times 10^{-3} \text{ m}^2 \text{ V}^{-1} \text{ s}^{-1}$ and $2.11 \times 10^{-3} \text{ m}^2 \text{ V}^{-1} \text{ s}^{-1}$ respectively. It has been observed that the mobility is improved 5 times under illumination compared to the dark condition.

1. Introduction

For the sake of conservation of energy, a low cost sustainable power source is extremely essential for the well being of the human kind [1]. The conventional solar cells being very costly, it requires a search for materials for solar energy conversion. Photovoltaic cells based on I–III–VI compounds have shown a lot of promises for solar energy harvesting. Copper indium selenide (CuInSe₂) is one of those promising materials and a ternary chalcopyrite IB–IIIA–VIA compound semiconductor. It (CIS) has been one of the most potential absorber materials because few of its alluring characteristics for photovoltaic application such as high optical absorption coefficient, suitable band gap [2,3] that can harvest a wide range of visible lights which are ideal for the development of photovoltaic devices. This material has gained much attention for the researchers everywhere throughout the world also because of its good stability under radiation, low toxicity and high

efficiency of PV devices [4]. Furthermore, one can reduce the absorption layer up to a several micrometers and by substituting of In³⁺ by Ga³⁺ the band gap can be adjusted from 1.00 eV to 1.68 eV [2]. In view of such optical and electrical properties it has become one of the most significant photovoltaic materials. Various researchers have paid their attention for the measurements of thermal conductivity, optical absorption, Raman spectra and magneto-resistance on both single and polycrystalline samples [5–9]. R. Bouferra et al. [10] reported the AC conductivity of n-CuInSe₂ material utilizing impedance spectroscopy (IS) over a broad range of temperatures [80 K–300 K] and frequencies [20 Hz–1 MHz]. The report also provided some useful insight about the conduction mechanism in the material. However, metal-semiconductor (MS) contacts are mostly used as rectifying junction for different electronic devices like solar cells, ICs and photosensitive detectors [11–15]. As the MS junction plays a pivotal role in different microelectronic devices, the study of the influence of this material on the performance of electronic

* Corresponding author.

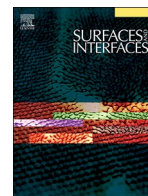
E-mail addresses: partha@phys.jdvu.ac.in, parthapray@yahoo.com (P.P. Ray).

<https://doi.org/10.1016/j.jpcs.2020.109878>

Received 6 September 2020; Received in revised form 20 October 2020; Accepted 25 November 2020

Available online 1 December 2020

0022-3697/© 2020 Elsevier Ltd. All rights reserved.



Electrical and photocatalytic properties of composites of manganese and titanium oxides

Bharati Debi Biswas^a, Joydeep Datta^b, Moushumi Dutta Purkayastha^a, Dhananjoy Das^b, Partha Pratim Ray^b, Abhigyan Dutta^c, Tapas Pal Majumder^{a,*}

^a Department of Physics, University of Kalyani, Kalyani 741235, West Bengal, India

^b Department of Physics, Jadavpur University, Kolkata 700032, West Bengal, India

^c Department of Physics, University of Burdwan, Burdwan 713104, West Bengal, India

ARTICLE INFO

Keywords:

Nanocomposite

Mesoporous

Photoactivity

Carrier transport properties

ABSTRACT

In this study, mesoporous manganese oxide-titanium dioxide ($\text{Mn}_2\text{O}_3/\text{TiO}_2$) nanocomposites have been synthesized following sol-gel method. Different molar ratios of Mn/Ti were evaluated and MT2 (5:1) showed the best photoactivity as well as carrier transport properties. The Langmuir–Hinshelwood model was delineated to calculate the reaction rate which was found to be highest for MT2 (min^{-1}). Several parameters including pore size distribution, pore volume, adsorption isotherms have been analyzed as per Brunauer–Emmett–Teller (BET) method. That was attributed to the high surface area ($121.81 \text{ m}^2/\text{g}$). The space charge limited current (SCLC) theory was employed to calculate the mobility and transit time. MT2 showed the highest carrier mobility ($326 \times 10^{-7} \text{ m}^2 \text{ V}^{-1} \text{ s}^{-1}$) and lowest transit time ($0.08 \times 10^{-5} \text{ s}$) which are desirable for efficient photoactivity.

1. Introduction

The synthesis of mesostructured materials has been recently attracted tremendous research interest [1]. TiO_2 is the most widely investigated mesoporous metal oxide exhibiting excellent potential applications as catalysts, electrode materials, photocatalysts, sensors, solar cells and in bioanalytical chemistry [2–6]. However, its high bandgap energy restricts its applicability. So, TiO_2 in other medium as a dispersed material or as a constituent of a nanocomposites seems to be considered as an attractive approach for the fabrication in support of its suitable application in diverse field. Because of its poor dispersity, reduced surface area and pore sizes etc. are still regularly practiced so that it can be extended using the absorption properties of TiO_2 to the visible range as well as to change the equilibrium concentration of electrons and holes of such with the variation of concentration of dopant.

Many attempts have been made to modify the physical, chemical and optical properties by mixing TiO_2 with other oxides [7–9]. Among them, the coupled $\text{Mn}_2\text{O}_3/\text{TiO}_2$ seems to present the interesting optical and photocatalytic properties which may also prove to be a perspective material for solar energy conversion. Non-toxicity and earth abundance have been recently featured due to the introduction of Mn_2O_3 in $\text{Mn}_2\text{O}_3/\text{TiO}_2$ mixed system. These composites may be explicitly used for

the fabrication of materials which may provide mainly capacitance in nature [10, 11], and also may be allowed for absorption of visible light which theoretically can be extended up to infrared region [12–16]. However, a few works have been reported till now in literature related to the application of such composites in photocatalysis [5, 17, 18]. Topoglidis et al. [5] synthesized a series of visible light driven mesoporous structured $\text{MnO}_2/\text{TiO}_2$ nanocrystal photocatalysts with large pore size. Purkayastha et al. [17] reported about the photodegradation capability of low temperature synthesized phase pure rutile titanium oxide nanostructured materials. Waris et al. [18] reported about the photocatalytic degradation of palm oil mill effluent using the synthesized manganese oxide-modified titanium oxide nanocomposites. They emphasized about the improved photocatalytic efficiency because of the effective significant separation of photogenerated electrons and holes pairs. On the basis of these findings, in the present paper, we have not only tried to focus on the optical properties of manganese oxide-titanium dioxide nanocomposites ($\text{Mn}_2\text{O}_3\text{--TiO}_2$) but have also informed about the effectiveness of spherical like $\text{Mn}_2\text{O}_3/\text{TiO}_2$ in dye degradation because of ultraviolet (UV) irradiation. Since TiO_2 has a high bandgap having behavior of inertness in activity and Mn_2O_3 has the capability for photodegradation as well as high oxidation reagent, therefore, the introduction of TiO_2 in Mn_2O_3 system makes its fruitful for having high photocatalytic reactivity barring the capability of photodegradation.

* Corresponding author.

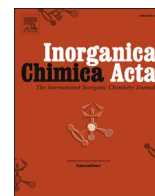
E-mail address: tpmajumder1966@gmail.com (T.P. Majumder).

<https://doi.org/10.1016/j.surfin.2020.100606>

Received 2 June 2020; Accepted 20 July 2020

Available online 25 July 2020

2468-0230/ © 2020 Elsevier B.V. All rights reserved.



Research paper

Cd(II) coordination polymer of fumaric acid and pyridyl-hydrazide Schiff base: Structure, photoconductivity and theoretical interpretation

Angeera Chandra^a, Dhananjay Das^b, Joaquín-Ortega Castro^c, Kaushik Naskar^a, Srikanta Jana^a, Antonio Frontera^{c,*}, Partha Pratim Ray^{b,*}, Chittaranjan Sinha^{a,*}

^a Department of Chemistry, Jadavpur University, Jadavpur, Kolkata 700 032, India

^b Department of Physics, Jadavpur University, Jadavpur, Kolkata 700 032, India

^c Departament de Química, Universitat de les Illes Balears, Crta. de Valldemossa km 7.5, 07122 Palma de Mallorca, Balears, Spain

ARTICLE INFO

Keywords:

Pyridyl-hydrazone

Fumarate

Cd(II)

Photoconductivity

The computational study

ABSTRACT

A 2-D coordination polymer, $\{[\text{Cd}_4(\text{ppmh})_4(\text{fum})_4(\text{H}_2\text{O})_4] \cdot 3\text{H}_2\text{O}\}_n$ (CP) (H₂fum, fumaric acid; **ppmh**, N-Pyridin-2-yl-N'-pyridin-4-ylmethylene-hydrazine) has been synthesized and structurally characterized by single-crystal X-Ray diffraction study. The structure shows that the coordination polymer is constituted by fumarate bridging via chelation/bidentate coordination to neighbouring Cd(II) centers. The ligand, **ppmh** has two terminal pyridyl-N and hydrazino-N binding centers. One of the pyridyl-N and hydrazino-N forms a five-member chelate ring with Cd(II) while other pyridyl-N coordinates to adjacent Cd(II) ion. The 2D CP extended itself to 3D supramolecular array by virtue of $\pi-\pi$ interaction and H-bonding. The optical bandgap of the CP is 3.29 eV which implies semiconducting nature and has been supported by the ground state computational analysis. The electrical conductivity and I-V characteristic have shown that the conductivity is improved upon light irradiation (DC conductivity: dark, 0.87×10^{-3} and light, $2.45 \times 10^{-3} \text{ Sm}^{-1}$) and approves the Schottky Barrier Diode (SBD) feature. The DFT computation and the partial density of states (PDOS) calculation show that the π -character of the aromatic hydrazone ligand dominates the valence and conduction bands with negligible participation of the Cd orbitals.

1. Introduction

Pyridyl-N containing π -deficient molecules are excellent photoactive and electroactive coordination polymer (CPs) forming ligands [1–11]. Functionalization of such organic motifs may have advantages to serve as bridging ligands to bring many (same or different) cation centers together which may assist light-harvesting mechanism, improve conductivity, magnetism etc. The coordination polymer, a multinuclear platform, is made by organic linkers and the metal knots [5–11]. Judicious selection of components of CPs in the designing pathway is an important aspect because the properties of CPs have been highly influenced by the nature of metal ions, functionality and flexibility of the ligands [12,13]. Dicarboxylates are used as bridging linkers for the preparation of different classes and dimensions of CPs with different coordinating modes and sizes [14–16]. The electrical properties of CPs are dependent on the steric and electronic nature of bridging ligands [13–15]. The CPs are highly sensitive towards external stimuli like luminescence [17,18], thermal, electric, magnetic and optical fields

[19]. The CPs synthesized from aliphatic carboxylate linkers with d^{10} metal ions such as Zn^{2+} , Cd^{2+} are found to exhibit semiconducting properties and have been used in photonic and electronic devices [20–25]. Band gap of the CPs can be tuned by changing the size and the conjugation of the bridging ligands. In this view, mixed ligand CPs are the promising hybrid CP to design electrical, electronic and photonic devices. Pyridyl donors are the useful ligand to generate such stimuli sensitive materials [15,20]. Pyridyl-hydrazones can bind in different coordination modes to metal ions giving rise to stable crystalline CPs with interesting structural aspects [26–28]. Fumaric acid has also been used to supply a platform to prepare coordination polymers [29,30]. In this work, we have designed pyridyl-hydrazone Schiff base that bridges in different fashion along with fumaric acid to bring Cd(II) centers together to synthesize a CP, $\{[\text{Cd}_4(\text{ppmh})_4(\text{fum})_4(\text{H}_2\text{O})_4] \cdot 3\text{H}_2\text{O}\}_n$ (**ppmh**, N-Pyridin-2-yl-N'-pyridin-4-ylmethylene-hydrazine). The characterization of the CP has been done by several spectroscopic procedures (FT-IR, UV–Vis) and the Single Crystal X-ray Diffraction study approves the structure. **Ppmh** has two types of coordination modes- it coordinates

* Corresponding authors.

E-mail addresses: toni.frontera@uib.es (A. Frontera), parthapray@yahoo.com (P. Pratim Ray), crsjuchem@gmail.com (C. Sinha).

<https://doi.org/10.1016/j.ica.2021.120253>

Received 1 September 2020; Received in revised form 4 January 2021; Accepted 4 January 2021

Available online 12 January 2021

0020-1693/© 2021 Elsevier B.V. All rights reserved.

PAPER

[View Article Online](#)
[View Journal](#) | [View Issue](#)Cite this: *Mater. Adv.*, 2023,
4, 215

Improved electrical conductivity of Co(II) and Cu(II) ladder polymers in the fabrication of photoresponsive Schottky devices†

Basudeb Dutta,^{‡,ab} Dhananjay Das,^{‡,c} Kumari Raksha,^a Chittaranjan Sinha,^{‡,d} Sumit Khanra,^{*a} Partha Pratim Ray^c and Mohammad Hedayetullah Mir^{‡,b}

In this work, two new Cu(II) and Co(II) based coordination polymers (CPs), [Co₂(bpd)₂(nac)₂]·2CH₃OH·H₂O (**Co-CP**) and [Cu₂(bpd)₂(nac)₂]·2CH₃CN·2H₂O (**Cu-CP**) respectively, have been synthesized using a bidentate pyridyl ligand, *N,N'*-bis(1-pyridine-4-yl-ethylidene) (bpd), linker with the less explored 3-(1-naphthyl)acrylic acid (nac) ligand appended at the metal centre to fulfil the molecular geometry. Here, **Co-CP** forms a one-dimensional (1D) ladder polymer, whereas **Cu-CP** consists of a combination of 1D chains and 1D ladder polymers. Interestingly, both the CPs exhibit semiconducting behaviour with increased conductivity upon illumination, signifying the photosensitive nature. However, **Cu-CP** reveals better conductivity as compared to **Co-CP**. This is obvious from the field emission electron microscopy (FESEM) study, where **Cu-CP** with flower-like morphology shows a higher surface area with respect to the rod-shaped morphology of **Co-CP**, resulting in higher charge transport. To the best of our knowledge, Co/Cu based CPs showing photosensitivity seem to be scarce. Thus, this study opens a new avenue in the fabrication of photoresponsive electronic devices.

Received 19th September 2022,
Accepted 9th November 2022

DOI: 10.1039/d2ma00911k

rsc.li/materials-advances

Introduction

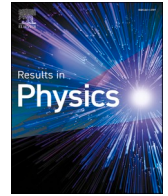
The dramatic revolution of laboratory to land applications of materials chemistry propagates at an extraordinary pace. Application of materials has directly been governed by the structural architecture and morphology. In this regard, coordination polymers (CPs)^{1–9} have attracted materials researchers mostly because of their unique molecular structures and excellent stabilities. These hybrid molecular systems are constructed through inorganic metal ions or metal clusters and organic ligands.^{10–15} Hence, the molecular properties as well as applications are also regulated by the nature of the metal centers and ligands. A combination of organic components (O-donor and N-donor ligands) is commonly exploited to achieve structural

varieties and desired molecular properties.^{16–18} In these coordination systems, metal salts or organic linkers are judiciously selected to confer the application field. In fact, there is an essential relationship between the structural architecture, properties and utilities of the materials. Rational construction and scientific judgment during the engineering of these crystalline materials make them easier to characterize and illustrate important structure–property relationships. In the construction of higher dimensional supramolecular architecture, various supramolecular interactions such as hydrogen bonding, $\pi \cdots \pi$, C–H $\cdots \pi$, cation $\cdots \pi$, anion $\cdots \pi$, halogen \cdots halogen, halogen $\cdots \pi$ and van der Waals interactions play the crucial role.^{19–21} Sometimes, these self-assembled structures are entirely unlike and more proficient than the unassembled forms. The discussed inorganic–organic hybrid materials are extremely applicable in the territory of gas sorption, molecular storage and separation, ion exchange, electrochemical catalysis, energy technology, drug delivery, temperature-dependent magnetism, sensing and detection of noxious ions and emerging analytes, proton conductance, electrical conductivity, electronic device fabrication, etc.^{22–34}

Of these, utilization of CPs in electrical conductivity and device fabrication is particularly important as these CPs can be explored to overcome the energy crisis situation and for technological interest. However, in CPs, the poor extended electronic coupling among the metal nodes and the ligands impedes competent charge transport.^{35–38} The consequential electronic

^a Department of Chemical Sciences, Indian Institute of Science Education and Research Kolkata, Mohanpur, West Bengal 741246, India.E-mail: sumit.khanra@iiserkol.ac.in^b Department of Chemistry, Aliah University, New Town, Kolkata 700 156, India.E-mail: chmmir@gmail.com^c Department of Physics, Jadavpur University, Jadavpur, Kolkata 700 032, India^d Department of Chemistry, Jadavpur University, Jadavpur, Kolkata 700 032, India† Electronic supplementary information (ESI) available: Experimental section, Tables S1–S5, Fig. S1–S12, Scheme S1 and X-ray crystallographic data in CIF format for compounds **Co-CP** and **Cu-CP**. CCDC 2203412 (**Co-CP**) and 2203413 (**Cu-CP**). For ESI and crystallographic data in CIF or other electronic format see DOI: <https://doi.org/10.1039/d2ma00911k>

‡ These authors contributed equally.



Findings of inhomogeneity in barrier height of Schottky junction Al/rGO-SnO₂ having anomaly in theoretical and experimental value of Richardson constant: A Gaussian approach

Pubali Das^a, Baishakhi Pal^a, Mrinmay Das^{a,b,c}, Sayantan Sil^{a,d}, Dhananjay Das^a, Animesh Layek^a, Partha Pratim Ray^{a,*}

^a Department of Physics, Jadavpur University, Jadavpur, Kolkata 700032, West Bengal, India

^b School of Applied and Interdisciplinary Sciences, Indian Association for the Cultivation of Science, Jadavpur, Kolkata 700032, West Bengal, India

^c Department of Physics, Sister Nivedita University, New Town, Kolkata 700156, West Bengal, India

^d Department of Physics, University of Engineering and Management, University Area, Action Area III, B/5, Newtown, Kolkata 700160, West Bengal, India

ARTICLE INFO

Keywords:

rGO-SnO₂ nanocomposite
Defects
Schottky diode
Barrier height
Interface
Inhomogeneity
Gaussian distribution

ABSTRACT

In this research, the temperature dependent dynamical behavior of Schottky junction Al/rGO-SnO₂ has been investigated with thermionic emission (TE) theory within the temperature regime 303 K to 423 K at interval 20 K. During analysis of electrical charge transport behavior an anomalous change is observed in the value of ideality factor and barrier height with rising temperature for the junction. Experimentally derived Richardson constant (of the order 10⁻⁵ A/m²K²) using TE theory is exceptionally substandard to the theoretical (of the order 10⁶ A/m²K²) values. The beauty of this work is to find out the underline physics for this discrepancy in measurement of Richardson constant (might arose due to inhomogeneity in barrier of metal-semiconductor junction) by assuming the Gaussian distribution of the barrier height with TE theory at the junction. It is obvious that the occurrence of barrier inhomogeneity across the junction leading charge transport phenomena which mostly impacting upon the parameters of Schottky diodes and its nature because of intrinsic formation of ripples and ridges. In this study, it is found that the charge transport mechanism is highly follows the single Gaussian distribution. The material characterization and its Schottky behavior in normal temperature had been published elsewhere.

Introduction

Thin film based Metal-Semiconductor (MS) Schottky Barrier Diode (SBD)s [1] have attracted huge attention for its wide range of applications, especially in the micro-electronic devices such as optoelectronic [2], bipolar integrated circuits [3] and high frequency device applications [4]. Several current transport mechanism such as thermionic emission (TE), barrier tunneling and carrier generation-recombination at space charge region have been studied to explain various MS junction. Moreover, for the unique features like high conductivity, wide optical transparency and great compatibility for thin film fabrication, graphene composite has proven itself as an important candidate for application in Schottky barrier diodes (SBDs) [5]. As various defects in the crystalline structure effect on material's characteristics under the impact of different environments, having high grain boundary density

graphene composites can be influenced by the operating environment [6]. The current conduction mechanism of SBDs depends upon numerous parameters like the operating temperature of the device, barrier height inhomogeneities at MS junction, internal series resistance, functional bias voltage, process of diode preparation [7]. Moreover, there has been growing interest towards rGO-SnO₂ nanocomposite in bio sensors [8], Schottky diodes etc. [9]. The reported band gap value of rGO-SnO₂ is nearly 3.1 eV for the rutile structured SnO₂ decorated in rGO layers [10]. The performance and reliability of rGO-SnO₂ based SBD is dominated by ideality factor, Schottky barrier height (SBH), active metal semiconductor interface, density of interface states and internal series resistance at the metal-semiconductor (MS) junction [11]. For an ideal SBD, ideality factor is 1 and the barrier height is measured simply by the difference between the work function of the metal and the electron affinity of the semiconductor [12]. Barrier height (BH) influences

* Corresponding author.

E-mail address: parthap.ray@jadavpuruniversity.in (P.P. Ray).

<https://doi.org/10.1016/j.rinp.2022.105996>

Received 18 July 2022; Received in revised form 11 September 2022; Accepted 15 September 2022

Available online 16 September 2022

2211-3797/© 2022 The Authors. Published by Elsevier B.V. This is an open access article under the CC BY-NC-ND license (<http://creativecommons.org/licenses/by-nc-nd/4.0/>).



Cite this: *CrystEngComm*, 2023, 25, 162

Designing of a Zn(II)-isonicotinohydrazido thiophenyl based 2D coordination polymer: structure, augmented photoconductivity and superior biological activity†

Kingshuk Debsharma,^{‡a} Sunanda Dey,^{‡bc} Dhananjay Das,^d Satyajit Halder,^e Joaquin Ortega-Castro,^{id f} Sarita Sarkar,^g Basudeb Dutta,^{id h} Suvendu Maity,^b Kuladip Jana,^{*e} Antonio Frontera,^{id *f} Partha Pratim Ray^{*d} and Chittaranjan Sinha^{id *b}

Thiophenyl-isonicotinohydrazide, a multidentate Schiff base, acts as a tridentate N,O,N donor out of which N,O-chelates to one Zn(II) and pyridyl-N links to the adjacent Zn(II) to constitute a 2D coordination polymer, {[Zn(SIZ)₂·DMF]_n} (CP1) (HSIZ = (E)-N'-(thiophen-2-ylmethylene)isonicotinohydrazide, DMF = N,N-dimethylformamide). CP1 has been characterized by different physicochemical data and confirmed by single crystal X-ray crystallographic measurement. The H-bonding, C-H...π and π...π interactions in the 2D geometry of the coordination polymer creates a 3D architecture. The Tauc plot for CP1 indicates an optical band gap of 2.91 eV (calc., 2.48 eV) (direct)/2.80 eV (calc., 2.50 eV) (indirect) and CP1 is non-conducting ($2.53 \times 10^{-9} \text{ Sm}^{-1}$) in the dark while it is enhanced by ~23 000 times ($5.97 \times 10^{-5} \text{ Sm}^{-1}$) upon light irradiation (1000 Wm^{-2}). Considering the biological importance of isoniazid and Zn(II) the antimicrobial activities of CP1 is measured against *Staphylococcus aureus* and *Escherichia coli* (MIC, 20 $\mu\text{g mL}^{-1}$). The cytotoxic potency of CP1 is examined on thirty different cancer cell lines which has been found active against four cancer cell lines, HCT-116 (colon cancer), HeLa (cervical cancer), MDA-MB-231 (human breast cancer cell), and HepG2 (hepatocellular carcinoma) and the results are compared with the human normal kidney epithelial cell line, NKE. However, CP1 shows the highest anticancer efficiency against HeLa (IC₅₀: $9.13 \pm 2.32 \mu\text{g mL}^{-1}$) cells. The mechanism of cell killing activity may presumably be the generation of intracellular reactive oxygen species as suggested by the caspase 3/7 activation assay.

Received 17th August 2022,
Accepted 12th November 2022

DOI: 10.1039/d2ce01128j

rsc.li/crystengcomm

Introduction

In the past few decades, the scientific community has witnessed a considerable switching in the mode of research in chemistry from the fundamental area to diverse real-world applications. Subsequently, the current drift in research specially in inorganic chemistry has increasingly been focused in the designing of different coordination polymers (CPs)/ metal-organic frameworks (MOFs) owing to their diversity in structural frameworks, easy synthetic procedure, high thermal and chemical stability, excellent level of purity in their native crystalline form, large surface area, high porosity (MOFs) and tunable structure-property relationship.^{1–4} The physical properties of MOFs make them attractive for various practical applications in the field^{5–11} of sorption, separation of gases, sensing of ions, catalysis, magnetism, photoconductivity, etc. The promising involvement of MOFs in numerous environmentally benign applications such as fuel storage, fuel cells, batteries, superconductivity, supercapacitors and photo-

^a Department of Chemistry, Indian Institute of Technology Madras, Chennai 600036, India

^b Department of Chemistry, Jadavpur University, Kolkata 700032, India. E-mail: crsjchem@gmail.com

^c Department of Chemistry, Mrinalini Datta Mahavidyalaya, Birati, Kolkata 700051, India

^d Department of Physics, Jadavpur University, Jadavpur, Kolkata 700 032, India. E-mail: parthap.ray@jadavpuruniversity.in

^e Division of Molecular Medicine, Bose Institute, Kolkata-700 056, India. E-mail: kuladip.jana@gmail.com

^f Departament de Química, Universitat de les Illes Balears, Crta de Valldemossa km 7.5, 07122 Palma de Mallorca, Balears, Spain. E-mail: toni.frontera@uib.es

^g Department of Biotechnology, School of Science and Technology, The Neotia University, Diamond Harbour, West Bengal 743 368, India

^h Department of Chemical Sciences, Indian Institute of Science Education and Research Kolkata, Mohanpur, West Bengal 741 246, India

† Electronic supplementary information (ESI) available. CCDC 2169715. For ESI and crystallographic data in CIF or other electronic format see DOI: <https://doi.org/10.1039/d2ce01128j>

‡ Both the authors contributed equally.

RESEARCH ARTICLE

View Article Online

View Journal | View Issue



Cite this: *Inorg. Chem. Front.*, 2019, **6**, 1245

Synthesis of a Zn(II)-based 1D zigzag coordination polymer for the fabrication of optoelectronic devices with remarkably high photosensitivity†

Basudeb Dutta,^a Dhananjay Das,^b Joydeep Datta,^b Angeera Chandra,^c Srikanta Jana,^c Chittaranjan Sinha,^{id} Partha Pratim Ray^{id}*^b and Mohammad Hedayetullah Mir^{id}*^a

A Zn(II) based one-dimensional coordination polymer (1D CP), [Zn₄(adc)₄(4-cltpy)₄]·CH₃OH·2H₂O (**1**) (H₂adc = acylenedicarboxylic acid and 4-cltpy = 4'-chloro-[2,2';6',2''] terpyridine), has been synthesized by a slow diffusion method and characterized by X-ray crystallography. Here, the linear adc ligand acts as the linker between two Zn(II) centers and a chelating 4-cltpy ligand is appended at the metal node. The connectivity of the ligands with metal ions generates a 1D zigzag polymeric chain. The zigzag chains are aggregated through various secondary interactions to construct a three-dimensional (3D) structure. The optical band gap has been determined and correlated with the theoretical band gap calculated by density functional theory (DFT) computations, which reveals that compound **1** possesses semiconducting properties. Moreover, compound **1** shows remarkably high photosensitivity ($P_s = 1134$) upon illumination by light. Therefore, compound **1** has the potential to be used in optoelectronic devices and solar cells.

Received 14th February 2019,
Accepted 26th March 2019

DOI: 10.1039/c9qi00162j

rsc.li/frontiers-inorganic

Introduction

In the modern era of the scientific community, application based research works are much more important due to their necessity to help living beings and save the environment from disaster. In this regard, materials science claims to be an active participant in the game of scientific evolution. It gathers chemistry, physics and biology within a single umbrella. However, only chemistry has the opportunity to design and synthesize the materials, whereas physics or biology uses them for different applications. The polymeric form of a coordination compound, *i.e.* the coordination polymer (CP),^{1–9} is one important area in materials chemistry or materials science. CPs are occasionally called hybrid materials as they are designed from both organic and inorganic compounds. From the structural point of view, inorganic metal ions or metal clusters act as nodes, while organic O, N, S, and P donor ligands

act as spacers. Judicious choices of nodes and spacers have demonstrated the structural diversity of CPs.^{10–13} By tuning the structural architecture, one can easily regulate the properties of CPs.^{14–18} It is also an eternal focus of chemists to correlate between the structure and properties of a compound or material. The properties of a material are affirmed by their application. Thus, there are inevitable relations among structure, properties and applications. In the case of CPs, the properties are altered with the dimensionality, as one-dimensional (1D), two-dimensional (2D) or three-dimensional (3D) according to the difference in chemical atmosphere.

CPs provide many possible options for the fabrication of photonic and optoelectronic devices, however, the area has attracted much less attention than the typical numerous applications of such materials. During the last few years, polymeric organic compounds have been used as semiconducting materials,^{19–24} but their poor thermal stability has them back. As a consequence, coordination polymeric compounds could be a potential candidate for use in optoelectronic devices. As the organic components perform a crucial role in shaping the overall electronic properties, these materials can be tailored by the judicious selection of organic ligands. The relatively strong covalent bonds designed by the self-assembly process facilitate the rational design and provide high thermal and chemical stability to the CPs.^{25–29}

Recently, we have been able to synthesize a series of 1D and 2D CPs mainly based on monodentate N-donor ligands, where

^aDepartment of Chemistry, Aliah University, New Town, Kolkata 700 156, India.
E-mail: chmmir@gmail.com

^bDepartment of Physics, Jadavpur University, Jadavpur, Kolkata 700 032, India.
E-mail: partha@phys.jdvu.ac.in

^cDepartment of Chemistry, Jadavpur University, Jadavpur, Kolkata 700 032, India

†Electronic supplementary information (ESI) available: Fig. S1, Tables S1 and S2, TGA results, PXRD patterns, DFT tables, Fig. S4 and X-ray crystallographic data in CIF format for compound **1**. CCDC 1895972. For ESI and crystallographic data in CIF or other electronic format see DOI: 10.1039/c9qi00162j

Elucidation of Inhomogeneous Heterojunction Performance of Al/Cu₅FeS₄ Schottky Diode With a Gaussian Distribution of Barrier Heights

Sayantan Sil^{ID}, Rajkumar Jana, Animesh Biswas, Dhananjay Das, Arka Dey, Joydeep Datta, Dirtha Sanyal, and Partha Pratim Ray^{ID}

Abstract—Here, we analyze inhomogeneities in the barrier height (BH) of Al/Cu₅FeS₄ Schottky device from the electrical (I - V) measurements with a temperature range between 303 and 408 K. The temperature-dependent performance of our fabricated device is analyzed by using the thermionic emission (TE) theory. Some important diode parameters like BH (Φ_{bo}), ideality factor (η), and series resistance (R_s) are evaluated from the forward current-voltage characteristic curves. The calculated η and R_s of the Schottky barrier diode (SBD) decrease, whereas the Φ_{bo} of the device increases with the increase in temperature. The value of Richardson constant (A^*) for our material is obtained as $1.94 \times 10^{-4} \text{ A cm}^{-2} \text{ K}^{-2}$ in the temperature range 303–408 K, which is found as much lesser than the theoretical value of $29.90 \text{ A cm}^{-2} \text{ K}^{-2}$. The discrepancy of A^* from the theoretical value has been well explained by TE theory with the assumption of Gaussian distribution (GD) of BHs due to the existence of BH inhomogeneities at metal semiconductor (MS) junction. The obtained values of the mean BH Φ_{bo} and the standard deviation σ_s are 1.026 eV and 173 mV in the corresponding temperature range. The mean BH (1.199 eV) and Richardson constant ($29.73 \text{ A cm}^{-2} \text{ K}^{-2}$) are determined from the modified Richardson plot depending on the inhomogeneity of BHs. Apparent BH consists of mean BH (Φ_{bo}) and standard deviation (σ_s). The σ_s contributes significantly to the modification of Richardson constant and mean BH. The calculated value of the modified Richardson constant is in close agreement with the theoretical value. From

C - V measurements built-in voltage and effective BH of this structure were calculated as a function of frequency.

Index Terms—Al/Cu₅FeS₄ Schottky diode, barrier inhomogeneities, Gaussian distribution (GD), I - V characteristics, Richardson constant.

I. INTRODUCTION

THE ternary chalcogenide materials have enjoyed much attention and plenty of prospects in the field of material science due to its promising physical properties [1], [2]. Bornite (Cu₅FeS₄) is a common and widespread copper sulfide mineral that has been well known for many years due to its fascinating electrical and magnetic properties [3], [4]. The current conduction mechanism of Schottky barrier diodes (SBDs) is dependent on various parameters, such as the device temperature, process of surface preparation, inhomogeneities of barrier height (BH) at metal semiconductor (MS) interface, the series resistance of the device, and applied bias voltage [5], [6]. Many researchers have paid their attention to study the current transport properties through the SBD at room temperature, but the information about the conduction process or the nature of barrier formation at the MS interface could not be described with room temperature I - V analysis [7], [8]. Therefore, it is crucial to study the temperature-dependent analysis of SBDs, which allows us to realize the different views of conduction mechanisms and barrier formation at MS interface [9], [10]. In this article, the forward bias I - V measurements have been carried out in the temperature range 303–408 K on Al/Cu₅FeS₄ SBDs. On the other hand, to the best of our knowledge, the temperature-dependent analysis of Al/Cu₅FeS₄ SBD has not yet been reported. The unusual behavior of the temperature dependence SBD parameters, such as BH, ideality factor, Richardson's constant, and series resistance, is evaluated on the assumption of a Gaussian distribution (GD) of BHs.

II. EXPERIMENTAL SECTION

A. Materials and Synthesis

All the analytical reagent (AR) grade reagents are purchased from Sigma-Aldrich. All reagents are used as it is procured. Cu₅FeS₄ (Bornite) is prepared by the hydrothermal synthesis technique. The synthesis procedure is reported in the previous work [2].

Manuscript received January 12, 2020; accepted March 23, 2020. Date of publication April 10, 2020; date of current version April 22, 2020. The work of Partha Pratim Ray was supported by the Science and Engineering Research Board-Department of Science and Technology (SERB-DST), Government of India under Grant EMR/2016/005387. The review of this article was arranged by Editor J. Mateos. (Corresponding author: Partha Pratim Ray.)

Sayantan Sil, Rajkumar Jana, Dhananjay Das, Joydeep Datta, and Partha Pratim Ray are with the Department of Physics, Jadavpur University, Kolkata 700032, India (e-mail: partha@phys.jdvu.ac.in).

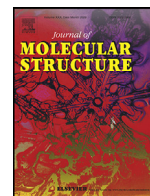
Animesh Biswas is with the Department of Physics, Jadavpur University, Kolkata 700032, India, and also with the Department of Physics, Sreegopal Banerjee College, Hooghly 712148, India.

Arka Dey is with the Department of Condensed Matter Physics and Material Sciences, S. N. Bose National Center for Basic Sciences, Kolkata 700106, India.

Dirtha Sanyal is with the Variable Energy Cyclotron Center, Kolkata 700064, India, and also with the Training School Complex, Homi Bhabha National Institute, Mumbai 400094, India (e-mail: dirtha@vecc.gov.in).

Color versions of one or more of the figures in this article are available online at <http://ieeexplore.ieee.org>.

Digital Object Identifier 10.1109/TED.2020.2983489



Intriguing π -interactions involving aromatic neutrals, aromatic cations and semiconducting behavior in a pyridinium-carboxylate salt

Prantika Das, Samiul Islam, Dhananjay Das, Partha Pratim Ray, Saikat Kumar Seth*

Department of Physics, Jadavpur University, Kolkata 700032, India

ARTICLE INFO

Article history:

Received 12 January 2023

Revised 6 March 2023

Accepted 7 March 2023

Available online 11 March 2023

Keywords:

Extended π -network

Theoretical studies

UV-Vis spectroscopy

I-V characteristics and semiconducting behavior

Impedance study and Nyquist plot

ABSTRACT

A new pyridinium-carboxylate salt (**1**) has been synthesized and characterized by elemental analysis, spectroscopy, electrical studies, and single-crystal X-ray diffraction. X-ray structure of 4,4'-oxybis(benzoic acid) with 4-(Dimethylamino)pyridine is stabilized through hydrogen bonds, C-H $\cdots\pi$, and numerous π -interactions together with $\pi\cdots\pi$, $\pi\cdots\pi^+$, and $\pi^+\cdots\pi^+$ stacking. The cooperativity of the weak noncovalent interactions has been explored well that plays a crucial role in building diverse extended supramolecular frameworks. The hydrogen bonds dictate the basic structural motifs representing the supramolecular association. However, the cooperativity of the weak noncovalent contacts plays a significant role in constructing the final solid-state structure. The entire assembly produces a rare combination of $\pi\cdots\pi/\pi\cdots\pi^+/\pi^+\cdots\pi^+/\pi^+\cdots\pi$ extended network. The binding energies of the noncovalent interactions have anticipated the usage of DFT calculations. Intricate combinations of these noncovalent interactions are characterized through computational studies by using Bader's theory of "Atoms-in-Molecules" (AIM) and "noncovalent interaction" (NCI) plot index. The evaluation of topological parameters at (3, -1) BCPs ensured the 'closed-shell' nature of the intermolecular interactions. By employing Tauc's plot, the optical band gap was calculated from UV-Vis spectroscopy. A device was fabricated for the analysis of I-V characteristics of the compound. An impedance study was carried out and consequently, Nyquist plot was represented for the further investigation of the semiconducting behavior of the compound.

© 2023 Elsevier B.V. All rights reserved.

1. Introduction

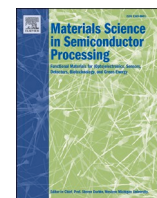
Development in crystal engineering is based on the Cambridge Structural Database which is used to interpret, analyze, and design a crystal involving non-covalent interactions [1]. In crystals, there is the sum of a series of molecular recognition called self-assembly built upon the various types of weak non-covalent interactions through several forces between functional solids [1–4]. Initially, supramolecular chemistry was defined as the non-covalent interaction between hosts and guests [2,3]. The rapid expansion in supramolecular chemistry over the past 20 years encompasses that it is not only a host-guest system but also the idea behind it can be used in making of molecular devices and machines, molecular recognition, so-called 'self-process' such as self-assembly and self-organization [4–8].

The use of reversible interactions between ions and aromatic rings as a leading force for self-assembly or ion binding continues

to be an active area of research [8,9]. Noncovalent interactions are the object of interest due to their impeccable contribution in forming supramolecular architectures in organic solids [10,11]. Hydrogen bonds are leading among weak noncovalent interactions and are widely used in processing molecular recognition in crystalline materials [10–12]. On the other hand, the character of the aromatic systems whose electronic structure is determined by the composition of carbon atoms in their sp^2 hybridization mainly makes the interaction of aromatic rings (π -ring) unique [11,12]. Incorporating this π -ring, there is various kind of weak interactions such as C-H $\cdots\pi$, π -stacking, cation $\cdots\pi$, anion $\cdots\pi$, and lone pair $\cdots\pi$ interactions which are taken into consideration in building different types of supramolecular architectures [13,14]. The dispersive nature of $\pi\cdots\pi$ stacking interaction takes part in a significant role in crystal engineering and molecular recognition. However, $\pi^+\cdots\pi$ and $\pi^+\cdots\pi^+$ interactions are more robust than usual $\pi\cdots\pi$ interactions as formers are more favorable in magnitude and different in directionality [14,15]. Moreover, the molecular entity of π systems having π^+ or π^- moieties is a fascinating subject in the study of stacking interaction. The interaction is more indulgent when two types of species, π -electron rich and π -electron deficient, come

* Corresponding author.

E-mail addresses: dasprantika2013@gmail.com (P. Das), samiulislam361@gmail.com (S. Islam), dhananjaydas404@gmail.com (D. Das), parthapray@yahoo.com (P.P. Ray), saikat.k.seth@jadavpuruniversity.in (S.K. Seth).



Improved device performance of rod like ZnO in a Schottky type photosensor compared to particle like ZnO: Analysis of charge transport

Mrinmay Das^{a,b}, Pubali Das^b, Joydeep Datta^b, Dhananjay Das^b, Somobrata Acharya^a, Partha Pratim Ray^{b,*}

^a School of Applied and Interdisciplinary Sciences, Indian Association for the Cultivation of Science, Jadavpur, Kolkata, 700032, West Bengal, India

^b Department of Physics, Jadavpur University, Jadavpur, Kolkata, 700032, West Bengal, India

ARTICLE INFO

Keywords:

Morphology
Schottky
Metal-semiconductor interface
Photoresponse
Space charge limited current
Charge transport

ABSTRACT

In this work, we report two different synthesis process of semiconducting ZnO which modifies the morphology of the ZnO materials and its impact in photosensing Schottky diode. Hydrothermal and co-precipitation method were used to synthesize ZnO which gave rise to rod like (ZnO HT) and particle like ZnO (ZnO COP), respectively. From UV-Vis analysis, ZnO HT exhibited greater optical absorption. Al/ZnO (HT and COP)/ITO Schottky diodes were fabricated and the photoresponse as well as diode parameters were investigated by current-voltage and capacitance voltage measurements. Then charge transport properties were determined by space charge limited current theory and impedance spectroscopy. The results showed that the ZnO HT based SBD delivered a responsivity of 0.144 A/W which is 121% higher than the responsivity showed by ZnO COP based SBD (0.065 A/W). The specific detectivity of ZnO HT was measured at 7.54×10^9 Jones, a noticeable improvement from the 4.10×10^9 Jones of ZnO COP. The carrier mobility, lifetime and diffusion length of the ZnO HT based device were found to be $0.0014 \text{ cm}^2 \text{ V}^{-1} \text{ s}^{-1}$, $72.35 \text{ } \mu\text{s}$ and $72.37 \text{ } \mu\text{m}$ respectively which are again superior to its counterpart. The faster and better charge transport is facilitated by the rod like morphology of the former. The study demonstrates improved device performance of rod like ZnO based Schottky diode and provides detail analysis of the Al/ZnO interface which can be beneficial for future research on metal-semiconductor junction.

1. Introduction

For a long time, zinc oxide (ZnO) has been the centre of intensive research and it continues to be so due to its optical transparency, non-toxic environment friendly nature, simple cost effective synthesis procedure and promising applications. Due to hexagonal wurtzite crystal structure and noncentro symmetry of the oxygen atom in tetrahedral coordination geometry, ZnO exhibits exciting properties [1,2]. Equipped with these favourable attributes, ZnO has been extensively used for electronic, optoelectronic, and electrochemical applications such as Schottky diodes, lasers, thin-film transistors, piezoelectric devices, light-emitting diode, photovoltaic cell and gas sensors [3–18].

Among them, metal-semiconductor Schottky barrier diodes (SBDs) are one of the most important devices for radio frequency (RF) electronics, optoelectronics, and fast switching device application. Not only that, they offer an interesting platform for material characterization [19–21]. The performance of a Schottky diode is influenced by the

material properties and especially, by the morphology of the materials. Over the past decade, application of rod like structures of ZnO has received widespread attention due to a large surface-to-volume ratio with reduced dimension [2]. Significant time and effort is being devoted for high-quality ZnO-based Schottky diode fabrication and their characterization using a variety of techniques [22–27]. The morphology of ZnO can change depending upon the synthesis technique and that change can affect its performance in a Schottky device. To have a good understanding of the metal-semiconductor interface, along with current-voltage (I–V) characteristics, capacitance-voltage (C–V) and impedance spectroscopy measurements can play a pivotal role. In addition, the analysis of charge transport from I–V and impedance spectroscopy is very important.

So, in this paper, we report the synthesis of ZnO with particle (ZnO COP) and rod like (ZnO HT) morphology by coprecipitation and hydrothermal method, respectively. Thereafter Al/ZnO SBD are fabricated and their photoresponse is compared. To investigate the Al/ZnO

* Corresponding author.

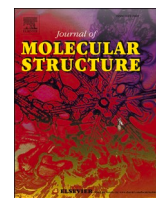
E-mail address: partha@phys.jdvu.ac.in (P.P. Ray).

<https://doi.org/10.1016/j.mssp.2021.105799>

Received 27 August 2020; Received in revised form 13 February 2021; Accepted 7 March 2021

Available online 23 March 2021

1369-8001/© 2021 Elsevier Ltd. All rights reserved.



Crystallographic, theoretical and conductivity studies of two new complexes [Ni(II) and Cu(II)] based on mixed ligands approach

Nirvik Ghosh^a, Mohd Afzal^b, Dhananjoy Das^c, Partha Pratim Ray^c, Samit Pramanik^a, Sudipta Pathak^{d,*}, Kinsuk Das^e, Rosa M. Gomila^f, Antonio Frontera^{f,*}, Subrata Mukhopadhyay^a

^a Department of Chemistry, Jadavpur University, Kolkata 700032, India

^b Department of Chemistry, College of Science, King Saud University, Riyadh 11451, Saudi Arabia

^c Department of Physics, Jadavpur University, Kolkata 700032, India

^d Department of Chemistry, Haldia Government College, Debhog, Purba Medinipur, West Bengal, India

^e Department of Chemistry, Chandernagore College, Hooghly, West Bengal 712136, India

^f Department of Chemistry, Universitat de les Illes Balears, Crta de Valldemossa km 7.5, Palma de Mallorca (Balears) 07122, Spain

ARTICLE INFO

Keywords:

Ni(II) and Cu(II) complexes
Non-covalent interactions
Antiparallel $\pi\cdots\pi$ stacking
DFT studies
Schottky Barrier Diode

ABSTRACT

Two new complexes [Ni(C₇H₃NO₅) (C₁₅H₁₁N₃)] · 4(H₂O) (**1**) and [Cu(C₇H₃NO₅) (C₁₅H₁₁N₃)] · 4(H₂O) (**2**) have been synthesized using mixed chelating ligands [4-hydroxypyridine-2,6-dicarboxylic acid (chelidamic acid) (C₇H₅NO₅) and 2,2':6',2''-terpyridine (C₁₅H₁₁N₃)] in aqueous medium. The two complexes were characterized by UV–visible, IR spectroscopy as well as by single-crystal X-ray diffraction analysis. The geometries of both the complexes are distorted octahedral with N₄O₂ chromophore. The non-covalent interactions found in the solid state architectures of complexes **1** and **2** have been described focusing on $\pi\cdots\pi$ stacking and hydrogen bonding interactions. These non-covalent interactions played an imperative role in building of multi-dimensional supramolecular architectures. These interactions have been explored theoretically by density functional theory (DFT) focusing on the antiparallel π - π stacking in self-assembled dimers and the hydrogen bonding networks mediated by the lattice water molecules. MEP surface calculations combined with QTAIM and NCI plot analysis were used to rationalize and characterize the non covalent interactions involved in the assemblies. The low optical band gaps of the two complexes exhibit semiconducting property leading to potentially fabricate Schottky Barrier Diode.

1. Introduction

Crystal engineering is the domain of science that includes the role of intermolecular interaction for building up molecular architectures [1–4]. Crystal formation, growth and stability depend on various non covalent interactions like H-bonds, halogen bonds, cation $\cdots\pi$, anion $\cdots\pi$, $\pi\cdots\pi$ stacking, lone pair $\cdots\pi$, C–H $\cdots\pi$ interactions, etc. of relatively weaker strength [5–11]. Among them, $\pi\cdots\pi$ stacking and hydrogen bonding interactions are two main pillars under non covalent category and so arrest interest of researchers for their decisive role in the building of the crystal packing [12,13]. Thus, a sound understanding of the aforesaid weak non-covalent interactions is needed for using them as motifs in making new strategy for synthesis. First of all, a successful route for the synthesis of unique complex compounds with attractive

topological structures has to be designed. Recently, synthetic routes for preparation of complex compounds with mixed ligands having polar functional groups (N- and O-donor centres) have been explored where interesting topological structures are shown [14]. Ligands with ONO donor chromophore have found immense interest in the field of crystal engineering [15–17]. The self-assemble process of coordination compounds generally depends on various factors like coordination geometry (octahedral, tetrahedral or square planar) of the central metal, nature of organic chelating ligand, polarity of solvent, pH of reaction medium, temperature, concentration of reactants during reaction, ratio of reactants, reaction time, and so on [4,18].

2,2':6',2''-Terpyridine plays a crucial role in metallo-supramolecular chemistry not only for their π stacking ability among aromatic rings but also for excellent chelating ability with various metal ions [19–24].

* Corresponding authors.

E-mail addresses: sudiptachemster@gmail.com (S. Pathak), toni.frontera@uib.es (A. Frontera).

<https://doi.org/10.1016/j.molstruc.2023.137106>

Received 1 September 2023; Received in revised form 17 October 2023; Accepted 15 November 2023

Available online 16 November 2023

0022-2860/© 2023 The Author(s). Published by Elsevier B.V. This is an open access article under the CC BY license (<http://creativecommons.org/licenses/by/4.0/>).

CURRENT TRENDS IN MATERIALS SCIENCE AND ENGINEERING 2021

Certificate of Participation



THIS IS PRESENTED TO

Dhananjay Das

Jadavpur University

For their active participation

IN INTERNATIONAL CONFERENCE ON CURRENT TRENDS IN MATERIALS SCIENCE AND ENGINEERING (CTMSE 2021)
ORGANIZED BY INSTITUTE OF ENGINEERING & MANAGEMENT, SALT LAKE DURING 11th TO 13th MARCH, 2021


DR. SATYAJIT CHAKRABARTI
PATRON




DR. ARUN KUMAR BAR
CHAIR




RANABIR BANIK
CONVENER




DR. SASWATI BARMAN
CONVENER





INTERNATIONAL CONFERENCE

On
RENEWABLE ENERGY

FEBRUARY 25-27, 2022

Organized by

CENTRE FOR NON-CONVENTIONAL ENERGY RESOURCES (CNCER), UNIVERSITY OF RAJASTHAN, JAIPUR, INDIA

INTERNATIONAL ASSOCIATION FOR HYDROGEN ENERGY (IAHE), USA & MRSI, RAJASTHAN CHAPTER



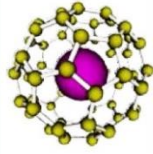
CERTIFICATE OF PARTICIPATION

This is to certify that **Mr. Dhananjoy Das** of **Department of Physics, Jadavpur University, India** has actively participated in the conference and presented a paper entitled **Analysis of equivalent circuit model and charge transport phenomena of metal-semiconductor interfaces in Zinc Phthalocyanine (ZnPc) based heterojunction Schottky diode**. His/her participation is highly appreciated.

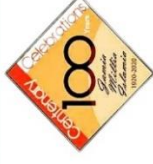

Prof. S.N. Dolia
Chairman & Director, CNCER


Prof. I.P. Jain
Hon'ble Chairman, ICRE-2022


Dr. Chhagan Lal
Convenor & Dy. Director, CNCER



ICNOC-2022



International Conference
on
Nanotechnology: Opportunities & Challenges

CERTIFICATE OF PARTICIPATION

This is to certify that

Dhananjoy Das

participated and presented a paper titled

Analysis Of The Charge Transport Phenomena And Equivalent Circuit Model Of The Metal-Semiconductor Interfaces In Zinc Phthalocyanine (ZnPc) Based Schottky Diodes

in the International Conference on Nanotechnology: Opportunities & Challenges (ICNOC-2022) in online mode, organized by Department of Applied Sciences & Humanities, Faculty of Engineering & Technology, Jamia Millia Islamia, New Delhi, India on November 28-30, 2022.



Prof. Zishan Husain Khan
Organizing Chair

Prof. Nafis Ahmad
Organizing Secretary

Dr. Mukesh Pratap Singh
Organizing Secretary





NATIONAL INSTITUTE OF TECHNOLOGY ROURKELA
(An Institution of National Importance)



Certificate of Participation

This is to Certify that the Paper titled

Investigation of the metal- semiconductor interfaces by equivalent circuit
model in Zinc Phthalocyanine (ZnPc) based Schottky diodes and its
charge transport properties

has been presented by the author(s)

Dhananjoy Das

from

Jadavpur University

In one of the technical sessions of An International Conference on **ADVANCES IN SMART MATERIALS, CHEMICAL & BIOCHEMICAL ENGINEERING (CHEMSMART-22)** organized by the Department of Chemical Engineering, NIT Rourkela, during December 16-18, 2022.

Dr. Krunal Gangawane
Convener-CHEMSMART-22

Prof. Abanti Sahoo
Chairman -CHEMSMART-22



SRM INSTITUTE OF SCIENCE AND TECHNOLOGY

Kattankulathur - 603 203, Tamil Nadu, India.

7th International Conference on Nanoscience and Nanotechnology (ICONN-2023)

(Virtual Conference) March 27 - 29, 2023

Certificate of Participation

This is to certify that Mr. / Ms. / Dr. **Dhananjay Das** has participated and presented a paper entitled **Effect of higher carrier mobility of reduced graphene oxide-zinc telluride nanocomposite towards efficient charge transfer facility and the photodecomposition of Rhodamine B** in the 7th International Conference on Nanoscience and Nanotechnology (ICONN-2023) organized by Department of Physics and Nanotechnology, SRM IST, India during March 27- 29, 2023, in association with Shizuoka University, Japan; National Yang Ming Chiao Tung University, Taiwan; GNS Science, New Zealand; University of Rome Tor Vergata, Italy; Asian Consortium on Computational Materials Science (ACCMS), Japan; Indian Ceramic Society; Indian Physics Association (IPA); Solar Energy Society of India (SESI); Innovation, Science & Technology Foundation - Tirupati (ISTF-T) and co-sponsored by Defence Research and Development Organization (DRDO), India; Council of Scientific & Industrial Research (CSIR), India; The Indian Science Congress Association (ISCA) and Springer Nature.



Head

Department of Physics and Nanotechnology
SRM IST, KTR


Chairperson

School of Applied Sciences
SRM IST, KTR





1ST DFT-M ONLINE HANDS-ON-TRAINING ON

DENSITY FUNCTIONAL THEORY MODELLING OF MATERIALS

(NANOPARTICLES, THIN FILMS, UNIT CELLS USING QUANTUM ESPRESSO)

Centre for Advanced Computational Studies, New Delhi, India

(Registered under Ministry of SME, Government of India for Research and Experimental Development on Natural Sciences and Engineering)

(ISO 9001:2015 Certification for Hands-on-Training on Computational Science including DFT calculation of Materials, Molecular Docking and Dynamics)

Website: <https://aimsdelhi.com>, Email: admin@aimsdelhi.com

Certificate of Participation

This is to certify that

Dhananjoy Das, Research Scholar, Jadavpur University, West Bengal

has actively participated in the 1st Workshop on Density Functional Theory Modelling of Materials (DFT-M)

organized by the Centre for Advanced Computational Studies, Delhi from 14th – 20th September 2023 via Online Mode.

Hands-on-Training program included 7 Interactive Sessions by DR. NIKHIL AGGARWAL on Density Functional

Theory Modelling of Materials at Nanoscale using Quantum Espresso and Burai Software applications.

Dr. Nikhil Aggarwal

Head of the Department & Convener



Certificate No.: 2023/DFT-M/W/1/93



1ST ONLINE HANDS-ON-TRAINING ON

RIETVELD REFINEMENT OF X-RAY DIFFRACTION (RRD)

(USING FULLPROF SOFTWARE PACKAGE)

Centre for Advanced Computational Studies, New Delhi, India

(Registered under Ministry of SME, Government of India for Research and Experimental Development on Natural Sciences and Engineering)
(ISO 9001:2015 Certification for Hands-on-Training on Computational Science including DFT calculation of Materials, Molecular Docking and Dynamics)

Website: <https://aimsdelhi.com>, Email: admin@aimsdelhi.com

Certificate of Participation

This is to certify that

DHANANJOY DAS, Research Scholar, Jadavpur University, West Bengal

has actively participated in the 1st Hands-on-Training on Rietveld Refinement of X-Ray Diffraction data (RRD) organized by the Centre for Advanced Computational Studies, Delhi from 1st – 7th January 2024 via Online Mode. Training program had

7 Interactive Sessions by DR. NIKHIL AGGARWAL on Rietveld Refinement of X-Ray Diffraction data using **FullProf**

Software Package.

Dr. Nikhil Aggarwal

Head of the Department & Convener



ISO Accreditation Body: United Accrediting
Services Limited, United Kingdom
Certificate No.: 2023/RRD/W/1/130